THE UNIVERSITY OF CHICAGO

STRUCTURE-PROPERTY RELATIONSHIPS OF ORGANIC FUSED CONJUGATED POLYMERS

A DISSERTATION SUBMITTED TO

THE FACULTY OF THE DIVISION OF THE PHYSICAL SCIENCES

IN CANDIDACY FOR THE DEGREE OF

DOCTOR OF PHILOSOPHY

DEPARTMENT OF CHEMISTRY

BY

ANDRIY NESHCHADIN

CHICAGO, ILLINOIS

DECEMBER 2020

TABLE OF CONTENTS

LIST OF TABLES

LIST OF SCHEMES

LIST OF FIGURES

ACKNOWLEDGEMENTS

First and foremost I would like to thank my research advisor prof. Luping Yu for his incredible patience and support over my years at the University of Chicago. I first met him during Physical Organic Chemistry classes, where I was enchanted by his approach to deeply understand physical phenomena surrounding organic molecules. During research talks I was enamored by rational design of functional organic materials where every atom played a role and promptly joined the group. Prof. Yu has always set high goals for my projects and has helped me develop and grow as a scientist. I owe him the great privilege of working on diverse and interesting topics with many collaborators all throughout the graduate school. I am extremely grateful to have him as a research supervisor and mentor.

I would also like to thank prof. Viresh Rawal and prof. Guangbin Dong for serving on my dissertation committee.

I owe my success and achievements to a lot of people who supported, taught, educated and otherwise guided me throughout my life. I would like to express my gratitude to my parents, Oleg and Olga Neshchadin, and family for raising me and giving all the opportunities to learn and develop.

I was blessed with great teachers in my high school in Lviv, Ukraine. Especially my chemistry teacher, Kernichna Svitlana Vasylivna, who opened the world of chemistry to me and was my mentor and coach in countless competitions.

My chemistry career would be impossible without the great people at the Department of Chemistry of Ivan Franko National University of Lviv, who helped me with both entry into the profession as well as my first research activities.

I am also extremely grateful to the Zavtra.ua scholarship program from Viktor Pinchuk foundation. My participation in 10th Yalta Annual Meeting, YES-2013, prompted me to seek greater experience and further education abroad.

Lastly I would like to thank a number of friends from Luping Yu group and beyond, who provided emotional support and helped me deal with challenges of grad school as well as helped me develop as a scientist: Valerii Sharapov, Polina Navotnaya, Vlad Kamysbaev, Igor Fedin, Na Zhang, Zhengxu Cai, Qinghe Wu, Wai-Yip Lo, Lianwei Li, Alex Schneider, Aireal Jenkins, Ahmad Awais, Kelliann Koehler and many others.

CHAPTER 1

INTRODUCTION

1.1 Ladder molecules - promising materials for OLET applications

Blue light emitting materials with high efficiency and stability are basic color components in the field of organic light emitting diode (OLED). Although a great effort is devoted to developing these materials, it is still a challenging task to generate ideal materials. Challenges are even tougher for designing materials for organic light emitting transistor (OLET) devices, in which charge carriers need to travel larger distance before recombination. Materials must exhibit highly efficient luminescence, high ambipolar mobility and excellent processability. Conceptually there is a trade-off between mobility and luminescence efficiency[1]. Intermolecular interactions like π-π stacking benefit charge transport, but simultaneously provide pathways for the excited states to undergo non-radiative relaxation. In order to address these issues we focus our attention on polymers. We found that polymers with semi-ladder structures are promising to find compromise between counteracting luminescence and mobility properties.

Fused aromatic rings is a promising approach for OLET materials because ladder structure minimizes vibrational relaxation, increasing quantum yield (QY) of fluorescence. Planar structure enhances mobility of material: no torsional barrier as in conventional conjugated polymers – all p-orbitals on carbon atoms are parallel and in perfect position for overlap. Planar structure also allows opportunities for π-π stacking which allows charge holes and electrons to hop from one molecule to the next. Energy levels can be tuned either by electron donating or withdrawing substituents or by alternating donor and acceptor moieties in the backbone.[2–4] Polymer materials exhibit the following advantages

- Higher mobility than small molecules because of chain transport and different conformations allowing for π-π stacking.
- The resulting films exhibit better mechanical strength and environmental stability.
- Solution processable materials are compatible with ink-jet printing in manufacturing

Therefore, for practical applications it is important to develop materials with the following aspects:

1. High mobility
2. High quantum yield of fluorescence
3. Tunable energy levels
4. Straightforward and reliable synthesis

1.2 Strategies to engineer high-mobility materials

1.2.1 Improvement of molecular packing

Donor-acceptor interactions greatly facilitate efficient interchain π-π stacking, as partial intermolecular charge transfer creates attractive electrostatic forces between different polymer chains.[5,6] Another crucial aspect in design of high mobility materials is efficient crystal packing. Since alkanes typically have 3.6-3.8 Å distances in single crystals and π-systems most often space only 3.4 Å apart, great steric hindrance between alkyl chains can be a major disrupting force in solid state.[7–11] The workaround is to have longitudal spacing between positions of alkyl chains on polymer backbone so that in solid state polymer chains can "slip" past each other with alkyl chains of one chain filling empty space between alkyl chains of a neighboring polymer.

Interaction between neighboring polymer chains is crucial for high charge carrier mobility. One of the approaches to rationally design such materials is molecular docking.[12] It means how well fragments of one chain fit into cavities or pockets formed by other chains. Pei and

coworkers explored this idea with 10 isoindigo-based polymers that have different donor units. They have found that centrosymmetric donors bestow on polymers few orders of magnitude higher hole mobility than axisymmetric ones by the means of better molecular packing. Likely reason is that centrosymmetric polymers have greater linearity and adopt rod-like conformations, while axisymmetric ones have greater backbone curvature which puts strain on the lamellar structure and makes π-π stacking less efficient. AFM images point to greater crystallinity and formation of fibrillary aggregates of centrosymmetric polymers, and axisymmetric ones are amorphous. Better lamellar packing of centrosymmetric polymers was also supported by GIXD measurements.

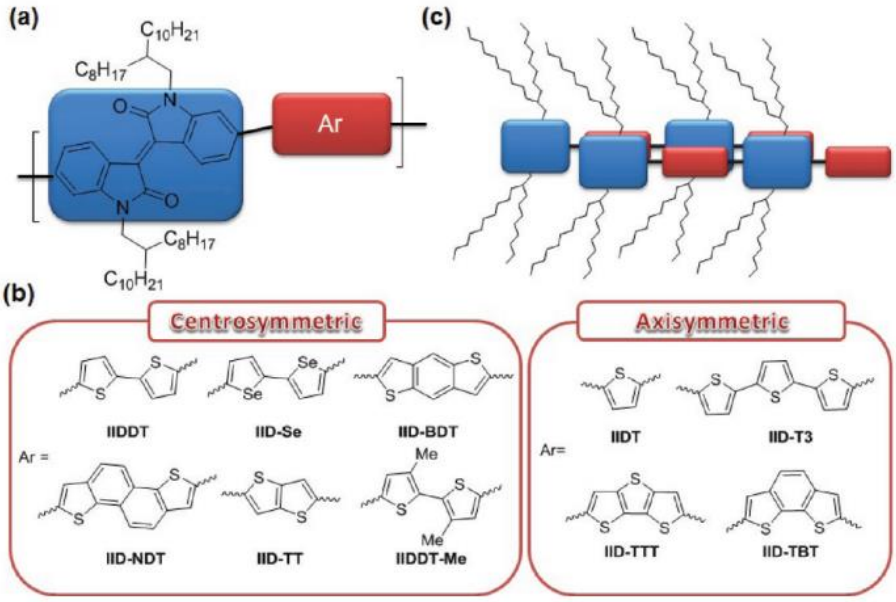

Figure 1-1. Dependence of hole mobility on symmetry of monomers. Reprinted with permission from Ref [12].

Similar conclusions can be made about other polymers based on NDI and DPP: linear polymer chains pack better and have greater mobilities than polymers with zigzag arrangement of repeating units.[13–20] Polymers with very electron-withdrawing NDI and BTD units reached electron mobility of 8.5 with hole mobility of 1.7 $cm^2V^{-1}s^{-1}$.[21]

Alkyl side chains are generally used as solubilizing groups for organic electronic materials. However, they also play a crucial role in determining how well organic polymers can interact with neighboring polymers via π-π stacking and therefore have direct effect on charge transport properties of conjugated polymers. Since holes and electrons need to hop from one polymer chain to the other, the closer the distance, the more efficient is charge transport. Branching point represents the greatest steric hindrance in alkyl chains. Control in its proximity to the conjugated backbone can modulate solubility and charge carrier mobilities. This was used extensively to optimize polymer structure for high mobility p-type[22–27], n-type[28,29] and ambipolar[30–32] materials. Kim et al. synthesized a series of polymers with DPP acceptor and selenophene vinylene selenophene SVS donor with varying alkyl chains[25]. The key chemistry lies in the reaction of 2-decyl-tetradecyl bromide with magnesium and copper chloride to afford alkylcuprates which next react with dibromoalkanes to afford alkyl bromides with C2-C9 spacer to branching point. Then DPP is alkylated and copolymerized with ditin-SVS. The Stille polymerization yields a series of polymers 25-DPP-SVS to 32-DPP-SVS.

Scheme 1-1. Synthesis of DPP-SVS polymers

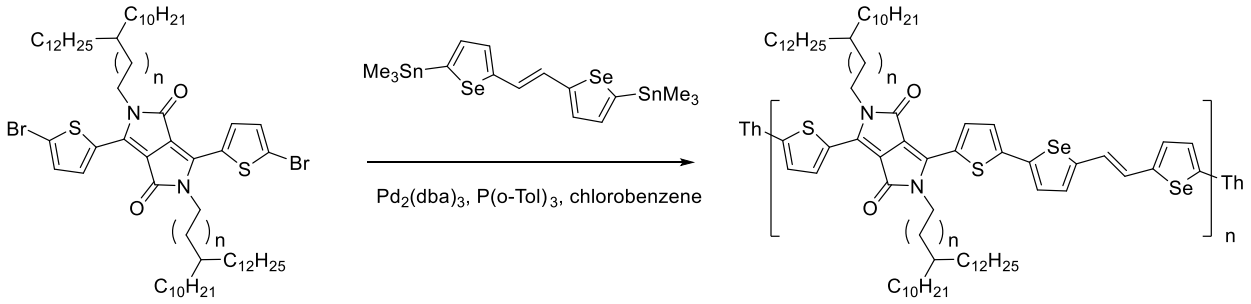

It was discovered that up to C6 spacer length there is an odd-even effect: for spacers with even number of carbon atoms d(100)-spacing between polymer chains is significantly smaller and their hole mobilities higher than for odd-carbon versions. If spacer is longer than 6 mobility

becomes lower due to insulating effect of alkyl chains. Solution-sheared thin film of 29-DPP-SVS with 6-carbon spacer showed the highest hole mobility of up to 17.8 $cm^2V^{-1}s^{-1}$. Molecular weight of polymers is known to have strong effect on charge carriers' mobility. Longer conjugated polymer chains can have more contact points with each other where holes and electrons can jump from one chain to the other. The observed odd-even trend follows closely the molecular weight variation of polymer samples that were studied: Mn=23.7, 19.8, 31.4, 25.6, and 34.1 kDa for 25-29-DPP-SVS polymers. However it is reasonable to assume that molecular weight isn't the culprit in observed structure-property relationships because it doesn't explain the data for 29-32-DPP-SVS polymers.

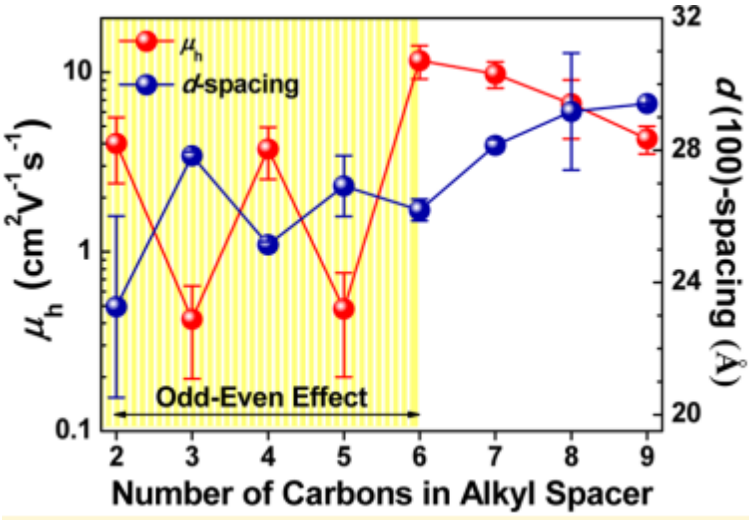

Figure 1-2. Dependence of hole mobility on spacer length of branched alkyl chains. Reprinted with permission from Ref [25].

1.2.2 Alignment of energy levels with electrodes.

Fluorination of monomers has become a workhorse in solar cell community to tune energy levels and device performance.[33–36] Yu and coworkers have synthesized a series of fluorinated versions of PTB7: with 1 fluorine on TT, with 2 on BDT and with 3 fluorines on both

TT and BDT.[37] Partial fluorination was best for material properties as PTBF1 showed highest PCE of 7.2% as compared to 2.3% for PTBF3. This improvement is due to .improved open-circuit volatage, which is determined by tuned HOMO and LUMO energy levels, as well as balanced effect of fluorination on film morphology and influence of phase separation between PCBM and polyfluorinated polymers.

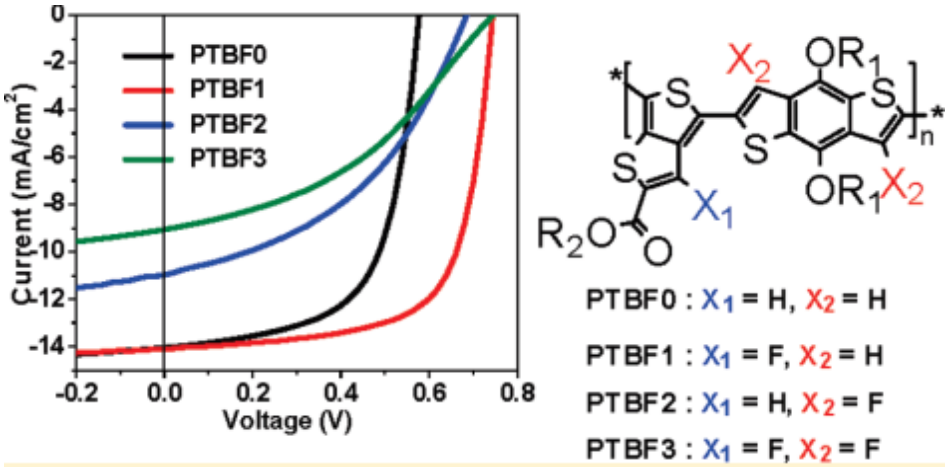

Figure 1-3. Solar cell performance of polythienothiophene-co-benzodithiophenes. Reprinted with permission from Ref [37].

Fluorine is very effective in this regard because it has the highest electronegativity among elements and its van der Waals radius is only 13% larger than hydrogens allowing to preserve coplanarity of monomer units in polymer chain. 3 Ambipolar polymers were synthesized based on isoindigo scaffold using Stille polymerization.[38] Dibromoisoindigo IID with 0, 1 or 2 fluorine atoms was copolymerized with ditrimethyltin difluorobithiophene 2FBT affording PIID-2FBT, P1FIID-2FBT and P2IID-2FBT. These materials showed excellent FET mobilities for holes and electrons: without fluorines on isoindigo 5.33 and 2.06, with 1 fluorine 6.41 and 6.76, with 2 fluorines 2.75 and 9.70 $cm^2V^{-1}s^{-1}$. Electron mobility clearly follows increase in number of fluorine atoms in repeating unit which is expected based on lower LUMO energy level and subsequently

lower injection barrier from gold electrodes. All polymers had high molecular weights: Mn=57.1, 50.5, and 59.0 kDa respectively for PIID-2FBT, P1FIID-2FBT and P2IID-2FBT. TGA curves showed that these materials are stable up to 400°C. CV showed both oxidation and reduction peaks. The redox processes were irreversible because reverse peaks were smaller than forward peaks. The fact that both reduction and oxidation were observed in all cases is consistent with ambipolar nature of materials. HOMO energy levels very weakly depend on fluorination, going from -5.66eV to -5.72eV, whereas LUMO decreases significantly from -3.46eV to -3.55eV to -3.64eV. UV-vis spectra for each polymer have 2 peaks in 600-800nm region. Fluorination slightly red-shifts the peaks as is expected from lowering LUMO and therefore bandgap. These trends were consistent with DFT calculations, which also revealed that 600-800 nm band originates from intramolecular charge transfer. XRD studies showed that fluorination reduces π-π stacking distance from 3.55 to 3.52 to 3.50 Å which can be explained by stronger intermolecular donor-acceptor interactions since fluorine atoms make isoindigo units more electron-deficient and, as authors note, greater coplanarity of monomer units. AFM imaging of polymer thin films revealed large crystalline regions in each sample. Overall the polymer without fluorines on isoindigo unit is a p-type semiconductor, with 1 fluorine – ambipolar and difluoro polymer is n-type dominant.

Scheme 1-2. Structures of PIID-2FBT, P1FIID-2FBT and P2IID-2FBT.

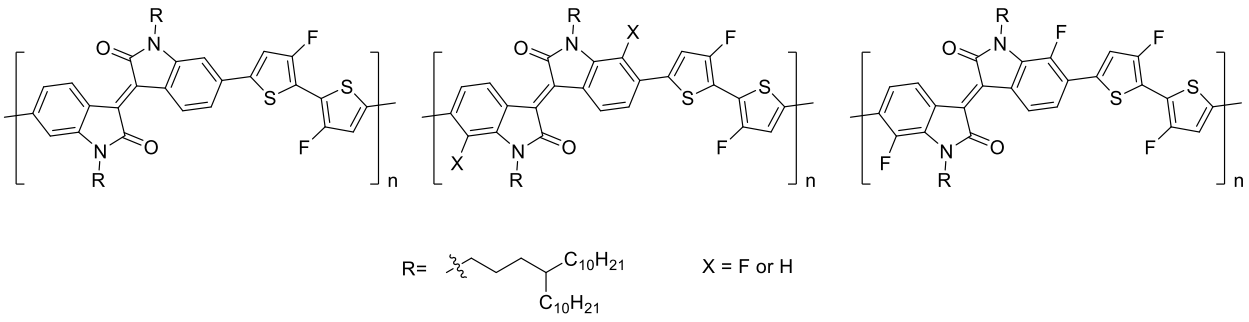

This work has been extended to polymers with even more fluorine atoms in the repeating unit. Gang and coworkers[39] have created a series of 6 polymers by copolymerizing IID and TVT monomers with various degrees of fluorination: P0F without any fluorine atoms, P2F with fluorines on isoindigo fragment, P4F with fluorines only on thiophenes, P6F with perfluorinated thiophenes and isoindigo, and also P6F-C3 with longer alkyl chain spacer and P6F-2TC3 with bithiophene instead of thienylvinylthiophene.

Scheme 1-3. Structures of P6F, P0F, P6F-C3, P6F-2TC3.

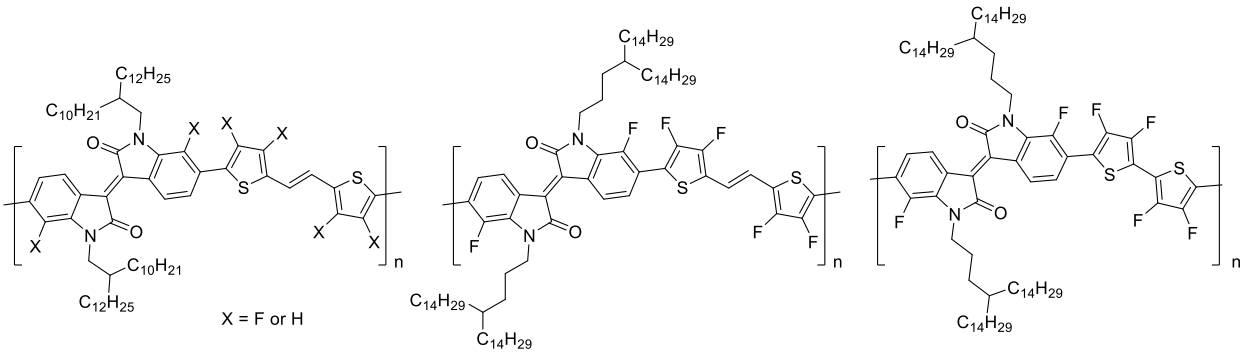

HOMO energy levels steadily decrease in this series from -5.48eV to -6.09eV, whereas LUMO's decrease only from -3.63 to -3.92eV. Greater dependence of HOMO energy levels on substitution can be explained by 2 factors. First, DFT calculations show that HOMO is much more delocalized than LUMO, which is located mostly on isoindigo fragments. Therefore, effects of fluorination affect HOMO stronger as more fluorine atoms are introduced into the polymer structure, since more of them are located near HOMO compared to LUMO. Secondly, increase in torsional angles because of C-H C-F and C-F C-F bonds repulsion weakens conjugation at each connection point between monomer units. According to DFT calculations HOMO spans over 3 repeating units, while LUMO only between 1 and 2 repeating units. This means that any increase in torsional angles affects HOMO more because it depends stronger on planarity between

monomer fragments. UV-vis spectra of all polymers have peaks in 600-800nm region which are attributed to intramolecular charge transfer HOMO-LUMO transition. P0F showed only hole-transporting behavior, while P2F, P4F and P6F are ambipolar semiconductors with P6F having the highest hole mobility up to 3.94 and electron mobility up to 3.5 $cm^2V^{-1}s^{-1}$. P6F-C3 and P6F-2TC3 are only n-type unipolar semiconductors due to very low HOMO energy levels, that create a barrier for hole injection from the Au electrode.

Liu group has designed a novel acceptor bis-pyridalthiadiazole BPT which is a dimer of benzothiadiazole with one of benzene carbons substituted for nitrogen.[40] Nitrogen substitution exerts two benevolent effects. First, it makes acceptor unit more electron-withdrawing, second, nitrogen lone electron pair provides much less steric hindrance for thiophene hydrogen, therefor increasing coplanarity of monomer units in polymer chain. Calculated LUMO level of BPT -3.42 eV is very close to that of NDI -3.40eV making it a very strong acceptor. When copolymerized with thienylvinylthiophene TVT the resulting polymer exhibits extraordinary high mobility for both holes and electrons: 6.87 and 8.49 $cm^2V^{-1}s^{-1}$ respectively. Key synthetic steps involve reacting dibromo-PT with 1 equivalent of thienylstannane with only 1 bromine activated by nitrogen participating in the coupling. NOE NMR doesn't show correlation between pyridine and thiophene hydrogens proving which bromine reacted. Next reaction with hexabutylditin creates BPT fragment, which after bromination with NBS can be used in Stille polymerization. This synthetic sequence is crucial for nitrogens of PT units to face in opposite directions and ensure regioregularity of final PBPTV polymer. Although this polymer has good solubility in common organic solvents it also shows strong aggregation in solution. In UV-vis spectra there is a strong charge transfer peak around 690nm with aggregation peak at 720nm in solution and 800nm in film. When solution is heated the aggregation peak gradually decreases. Strong aggregation in film and

solution is indicative of good π-π stacking, which facilitates charge transport in solid state. Cyclic voltammetry reveals PBPTV energy levels to be -5.61 and -3.66 for HOMO and LUMO respectively which is reasonably close to -5.0 eV level of gold electrodes. Although oxidation and reduction are irreversible, oxidative and reductive peaks are comparable in intensity as is expected from ambipolar charge transport. DFT calculations on the trimer show highly planar π-system with dihedral angles less than 25°. Additionally HOMO and LUMO orbitals are delocalized throughout the whole molecule explaining ambipolar properties further. Charge mobility of PBPTV strongly depends on annealing temperature, 180°C being best for both holes and electrons. AFM and GIWAXS studies on films before and after annealing show that annealing leads to larger crystalline domains.

Scheme 1-4. Synthesis of PBPTV

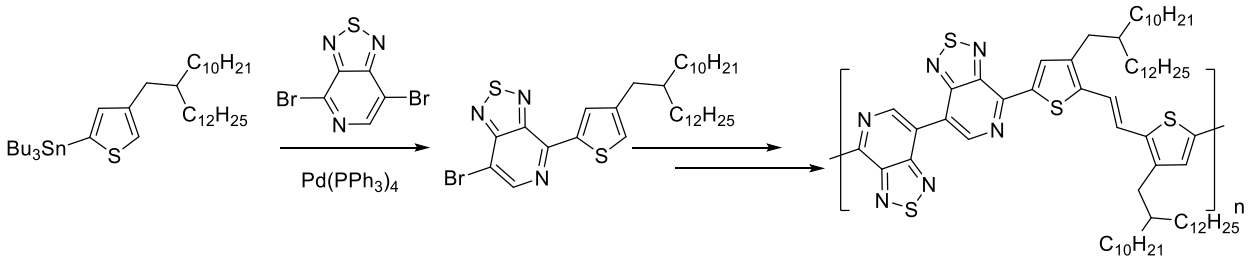

Regioregularity has a strong influence on charge carrier mobility[41]. Bazan and Heeger groups designed and synthesized 3 types of polymers from pyridalthiadiazole PT acceptor and cyclopentadithiophene CDT donor units. First polymer is synthesized by polymerizing asymmetrical monomer with bromine and tributyltin groups, which gives rise to a regioregular polymer P1 with all pyridine nitrogens facing the same direction. Regiochemistry of monomer is proven by lack of cross correlation between pyridine and thiophene hydrogens in NOE NMR experiment. Reacting ditin-CDT with 2 equivalents of dibromo-PT affords symmetrical dibromo-monomer which can be copolymerized with another equivalent of CDT. This polymer P2 has a

repeating unit with pyridine nitrogens facing each other. Random polymer P3 is synthesized by Stille polymerization of dibromo-PT and ditin-CDT. Regioregularity of polymers was supported by ^{13}C NMR signals of bridgehead carbon in CDT units.

Scheme 1-5. Structures of polymers P1, P2, P3.

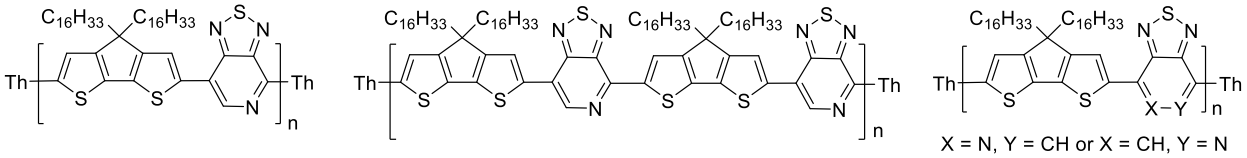

P1 P2 P3

Prepared polymers with number-averaged molecular weights in 28-40 kDa range were poorly soluble in common organic solvents, so authors also synthesized lower molecular weights samples for NMR characterization. Although the paper claims no phase transitions up to 300°C, the DSC data in supporting information clearly shows glass transition around 30°C for all of the samples. Interestingly, UV-vis spectra of P2 and P3 are very in o-dichlorobenzene at room temperature are very similar, peaks at 880 and 885nm, whereas P1 has a maximum at 930nm. At 110°C however all maxima shift to 800-810nm, giving solid evidence that at room temperature polymer chains are heavily aggregated in solutions in J-aggregate fashion. Regioregular polymer P1 has greatest shift consistent with aligned dipole moments of pyridine rings. CV data shows that P1-P3 polymers have the same LUMO energy of -3.70eV, however P1 has a slightly higher HOMO than P2 and P3, -5.07 vs -5.16 and -5.23 respectively. This can be explained by more planar structure of regioregular polymer since there is less steric repulsion between hydrogen and lone pair of nitrogen than there is between two hydrogens. Greater coplanarity leads to better conjugation of monomer units and therefore increased energy of delocalized HOMO. The same effect does not influence LUMO because it's tightly localized on the PT acceptor unit. Bottom

gate, top contact transistors made with synthesized polymers revealed high hole mobility of 0.4 and 0.6 for P1 and P2 respectively, whereas P3 had a hole mobility of only 0.005 $cm^2V^{-1}s^{-1}$. This finding suggests that making regioregular polymers is absolutely essential for high-mobility materials. Atomic force microscopy images show that clue to explaining this observation lies in organization of polymer chains. Despite similar surface roughness, thin films of P1 and P2 have large fiber-like crystalline domains: 177nm in length and 34nm in width for P1 and 127nm in length and 45nm in width for P2. GIWAXS measurements show that all polymers are quite amorphous as no clear values for lamellar structure or π-π stacking distance could be obtained, however P1 and P2 have stronger reflection intensities which suggests their greater crystallinity.

Donor-acceptor architecture is necessary to achieve high-mobility materials. For example, PDQT polymer comprised of diketopyrrolopyrrole DPP acceptor and quaterthiophene QT donor has strong inter and intramolecular D-A interactions which lead to spontaneous edge-on orientation in thin films and large size crystalline domains[16].

Scheme 1-6. Structure of PDQT

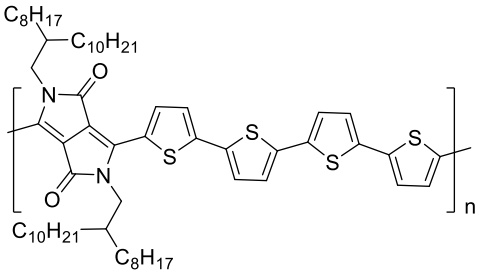

UV-vis spectra both in film and solution show a single peak, 777 and 790nm, which is consistent with charge-transfer from QT donor to DPP acceptor. Cyclic voltammetry indicated large irreversible oxidative peak, corresponding to HOMO level of -5.2 eV and only small reduction peak, which however wasn't used to determine LUMO energy level. Alkyl chains are

located only on the DPP unit so as not to break planarization of polymer π-system. Highly crystalline nature of thin films was proven by XRD, π-π stacking distance was determined to be 3.75 Å and lamellar structures 19.9 Å. AFM images show 20-30nm sized grains. Interestingly, hole mobility is only a little bit improved by thermal annealing: heating at 100°C leads to increase from 0.89 to 0.97 $cm^2V^{-1}s^{-1}$. Molecular weight of the polymer has great influence on the mobility. A batch of PDQT with slightly lowered molecular weight, Mw=50700 vs 60600 Da, had mobility of up to 0.39 $cm^2V^{-1}s^{-1}$. These measurements were done with GPC in trichlorobenzene at 160°C, however GPC performed with THF at 40°C showed more dramatic difference, 97200 vs 365000 Da. Differential scanning calorimetry showed that lower molecular weight polymer had slightly lower melting point temperature, 298 vs 300°C, and enthalpy of transition, 28.7 vs 34.1 J/g. These results suggest that slight increase in molecular weight of polymer sample can have a strong effect on how prone the polymer chains are to aggregation and how much it can influence charge mobility in thin films. Donor-acceptor structure of new polymers facilitates strong intermolecular interactions leading to higher mobility materials as charges can hope from one chain to the other through π-π stacks.

1.3 Light-emitting materials

1.3.1 Materials with high photoluminescence quantum yields

Energy levels tuning is not only important for efficient charge injection to the luminescent layer but also for long lasting stable device performance. Low HOMO energy level can prevent ambient oxygen from doping the light-emitting material and deteriorating it's photophysical properties[42]. Cicoira and coworkers attached phenyl through double bond to tetracene, which resulted in a material with HOMO level of -5.3eV. This material retains high

mobility of 0.2 $cm^2V^{-1}s^{-1}$ even after few months of exposure to air. Extending conjugation disrupts quenching in film resulting in PLQY of 7% vs 0.8% for unsubstituted tetracene.

Aspuru-Guzik and coworkers devised the approach to compute TADF singlet-triplet energy gap and oscillator strength of S1-S0 transition.[8] Efficient emitters should have low S-T energy difference to allow reverse intersystem crossing (RISC) and moderate to high oscillator strength *f* in order for a singlet to be emissive. Balance between the two is important with arbitrary cutoff of 0.100eV for energy and 0.010 for oscillator strength. Computations are done at ground state geometry using B3LYP 6-31G* and unrestricted for triplet. Second finer calculation is done at relaxed triplet geometry.

Blue fluorescent polymers offer an advantage because they are more likely than small molecules to be solution processable, and this makes manufacturing easier. There is a number of blue fluorescent polymers in the literature. Polyphenylenevinylenes is the most heavily developed class of blue emitting polymers for OLED.

In 2001 Ng et al.[43] synthesized a series of dialkoxypyridine polymers with various alkyl chains. Pyridine unit solubilizes these polymers in acidic environment due to protonation. This reactivity allows to deposit films not only from common solvents like chloroform but also from its mixture with trifluoroactic acid giving access to different morphologies.

TADF polymers[44] 2019 review present a rational design of OLED materials. Looking at the small molecules with TADF chemists incorporate these known units either into main chain or as side groups into polymers or dendrimers. One problem with such "extension" is that in polymer quenching interactions can be greatly amplified and side groups are more available and more flexible for such interactions. Most of these polymers heavily rely on incorporating carbazole or

triazine units into the structure. As other TADF materials orthogonally twisted units are usually needed. This approach however may present difficulties for OLET applications since twisted structure is bound to hinder mobility. Acene-fluorene polymers have been synthesized with different number of acene rings determining emission color: anthracene blue, tetracene green, pentacene red.

1.3.2 OLET principles and materials

OLET devices have more stringent requirements for luminescent materials than OLED. The difference stems from different device architectures. OLED's have very thin layer of active material on the scale of 100nm with holes and electrons flowing perpendicularly to the surface, while in OLET's light emission active zone has a length on the scale of microns. Thus OLET devices require materials not only with high luminescence efficiency but also with higher mobility of holes and electrons. Unipolar OLET, where only one type of charge carrier has high mobility, exhibit lower device performance, for example OLETs with tetracene[45–47] have only p-type characteristics and emit light only near drain electrode, where electrons can tunnel to the light-emitting area.

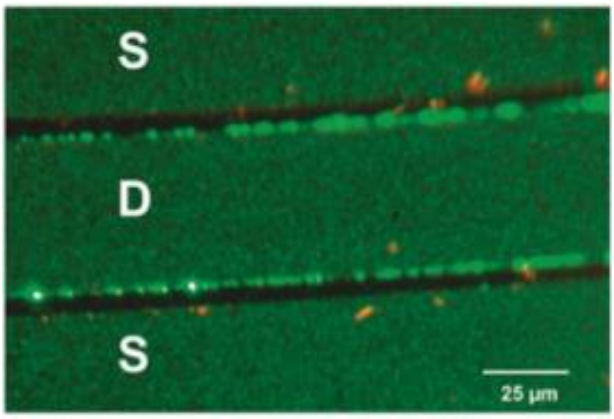

Figure 1-4. Close view of OLET device "interlocking fingers" architecture. Reprinted with permission from Ref.[45]

OLET can outperform OLED devices with the same material because of reduced exciton-charge and exciton-metal quenching.[48] Muccini et al. have developed a trilayer architecture for OLET devices by sequentially depositing electron transporting / light-emitting / hole-transporting semiconductors on top of PMMA-covered ITO glass serving as gate contact. Dihexyl tetrathiophene serves as a hole-transporting layer with its HOMO lower than light-emitting DCM/Alq_3, and di(perfluorohexyl)tetrathiophene is used as electron-transporting layer with its LUMO being higher than that of active material.

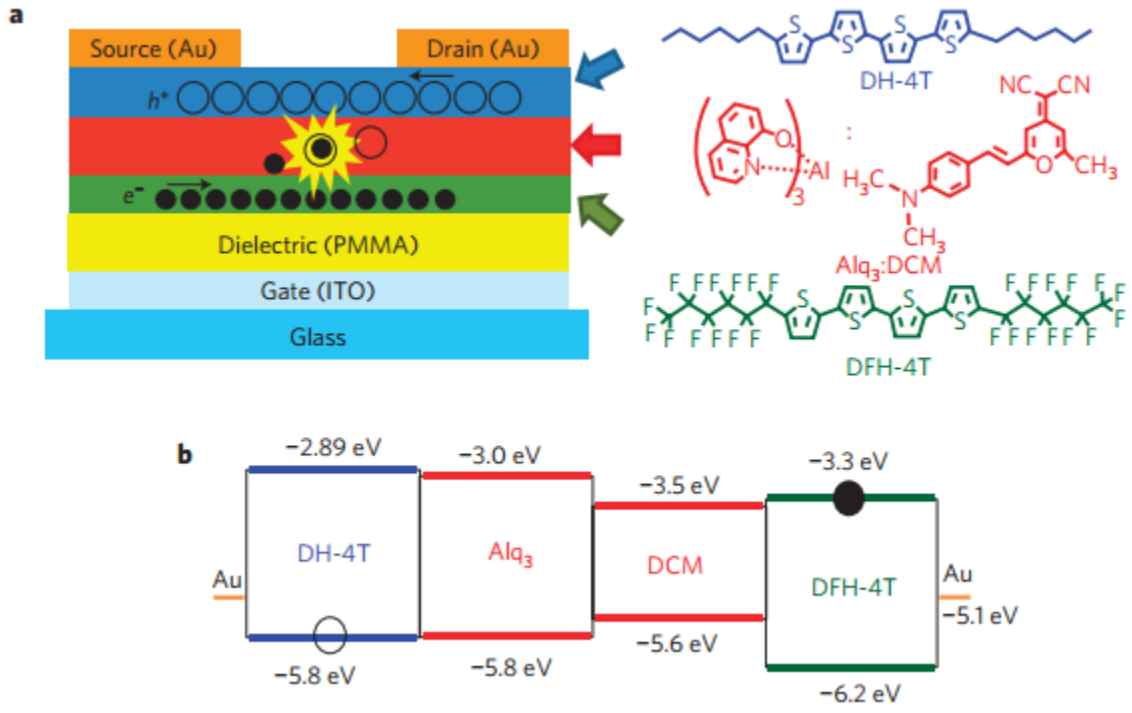

Figure 1-5. Typical scheme of OLET device (a) and corresponding energy diagram of used materials (b).Reprinted with permission from Ref.[48]

Preliminary studies showed that chosen p- and n-type semiconductors used in transistors without light-emitting layer have excellent mobilities of charge carriers up to 0.01 $cm^2V^{-1}s^{-1}$ and don't exhibit any electroluminescence. OLET device however has hole mobility severely lowered

to $5x10^{-5}$ $cm^2V^{-1}s^{-1}$ due to Alq_3:DCM layer being very rough. When DH-4T is deposited on top of 100-300nm aggregates of light-emitting matrix a uniform homogeneous thin film of hole-transporting layer cannot form properly as evidenced by AFM images.

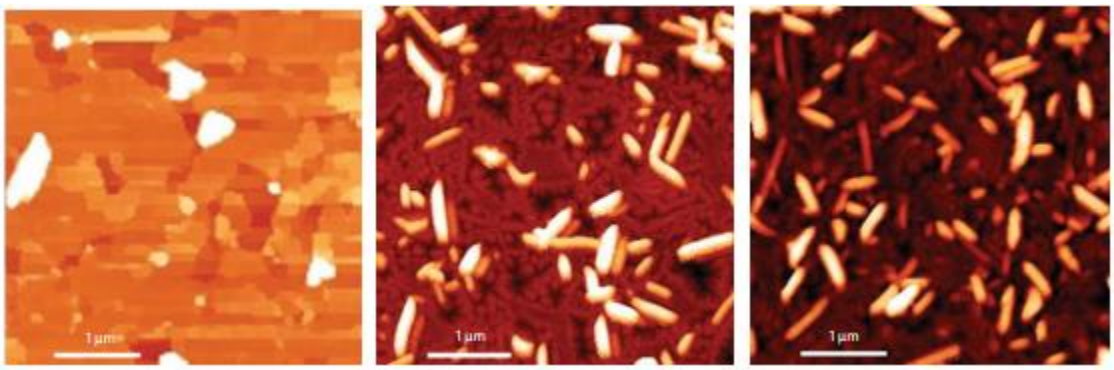

Figure 1-6. AFM images of DH-4T films. Reprinted with permission from Ref. [48]

Optical microphotographs reveal that light-emission begins in the middle of the channel. Spatial separation of light-emitting area from drain electrode prevents exciton quenching by metal of electrodes. At the same time trilayer structure ensures that charge density inside light emitting layer is smaller and so there is less probability of excitons encountering charge carriers thus preventing exciton-charge quenching. Further optimization of device by reversing positions of DH-4T and DFH-4T together with implementation of LiF/Al electrodes to facilitate electron injection afforded EQE of 5%.

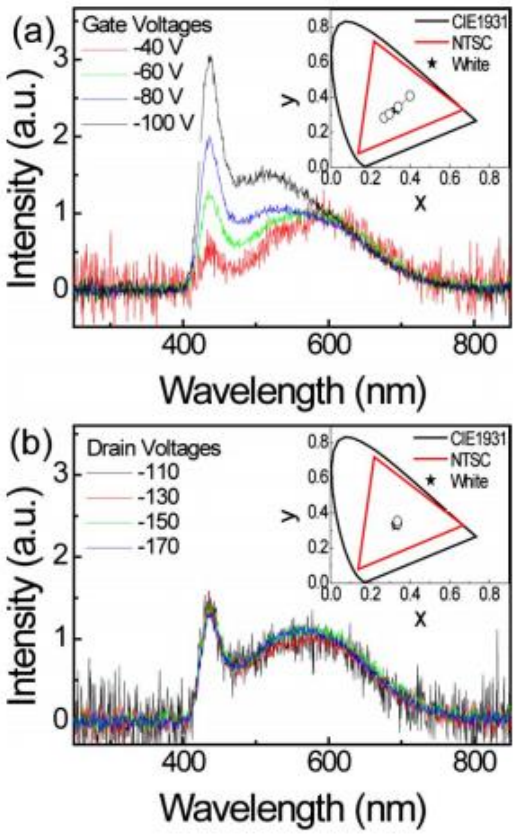

Figure 1-7. Electroluminescence spectra. Reprinted with permission from Ref.[48]

Emission color can be controlled even in single light emitting material OLET devices.[49] Luminescent small molecule SPYIN has only one peak in its emission spectrum however in device molecules close to the SiO2 interface have their electroluminescence spectra red-shifted. By changing gate and source-drain voltage electron-hole recombination zone can be shifted vertically, and so light emission can be occurring either from bulk of film or from interface with dielectric resulting either in blue or yellow colors.

Heeger group was first to develop solution processed blue light OLET based on polyfluorene PFO.[50] Surrounding light-emissive layer with hole- and electron-injecting layers allows good device performance irrespective of light-emitting material. Thus, MEH-PPV and SY were also used.

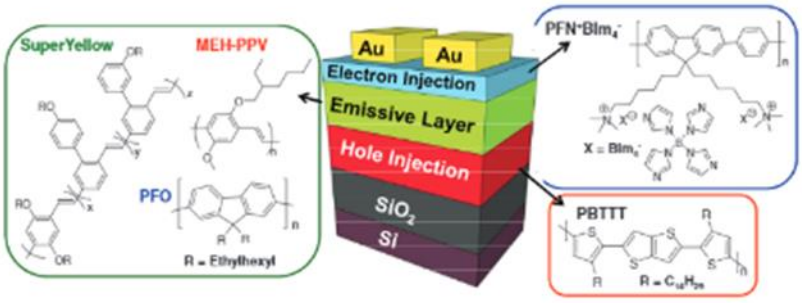

Figure 1-8. General schematics of tricolor OLET devices. Reprinted with permission from Ref.[50]

PFN plays a crucial role as a conjugated polyelectrolyte, because this structure allows to have an interfacial dipole moment at gold-PFN contact. Positively charged trimethylaminogroup orient closer to the gold surface, while hydrophobic polymer backbone is closer to SY layer. This creates a dipole with negative end pointing towards Au electrode raising its workfunction. So the actual barrier for electron injection is smaller than 5.1-2.7=2.4eV.

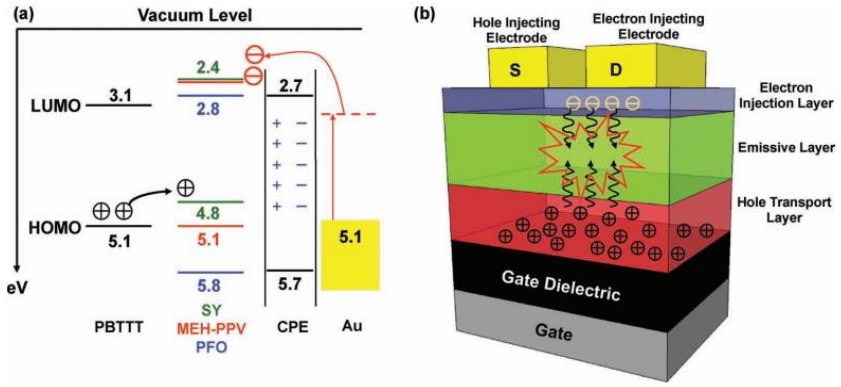

Figure 1-9. Energy diagram and electon-hole recombination zone. Reprinted with permission from Ref.[50]

Organic light emitting transistors offer an opportunity to control light emission with applied gate voltage. Another dimension of control comes from using external light source to influence

appropriately functionalized devices. Samori et al. have spin-coated dithienylethene photoswitches on top of known emissive polymers F8T2 (green), MDMO-PPV (red) and F8 (blue)[51]. In the more conjugated closed form photoswitch's HOMO energy is hundreds of meV higher than that of corresponding active material. When voltage is applied to the device, injected holes get trapped in cyclized molecules significantly reducing drain current and luminance compared to when photoswitch is in the less conjugated open form and no charge trapping can occur. Polyfluorene has lower HOMO energy than other polymers and requires a polyfluorinated photoswitch with accordingly lower energy level of its HOMO. During fabrication devices are annealed at low temperatures to facilitate diffusion of DAE molecules into polymer matrix.

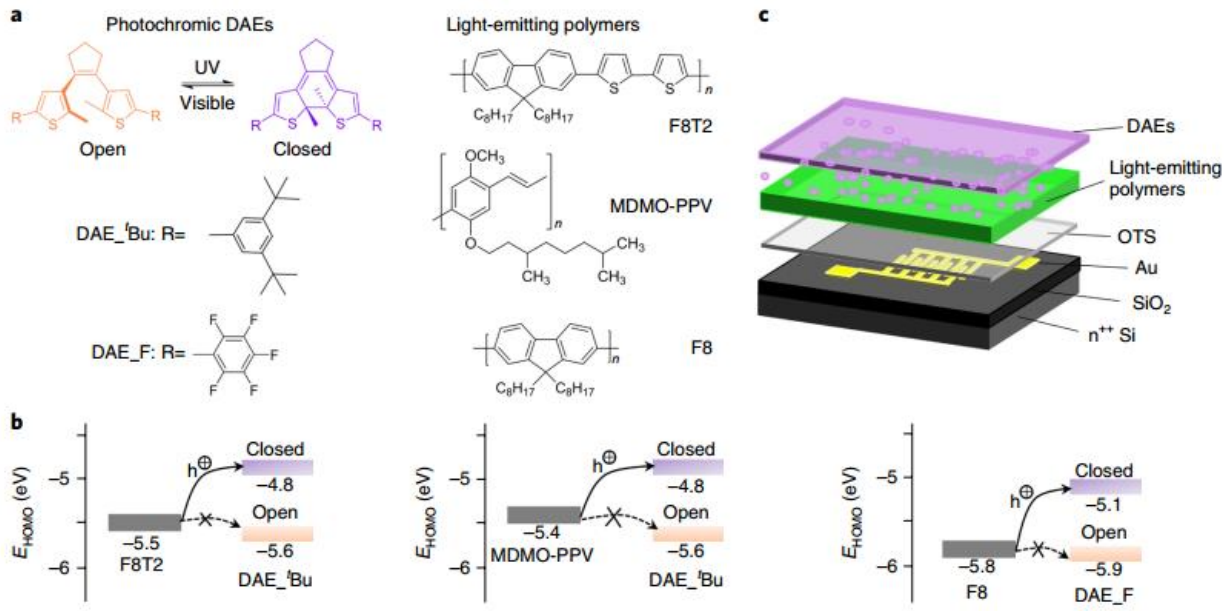

Figure 1-10. Materials used in light-switchable OLET device (a), energy levels in closed and open forms (b) and device architecture (c). Reprinted with permission from Ref.[51]

Nevertheless polymer films are thin enough for external light stimulation to switch open and closed forms with high efficiency over at least 5 cycles.

Charge carrier mobility in semiconductors depends critically on the intermolecular interactions. If π-systems have numerous contacts and their orbitals overlap, mobility is expected to be high. Intrinsic disorder of polymer chains therefore limits conductivity of conjugated organic polymers. A powerful workaround is offered by aligning polymer chains parallel to each other to afford a semicrystalline functional material. Namdas group has developed a technique of creating templating deposition of polymers onto substrate[52]. First, SiN_x/SiO_2 surface is scratched by a film with deposited diamond nanoparticles (ca. 100nm), and then this substrate is dipped into polymer solution at a slow withdrawal rate. Complete dissolution of polymer and slow evaporation of solvent are essential for producing ordered films. Fig. (a) and (b) show scratched and pristine substrate AFM images, (c) and (d) show same surfaces after DPP-DTT deposition. It is clear that morphology of the underlying surface determines crystallinity of the resulting polymer sample.

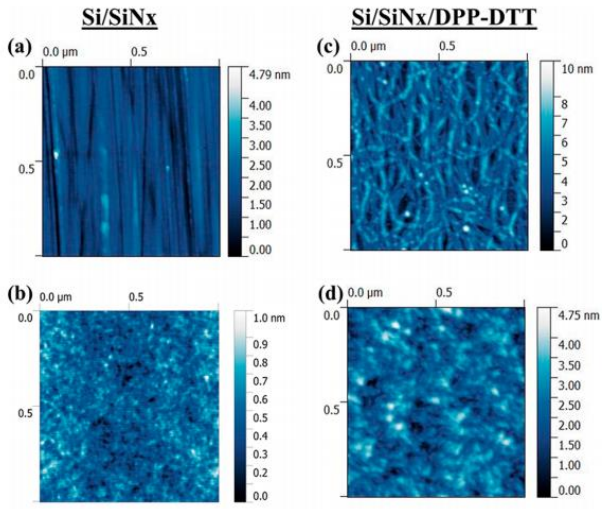

Figure 1-11. AFM images of scratched and pristine substrates (a, b) , same surfaces after DPP-DTT deposition(c, d). Reprinted with permission from Ref.[52]

XRD studies revealed lamellar structure corresponding to 21.7 A interlayer spacing consistent with packing of alkyl side chains for aligned samples and no signal for control samples.

Predictably, control films exhibit isotropic current behavior, whereas for films deposited on grooved substrates current parallel to the alignment direction is an order of magnitude larger than perpendicular to it. Nanoalignment of polymer chains is an effective tool to improve mobility. In the case of DPP-DTT effective mobility increased from 1.6 to 9.4 $cm^2V^{-1}s^{-1}$.

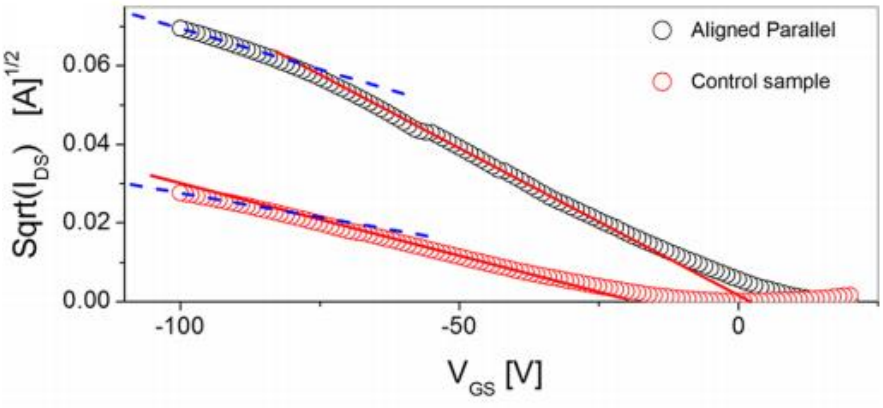

Figure 1-12. Transfer curves of aligned and control samples. Reprinted with permission from Ref.[52]

Heeger group has developed another approach for aligning polymer chains on the example of PCDTPT and CDTBTZ[53]. Sandwiched Si/SiO_2 substrates with nanogrooves are functionalized with perfluorodecyltrichlorosilane (FDTS), n-decyltrichlorosilane (DTS), and phenylhexyltrichlorosilane (PTS) or treated with piranha solution. Then solution of polymer in chlorobenzene moves inside the device due to capillary forces. Contact angle measurements and height of solutions drawn into the device predictably reveal that FDTS modification prevents solution from wetting the surface and prevents effective deposition of polymer.

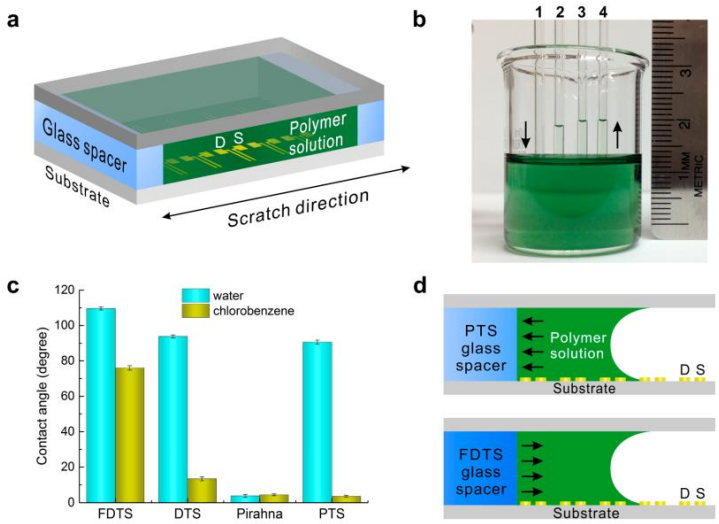

Figure 1-13. Sandwiched substrate schematics (a) , capillary action (b), difference in wettability of substrates (c), opposite capillary forces for hydrophobic and hydrophilic surfaces (d). Reprinted with permission from Ref.[53]

On the other hand films obtained from PTS-treated substrate exhibit clear alignment as evidenced by AFM images. Additionally polymer surface obtained from FDTS is relatively smooth (surface roughness 0.64nm), while the film obtained with PTS-modification has surface roughness of 1.55nm paralleling that of underlying Si/SiO_2 substrate.

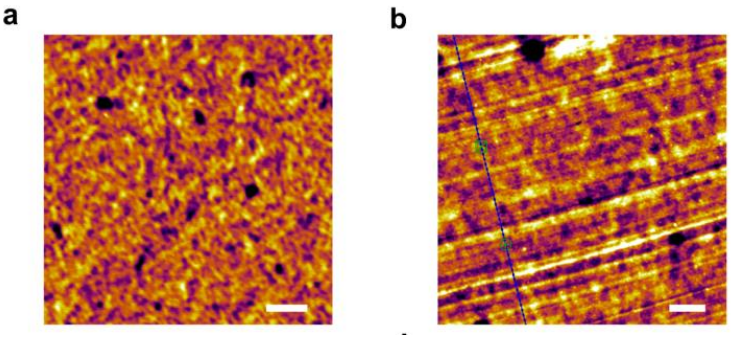

Figure 1-14. AFM images of control and aligned substrates (a, b). Reprinted with permission from Ref.[53]

GIWAXS studies show that films obtained on FDTS substrates are essentially amorphous, while on PTS ones films are semi-crystalline with lamellar thickness of 2.47nm and π-π stacking distance of 0.35nm. More ordered morphology of polymer films leads to improved hole mobility with highest value of 36.3 $cm^2V^{-1}s^{-1}$.

Previous work by the same group highlighted increased brightness of OLET devices to nanoalignmnet of polymer chains[54]. Key difference from other methods is a SiO_2 substrate scratched with diamond lapping film producing grooves few Å deep and few nm wide. Hole mobility is improved from 0.03 to 0.5 $cm^2V^{-1}s^{-1}$, which translates to imcreased brightness from 2000 cd/m^2 to 9000 cd/m^2. As expected mobility is anisotropic relative to the grooves direction.

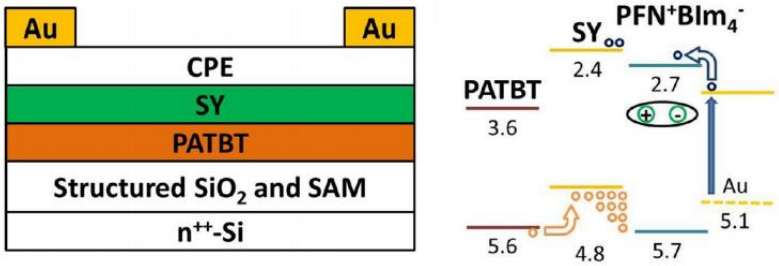

Figure 1-15. Device structure and energy diagram. Reprinted with permission from Ref.[54]

Trilayer device architecture is necessary due to unbalanced charge transport. PFN is used as an electron-injecting layer to prevent holes bypassing light-emitting layer of Super Yellow. PFN LUMO is close enough to that of SY, however its HOMO is significantly lower, thus creating a barrier for holes to reach gold electrode. PFN film is not continuous however so the direct injection of holes into SY layer is still possible. This device structure maximizes the probability of holes and electrons recombination in light emitting layer.

Miao et al. have expanded crystal engineering efforts on acenes with embedded cyclobutane rings[55]. This type of structure stabilizes π-system by introducing more Clar's sextets without changing the linear shape of molecules. Previously studied molecules 1a and 1b had phenyl and methyl substituents. By changing side chains to butyl, hexyl and octyl it is possible to change the packing of molecules in the solid state and therefore influence the mobility. According to Marcus theory hole mobility is proportional to transfer integral which accounts for overlap and nodal properties of molecular orbitals on adjacent molecules.

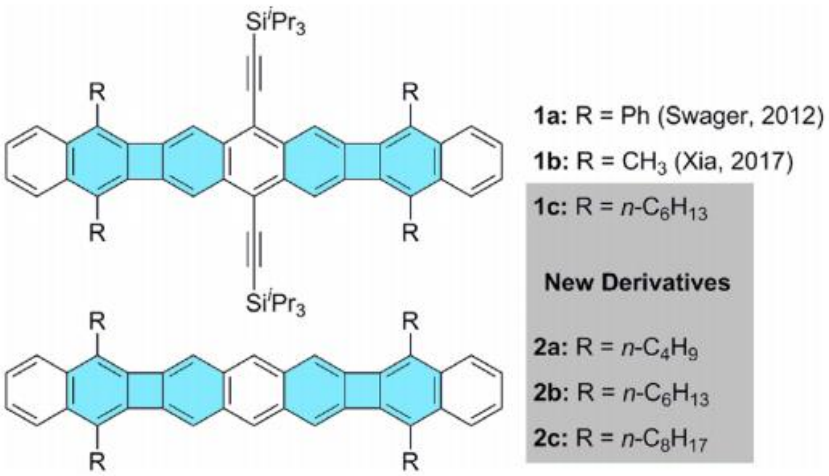

Figure 1-16. Chemical structures of studied acenes. Reprinted with permission from Ref.[55]

1b and 1c exhibit herring-bone crystal structures with neighbouring molecules slightly shifted from their neighbours along the length of the molecule due to large triisopropylsilyl groups. If there are only methyl side chains the π-systems overlap with about 5 rings. Larger hexyl chains push molecules away from each other and the overlap reduces to about 3 rings.

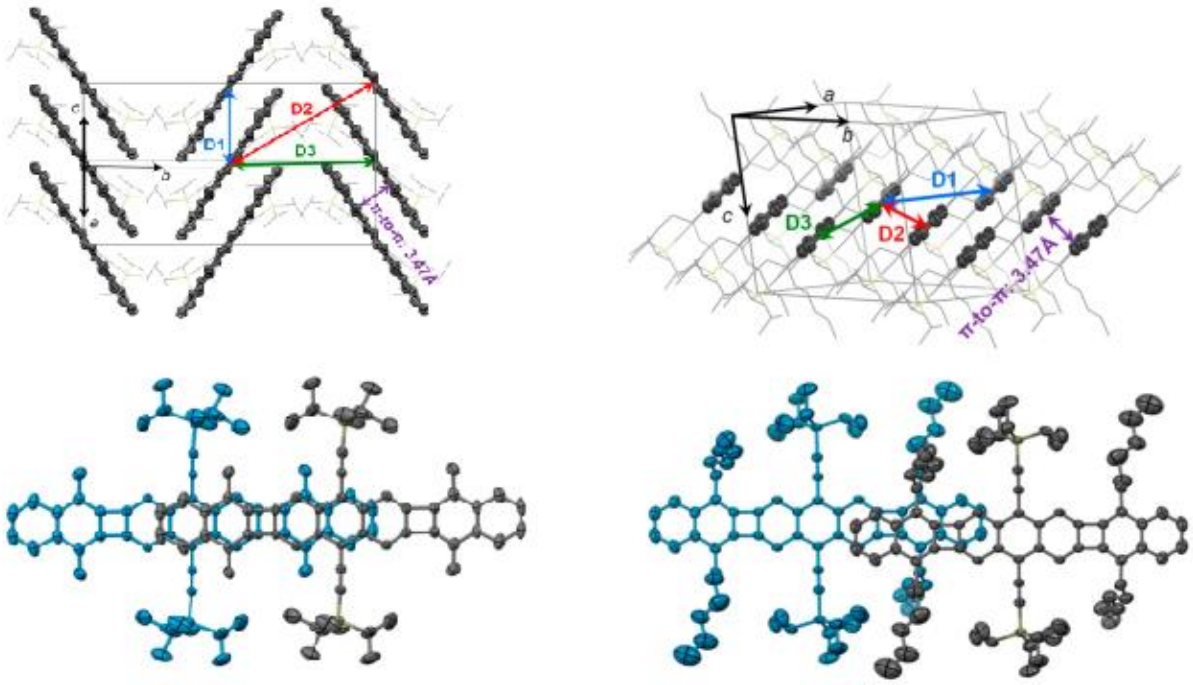

Figure 1-17. Crystal structure of 1b and 1c. Reprinted with permission from Ref.[55]

2a and 2c have a crystal structure were neighbouring molecules are shifted relative to each other along the short axis with overall herring-bone arrangement in the crystal. Only small overlap of the molecule's edges is possible.

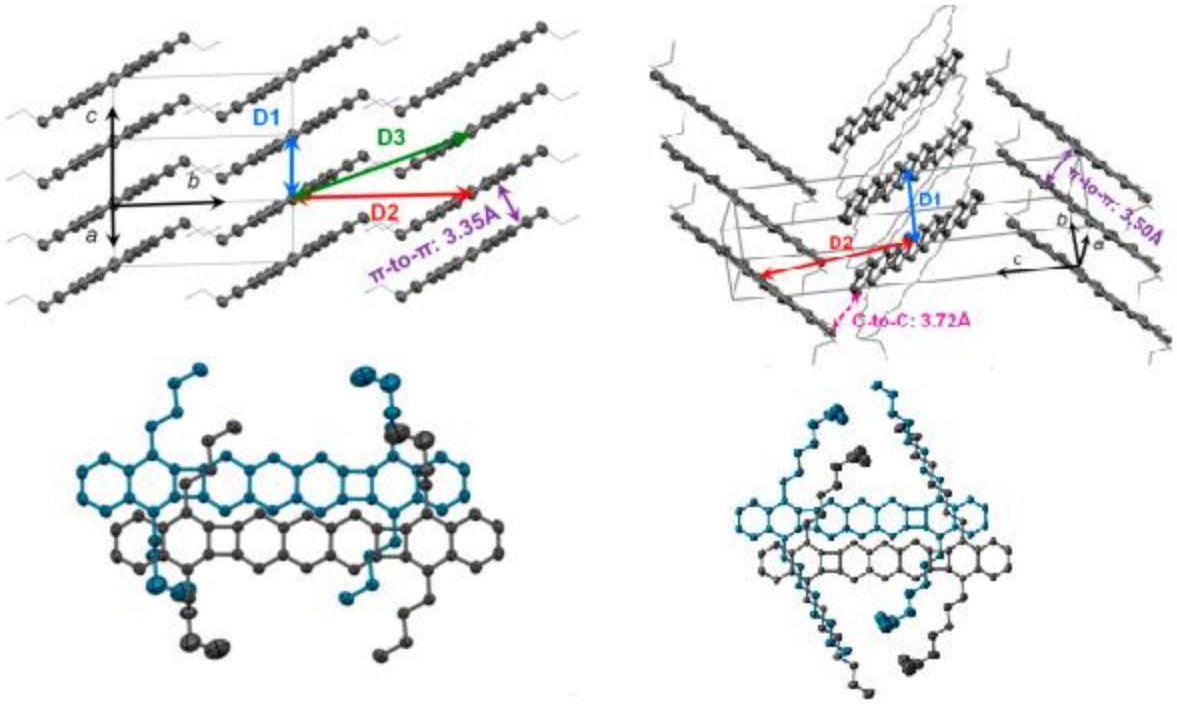

Figure 1-18. Crystal structure of 2a and 2c. Reprinted with permission from Ref.[55]

Unlike previous compounds 2b packs in a unique arrangement where molecules overlap with only one ring however each molecule can interface 4 other molecules. This crystal structure of perpendicular zig-zag type allows hole to travel in more than one direction unlike herring-bone structures above. As expected 2b has highest hole mobility of 2.9 $cm^2V^{-1}s^{-1}$, whereas mobilities for other molecules are in the range of 10^{-4}-10^{-2}.

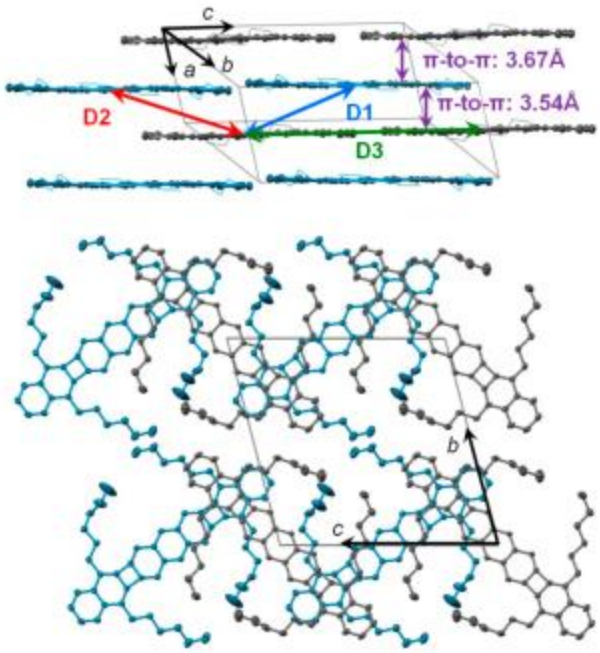

Figure 1-19. Crystal structure of 2b. Reprinted with permission from Ref.[55]

Ladder molecules have a few potential resonance structures. When designing these materials for practical applications it is important to consider the possibility of biradical character in these

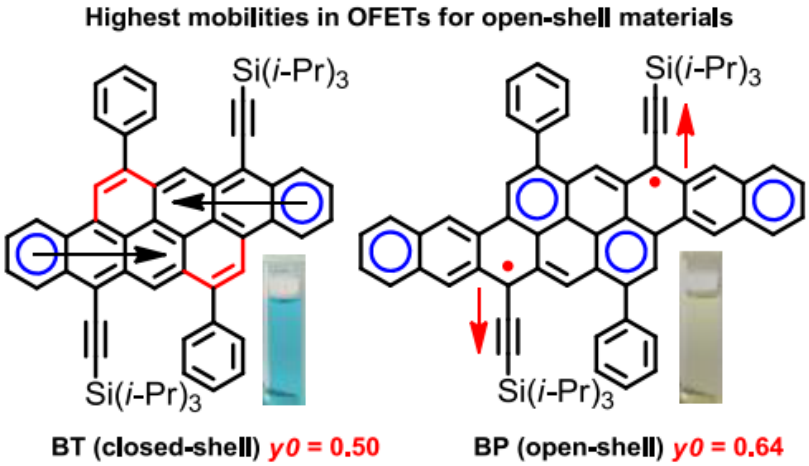

Figure 1-20. Open-shell molecules with highest mobilities. Reprinted with permission from Ref.[56]

molecules. Agachi et al. have synthesized tetracenotetracene and pentacenopentacene fused at the longer side at 3 benzene rings[56].

π-systems of these molecules can consist of a series of alternating double bonds or a number of localized aromatic sextets and delocalized radicals. By means of theoretical calculations as well as ESR and SQUID measurements it was found that TT is a closed shell acene and PP is a biradical in ground state.

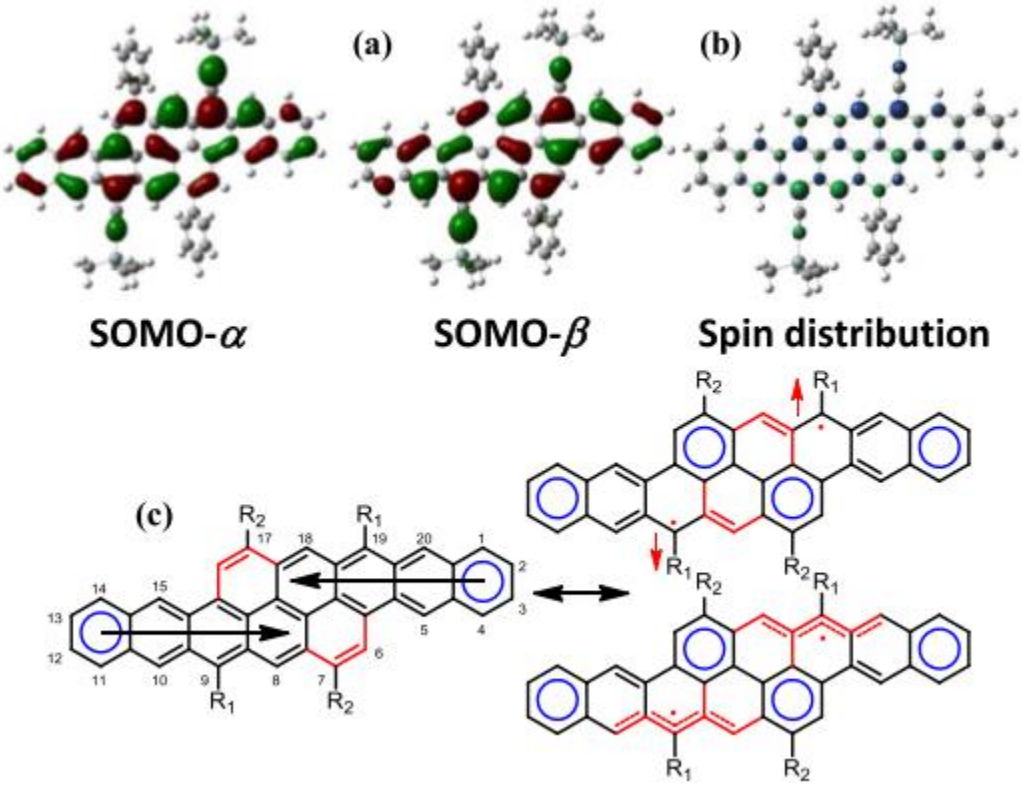

Figure 1-21. Frontier molecular orbitals (a) and spin distribution density (b). Reprinted with permission from Ref.[56]

Aromaticity of 4 benzene rings instead of only 2 is the driving force for creation of 2 radical centers that can be additionally stabilized by conjugation with TIPS-acetylene groups in R1 positions. Such radical change of electronic structure dramatically affects optical properties of

these 2 molecules. Their absorption and fluorescence spectra are quite similar with PP being red-shifted due to greater conjugation, however the TT derivative is highly fluorescent with QY of 63% while the PP derivative has a QY of only 0.8%. Biradical character makes PP unstable in solution even without exposure to air and light.

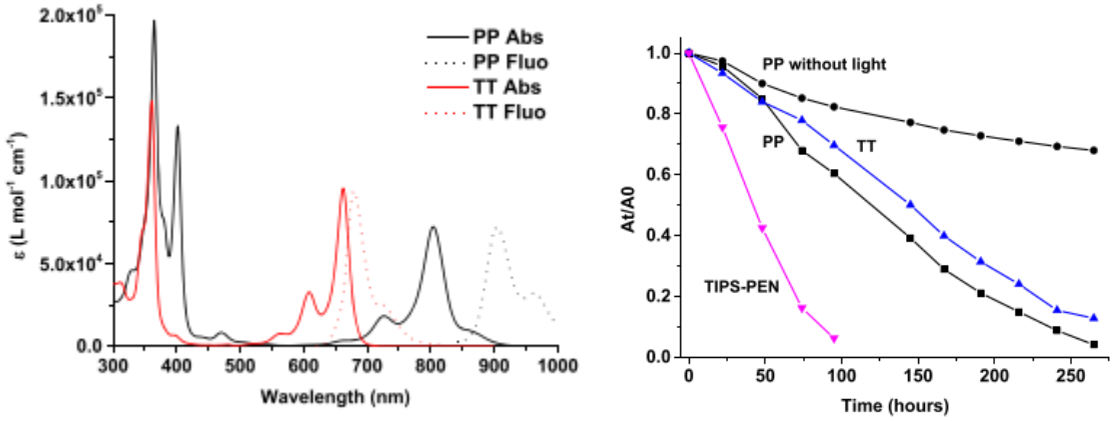

Figure 1-22. UV-vis absorption and fluorescence spectra of PP, TT and their stability in solution. Reprinted with permission from Ref.[56]

TT and PP can be considered ambipolar semiconductors, in bottom gate - top contact device PP exhibits balanced hole (0.07 cm^2V^{-1} s^{-1}) and electron (0.02 cm^2V^{-1} s^{-1}) mobilities. In a reverse configuration the highest hole mobilities were reaching 1.4 and 0.77 for PP and TT respectively. X-ray studies of single crystal of TT revealed that every molecules has contact with 4 other neighbors by means of 2 overlapping benzene rings at each end.

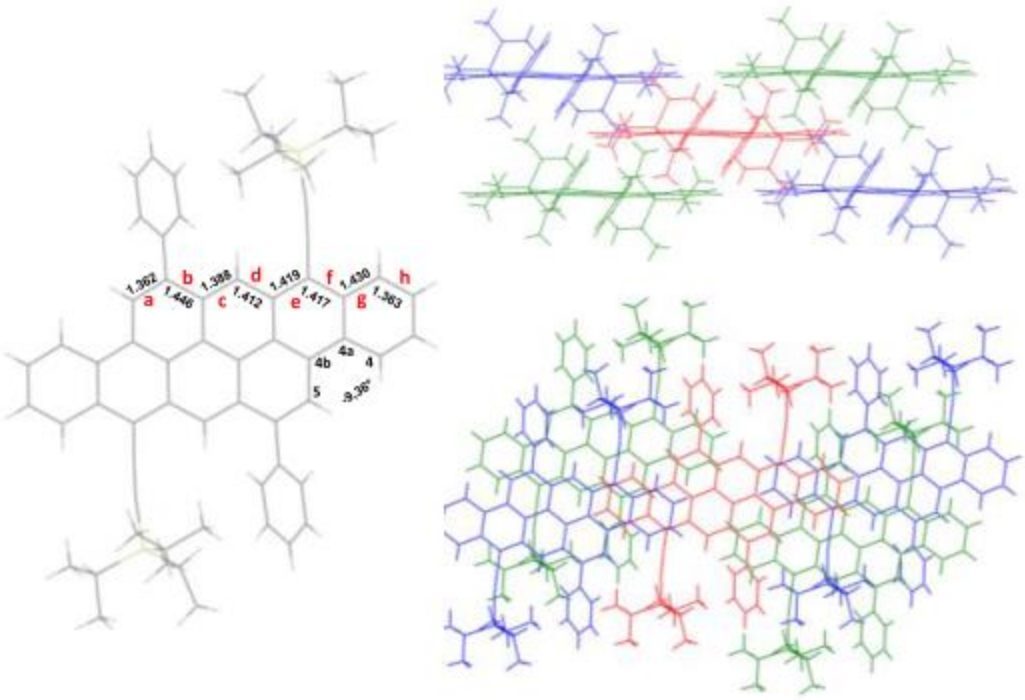

Figure 1-23. Crystal structure of TT. Reprinted with permission from Ref.[56]

1.4 Synthetic approaches to ladder structures

Yan Xia et al. from Stanford have made a series of molecules with fused antiaromatic cyclobutadiene inside ladder type stuctures[57]. Linear oligomers are more fluorescent than bent ones. The chemistry relies on interrupted Catellani reaction between aryl halide and norbornadiene or oxa-norbornadiene, the latter can be aromatized under acidic conditions allowing for conjugation. Oxa-norbornadiene has to have adjacent methyl groups for steric hindrance, as they prevent C-O bond opening in the intermediate adduct.

Same team has also made non-conjugated polymers with norbonadiene which have regiodefined kinks in 3D-structure of polymer and these materials can be used as membranes[58]. Antiaromaticity of these molecules can be questioned because of alternating double bond

Scheme 1-7. Synthesis of cyclobutane fused oligomers. Reprinted with permission from Ref.[57]

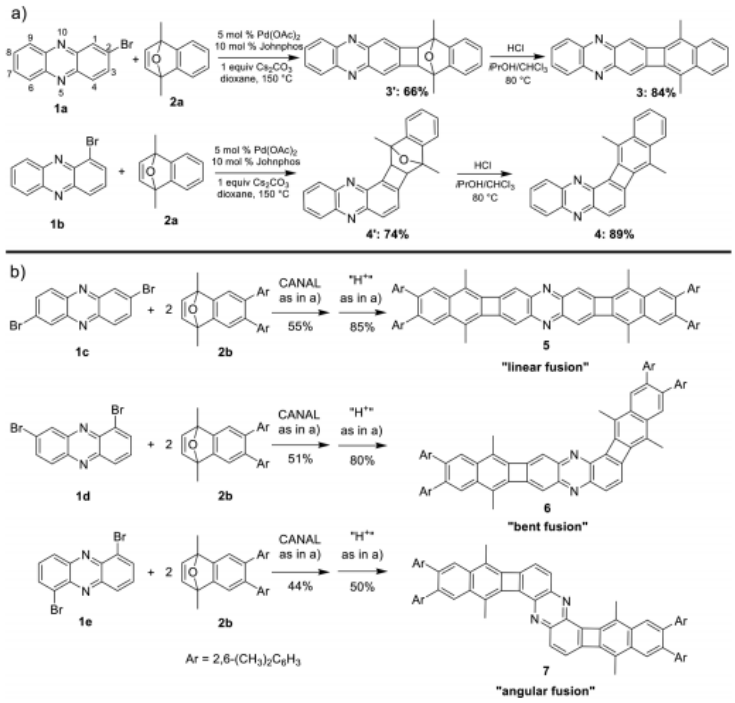

lengths and perhaps it is more accurate to view these chromophores as broken π-systems. Unfortunately no DFT for frontier molecular orbitals were calculated, however the antiaromaticity is supported by NICS (nuclear-independent chemical shift) calculations, according to calculated values 6-membered benzene rings are aromatic, but 4-membered rings in these structures are antiaromtic.

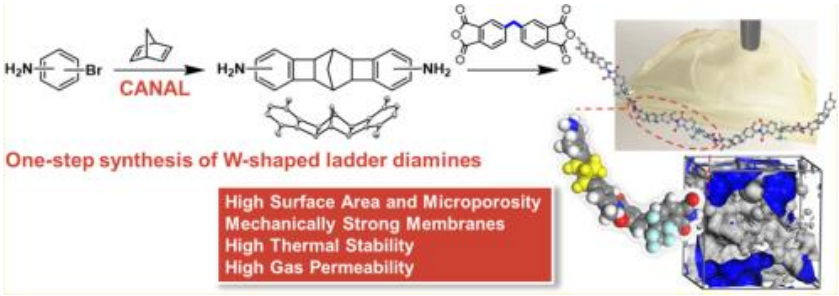

Figure 1-24. Zig-zag norbornadiene polymers. Reprinted with permission from Ref.[58]

Itami et al. have developed a living polymerization reaction between phenanthrene and dimethylsilole derivatives for the synthesis of well-defined graphene nanoribbons[59]. Crucial

feature of this methodology is hidden K-double bond in naphthalene ring of monomer M that is unmasked after cycloaddition and oxidation allowing further propagation steps. Resulting graphene nanoribbons are stable compounds and can continue polymerization if more of the monomer is added. Very narrow polydispersity of resulting ladder polymers ca. 1.2 doesn't change with Mn, which means that this methodology gives direct control not only on the structure and width of graphene nanoribbons but also their length.

Scheme 1-8. Syntheis of graphene nanoribbons through oxidative silole polymerizetion. Reprinted with permission from Ref.[59]

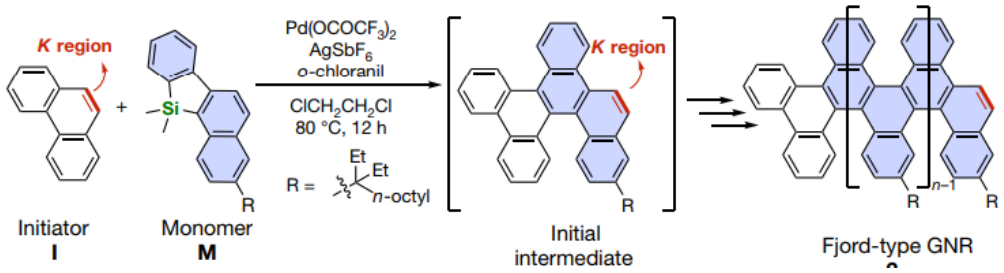

Tertiary diethyloctyl side chain is essential for good solubility and solution processing of obtained materials and their cyclized derivatives. Cyclization with $FeCl_3$ was studied with MALDI-TOF as main proof of high conversion, however species with m/z more than 10,000 could not be detected making it only a partial evidence. Cyclization leads to apparent lower Mn as measured by GPC, which could be explained by different hydrodynamic radii of graphene nanoribbons as compared to precursor ladder polymers.

UV-visible spectra of ladder in graphene nanoribbons are forbidden, and fluorescence can occur only after relaxation polymers don't show any shifts with molecular weight meaning that

Scheme 1-9. Oxidative closure of o-phenylene rings to form graphene nanoribbons. Reprinted with permission from Ref.[59]

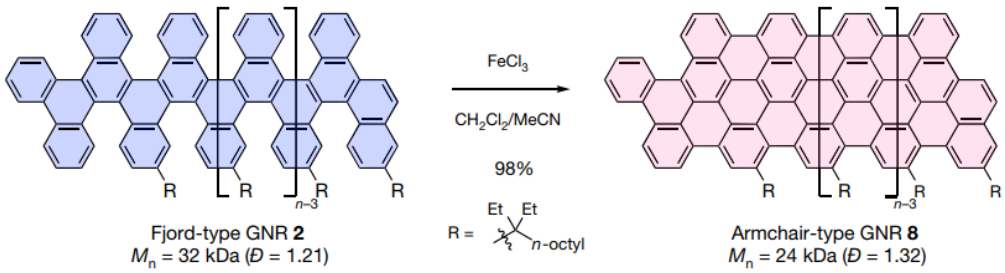

chromophore unit must be relatively small. It's interesting that fluorescence peaks depend on conjugation length and longer graphene nanoribbons have fluorescence peaks red-shifted. These facts suggest that HOMO-LUMO excitation.

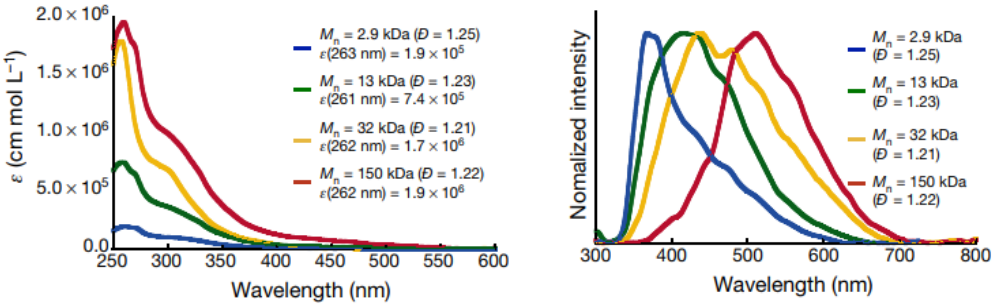

Figure 1-25. Absorption and fluorescence spectra of ladder polymers. Reprinted with permission from Ref.[59]

Cyclized graphene nanoribbons don't show any peaks in absorption spectra, however their fluorescence peaks are red-shifted compared to non-cyclized versions and also undergo red-shift with increase in molecular weight as is expected from greater conjugation.

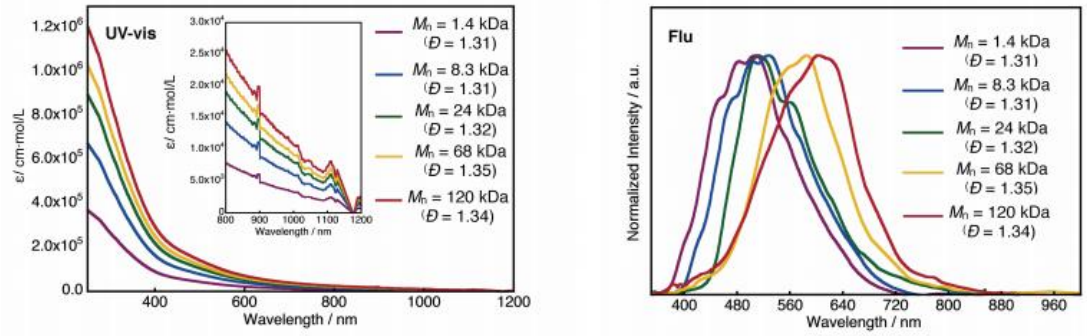

Figure 1-26. Absorption and fluorescence spectra of ladder polymers of cyclized nanoribbons. Reprinted with permission from Ref.[59]

Plunkett et al. have developed a sequence of cyclopentannulation and Scholl reactions to obtain ladder polymers with fused 5-membered rings in the backbone[60]. First, dibromoanthracene reacts with substituted acetylene to create twisted polymer precursors, which can be further cyclized by treatment with $FeCl_3$. Before carrying out the polymerization reaction conditions were studied on a model compound with only one triple bond reacting with dibromoanthracene and also on alkyne containing polymer reacting with arylbromide.

Scheme 1-10. Cyclopentannulation polymerization and subsequent Scholl reaction. Reprinted with permission from Ref.[60]

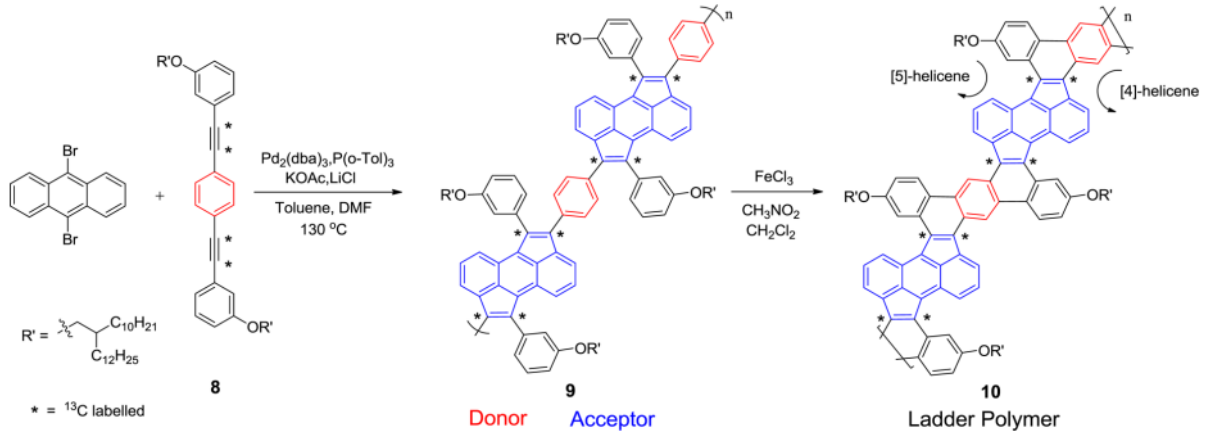

Solubility of ladder polymers is considerably lower than of their precursors. GPC traces provide circumstantial evidence for cyclization as apparent molecular weights increase after oxidation owing to the larger hydrodynamic radius of planarized rigid ladder polymers. Main evidence comes from ^{13}C NMR of isotopically labeled samples. After cyclization chemical shifts change in the same fashion as for model compounds. Worth noting however that signals are very broad, and do not provide quantitative information about non-fused defects.

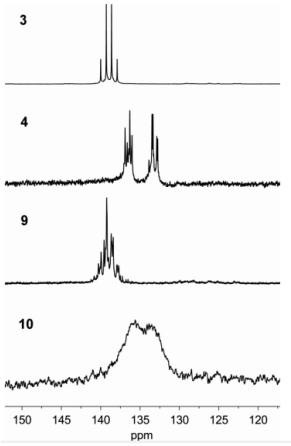

Figure 1-27. NMR peaks proving cyclization. Reprinted with permission from Ref.[60]

Researchers expanded this methodology to polymers containg thiophene and thienothiophene units. However this method has a limitation in that electron-rich fragments are necessary for successful Scholl reaction.

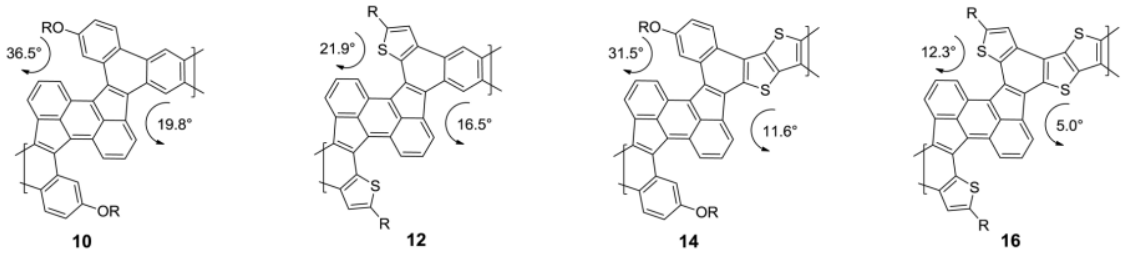

Figure 1-28. Dihedral angles and steric hindrance. Reprinted with permission from Ref.[60]

These materials were studied for FET applications, however they are unipolar semiconductors and their hole mobilities are in the range of 10^{-6}-10^{-5} $cm^2V^{-1}s^{-1}$. Likely this is due to still present helicene-like twists in every repeating unit. UV-vis spectra support this since peaks shift very little upon oxidative cyclization.

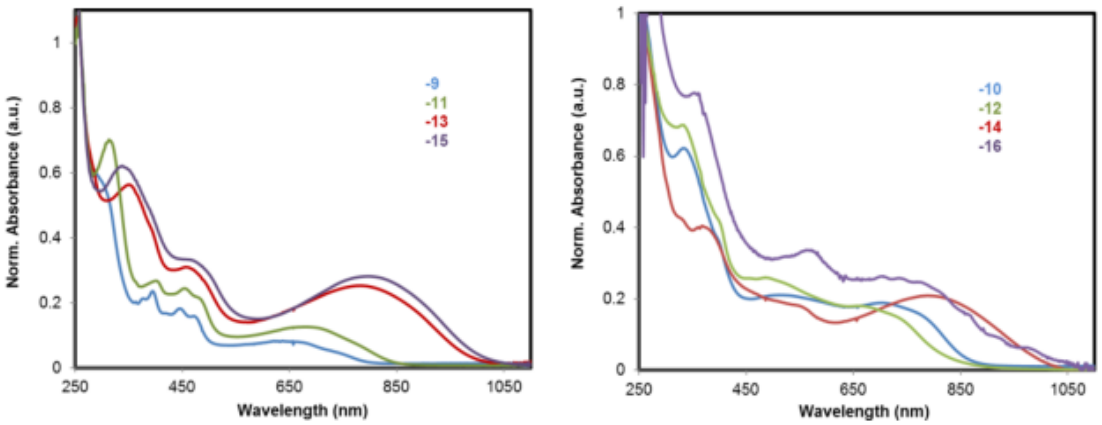

Figure 1-29. UV-visible spectra. Reprinted with permission from Ref.[60]

1.5 Conclusions

High charge carrier mobility and high quantum yields of luminescence are hard to achieve in the same material because mobility requires extensive π-π stacking which most of the time quenches fluorescent properties. However if balance between two can be achieved it is important to consider the balance between intermolecular donor-acceptor interactions.

Alkyl chains are a helpful tool in this regard as they not only provide sufficient solubility for materials to be processable, but also provide steric hindrance which can protect luminophore units from quenching.

Donor-acceptor structure is necessary for efficient crystal packing into lamellar structures with high mobility. Another important contribution of this design is alignment of materials HOMO and LUMO energy levels with that of electrodes of OLET device, most often -5.0eV for gold. If charge injection barrier is too high than its mobility will be impeded. Common guidelines include changing nature of donor and acceptor, for example addition of extra electron-rich thiophene rings to raise HOMO and increase hole mobility, or fluorination of acceptors to lower LUMO and increase electron mobility.

Common design strategies for fluorescent materials like TADF or AIE concepts are not directly applicable to OLET materials because their design inherently prevents achieving significant charge carrier mobilities due to twisted structures.

1.6 References

(1) Cicoira, F.; Santato, C. *Adv. Funct. Mater.* **2007**, *17* (17), 3421–3434.

(2) Cai, Z.; Awais, M. A.; Zhang, N.; Yu, L. *CHEMPR* **2018**, *4* (11), 2538–2570.

(3) Cai, Z.; Zhang, N.; Awais, M. A.; Filatov, A. S.; Yu, L. *Angew. Chemie - Int. Ed.* **2018**, *57* (22), 6442–6448.

(4) Cai, Z.; Lo, W. Y.; Zheng, T.; Li, L.; Zhang, N.; Hu, Y.; Yu, L. *J. Am. Chem. Soc.* **2016**, *138* (33), 10630–10635.

(5) Guo, X.; Watson, M. D. *Org. Lett.* **2008**, *10* (23), 5333–5336.

(6) Chen, Z.; Zheng, Y.; Yan, H.; Facchetti, A. *J. Am. Chem. Soc.* **2009**, *131* (1), 8–9.

(7) Boese, R.; Weiss, H.-C.; Bläser, D. *Angew. Chemie Int. Ed.* **1999**, *38* (7), 988–992.

(8) Sokolov, A. N.; Atahan-Evrenk, S.; Mondal, R.; Akkerman, H. B.; Sánchez-Carrera, R. S.; Granados-Focil, S.; Schrier, J.; Mannsfeld, S. C. B.; Zoombelt, A. P.; Bao, Z.; Aspuru-Guzik, A. *Nat. Commun.* **2011**, *2* (1), 437.

(9) Liang, Z.; Tang, Q.; Xu, J.; Miao, Q. *Adv. Mater.* **2011**, *23* (13), 1535–1539.

(10) Lei, T.; Zhou, Y.; Cheng, C.-Y.; Cao, Y.; Peng, Y.; Bian, J.; Pei, J. *Org. Lett.* **2011**, *13* (10), 2642–2645.

(11) Liu, Y.-Y.; Song, C.-L.; Zeng, W.-J.; Zhou, K.-G.; Shi, Z.-F.; Ma, C.-B.; Yang, F.; Zhang, H.-L.; Gong, X. *J. Am. Chem. Soc.* **2010**, *132* (46), 16349–16351.

(12) Lei, T.; Cao, Y.; Zhou, X.; Peng, Y.; Bian, J.; Pei, J. *Chem. Mater.* **2012**, *24* (10), 1762–1770.

(13) Yan, H.; Chen, Z.; Zheng, Y.; Newman, C.; Quinn, J. R.; Dötz, F.; Kastler, M.; Facchetti, A. *Nature* **2009**, *457* (7230), 679–686.

(14) Ha, J. S.; Kim, K. H.; Choi, D. H. *J. Am. Chem. Soc.* **2011**, *133* (27), 10364–10367.

(15) Bronstein, H.; Chen, Z.; Ashraf, R. S.; Zhang, W.; Du, J.; Durrant, J. R.; Shakya Tuladhar, P.; Song, K.; Watkins, S. E.; Geerts, Y.; Wienk, M. M.; Janssen, R. A. J.; Anthopoulos, T.; Sirringhaus, H.; Heeney, M.; McCulloch, I. *J. Am. Chem. Soc.* **2011**, *133* (10), 3272–3275.

(16) Li, Y.; Sonar, P.; Singh, S. P.; Soh, M. S.; Van Meurs, M.; Tan, J. *J. Am. Chem. Soc.* **2011**, *133* (7), 2198–2204.

(17) Li, Y.; Singh, S. P.; Sonar, P. *Adv. Mater.* **2010**, *22* (43), 4862–4866.

(18) Bürgi, L.; Turbiez, M.; Pfeiffer, R.; Bienewald, F.; Kirner, H.-J.; Winnewisser, C. *Adv. Mater.* **2008**, *20* (11), 2217–2224.

(19) Bijleveld, J. C.; Zoombelt, A. P.; Mathijssen, S. G. J.; Wienk, M. M.; Turbiez, M.; de Leeuw, D. M.; Janssen, R. A. J. *J. Am. Chem. Soc.* **2009**, *131* (46), 16616–16617.

(20) Sonar, P.; Singh, S. P.; Li, Y.; Soh, M. S.; Dodabalapur, A. *Adv. Mater.* **2010**, *22* (47), 5409–5413.

(21) Zhao, Z.; Yin, Z.; Chen, H.; Zheng, L.; Zhu, C.; Zhang, L.; Tan, S.; Wang, H.; Guo, Y.; Tang, Q.; Liu, Y. *Adv. Mater.* **2017**, *29* (4), 1–6.

(22) Lei, T.; Dou, J. H.; Pei, J. *Adv. Mater.* **2012**, *24* (48), 6457–6461.

(23) Fu, B.; Baltazar, J.; Sankar, A. R.; Chu, P. H.; Zhang, S.; Collard, D. M.; Reichmanis, E. *Adv. Funct. Mater.* **2014**, *24* (24), 3734–3744.

(24) Meager, I.; Ashraf, R. S.; Mollinger, S.; Schroeder, B. C.; Bronstein, H.; Beatrup, D.; Vezie, M. S.; Kirchartz, T.; Salleo, A.; Nelson, J.; McCulloch, I. *J. Am. Chem. Soc.* **2013**, *135* (31), 11537–11540.

(25) Back, J. Y.; Yu, H.; Song, I.; Kang, I.; Ahn, H.; Shin, T. J.; Kwon, S. K.; Oh, J. H.; Kim, Y. H. *Chem. Mater.* **2015**, *27* (5), 1732–1739.

(26) Kang, I.; Yun, H. J.; Chung, D. S.; Kwon, S. K.; Kim, Y. H. *J. Am. Chem. Soc.* **2013**, *135* (40), 14896–14899.

(27) Mei, J.; Kim, D. H.; Ayzner, A. L.; Toney, M. F.; Bao, Z. *J. Am. Chem. Soc.* **2011**, *133* (50), 20130–20133.

(28) Zhang, F.; Hu, Y.; Schuettfort, T.; Di, C. A.; Gao, X.; McNeill, C. R.; Thomsen, L.; Mannsfeld, S. C. B.; Yuan, W.; Sirringhaus, H.; Zhu, D. *J. Am. Chem. Soc.* **2013**, *135* (6), 2338–2349.

(29) Dou, J. H.; Zheng, Y. Q.; Lei, T.; Zhang, S. D.; Wang, Z.; Zhang, W. Bin; Wang, J. Y.; Pei, J. *Adv. Funct. Mater.* **2014**, *24* (40), 6270–6278.

(30) Lee, J.; Han, A.-R.; Kim, J.; Kim, Y.; Oh, J. H.; Yang, C. *J. Am. Chem. Soc.* **2012**, *134* (51), 20713–20721.

(31) Lee, J.; Han, A. R.; Yu, H.; Shin, T. J.; Yang, C.; Oh, J. H. *J. Am. Chem. Soc.* **2013**, *135* (25), 9540–9547.

(32) Yang, J.; Wang, H.; Chen, J.; Huang, J.; Jiang, Y.; Zhang, J.; Shi, L.; Sun, Y.; Wei, Z.; Yu, G.; Guo, Y.; Wang, S.; Liu, Y. *Adv. Mater.* **2017**, *29* (22), 1–7.

(33) Lu, L.; Zheng, T.; Wu, Q.; Schneider, A. M.; Zhao, D.; Yu, L. *Chem. Rev.* **2015**, *115* (23),

12666–12731.

(34) Liang, Y.; Yu, L. *Acc. Chem. Res.* **2010**, *43* (9), 1227–1236.

(35) Liang, Y.; Xu, Z.; Xia, J.; Tsai, S.-T.; Wu, Y.; Li, G.; Ray, C.; Yu, L. *Adv. Mater.* **2010**, *22* (20), E135–E138.

(36) Liang, Y.; Feng, D.; Wu, Y.; Tsai, S.; Li, G.; Ray, C. **2009**, No. d, 7792–7799.

(37) Son, H. J.; Wang, W.; Xu, T.; Liang, Y.; Wu, Y.; Li, G.; Yu, L. **2011**, 1885–1894.

(38) Yang, J.; Zhao, Z.; Geng, H.; Cheng, C.; Chen, J.; Sun, Y. *Adv. Mater.* **2017**, No. 29, 1702115.

(39) Gao, Y.; Deng, Y.; Tian, H.; Zhang, J.; Yan, D.; Geng, Y.; Wang, F. *Adv. Mater.* **2017**, *29* (13), 1606217.

(40) Zhu, C.; Zhao, Z.; Chen, H.; Zheng, L.; Li, X.; Chen, J.; Sun, Y.; Liu, F.; Guo, Y.; Liu, Y. *J. Am. Chem. Soc.* **2017**, *139* (49), 17735–17738.

(41) Ying, L.; Hsu, B. B. Y.; Zhan, H.; Welch, G. C.; Zalar, P.; Perez, L. A.; Kramer, E. J.; Nguyen, T. Q.; Heeger, A. J.; Wong, W. Y.; Bazan, G. C. *J. Am. Chem. Soc.* **2011**, *133* (46), 18538–18541.

(42) Cicoira, F.; Santato, C.; Dadvand, A.; Harnagea, C.; Pignolet, A.; Bellutti, P.; Xiang, Z.; Rosei, F.; Meng, H.; Perepichka, D. F. *J. Mater. Chem.* **2008**, *18* (2), 158–161.

(43) Ng, S.; Lu, H.; Chan, H. S. O.; Fujii, A.; Laga, T.; Yoshino, K. *Macromolecules* **2001**, *34* (20), 6895–6903.

(44) Wei, Q.; Ge, Z.; Voit, B. *Macromol. Rapid Commun.* **2019**, *40* (1), 1800570.

(45) Santato, C.; Capelli, R.; Loi, M. A.; Murgia, M.; Cicoira, F.; Roy, V. A. L.; Stallinga, P.; Zamboni, R.; Rost, C.; Karg, S. F.; Muccini, M. *Synth. Met.* **2004**, *146* (3), 329–334.

(46) Santato, C.; Manunza, I.; Bonfiglio, A.; Cicoira, F.; Cosseddu, P.; Zamboni, R.; Muccini, M. *Appl. Phys. Lett.* **2005**, *86* (14), 1–3.

(47) Hepp, A.; Heil, H.; Weise, W.; Ahles, M.; Schmechel, R.; von Seggern, H. *Phys. Rev. Lett.* **2003**, *91* (15), 1–4.

(48) Capelli, R.; Toffanin, S.; Generali, G.; Usta, H.; Facchetti, A.; Muccini, M. *Nat. Mater.* **2010**, *9* (6), 496–503.

(49) Ke, T. H.; Gehlhaar, R.; Chen, C. H.; Lin, J. T.; Wu, C. C.; Adachi, C. *Appl. Phys. Lett.* **2009**, *95* (6), 1–4.

(50) Seo, J. H.; Namdas, E. B.; Gutacker, A.; Heeger, A. J.; Bazan, G. C. *Adv. Funct. Mater.* **2011**, *21* (19), 3667–3672.

(51) Hou, L.; Zhang, X.; Cotella, G. F.; Carnicella, G.; Herder, M.; Schmidt, B. M.; Pätzel, M.; Hecht, S.; Cacialli, F.; Samorì, P. *Nat. Nanotechnol.* **2019**, *14* (April), 347–353.

(52) Chaudhry, M. U.; Muhieddine, K.; Wawrzinek, R.; Li, J.; Lo, S. C.; Namdas, E. B. *ACS Photonics* **2018**, *5* (6), 2137–2144.

(53) Luo, C.; Kyaw, A. K. K.; Perez, L. A.; Patel, S.; Wang, M.; Grimm, B.; Bazan, G. C.; Kramer, E. J.; Heeger, A. J. *Nano Lett.* **2014**, *14* (5), 2764–2771.

(54) Hsu, B. B. Y.; Seifter, J.; Takacs, C. J.; Zhong, C.; Tseng, H. R.; Samuel, I. D. W.; Namdas, E. B.; Bazan, G. C.; Huang, F.; Cao, Y.; Heeger, A. J. *ACS Nano* **2013**, *7* (3), 2344–2351.

(55) Wang, J.; Chu, M.; Fan, J.-X.; Lau, T.-K.; Ren, A.-M.; Lu, X.; Miao, Q. *J. Am. Chem. Soc.* **2019**, *141* (8), 3589–3596.

(56) Jousselin-Oba, T.; Mamada, M.; Marrot, J.; Maignan, A.; Adachi, C.; Yassar, A.; Frigoli, M. *J. Am. Chem. Soc.* **2019**, *141* (23), 9373–9381.

(57) Teo, Y. C.; Jin, Z.; Xia, Y. *Org. Lett.* **2018**, *20* (11), 3300–3304.

(58) Abdulhamid, M. A.; Lai, H. W. H.; Wang, Y.; Jin, Z.; Teo, Y. C.; Ma, X.; Pinnau, I.; Xia, Y. *Chem. Mater.* **2019**, *31* (5), 1767–1774.

(59) Yano, Y.; Mitoma, N.; Matsushima, K.; Wang, F.; Matsui, K.; Takakura, A.; Miyauchi, Y.; Ito, H.; Itami, K. *Nature* **2019**, *571* (7765), 387–392.

(60) Bheemireddy, S. R.; Hautzinger, M. P.; Li, T.; Lee, B.; Plunkett, K. N. *J. Am. Chem. Soc.* **2017**, *139* (16), 5801–5807.

CHAPTER 2

CATIONIC CONJUGATED POLYMERS FOR ELECTROCHROMIC APPLICATIONS

2.1 Introduction

Cationic conjugated polymers are widely used as sensors in cellular imaging, electrochromic materials and interfacial layers in devices.[61–64] However, most of these polymers rely on cationic quaternary amino groups in side chains. Therefore there is a lack of variety of conjugated cationic polymers.

Recently these types of materials have recaptured attention as agents for antibacterial and antitumor photodynamic therapy. Zhai et al. have synthesized a series of polymers based on fluorene-co-phenylene ethynylene moiety with alkyl groups bearing quaternary ammonium salts.[65] They discovered that polymers with donor-acceptor motifs produce reactive oxygen species more efficiently, however their studies were limited by only using few electron withdrawing groups on benzene ring for acceptor part of repeating unit.

Most prominent class of conjugated polymers with positive charges in main backbone is pyridinium version of polyphenylenes.[66,67] These materials include more recent poly(pyridinium-phenylene) developed by Swager group.[68,69] Their strategy relies on first synthesizing a polymer with neutral pyridines in the repeating unit, and then intramolecular postpolymerization cyclization creates cationic centers on pyridine nitrogens. This approach however relies on high effectiveness of the last step and is not therefore general. Interestingly, this new material can be used as a sensor for caffeine in aqueous solutions with sensitivity up to 25μM.

Another important work in this area focuses on attempts to incorporate triphenylmethyl cation center into conjugated polymer backbone.[70] As interesting as this material is conceptually

it is impractical for any application as these cations are readily quenched with nucleophilic anions, for example methoxide.

Considering the aforementioned works there is an unmet need in new classes of conjugated polymers with positive charges incorporated into the π-system, which can be used for further exploration of new properties.

2.2 Results and discussion

We have synthesized a series of cationic polymers by Stille polycondensation. The polymers have positive charge in conjugated backbone. Our basic structural unit is based on monomer 5 with its thienoquinolizinium system. In this structure, the positive charge is formally located on nitrogen, yet it is delocalized around the heterocyclic rings in other resonance structures and into the polymer chain. This structure infers that any change in local environment around cation or its reduction will have great impact on electronic properties of the polymer, which can be useful for sensing or applications in electrochromism.

PTQ-16 incorporates common donor benzodithiophene and thienoquinolizinium acceptor, 16 refers to the number of sp3 carbons per repeating unit. PTQ-40 has additional long alkyl chains with OH groups at the end to improve solubility and avoid making polymer to hydrophobic. PTQ-A has alkoxy groups instead of thiophenes on the donor unit, and also lacks alkyl chains on the acceptor unit. We envisioned that PTQ-40 would be more stable in electrochemical processes since the C-C bond would be harder to break than C-O. We also synthesized PTQ-B which has broken conjugation between acceptor units and serves as a reference. We have chosen 3 CH_2 groups as a spacer, so that conjugation cannot be restored even if spacer group is oxidized to form a double bond during device operation. These 4 polymers explore chemical space around our conjugated

system for optimal solubility and provide a negative control to distinguish properties of the polymer versus effects arising from single acceptor fragments.

Scheme 2-1. Structures of synthesized materials.

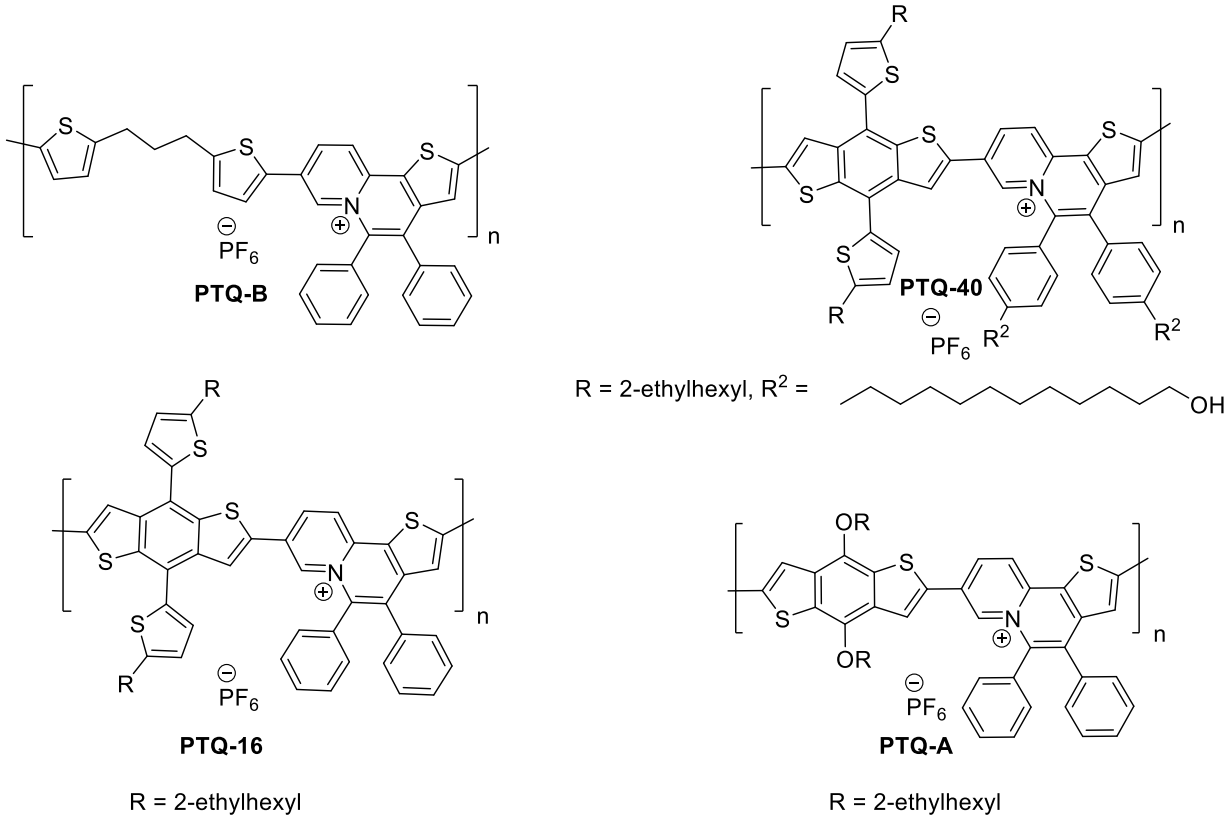

2.2.1 Synthesis

Synthesis of the first polymer in the series began with the Stille cross-coupling of 5-bromo-2-iodopyridine with thienyltributylstannane. It was then smoothly brominated into the 2-position of thiophene with NBS in chloroform-acetic acid mixture. The key step in the synthesis of monomer 5 involves coordination of Ru(p-cumene) catalyst to pyridine nitrogen of 3. Next C-H activation by Ru insertion creates reactive center on 3 position of thiophene, which in turn reacts with diphenylacetylene.[71] This intermediate then undergoes reductive elimination of Ru catalyst and cyclization on pyridine nitrogen. As a side reaction Br in 3-position of pyridine gets reduced

and this monobrominated impurity needs to be carefully separated from the monomer 5. Finally, The Stille polycondensation of 6 and 5 under Pd catalysis afforded polymer PTQ-16 after ion exchange. Prolonged reaction times are required to achieve reasonable molecular weight. Mechanistically this can be explained by reaction slowing down due to repulsion of positively charged monomers and growing polymer chain.

Scheme 2-2. Synthesis of PTQ-16.

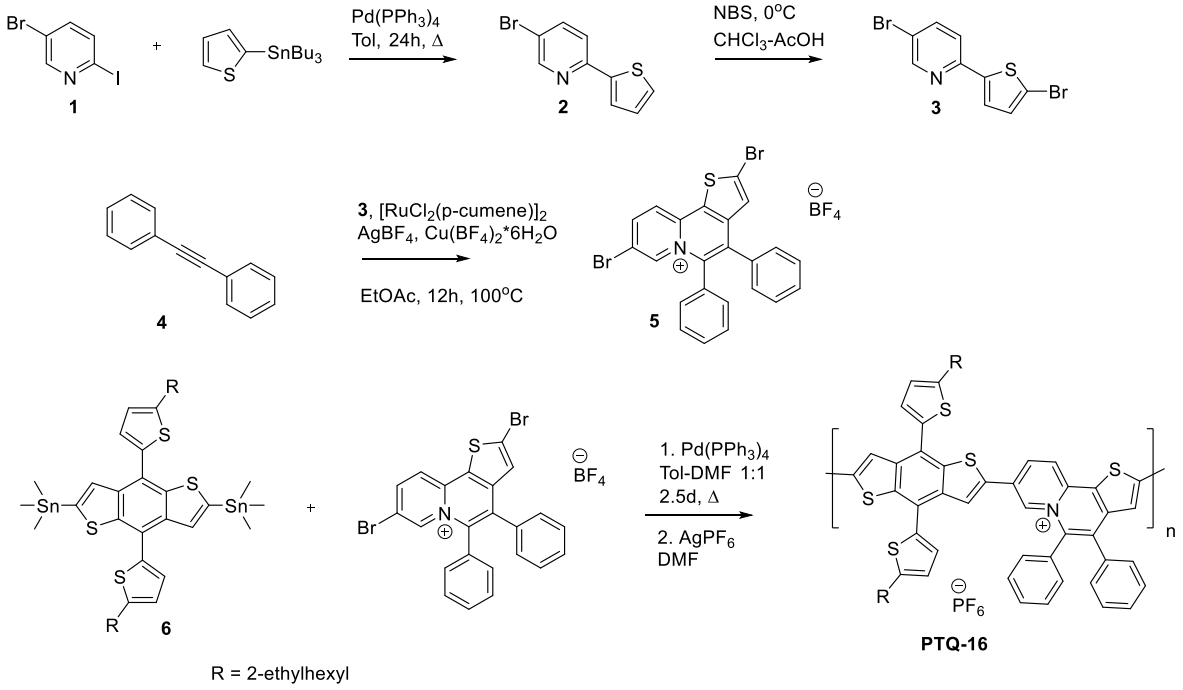

Synthesis of our next polymer is similar, but requires an additional alkyl chain monomer. Therefore, we used alcohol protection with MOMCl to afford alkyl bromide 7, which then afforded Grignard reagent 8. Sonogashira coupling of 2 equivalents of 1-bromo-4-iodobenzene with 1 equivalent of TMS-acetylene proceeded with simultaneous removal of TMS group and afforded alkyne precursor 9. Pd-catalyzed Kumada coupling with synthesized dibromodiphenylacetylene yielded alkyne 10. Next C-H activation-alkyne insertion sequence gave rise to compound 11.

Notice that MOM protecting group turned out not be stable under these conditions. After ion exchange and polymerization, we obtained polymer PTQ-40.

Scheme 2-3. Synthesis of PTQ-40.

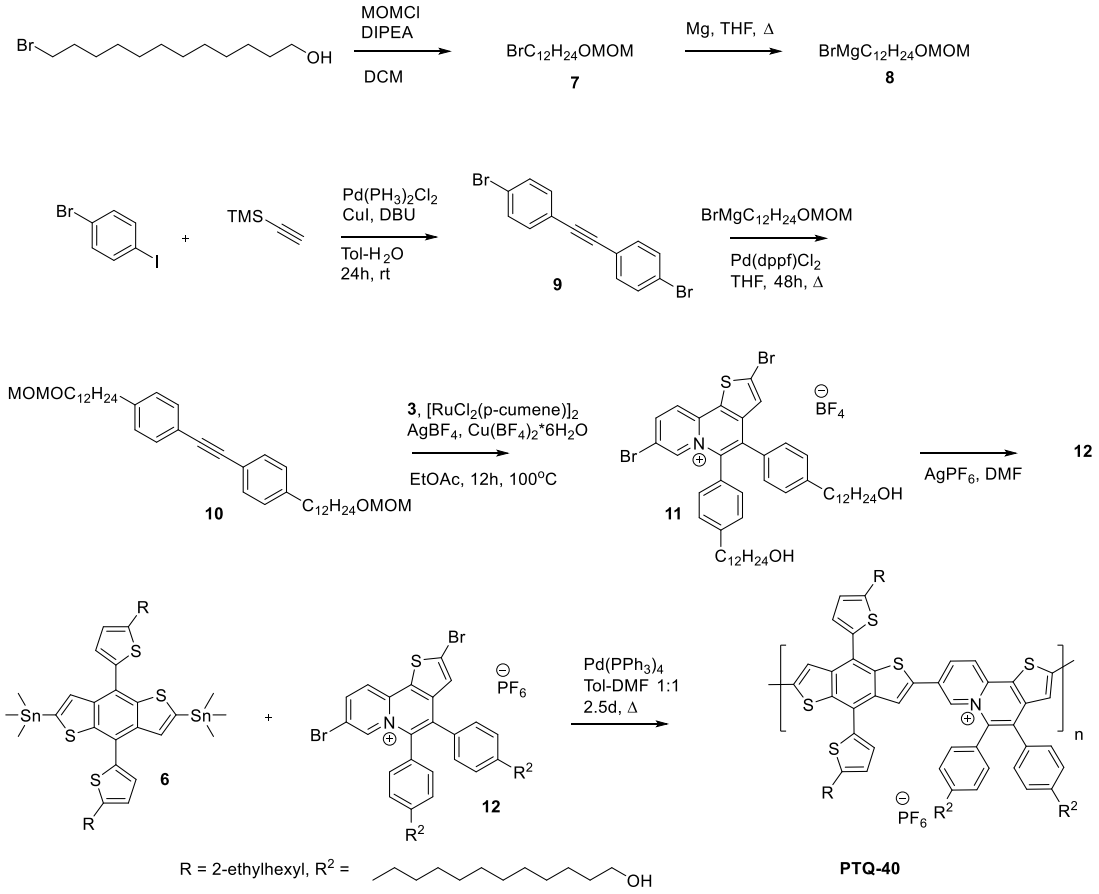

Synthesis of PTQ-A is analogous, however we used benzodithiophene monomer 16 with alkoxy groups instead of thienyl groups. It was prepared by one-pot reduction and alkylation of compound 13 with Zn and 2-ethylhexyl tosylate to give 14. Treatment with n-butyl lithium at -78°C and stannylation with trimethyltin chloride afford monomer 15. Polymerization with $Pd_2(dba)_3$ and tri-(2-tolyl)-phosphine afforded polymer PTQ-A.

Scheme 2-4. Synthesis of PTQ-A.

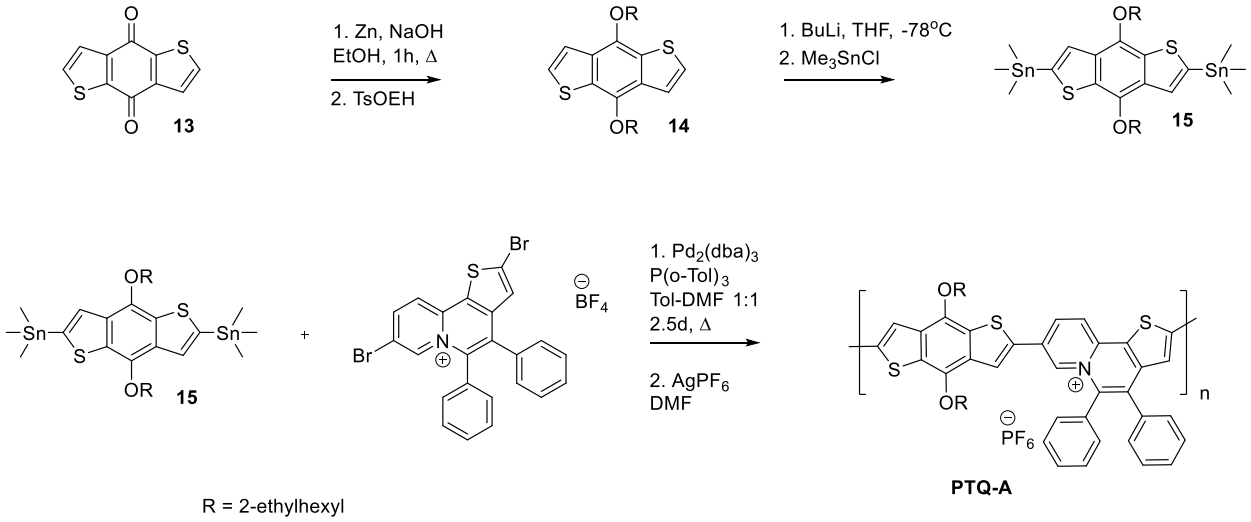

For polymer PTQ-B we prepared dithienylpropane 16 by deprotonating thiophene with n-BuLi and quenching with dibromopropane. Further deprotonation with excess n-BuLi and stannylation with trimethyltin chloride afford monomer 17, which is polymerized with monomer 5 to give polymer PTQ-B.

Scheme 2-5. Synthesis of PTQ-B.

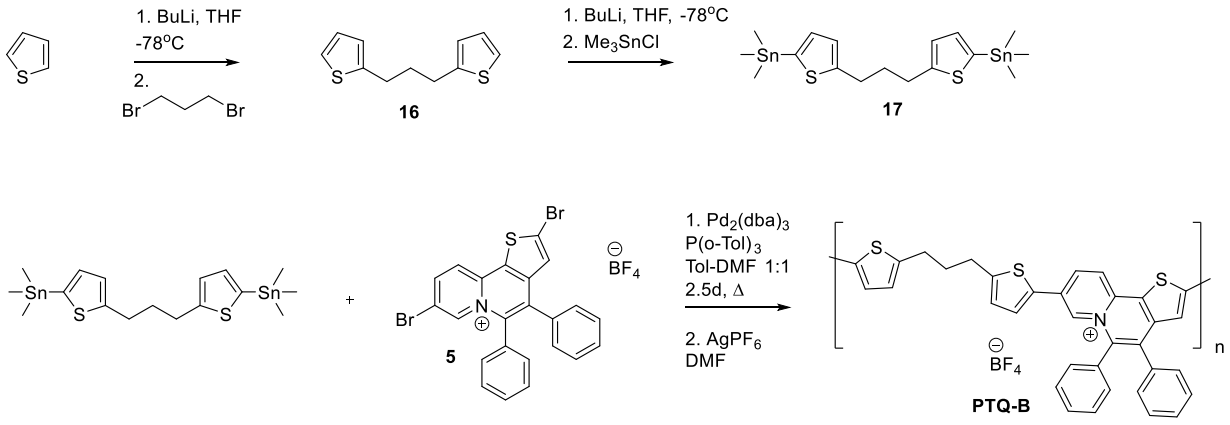

2.2.2 Optoelectronic properties of synthesized polymers

After successful synthesis of this series of polymers we investigated their oproelectronic properties by means of CV and UV-vis spectroscopy.

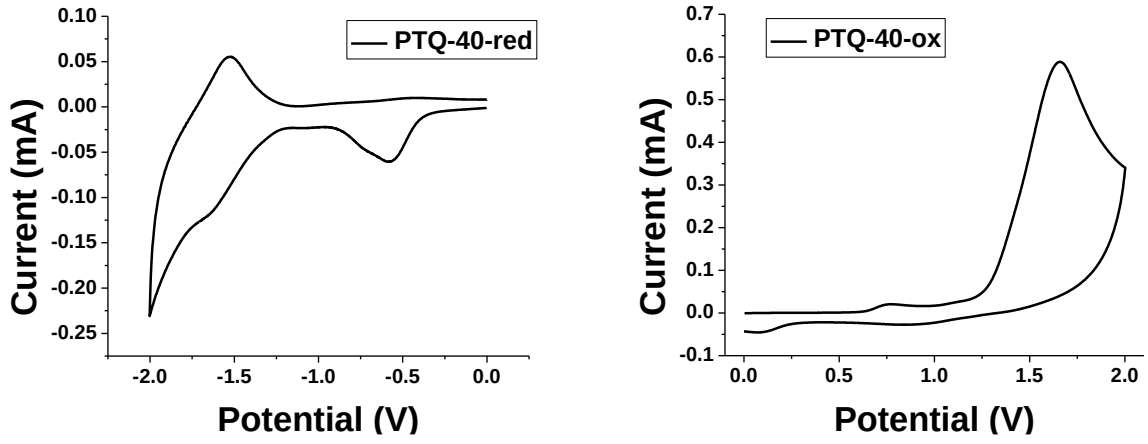

Figure 2-1. PTQ-40 CV reduction and oxidation scans

From reduction and oxidation potantials in CV we learned that HOMO of PTQ-40 lies at -5.54eV, and LUMO at -3.97eV. Separately performed reduction and oxidation scans for PTQ-40 tell us that redox processes are irreversible, because there is no reverse wave for reduction and oxidation peaks. It is worth noting that second full scan is different from the first in both reduction and oxidation peaks, however the oxidation part of the first full scan is the same as an oxidation scan performed separately. This means that reduction and oxidation happen on different units, because irreversible reduction does not influence oxidation scan. This notion is further supported by double oxidation scan. When the oxidation scan is performed second time the oxidation peak is greatly diminished.

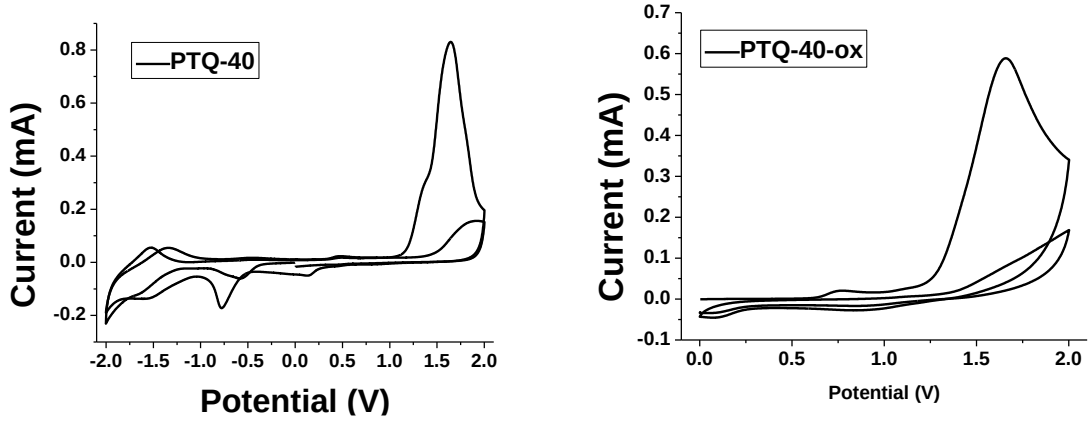

Figure 2-2. PTQ-40 CV multiple cycle scans

To further extract information from CV we performed a Tafel analysis of CV curves by plotting logarithm of current versus potential.[72] (ref to a book p. 144) Since the CV was performed with a film of insoluble polymer we cannot have a steady-state conditions like in the case of rotating electrode and soluble electroactive species. Therefore we approximate peak's onset as a steady state condition when only a small fraction of molecules underwent electron transfer. According to Butler-Volmer theory rate of electron transfer depends exponentially on the potential applied.

Tafel equation ln[Ired]=-αThe slope of the linear fragment of CV curve in Tafel coordinates corresponds to the transfer coefficient which has a physical meaning of position of transition state between reactants and products on the reaction coordinate, and typically is assumed to be 0.5. In our case the transfer coefficient turns out to be 0.32 for the onset of reduction peak and 0.27 for the onset of oxidation peak. Tafel analysis also indicates that only 1 electron participates in each electron transfer step, otherwise the dependence of current on voltage would be much steeper.

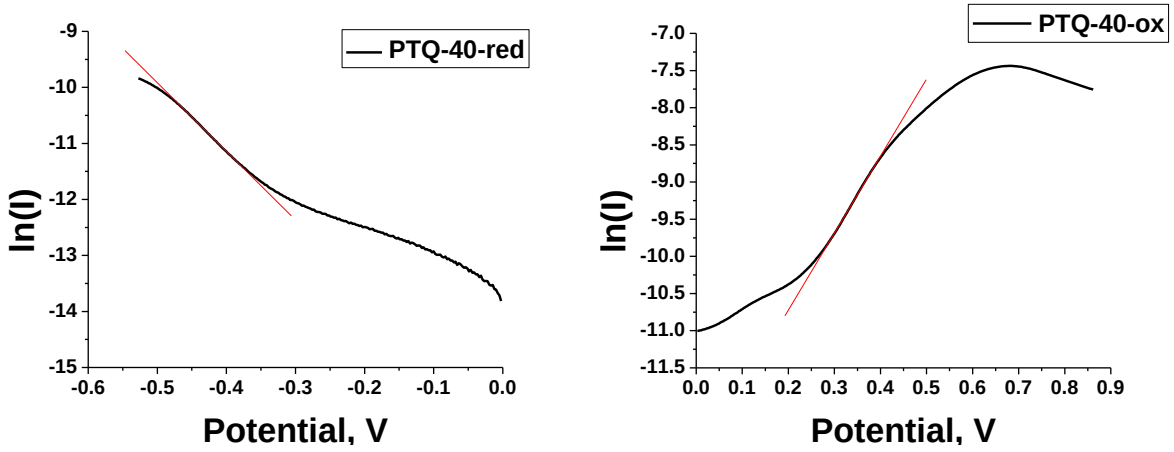

Figure 2-3. Tafel plots of CV data for PTQ-40

This indicates that either the electron transfer transition state is early, or that electron transfer is slowed down by a coupled process like slow diffusion of counterions.

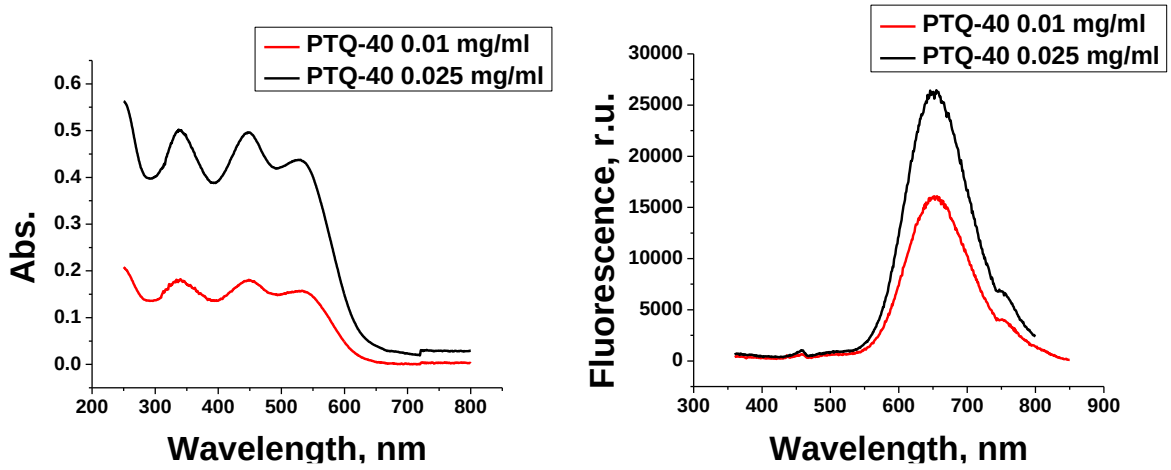

Figure 2-4. PTQ-40 UV-vis and fluorescence spectra

Onset of UV-vis spectrum of PTQ-40 is at 620 nm, which corresponds to optical bandgap of 2.0 eV, whereas electrochemical bandgap was calculated to be 1.57 eV. When optical bandgap is smaller than electrochemical it indicates that upon excitation hole and electron are strongly interacting with each other. From obtained results we can conclude that electrochemically reduced

state of the polymer is more stabilized than pristine polymer LUMO with electron after photoexcitation. When electron is injected into positively charged polymer chain it converts positively charged nitrogen into tertiary amine with formation of the delocalized radical. The energy stabilization can be attributed to the quinoidal structure that can form from two intrachain radicals.

Scheme 2-6. Formation of quinoidal structure after electrochemical reduction.

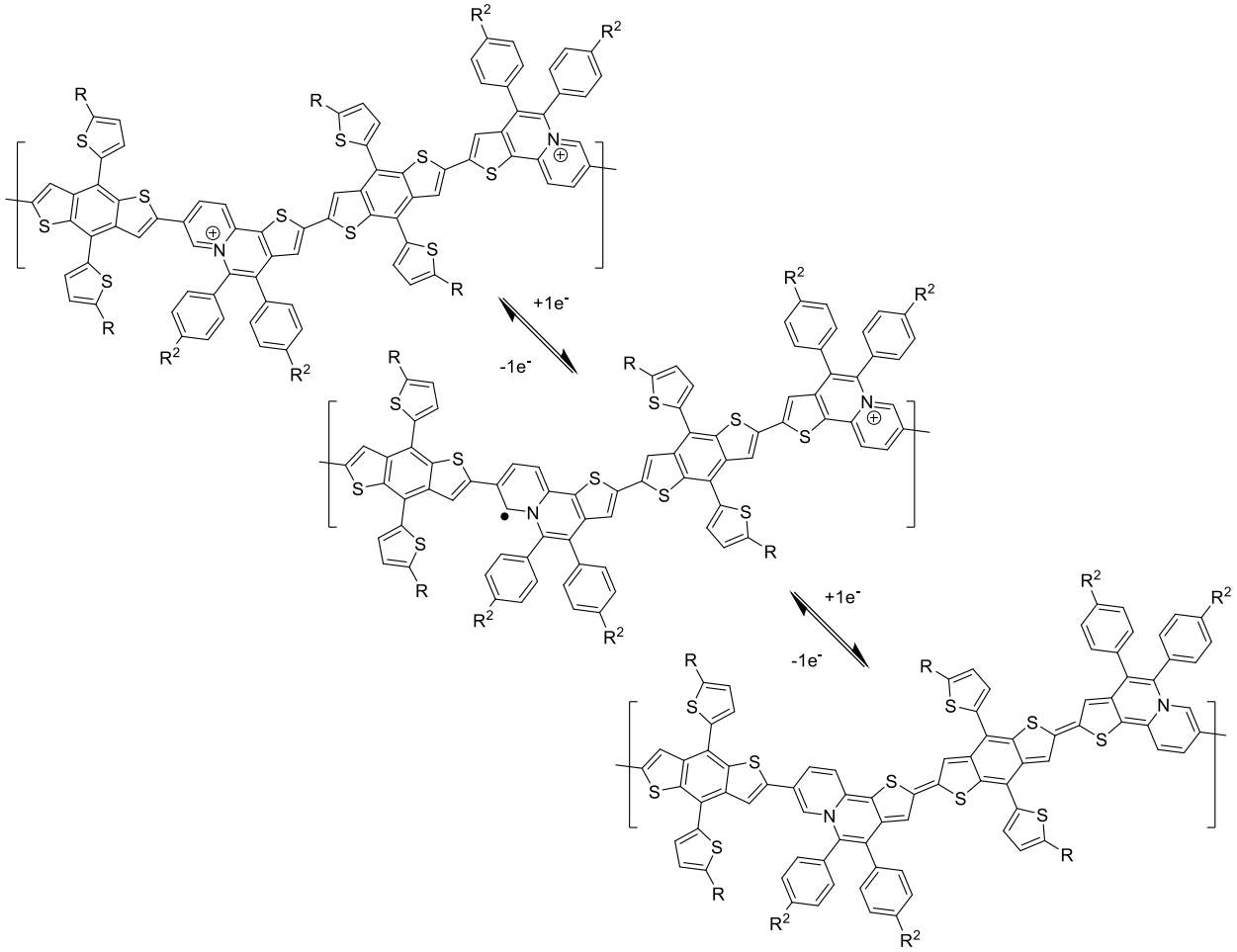

Positions of the peaks in the absorption spectrum practically don't change with change in concentration which shows that there is no strong aggregation of polymer chains in dilute solution.

Conc, mg/ml	Peaks		
0.1	338 nm	448 nm	529 nm
0.01	340 nm	449 nm	534 nm
0.0025	338 nm	448 nm	530 nm

Table 2-1. PTQ-40 UV-vis data

This is further supported by fluorescence peaks, not shifting with concentration as well. Quantum yield of fluorescence was measured by comparison with diphenylanthracene to be 0.4%. Such a low value of quantum yield combined with donor-acceptor structure of the polymer suggests electron transfer from donor to acceptor as major pathway for the evolution of the excited state. Large Stokes shift of 100 nm indicates that there is a big difference in geometry of ground and excited states.

PTQ-16

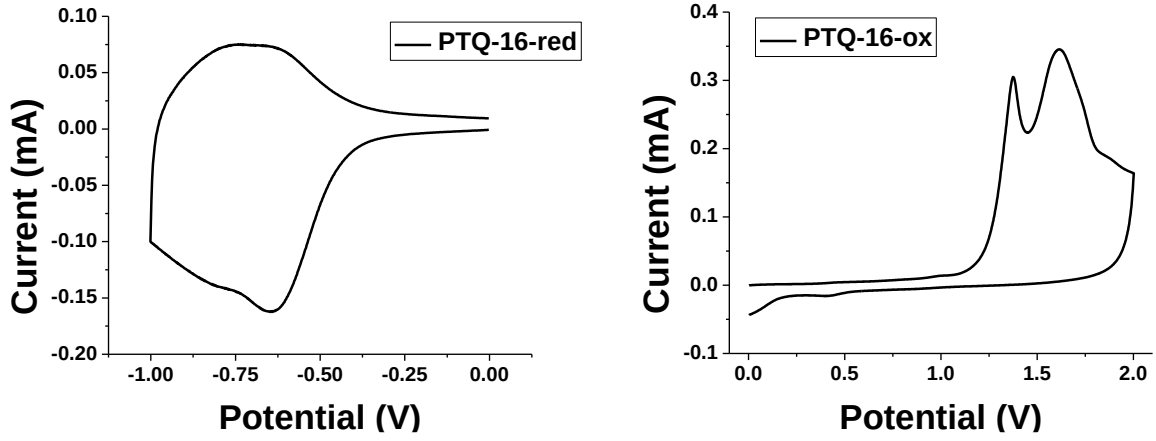

Figure 2-5. PTQ-16 reduction and oxidation scans

From CV of PTQ-16, we determined its HOMO to be -5.60eV, and LUMO -3.94 eV, which is very close to PTQ-40 as expected from the same backbone that these polymers share. Both

polymers undergo irreversible reduction and oxidation, since there is no clear reverse peak in reduction and no peak at all in oxidation scans. However unlike PTQ-40, PTQ-16 has 2 peaks in the oxidation scan and a wide reverse peak in the reduction scan. Structures of PTQ-16 and 398 differ only in that PTQ-40 has long alkyl chains on phenyl moieties, therefore it's hard to explain differences in CV based on polymer structure. More likely second oxidation peak and broad back peak in reduction scan rise from the DMF residue in the polymer film on the electrode.

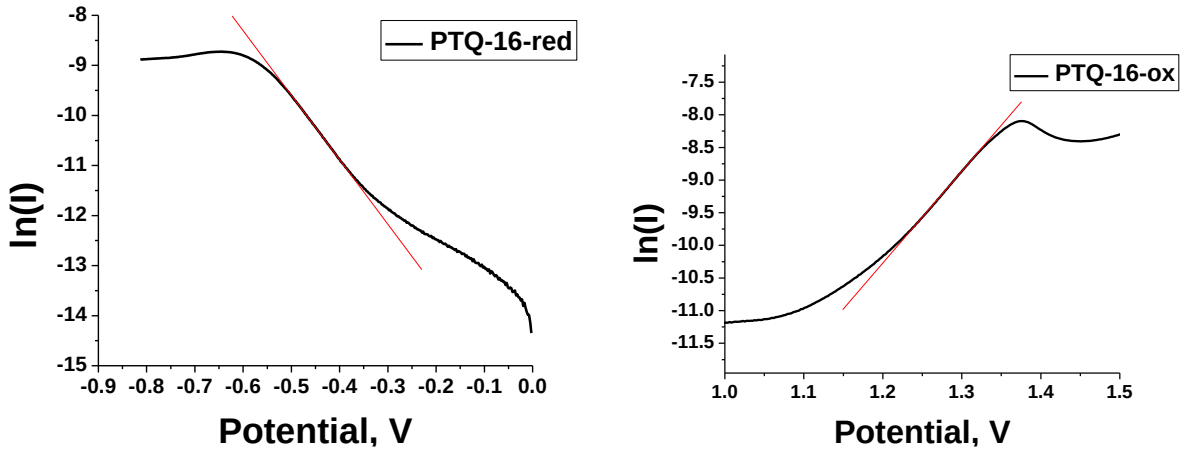

Figure 2-6. Tafel plots of CV data for PTQ-16

Analyzing CV of PTQ-16 in Tafel coordinates, we calculated its transfer coefficient for reduction onset to be 0.33, and for oxidation 0.36. These values are still lower than expected 0.5, but they are larger than for PTQ-40 meaning that rate of electron transfer depends on potential steeper. This difference in electrochemical behavior can be explained by long alkyl chains of PTQ-40 slowing down counter-ion diffusion to and from the film.

PTQ-16 is insoluble in chloroform and unlike other polymers, its spectra were taken in DMF.

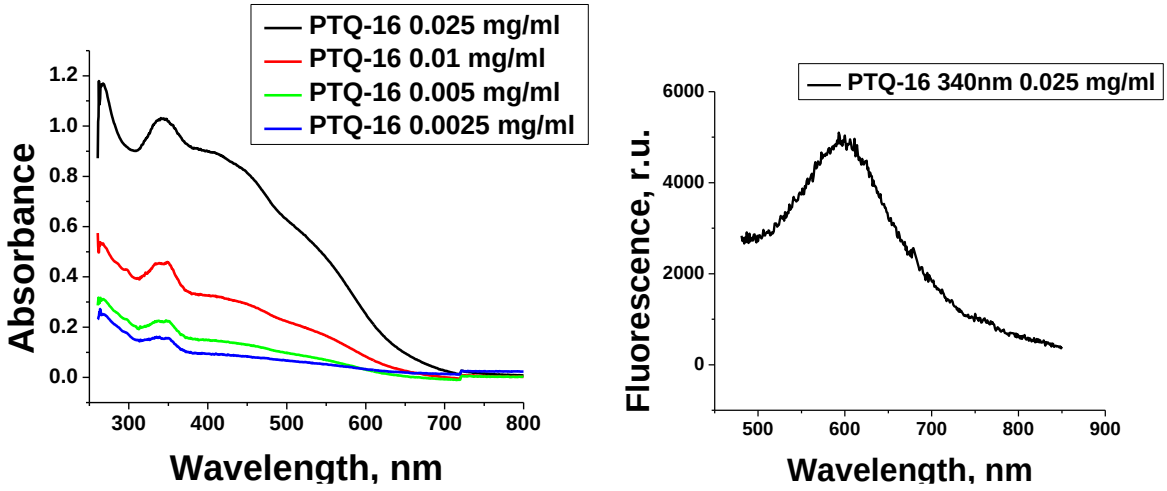

Figure 2-7. PTQ-16 UV-vis and fluorescence spectra

UV-vis spectrum of PTQ-16 in DMF indicates very strong aggregation, as evidenced by the continuous shoulder from 400 to 700nm. This shoulder has features of changing slope, which roughly correspond to the peaks in spectra of related polymers PTQ-40 and PTQ-A.

Conc, mg/ml	**Peaks**	**Shoulders**	
0.025	341nm	436nm	545nm
0.01	349nm	447nm	545nm
0.005	347nm	455nm	546nm
0.0025	335 nm	-	-

Table 2-2. PTQ-16 UV-vis data

Despite the spectrum lacking clear peaks of other polymers, PTQ-16 has almost the same optical bandgap as PTQ-40 and PTQ-A, 630 nm as compared to 620nm. The difference is quite small and suggests that despite bad solubility, the underlying electronic properties of polymers are similar.

PTQ-16 has a very low quantum yield of fluorescence 0.2%, which is expected from strong aggregation. Its fluorescence maximum at 593 nm is blue-shifted compared to 650nm of PTQ-40, however because of different solvents used, DMF and chloroform, we cannot claim that the shift is because of aggregation. Since our polymers have a donor-acceptor structure their spectra should be sensitive to polarity of solvent.

PTQ-B

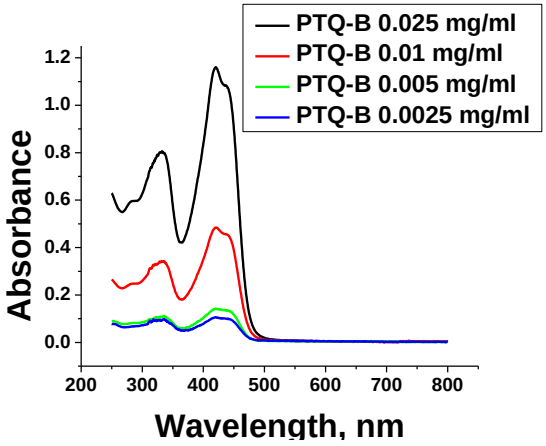

Conc, mg/ml	Peaks	
0.025	333 nm	421 nm
0.01	333 nm	421 nm
0.005	335 nm	420 nm
0.0025	335 nm	420 nm

Figure 2-8. PTQ-B UV-vis spectra and data

Unlike PTQ-40 PTQ-B has only 2 peaks in UV-vis, each peak has a shoulder. Optical bandgap of AN -449 is only 475 nm, much smaller than that of PTQ-40, which is expected based on the lack of conjugation. Peaks in the absorption spectrum change very little with concentration, however shoulders become less pronounced with increase in concentration.

One explanation of this is that there is weak interaction between polymer chains in solution. However because, shoulders are red and blue-shifted relative to their major peaks, we cannot assign J- or H-aggregates as a cause of shoulders in the spectrum. Alternative explanation is that phenyl rings not completely conjugated with the main chromofor are responsible for shoulder of

absorption around 300nm, and thiophene twisted from main chromofore is responsible for 450nm shoulder.

PTQ-B is more fluorescent than PTQ-40 with quantum yields of 4% when excited at 330nm, 9% when excited at 430nm. Higher fluorescence can be explained by the absence of benzodithiophene strong donor unit in the polymer, and so electron transfer is greatly diminished as a competing pathway for the excited state relaxation. It's also interesting that irrespective of excitation wavelength fluorescence occurs around 483 nm. Meaning that higher excited state can relax to lower excited state and then fluoresce.

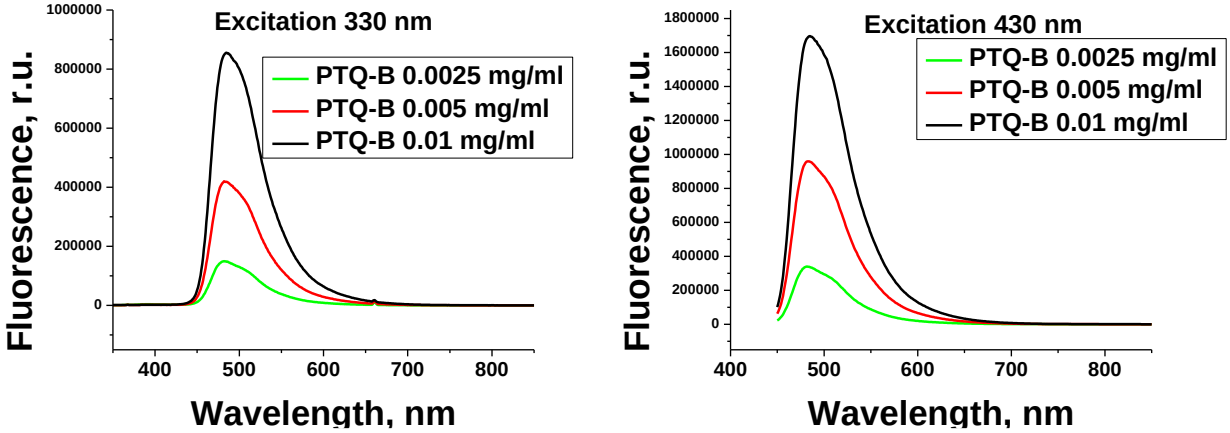

Figure 2-9. PTQ-B fluorescence spectra at different excitation wavelengths.

Fluorescence peaks depend on concentration slightly, undergoing tiny red shift with increase in concentration. This could be an indication of weak interchain interaction in solution akin to J-aggregation. J-aggregation would be weak because of positive charges of individual chromofores repelling each other, however J-aggregation would be more likely than H-aggregation because in face-to-face interaction repulsion would be greater than in head-to-tail. It's also interesting to notice that fluorescence with excitation at 430 nm becomes greater than from

Conc, mg/ml	Peak 330nm	Peak 430nm	Abs 430/330	Fluo 430/330
0.01	485 nm	485 nm	1.42	1.98
0.005	482 nm	483 nm	1.28	2.28
0.0025	482 nm	481 nm	1.09	2.27

Table 2-3. PTQ-B UV-vis and fluorescence data

excitation at 330nm as solution becomes more dilute. The fact that ratio between absorption and fluorescence peaks depends on concentration points to aggregation. HOMO-LUMO transition is more favored in the aggregates, than in the more dilute solution. At the same time fluorescence from 430nm excitation becomes weaker compared to 330 nm excitation, which makes sense considering the quenching effect of aggregation and greater quenching effect on a more fluorescent process. Aggregation of PTQ-B could anticipated from its structure since it does not have solubilizing alkyl chains that could present steric hindrance for inter-chain interactions.

PTQ-A

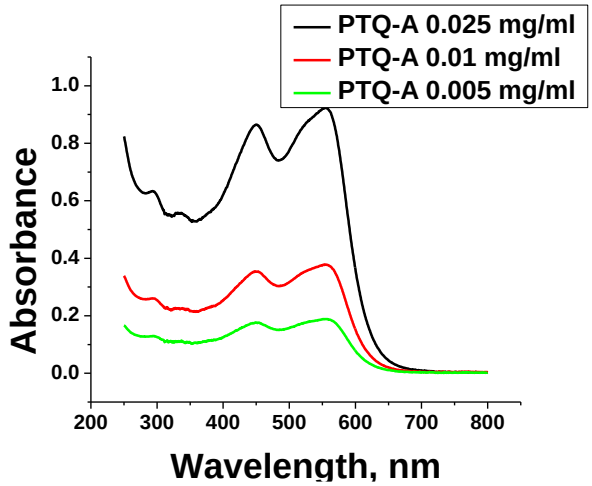

Figure 2-10. PTQ-A UV-vis spectra

PTQ-A optical properties are similar to PTQ-40. Optical bandgap is the same 620 nm, and the polymers is non-fluorescent with quantum yields exciting at 450nm 0.04%, and exciting at 550nm 0.03%. This is expected considering close similarity of polymers to each other, namely the same conjugated backbone and donor-acceptor nature. Unlike PTQ-40 PTQ-A has only 2 peaks in its absorption spectrum. Considering structural differences between the 2 polymers we can make a conclusion that a 340nm peak in the UV-vis spectrum of PTQ-40 arises from exciting alkylthiophene units on BDT.

Comparing PTQ-A and PTQ-B we can conclude that phenyl rings on the acceptor fragment lead to absorption around 290 and 330nm, giving UV peaks in spectrum of PTQ-A and UV shoulders for PTQ-B. Peak positions in the absorption spectrum of PTQ-A are independent of concentration. Changes are only a few nm in magnitude and without apparent trend.

Conc, mg/ml	**Peaks**			
0.025	293 nm	332 nm	450 nm	555 nm
0.01	294 nm	333 nm	449 nm	555 nm
0.005	296 nm	332 nm	449 nm	557 nm

Table 2-4. PTQ-A UV-vis spectra and data

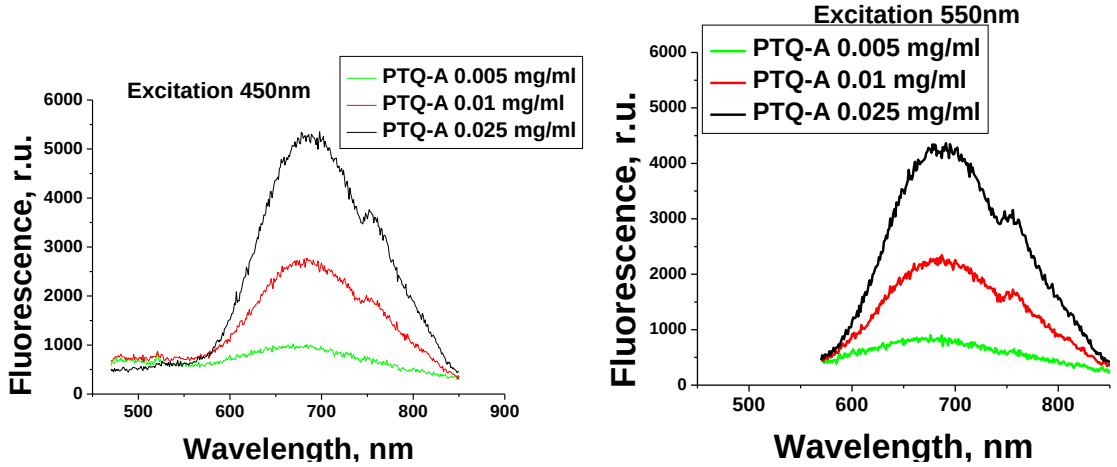

Figure 2-11. PTQ-A fluorescence spectra

Fluorescence spectrum of PTQ-A has very weak dependence on concentration. Peaks undergo small red-shift with increasing concentration, however this trend is unreliable because of very low fluorescence and sensitivity to noise. Fluorescence spectra feature a shoulder around 750nm, which gets more pronounced with increasing concentration, hinting at J-aggregation.

It's interesting to notice that in PTQ-A exciting HOMO-LUMO transition at 550nm leads to a slightly decreased fluorescence, whereas in broken conjugation polymer PTQ-B, it was the opposite. The donor-acceptor nature of PTQ-A ressults in a charge transfer nature and electron moves from BDT to positively charged acceptor.

Conc, mg/ml	Peak 450nm	Peak 550nm
0.025	689nm	691nm
0.01	684nm	687nm
0.005	684nm	687nm

Table 2-5. PTQ-A fluorescence data

2.2.3 Electrochromic properties

Synthesized polymers exhibit strong electrochromism. Fig. 2-12 shows the device based on PTQ-40 and PMMA/acetonitrile/propylene carbonate/$LiClO_4$ electrolyte. Polymer undergoes visible changes from initial red to intense green in the reduced state.

Figure 2-12. Electrochromic devices based on PTQ-40

We studied electrochromic properties of PTQ-40 under different applied biases. As voltage is gradually reduced from 0 to -3V UV-vis absorption peaks at 450 and 550nm decrease in intensity while the absorption in 700-800nm increases. Isosbestic point where reduced and oxidized forms of polymer have the same absorption is around 610nm. Monitoring this behavior at longer wavelengths shows that reduction leads to apparent absorption in whole NIR region with 2 bands appearing from 600 to 900 nm and 900 to 1600nm. Increase in NIR absorption indicates formation of well-delocalized quinodal structure or polarons. Upon oxidation 450 and 550nm peaks increase in intensity, while those in NIR decrease highlighting reversibility of redox processes. Figure 2-13 also shows dependence of transmission of devices at 670nm over time. Reduced transmission corresponds to increase in absorption on other graphs. As we can see efficiency drops over first 3 cycles and then plateaus over the next 3, which means that during first 3 cycles a fraction of chromophores irreversibly converts to the reduced form which creates a permanent drop in transmission at 670nm for the oxidized state. This stabilization can be explained by changed morphology of the polymer film. During shrinking and swelling of polymer film as ions move out and into the film during reduction and oxidation respectively, some parts of the film become inaccessible to electrolyte, while others establish efficient pathways for ions movement.

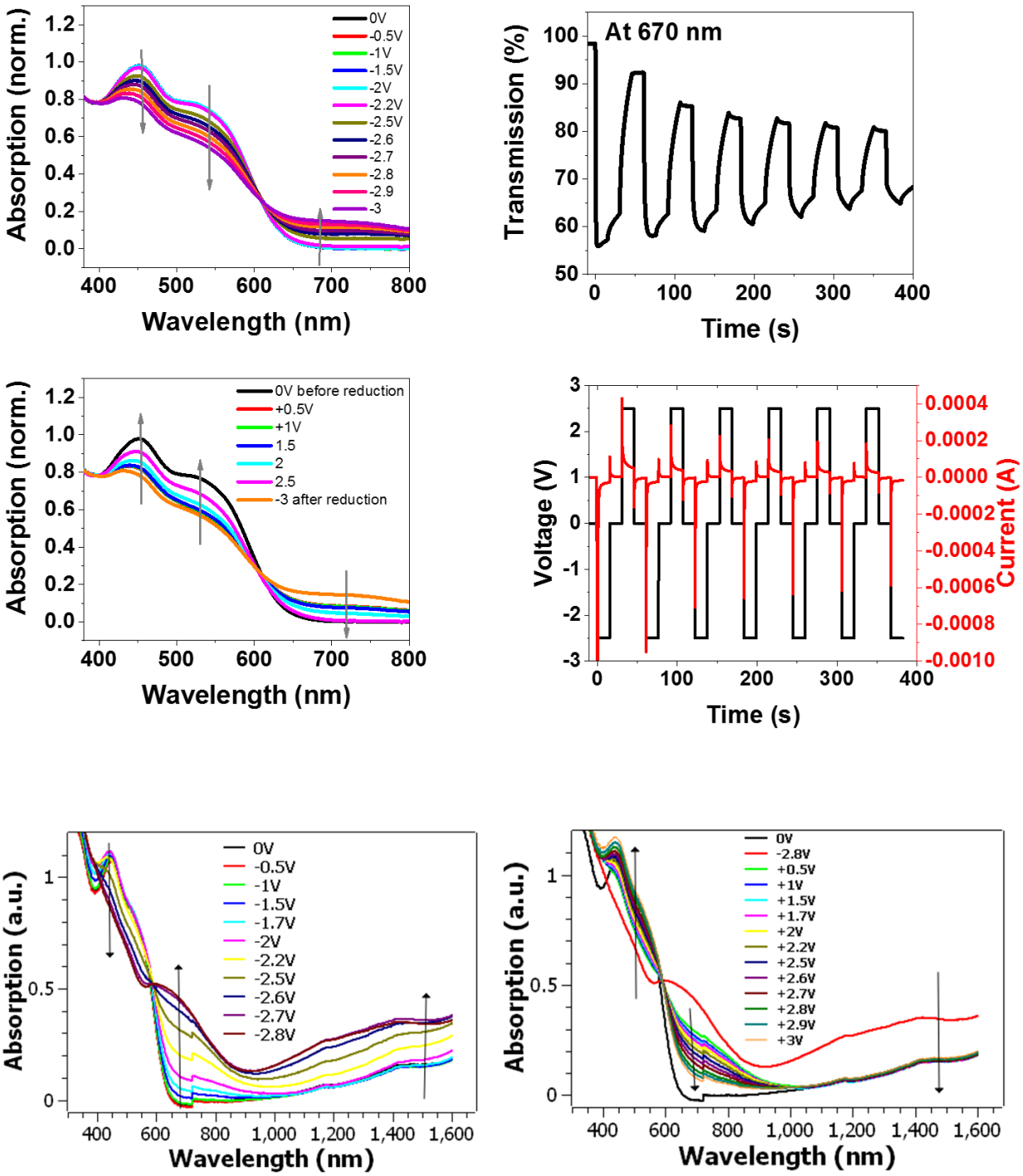

Figure 2-13. Electrochromic properties of PTQ-40: reduction, oxidation, cycling efficiency.

Figure 2-14 shows zoomed dependence of transmission and current versus time during the first reduction and oxidation. Drop in transmission clearly corresponds with large current, meaning that the polymer indeed undergoes reduction to quinoidal structure instead of changing in absorption due to swelling or solvation in electrolyte. Once voltage is set to 0, a small bump in current is observed which is likely faradeic in nature and corresponds to redistribution of electrolyte and associated marginal oxidation of associated polymer or dedoping. When voltage is set to +2.5V at 30s large oxidative current is observed which means influx of counterions back into polymer film. When bias is removed small current indicates redistribution of electrolyte. Smaller oxidative current compared to reductive current can be rationalized by ions movement. During reduction PF_6^- counterions move into solution and polymer film shrinks, making it harder for electrolyte counter-ions to penetrate the film during subsequent oxidation. To get further insight into these electrochemical processes we measured time it takes to switch transmission intensity from 90% to 10% of original absorption, ignoring 2 relaxation plateaus. For example, oxidation time of 12.3s in the table corresponds to part of plot from 30 to 42s. During cycling reduction takes longer to achieve in each cycle, while oxidation takes the same time, almost order of magnitude longer in the first cycle. When the film is reduces, electrolyte cannot penetrate back between polymer chains chains as quickly as it could move out. Longer and longer reduction times can be explained by changes in morphology of the film: after each reduction polymer chains that were strongly repelled from each other are in neutral form and can π-π stack with each other much stronger. Each cycle more efficient packing and interchain interactions are achieved making it harder for the film to undergo electrolyte efflux in the next cycle.

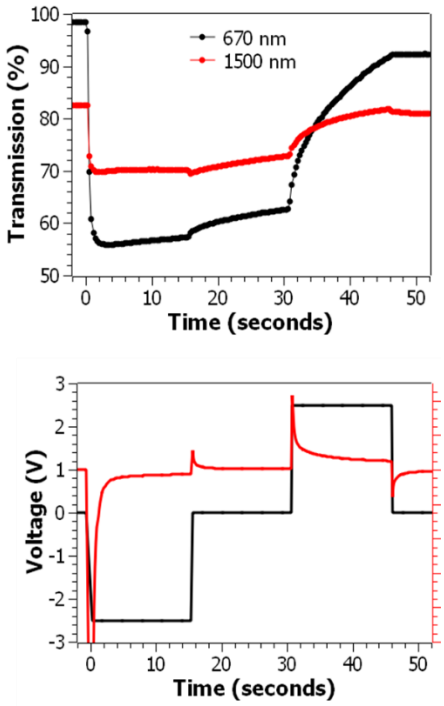

Switching #	Switching time (seconds)	
	Reduction	Oxidation
1	0.9	12.3
2	2.4	11.7
3	3.0	12.0
4	4.2	12.0
5	5.7	12.0
6	6.6	12.0

Figure 2-14. Zoomed in view on current vs time dependence during switching of polarity.

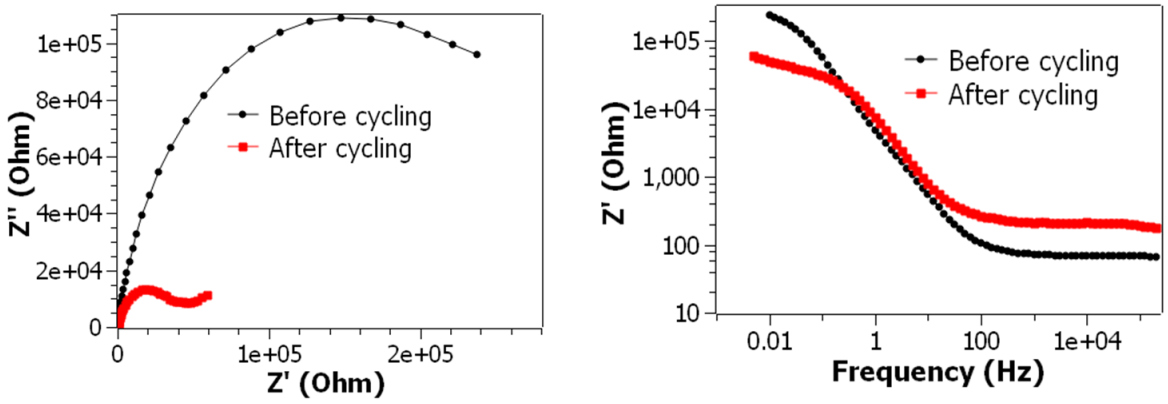

Figure 2-15. Impedance spectroscopy for PTQ-40 devices.

Switching potentially could be accompanied by material or electrolyte decomposition. To test whether this happens we performed impedance spectroscopy measurements. Fig. 2-15 shows Nyquist and Bode plots of imaginary part of impedance vs real and vs different frequency of 0.01V oscillating voltage, which are extracted from total impedance and phase difference. If electrolyte

decomposed then device would become more resistive. As our device operates in DC mode, we need to look at resistance intrapolation to 0 frequency: right plot at low frequency corresponds to DC current. As we can see, resistance R=Z' is lower after cycling which means device became more conductive so electrolyte didn't decompose, and increase in conductance must correspond to polymer counterions increasing concentration of electrolyte in solution, which would also confirm previous conclusion that part of polymer stays in the reduced state in the film permanently.

Next we investigated the effect of electrolyte counterionon device performance by doing the same measurements with PMMA/acetonitrile/propylene carbonate/LiTFSI electrolyte. TFSI counter-ion $(CF_3SO_2)_2N^-$ decreased all switching times significantly. This result is due to its weaker solvation and therefore smaller size of solvation sphere, which makes movement in and out of the film easier. This suggests that device performance can be improved by using smaller counter-ions.

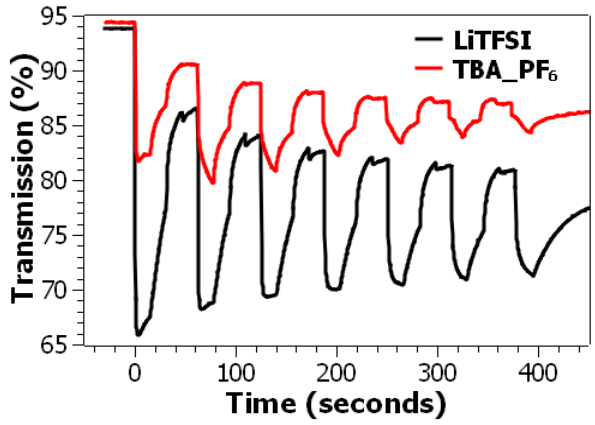

Switch #	Switching time (seconds)	
	Reduction	Oxidation
1	0.6	9.6
2	0.9	9.6
3	1.2	9.6
4	1.8	9.6
5	3.3	9.6
6	5.1	9.6

Figure 2-16. Switching efficiency of TBAPF6 and LiTFSI electrolytes. Switching times for LiTFSI

Figure 2-17 shows electrochromic performance of another polymer PTQ-16. We can see that spectral changes are almost exactly the same as with PTQ-40. During reduction peaks at 460 and 560nm decrease, while NIR band beginning at 650 nm gains in intensity. During oxidation opposite changes occur. Unlike PTQ-40 however, PTQ-16 does not have a well-defined isosbestic point where reduced and oxidized form would have the same extinction coefficient. We explain this by much stronger interchain interactions , which can be deduced from lower solubility of PTQ-16. As counterions leave the film it achieves more and more efficient packing and becomes impenetrable for electrolyte. Therefore unlike previously described polymer PTQ-16 does not return to the initial spectrum after oxidation as can be seen from the right plot curves in black and purple. After oxidation there is only a broad plateau from 425 to 530 nm instead of 2 clear peaks in the initial film.

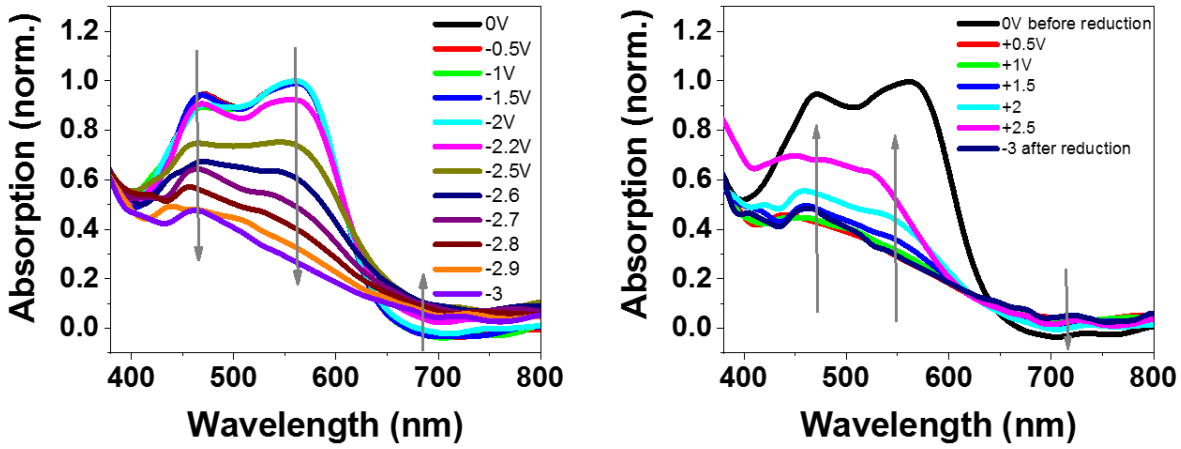

Figure 2-17. Electrochromic properties of PTQ-16: reduction, oxidation, cycling efficiency.

PTQ-A shows similar performance to that of PTQ-16 with peaks decreasing in the visible and increasing in NIR during reduction and opposite during oxidation. However this material has much lower stability during cycling which can be explained by material decomposition.

Specifically oxidation of benzodithiophene moiety into quinone units with elimination of alkyl chains.

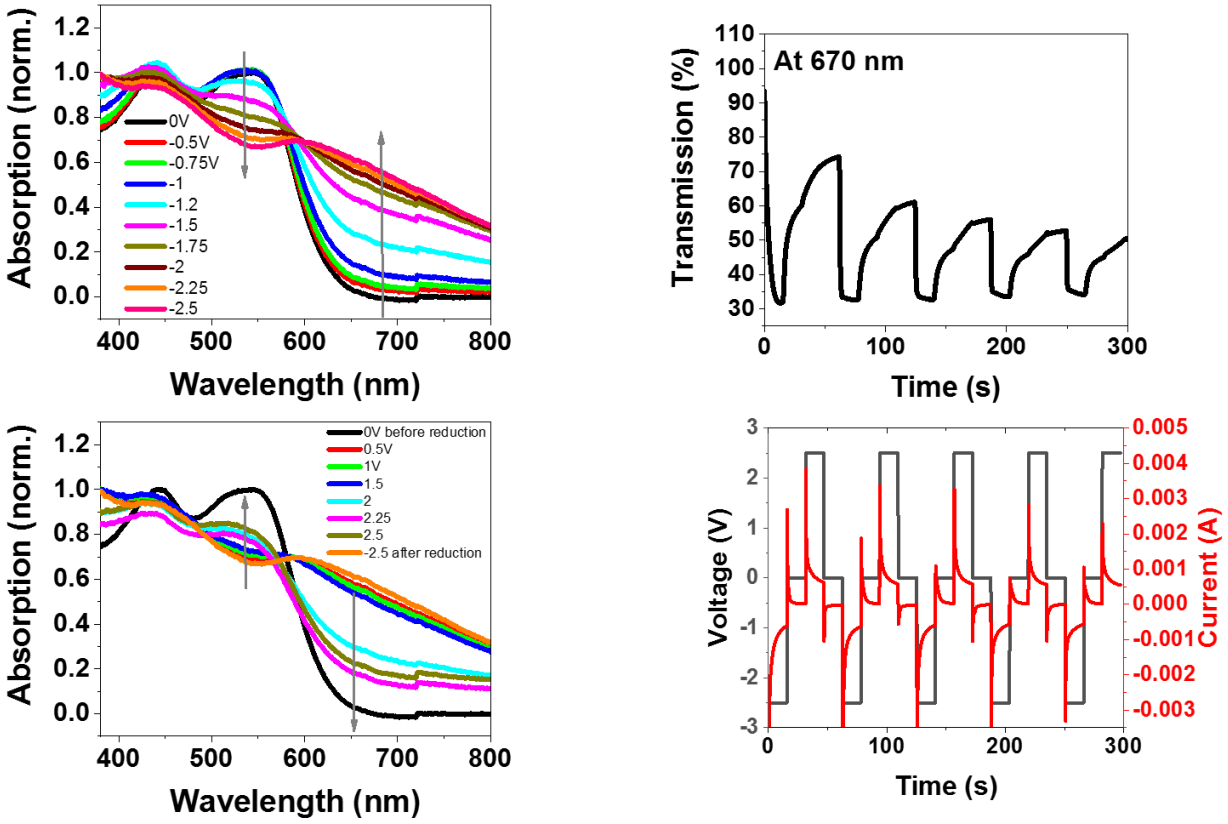

Figure 2-18. Electrochromic properties of PTQ-A: reduction, oxidation, cycling efficiency.

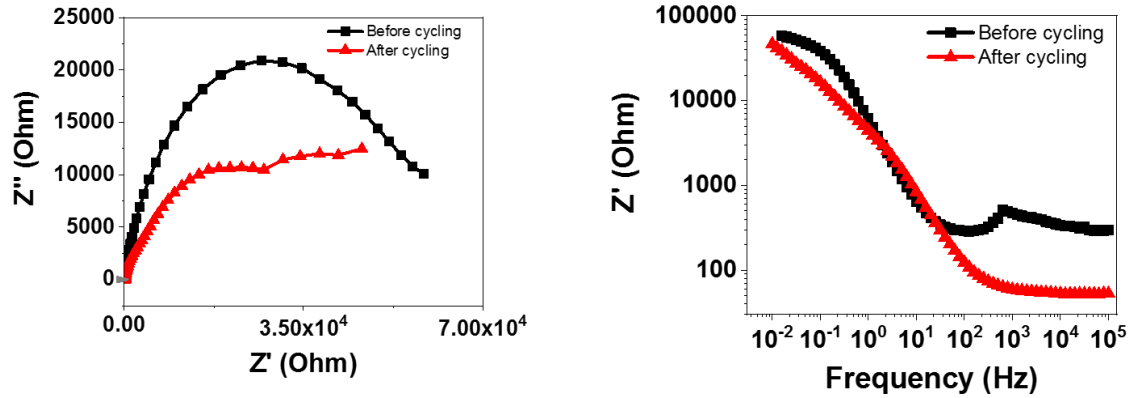

Figure 2-19. Impedance spectroscopy for PTQ-A devices.

Our negative control polymer PTQ-B does not exhibit the same electrochromic properties as other materials. Over time it undergoes steady decrease in absorption intensity. This material is partially soluble in electrolyte, while the other polymers were not. During device operation the solution becomes brown from initial yellow.

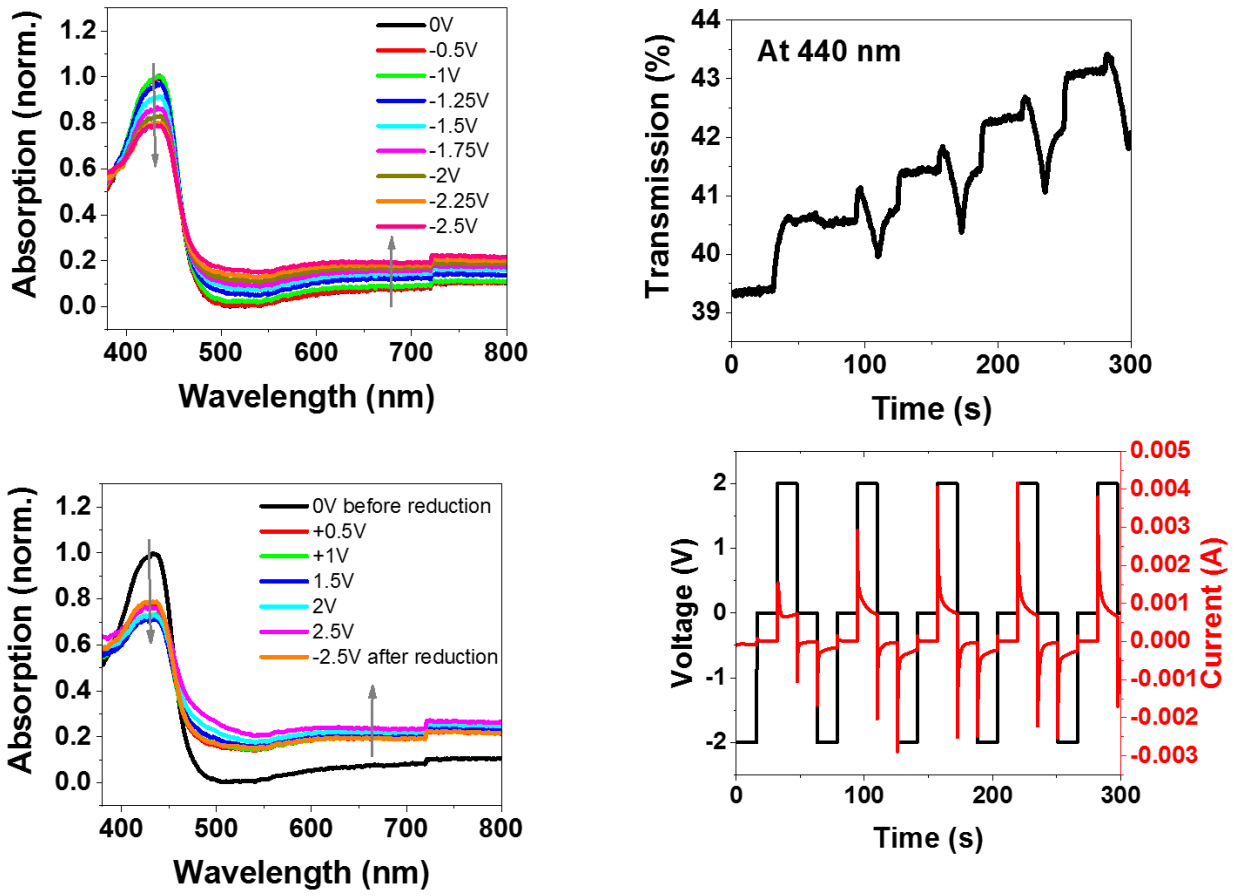

Figure 2-20. Electrochromic properties of PTQ-B: reduction, oxidation, cycling efficiency.

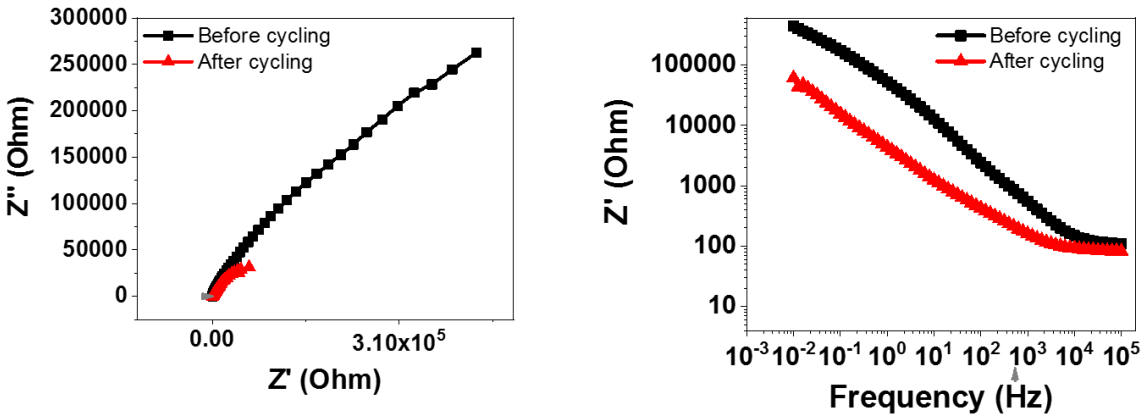

Figure 2-21. Impedance spectroscopy for PTQ-B devices.

2.3 Conclusions

We have synthesized a series of 4 conjugated polymers with cationic charge localized in the main chain. These materials represent a new class of conjugated cationic polymers, different from polymers with positive charges in side chains or alkylated polypyridines. We found that polymerization requires extended reaction times to achieve reasonable molecular weights of synthesized polymers. Unlike other synthetic approaches where positive charge is introduced into the structure as a last step, in our approach there is no uncertainty about the degree of functionalization or in other words proportion of repeating units with cationic centers vs neutral fragments. The electronic spectra revealed that alkyl chain substitution has weak effect on underlying HOMO and LUMO energy levels of synthesized materials. However, proper positioning of alkyl chains is necessary to afford solution-processable polymers without strong aggregation. Relatively rare red-green electrochromism was observed and it was found that PTQ-40 exhibits the most stable electrochromic effect out of the series. During redox cycles oxidation time doesn't vary from cycle to cycle, while reduction becomes slower due to the changes in film morphology and associated ion movement. Comparison of these properties with a control polymer

confirmed that observed effects are due to positive charge being delocalized along the conjugated polymer backbone as opposed to changes to individual repeating units.

2.4 Experimental section

Unless otherwise stated, all chemicals obtained from commercial suppliers were used without further purification. THF was distilled over sodium prior to use, toluene was passed through MBraun solvent purification system. Other solvents were purified by distillation prior to use. ^{1}H and ^{13}C NMR were recorded by using 400MHz Bruker DRX-400 or Bruker Avance II+ 500 MHz spectrometers. Mass spectra were obtained on Agilent 6224 Tof High Resolution Accurate Mass Spec (HRA-MS) system. Column chromatography was carried out on silica gel (silica 60M, 400-230 mesh). Optical properties were measured by using a Shimadzu UV-2401PC UV-Vis spectrophotometer. Molecular weights of polymers were determined by using GPC with a Waters Associates liquid chromatography equipped with a Waters 510 HPLC pump, a Waters 410 differential refractometer and a Waters 486 tunable UV-vis detector. Polystyrene standards were used for calibration and chloroform as eluent.

Compound 2[73]: 5-bromo-2-iodopyridine 1 (2.839 g, 10 mmol, 1eq), 2-(tributylstannyl)thiophene (3.732g, 10 mmol, 1 eq), $Pd(PPh_3)_4$ (577.8mg, 0.5 mmol, 5% eq) were combined in a dry round bottom flask. After 3 nitrogen-vacuum cycles, anhydrous toluene (120ml) was added and solution was purged with nitrogen for 30 min. Solution was stirred under reflux for 24h. Reaction mixture was cooled to rt and filtered through celite washing with DCM-hexanes 1:1. After concentration on rotary evaporator the residue was chromatographed with gradient hexanes – 30%DCM-hexanes to afford yellowish solid (1.36g, 57%). ^{1}H NMR ($CDCl_3$, ppm): δ 8.64 (d, J = 2.4 Hz, 1H), 7.84 (dd, J = 8.6, 2.6 Hz, 1H), 7.63 (dd, J = 3.7, 1.3 Hz, 1H), 7.58 (d, J = 8.3 Hz, 1H), 7.45 (d, J = 5.1 Hz, 1H), 7.14 (dd, J = 5.0, 3.7 Hz, 1H).

Compound 3[74]: Compound 2 (1.36 g, 5.7 mmol, 1eq) was dissolved in 60 ml of chloroform with 1 drop of glacial acetic acid. Solution was cooled to 0°C, and then N-bromosuccinimide (1.109g, 6.2 mmol, 1.1 eq) was added in small portions. The mixture was stirred overnight and then washed with 1M aqueous $Na_2S_2O_3$. Organic layer was washed 3 times with aqueous Na_2CO_3, dried and concentrated in vacuo affording 1.607g of product (88%). ^{1}H NMR (500 MHz, $CDCl_3$) δ 8.57 (dd, *J* = 2.4, 0.8 Hz, 1H), 7.79 (dd, *J* = 8.5, 2.3 Hz, 1H), 7.46 (dd, *J* = 8.5, 0.8 Hz, 1H), 7.29 (d, *J* = 3.9 Hz, 1H), 7.06 (d, *J* = 3.9 Hz, 1H).

Compound 5: Compound 3 (1.607 g, 5.0 mmol, 1eq), diphenylacetylene (1.069 g, 6 mmol, 1.2eq), $[RuCl_2(p\text{-cymene})]_2$ (61.2 mg, 0.1 mmol, 2% eq), $AgBF_4$ (97.4 mg, 0.5 mmol, 0.1eq), and $Cu(BF_4)_2x6H_2O$ (2.372 g, 10 mmol, 2eq) were combined in pressure flask, degassed 3 times with vacuum-nitrogen cycles. Nitrogen purged ethyl acetate (35ml) was added with a syringe. The flask was sealed and heated at 100°C for 19 hours. When the reaction was completed, the mixture was diluted with CH_2Cl_2 (100 mL) and filtered through celite and celite was washed several times with CH_2Cl_2 (100 mL). The combined filtrate was concentrated in vacuo and the residue was purified by column chromatography on a silica gel column using DCM/acetone (85:15) as eluent to afford the desired pure product 5 (2.11 g, 72%) after 3 recrystallizations from DCM-EtOAc. ^{1}H NMR (500 MHz, DMSO-d6) δ 8.95 (d, *J* = 9.2 Hz, 1H), 8.77 (dd, *J* = 9.2, 1.7 Hz, 1H), 8.52 (d, *J* = 1.7 Hz, 1H), 7.52 (dt, *J* = 6.0, 2.6 Hz, 3H), 7.48 (dd, *J* = 6.8, 3.0 Hz, 2H), 7.44 (d, *J* = 0.8 Hz, 1H), 7.36 (dt, *J* = 4.9, 2.6 Hz, 3H), 7.26 – 7.21 (m, 2H); ^{13}C NMR (101 MHz, DMSO) δ 143.48, 140.66, 139.97, 136.79, 134.55, 134.28, 133.87, 132.38, 130.98, 130.80, 129.77, 129.54, 129.34, 128.78, 128.54, 128.15, 127.23, 125.11, 117.79.

Compound 6[75]: ^{1}H NMR (500 MHz, $CDCl_3$) δ 7.68 (s, 2H), 7.31 (d, *J* = 3.4 Hz, 2H), 6.90 (dd, *J* = 3.5, 0.9 Hz, 2H), 2.93 – 2.81 (m, 4H), 1.69 (p, *J* = 6.3 Hz, 2H), 1.51 – 1.36 (m, 16H), 0.99 – 0.88 (m, 12H), 0.39 (s, 18H).

Typical polymerization, PTQ-16: compounds 5(210.9mg, 0.3617mmol, 1eq) and 6 (327.2 mg, 0.3617 mmol, 1 eq) and $Pd(PPh_3)_4$ (20.9 mg, 0.018 mmol, 5% eq) were combined in a dry round bottom flask. After 3 nitrogen-vacuum cycles, anhydrous toluene (8.5ml) and DMF (8.5ml) were added and solution was degassed by 3 freeze-pump-thaw cycles. Reaction flask was submerged into preheated to 115°C oil bath and stirred at this temperature for 2.5 days. Reaction mixture was cooled to room temperature and precipitated in diethyl ether. Polymer was redissolved in DMF and precipitated in diethyl ether. Polymer was redissolved in DMF, stirred with excess of $AgPF_6$ and precipitated in water giving 402 mg of PTQ-16 (99%). Solution was stirred under reflux for 24h. Reaction mixture was cooled to rt and filtered through celite washing with DCM-hexanes 1:1. After concentration on rotary evaporator the residue was chromatographed with gradient hexanes – 30% DCM-hexanes to afford yellowish solid (1.36g, 57%). ^{1}H NMR (500 MHz, DMSO 100°C) δ 8.88 (s, 1H), 8.68 (s, 1H), 8.09-7.02 (br. m, 18H), 2.91 (br, 4H), 1.95-1.20 (br, 18H), 1.20-0.80 (br, 12H).

Compound 7[76]: $BrC_{12}H_{24}OH$ (10.894 g, 41 mmol, 1 eq) and DIPEA (8.6 ml, 49.3 mmol, 1.2eq) were dissolved in anhydrous DCM (41 ml). Cooled down to 0°C MOMCl (3.75 ml, 49.3 mmol, 1.2eq) was added dropwise and the reaction mixture was allowed to stir overnight. Reaction mixture was concentrated and column chromatography with hexanes – 5% ethyl acetate-hexanes gradient yielded 11.944g of product (94%). ^{1}H NMR (500 MHz, $CDCl_3$) δ 4.62 (s, 2H), 3.51 (t, *J* = 6.7 Hz, 2H), 3.40 (t, 2H), 3.35 (s, 3H), 1.85 (dt, *J* = 14.5, 6.9 Hz, 2H), 1.58 (dt, *J* = 8.5, 6.4 Hz, 2H), 1.46 – 1.38 (m, 2H), 1.38 – 1.33 (m, 2H), 1.33 – 1.24 (m, 12H).

Compound 9[77]: 49%. 1H NMR (500 MHz, CDCl3) δ 7.49 (d, J = 8.3, 4H), 7.38 (d, J = 8.3, 4H).

Compound 10: 2.114 g of Magnesium were mixed with 10ml of THF and 0.1ml of 1M DIBAL-H was added under nitrogen. After 20 min. compound 7 (11.944g) in 10ml of THF was added dropwise and the mixture was brought to reflux. After 2h of reflux solution was cannulated into the mixture of compound 9 (2.93g, 8.7mmol, 1eq), Pd(dppf)Cl_2 (446 mg, 0.61 mmol, 7 mol %) and 50ml of THF. Reaction mixture was refluxed until completion by TLC, then quenched with methanol. Ethyl acetate-water extraction, drying and concentration of organic layer yielded crude oil, which was purified by column chromatography with hexanes-DCM gradient. Product was recrystallized from ethanol with addition of activated carbon, yielding white needles (4.068g, 6.49 mmol, 75%). ^{1}H NMR (500 MHz, $CDCl_3$) δ 7.43 (d, *J* = 8.1 Hz, 4H), 7.17 – 7.12 (m, 4H), 4.62 (s, 4H), 3.51 (t, *J* = 6.7 Hz, 4H), 3.36 (d, *J* = 0.5 Hz, 6H), 2.63 – 2.57 (m, 8H), 1.65 – 1.53 (m, 8H), 1.33 (m, 8H), 1.30 – 1.23 (m, 20H). HRAMS m/z: $C_{42}H_{66}O_4$, Calcd, 634.4961. Found, (M^+), 634.4937.

Compound 11: 93%. ^{1}H NMR (500 MHz, $CDCl_3$) δ 8.72 (d, *J* = 1.7 Hz, 1H), 8.45 (d, *J* = 9.2 Hz, 1H), 8.30 (dd, *J* = 9.2, 1.8 Hz, 1H), 7.33 (d, *J* = 7.9 Hz, 1H), 7.30 – 7.21 (m, 4H), 7.09 (q, *J* = 8.1 Hz, 4H), 4.05 (t, *J* = 6.8 Hz, 4H), 2.65 – 2.58 (m, 2H), 2.58 – 2.51 (m, 2H), 1.66 – 1.59 (m, 4H), 1.33 – 1.23 (m, 36H).

Compound 12: 87%. ^{1}H NMR (500 MHz, $CDCl_3$) δ 8.73 (d, *J* = 1.7 Hz, 1H), 8.35 (dd, *J* = 9.2, 0.7 Hz, 1H), 8.28 (dd, *J* = 9.2, 1.7 Hz, 1H), 7.29 (d, *J* = 8.1 Hz, 1H), 7.28-7.21 (m, 4H), 7.08 (br, 4H), 4.05 (td, *J* = 6.8, 0.7 Hz, 4H), 2.66 – 2.59 (m, 2H), 2.58 – 2.52 (m, 2H), 1.61 (q, *J* = 6.9 Hz, 4H), 1.32 (m, 4H), 1.27 (m, 36H); ^{13}C NMR (101 MHz, $CDCl_3$) δ 171.43, 146.13, 144.46, 143.87, 140.42, 140.30, 137.08, 135.52, 134.16, 131.22, 130.93, 129.98, 129.47, 128.74, 128.60, 127.24,

126.77, 124.97, 118.28, 64.78, 35.81, 35.71, 31.23, 31.01, 29.76, 29.72, 29.69, 29.64, 29.58, 29.56, 29.37, 29.32, 29.21, 28.70, 26.01, 21.12.

PTQ-A: Crude – quantitative, $CHCl_3$ fraction 38%. Could not be characterized by NMR due to solubility. GPC: Mw=75.9 kDa, PDI=1.99.

PTQ-40: 95%. ^{1}H NMR (500 MHz, $CDCl_3$) δ 8.78 (s, 1H), 8.58 (s, 1H), 8.09-7.02 (br. m, 16H), 4.05 (s, 4H), 2.90 (br, 4H), 2.60 (br, 4H), 1.95-1.20 (br, 38H), 1.20-0.80 (br, 12H). ^{1}H NMR (500 MHz, $CDCl_3$) δ 7.26 (s, 22H), 7.13 (s, 2H), 6.99 (s, 1H), 2.90 (s, 1H), 2.04 (s, 7H), 1.32 (s, 30H), 0.95 (s, 9H). GPC: Mw=18 kDa, PDI 1.25.

PTQ-B: Crude – quantitative, $CHCl_3$ fraction 33%. ^{1}H NMR (500 MHz, $CDCl_2CDCl_2$) δ 8.63 (br s, 1H), 8.54 (br s, 1H), 8.46 (br s, 1H), 7.56 (br s, 3H), 7.48 (br s, 2H), 7.40 (br s, 4H), 7.32 (br s, 2H), 7.17 (br s, 2H), 6.87 (br s, 2H), 2.15 (s, 2H), 1.55 (s, 2H), 1.38 (s, 2H). GPC: Mw=72.1 kDa, PDI=2.29.

Compound 15[36]: 66%. ^{1}H NMR (500 MHz, $CDCl_3$) δ 7.51 (s, 2H), 4.18 (d, J = 5.4 Hz, 4H), 1.80 (m, J = 6.0 Hz, 2H), 1.76 – 1.34 (m, 16H), 1.02 (t, J = 7.4 Hz, 6H), 0.94 (t, J = 7.4 Hz, 6H), 0.44 (s, 18H).

Compound 16[78]: 20%. ^{1}H NMR (400 MHz, $CDCl_3$) δ 7.13 (dd, J = 5.1, 1.2 Hz, 2H), 6.93 (dd, J = 5.2, 3.4 Hz, 2H), 6.81 (dq, J = 3.3, 1.0 Hz, 2H), 2.90 (td, J = 7.6, 0.9 Hz, 4H), 2.07 (tt, J = 8.0, 7.1 Hz, 2H). HRAMS m/z: $C_{11}H_{12}S_2$, Calcd, 208.038. Found, (M^+), 208.0423.

Compound 17[78]: 51%. ^{1}H NMR (500 MHz, $CDCl_3$) δ 7.03 (d, J = 3.1 Hz, 2H), 6.93 (d, J = 3.1 Hz, 1H), 2.94 (t, 4H), 2.09 (t, 2H), 0.36 (m, 18H).

2.5 References

(61) Thomas, S. W.; Joly, G. D.; Swager, T. M. *Chem. Rev.* **2007**, *107* (4), 1339–1386.

(62) Zhu, C.; Liu, L.; Yang, Q.; Lv, F.; Wang, S. *Chem. Rev.* **2012**, *112* (8), 4687–4735.

(63) Yang, R.; Wu, H.; Cao, Y.; Bazan, G. C. *J. Am. Chem. Soc.* **2006**, *128* (45), 14422–14423.

(64) Yang, P. J.; Chu, H. C.; Lee, Y. H.; Kobayashi, T.; Chen, T. C.; Lin, H. C. *Polymer (Guildf).* **2012**, *53* (4), 939–946.

(65) Zhai, L.; Zhang, Z.; Zhao, Y.; Tang, Y. *Macromolecules* **2018**, *51* (18), 7239–7247.

(66) Marsella, M. J.; Fu, D.; Swager, T. M. *Adv. Mater.* **1995**, *7* (2), 145–147.

(67) Fu, D.; Xu, B.; Swager, T. M. *Tetrahedron* **1997**, *53* (45), 15487–15494.

(68) Rochat, S.; Swager, T. M. *J. Am. Chem. Soc.* **2013**, *135* (47), 17703–17706.

(69) Rochat, S.; Swager, T. M. *Angew. Chemie - Int. Ed.* **2014**, *53* (37), 9792–9796.

(70) Voortman, T. P.; de Gier, H. D.; Havenith, R. W. A.; Chiechi, R. C. *J. Mater. Chem. C* **2014**, *2* (17), 3407–3415.

(71) Luo, C.-Z.; Gandeepan, P.; Cheng, C.-H. *Chem. Commun.* **2013**, *49* (76), 8528.

(72) Compton, R. G.; Banks, C. E. *Understanding Voltammetry*; IMPERIAL COLLEGE PRESS, 2010.

(73) Venkatesan, K.; Kouwer, P. H. J.; Yagi, S.; Müller, P.; Swager, T. M. *J. Mater. Chem.* **2008**, *18* (4), 400–407.

(74) Yamamoto, T.; Zhou, Z.; Kanbara, T.; Shimura, M.; Kizu, K.; Maruyama, T.; Nakamura,

Y.; Fukuda, T.; Lee, B.-L.; Ooba, N.; Tomaru, S.; Kurihara, T.; Kaino, T.; Kubota, K.; Sasaki, S. *J. Am. Chem. Soc.* **1996**, *118* (43), 10389–10399.

(75) Busireddy, M. R.; Mantena, V. N. R.; Chereddy, N. R.; Shanigaram, B.; Kotamarthi, B.; Biswas, S.; Sharma, G. D.; Vaidya, J. R. *Org. Electron.* **2016**, *37*, 312–325.

(76) Villorbina, G.; Roura, L.; Camps, F.; Joglar, J.; Fabriàs, G. *J. Org. Chem.* **2003**, *68* (7), 2820–2829.

(77) Mio, M. J.; Kopel, L. C.; Braun, J. B.; Gadzikwa, T. L.; Hull, K. L.; Brisbois, R. G.; Markworth, C. J.; Grieco, P. A. *Org. Lett.* **2002**, *4* (19), 3199–3202.

(78) Zhao, Y.; Zhao, X.; Zang, Y.; Di, C.; Diao, Y.; Mei, J. *Macromolecules* **2015**, *48* (7), 2048–2053.

CHAPTER 3

MODEL LADDER COMPOUNDS AND THEIR OPTOELECTRONIC PROPERTIES

3.1 Introduction

Our long-lasting interest in ladder type molecules is due to their unique properties of extended conjugation that can be utilized in a number of applications, including luminescent materials, materials for field-effect transistors and organic solar cells, non-linear optics materials and singlet fission.[79–84]

There is a number of synthetic approaches to combine efficient synthesis and molecular design of ladder structures in small molecules.[2,85–87] Broadly, they can be divided into oxidation and cross-coupling categories. First features favorably positioned relatively electron rich C-H bonds while second relies on C-H and C-Hal moieties to undergo usually transition metal catalyzed reactions. Another established approach - APEX, annulative π-extension, relies on cross-coupling and subsequent thermal cyclodehydrogenation.[88]

One of the recent developments in this field by Dong group utilizes this type of substrate but instead of transition metal, photochemical cyclization takes place creating fused ring ladder polymer.[89–91]

In broader context these transformations often go hand in hand with C-H activation methodologies. A number of new techniques have been discovered in this direction. Usually they rely either on sterically proximate groups to create 5- and 6-membered rings or on large excess, up to being used as a solvent, of second coupling partner.

Molecular wires are a class of conjugated organic molecules with 2 anchoring groups (i.e. thiol) at each end. This motif allows one of them to bind to the golden STM tip, while the other is

connected to the gold surface under bias. This setup allows to measure current flowing through the organic molecules and therefore measure its conductance and other properties. Our group has prolifically explored this area and introduced more complicated structures, including molecular diodes, transistors and logic gates.[4,92–95] Studying donor-acceptor molecular wires we have found that their conductance quickly decreases with length of π-system.[4] For most applications of conjugated organic materials highly conductive small molecules and polymers are desired. We hypothesize that "widening" the π-system could be a reliable design to achieve these properties. Larger π-system could facilitate both tunneling and charge hopping through the molecular wire due to flat structure and greater conjugation.

3.2 Results and discussion

We studied 2 general approaches to ladder structures. First one is based on fusing conventional conjugated molecules by oxidation. This approach relies on simpler starting materials that don't need to have any reactive group, however the chemistry presents challenges in selectivity of oxidation. Second approach is to have pre-positioned halogen atoms that can undergo intramolecular Heck arylation.

3.2.1 Synthesis

For oxidation route to ladder structures we designed a model compound 5. It has central benzene ring connected on each side with electron-rich alkylthiophene and adjacent to it even more electron-rich BDT. 6 Ethyl-hexyl chains provide good solubility in organic solvents, TIPS groups protect sensitive 2-positions of BDT. Synthesis begins with Stille coupling of dibromodiiodobenzene with ethylhexyl-thiophene-trimethyltin. Next Stille coupling puts BDT-

units in place. It was noted that the reaction requires 3 days at 130°C to proceed quantitatively. Reaction rate is slow because of steric hindrance of *ortho*-thiophene in compound 3.

Scheme 3-1. Synthesis of model compound 5 for methodology exploration.

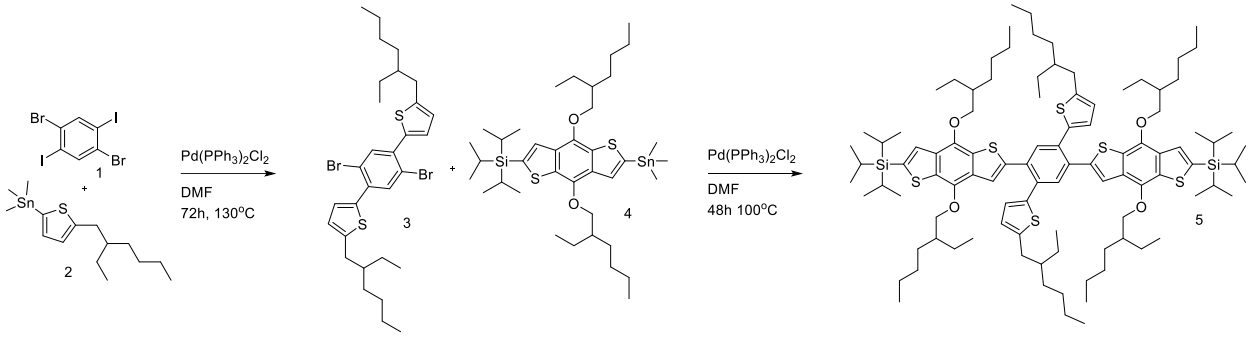

We studied different oxidation conditions that could yield cyclized structure. In literature a lot of Rh-catalyzed reactions become a new alternative to Pd-catalyzed ones.[96–98] However in our model molecule C-H bonds are not activated by any electron-withdrawing groups, making C-H activation more challenging. Wilkinson catalyst requires a directing group, usually amino, amide or carbonyl, which is absent in our case.

Cyclooxidation can be done catalytically with Pd catalyst and sacrificial oxidant or by using high oxidation state metal salt. In this regard it is essential to find a perfect ligand among different phosphines, N-heterocyclic carbenes or even thioethers.[99,100] We also tried conditions for oxidative dimerization that Sanford group has developed for pyridine directing group.[101] Another approach utilizes silver salts together with Pd catalyst.[102] Oxidation with $FeCl_3$ was found to be the most reliable and high-yielding method to access this molecule, it was done 3 times for other synthetic needs giving identical 25% yields. Pd-catalyzed oxidation shows promise, but suffers from low yields and unidentifiable oxidation by-products.

Scheme 3-2. Cyclization of the model compound.

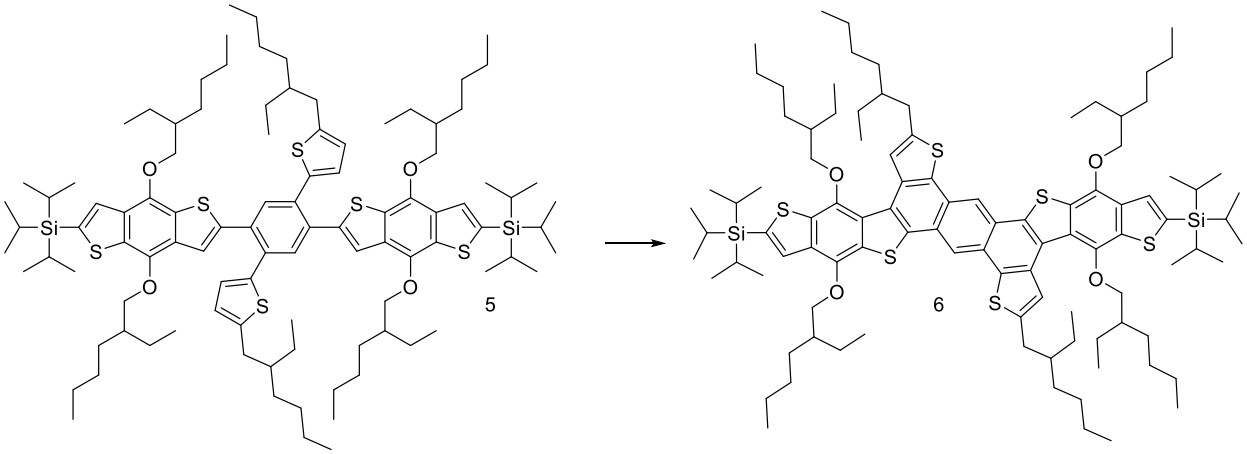

Table 3-1. Oxidative cyclization of model small molecule 5

Oxidant	Conditions	Yield
$Rh(PPh_3)_3Cl$, $Cu(OAc)_2$	CF_3COOH, mesitylene, 24h,160°C	NR [b]
I_2, hv	Benzene, O_2, 8h	20%[a,c]
$Pd(OAc)_2$, $K_2S_2O_8$	i-PrOH, DCM, o.n., rt	NR [b]
$Pd(OAc)_2$, $Cu(OAc)_2$	CsOPiv, pivalic acid, 72h, 150°C	10%[a,b,c]
$Pd(OAc)_2$, $Cu(OAc)_2$	CsOPiv, pivalic acid, 24h, 150°C	17%[a,b,c]
$Pd(OAc)_2$, $Cu(OAc)_2$	CsOPiv, pivalic acid, $CHCl_3$, 24h, 150-200°C	NR [a]
$Pd(OAc)_2$, $K_2S_2O_8$	CsOPiv, pivalic acid, 48h, 150°C	Trace[a,b,c]
$Pd(OAc)_2$, $AgNO_3$	AcOH, DMSO, 24h, 100°C	Trace[a,b]
$Pd(OAc)_2$, Ag_2CO_3	pivalic acid, 24h, 150°C	Trace [a]
$Pd(OAc)_2$, K_2CO_3	pivalic acid, open air, 24h, 110-200°C	Trace[a,b,c]
$MoCl_5$ (4.2eq)	DCM, 24h, rt	Inseparable[a,b,c,d]
$MoCl_5$ (4.2eq)	$TiCl_4$ (4.2eq), DCM, 24h,rt	Trace
$MoCl_5$ (4eq)	$TiCl_4$ (4eq), DCM, 3h,rt, portionwise addition	NR[a,b,c]
$MoCl_5$ (4eq)	Pyridine, DCM, rt	NR[b]
$MoCl_5$ (36eq)	DCM, 1h, rt	NR[a]
$MoCl_5$ (4eq)	DCM, 45min, rt	19%
$MoCl_5$ (6eq)	$TiCl_4$ (6eq), 3h	Trace[a]
$TiCl_4$	DCM, 3h	NR[a,b,c]
$FeCl_3$	CH_3NO_2, DCM, 45min, rt	25%

[a] TLC indicated decomposition products that could not be identified.

[b] Incomplete conversion, starting material present.

[c] Monocyclized present

[d] Inseparable mixture, 60% by weight, product is largest spot on TLC.

Scheme 3-3. Synthesis of model compound 11.

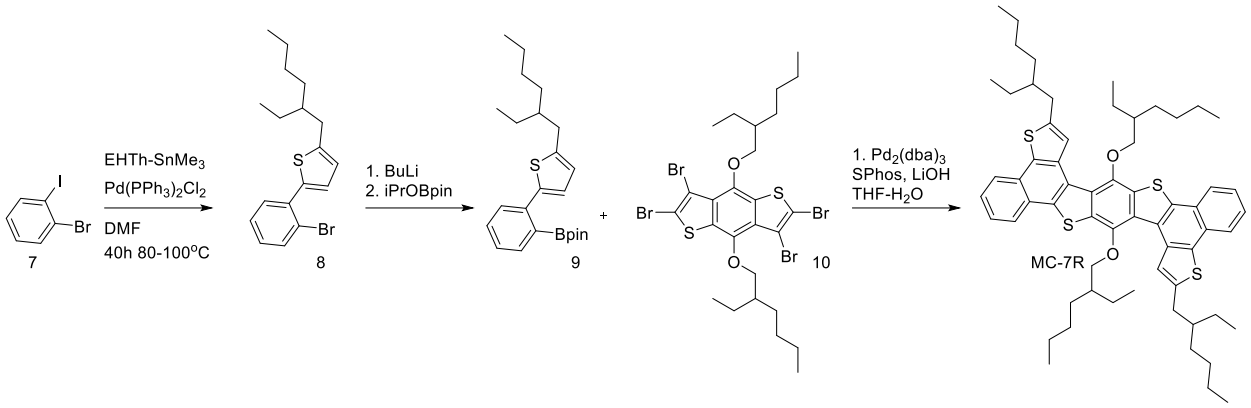

To study second approach to ring fusion we synthesized another molecule – MC-7R – that has structure "inverted" to that of compound 6: BDT unit on the inside and benzenes with ortho-thiophenes on the outside. The benzene rings must provide greater stability in electronic applications since there is no electron-rich 2-position of thiophene in the molecule anymore. Synthesis involves coupling of 2-iodobromobenzene with EH-Th-SnMe3 and exchange of bromine for Bpin group through lithiation with BuLi. Next Suzuki reaction with tetrabromobenzodithiophene allows to obtain compound X. Worth noting that during this reaction, cyclization into ladder structures already partially occurs. That's why crude compound X was subjected to harsher Heck-reaction conditions without purification yielding 11 in 75% yield after 36h. It is essential to use Pd^0 catalyst for this step. When $Pd(OAc)_2$ and $P(o\text{-}Tol)_3$ were used instead the reaction mixture contained mostly starting material after 36h.

Scheme 3-4. Synthetic approach to pyrazine-containing ladder molecule

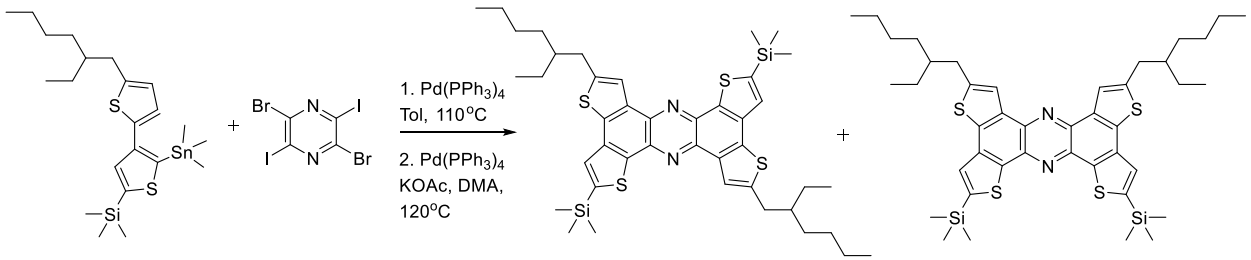

Using iodo-bromo compounds for synthesis of ladder molecules has its nuances. When we tried to make a pyrazine version following similar route as to the 7-ring compound above we discovered that final product has extra aromatic signals in NMR spectrum (tentative assignment), which is likely because of iodine vs bromine selectivity in the first cross-coupling step. The close NMR signals observed can be explained if side product comes from reaction of 1 iodine and 1 bromine instead of 2 iodines in dibromodiiodopyrazine. Electron-withdrawing nature of pyrazine nitrogens activates both I and Br, justifying observed lack of selectivity.

One of our research interests is synthesis and design of luminescent materials for applications in organic light emitting transistors. Therefore we explored how the structures of our model compounds can be modified to make them more luminescent. Low quantum yields of small ladder molecules might be caused by quenching and thermal relaxation of excited states. In order to disrupt possible quenching we have synthesized a ladder molecule with phenyl substituted benzodithiophene, since steric interactions should keep phenyl rings out of BDT-plane (more information in section 3.2.3). Lithium-bromine exchange in compound 11, followed by nucleophilic addition to BDT carbonyl groups, after next reduction and stannylation afforded compound 12. This molecule was cross-coupled with compound 8 and after oxidation yielded compound MC-7P.

Our next step in this project was to study single-molecule conductance of ladder structures. To this end we synthesized 3 molecular wires that have 3, 5 and 9 fused rings capped with protected thiol groups at the ends. Compound 3 is known benzodithiophene molecular wire that serves as a reference.

Scheme 3-5. Synthesis of MC-7P

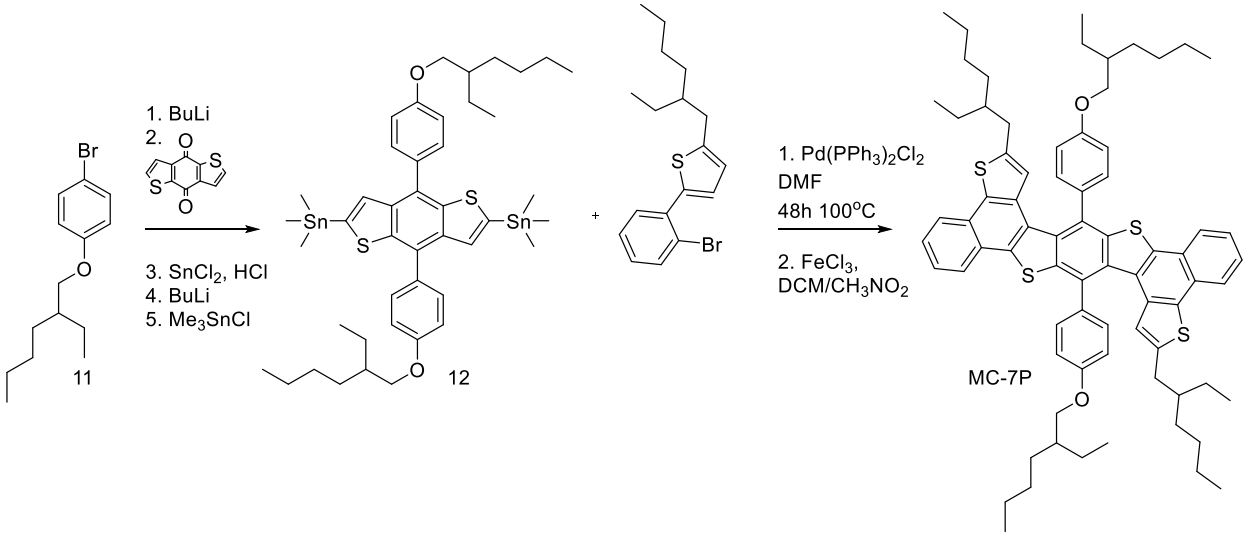

Scheme 3-6. Synthesis of MW-3r

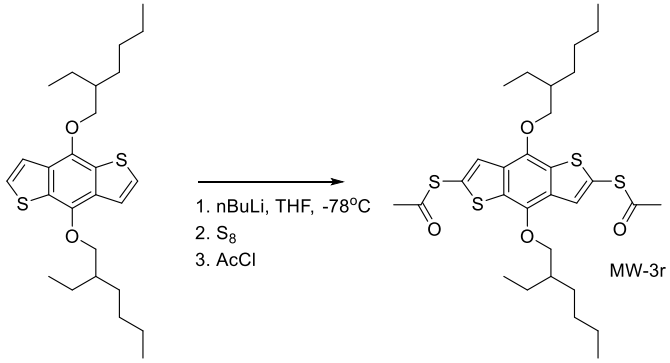

5-ring compound utilizes known aromatic core made by Feng He. Synthesis of the MW-5r involves oxidative cyclization with $FeCl_3$ and Pd-catalyzed thiolation.

Scheme 3-7. Synthesis of MW-5r

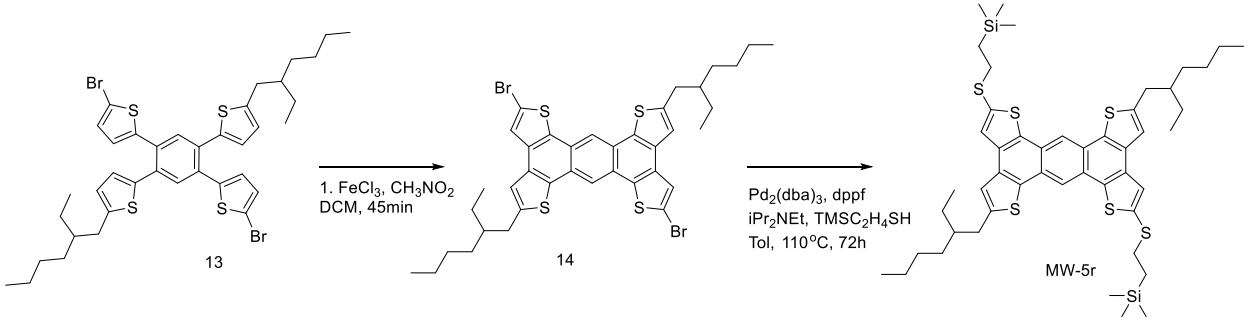

For the synthesis of 9-ring compound we brominated 2-positions of thiophenes of MC-9R by lithiation with BuLi and treatment with CBr_4. Next we reacted obtained dibromide with 2-(trimethylsilyl)ethanethiol under palladium catalysis to yield final MW-9r.

Scheme 3-8. Synthesis of MW-9r

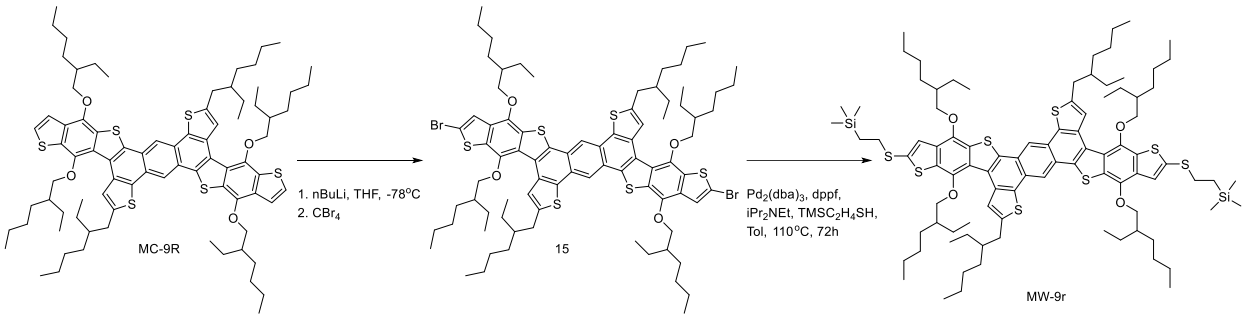

MW-7r was synthesized analogously to MC-7R with TMS-thiophene instead of phenyl. Lithiation, bromination and Pd-catalyzed coupling with thiol yield the final product. However, this molecule is very electron-rich and readily oxidizes in air, making its purification very difficult, thus is not investigated further.

Scheme 3-9. Synthesis of MW-7r

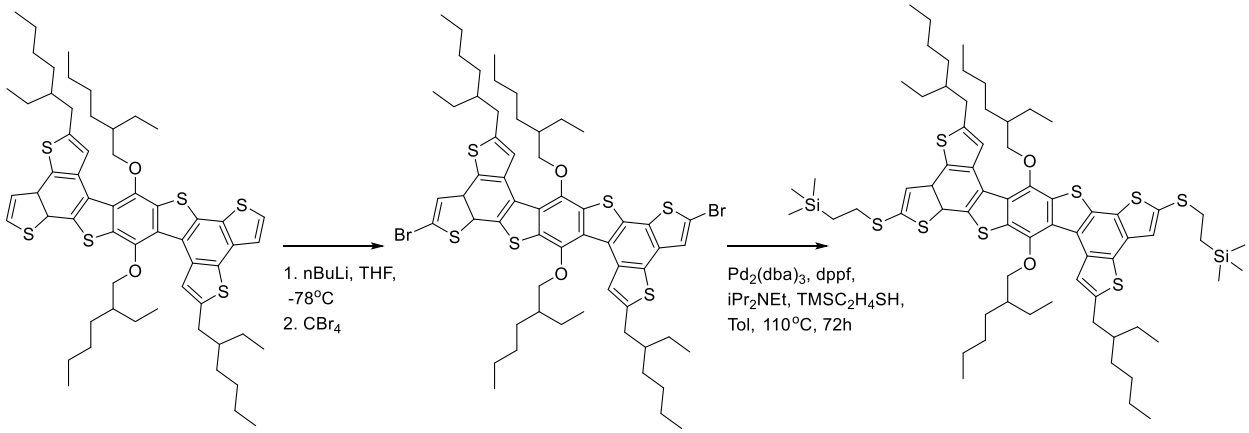

Table 3-2. Summary of optoelectronic properties of synthesized materials

Compound	HOMO	LUMO	Eg,opt	Eg, el	QY
MC-9R	-5.43eV	-3.50eV	2.57eV	1.93eV	5.2%
MC-7R	-5.62eV	-3.51eV	2.92eV	2.11eV	3.5%
MC-7P	-5.6eV	-3.3eV	2.86eV	2.3eV	2.5%

3.2.2 DFT results for ladder polymers

DFT calculations at B3LYP level of theory using 6-31G** basis set for MC-9R estimate energy levels at -4.95eV for HOMO and -1.94eV for LUMO. DFT calculations predict a slightly twisted geometry with 21.8^0 dihedral angle OCCC and ether linkages perpendicular to the main core. Interestingly there is no contribution to HOMO or LUMO from oxygen atoms. Steric hindrance prevents overlap between oxygen lone pairs and conjugated system.

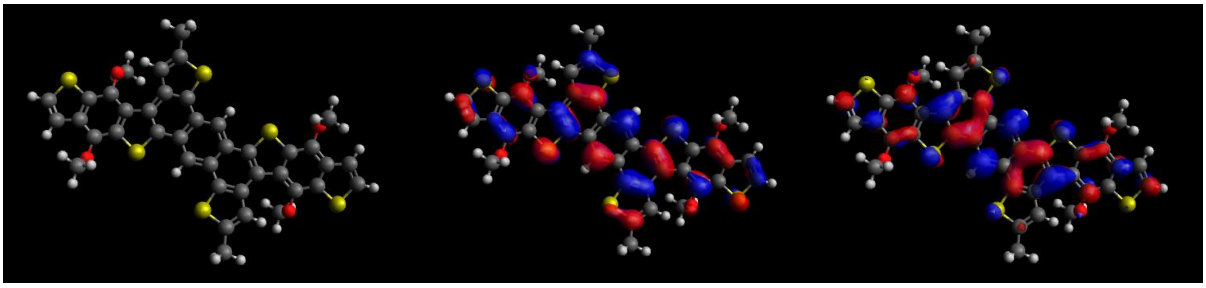

Figure 3-1. DFT results on conformation of trimer of MC-9R and HOMO/LUMO

Similarly, for MC-7R calculations predict HOMO energy level at -5.15eV and LUMO energy at -1.62eV. Geometry optimization predicts a slightly twisted structure with 17^0 dihedral angle OCCC and ether groups being perpendicular to the main π-system, like for MC-9R.

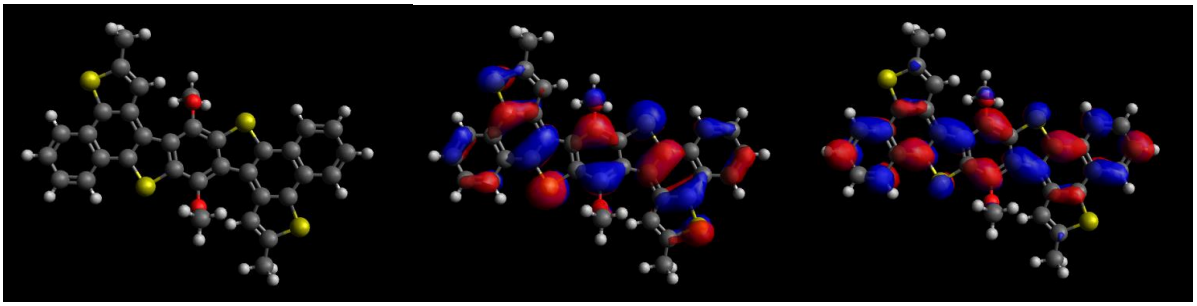

Figure 3-2. DFT results on conformation of trimer of MC-7R and HOMO/LUMO

MW-3r S-S distance according to calculations is predicted to be 1.0555nm, which agrees perfectly with previous calculations.[4] HOMO at -5.515 eV, LUMO -1.520eV.

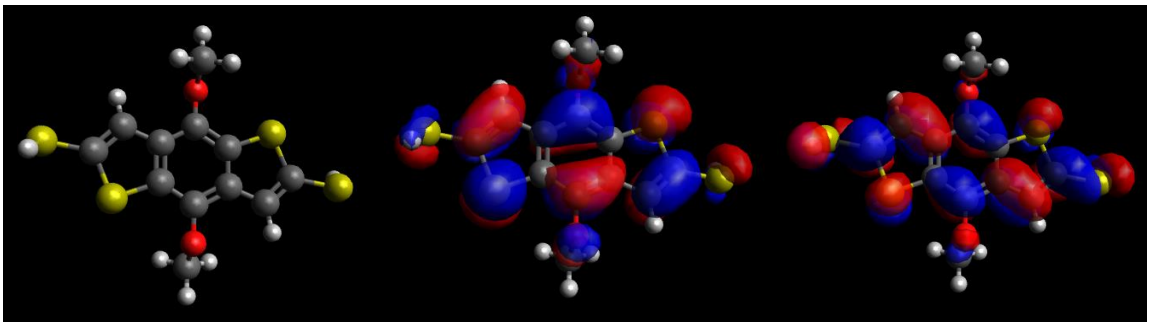

Figure 3-3. DFT results on conformation of trimer of MW-3r and HOMO/LUMO

MW-5r is predicted to have S-S distance 1.4107nm, HOMO energy level at -5.281eV, and LUMO at -1.932eV. Compared with 3-ring compound HOMO energy level becomes higher, while LUMO energy level decreases. This calculation agrees well with expectations of extended conjugation decreasing bandgap.

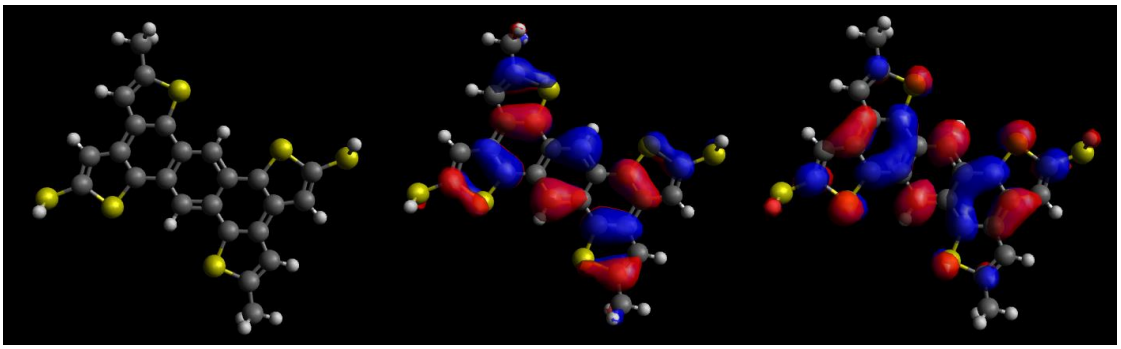

Figure 3-4. DFT results on conformation of trimer of MW-5r and HOMO/LUMO

MW-9r is predicted to have S-S distance of 2.3305nm, HOMO energy level at -5.045eV, and LUMO at -2.058eV. DFT calculated geometries provide a strong argument for planarity of studied systems and eliminate possibility of different conformations of the main backbone. Additionally energy levels progression confirms the notion of conjugation extending through the whole molecule, also supported by HOMO and LUMO being delocalized from end to end of the molecule.

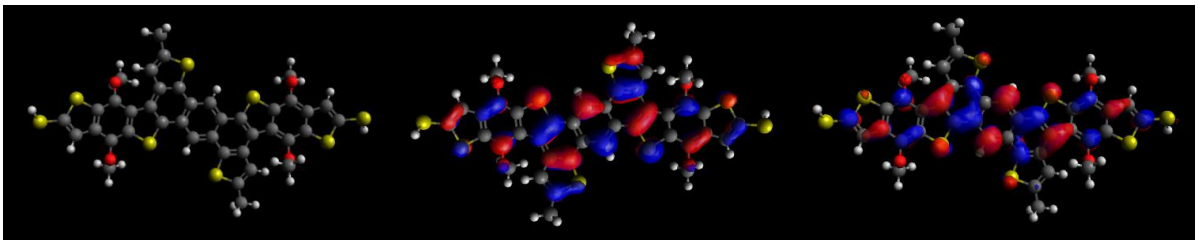

Figure 3-5. DFT results on conformation of trimer of MW-9r and HOMO/LUMO

Delocalization of π-electrons makes polyacene structure a perfect example of applied particle in the box model. It was observed previously, that bandgaps of polyacenes linearly correlate with 1/n, where n is the number of rings.[79] For studied molecular wires this relationship holds as well, as can be seen from Fig. 3-6. Energy bandgaps of ladder molecules are inversely proportional to their conjugation length.

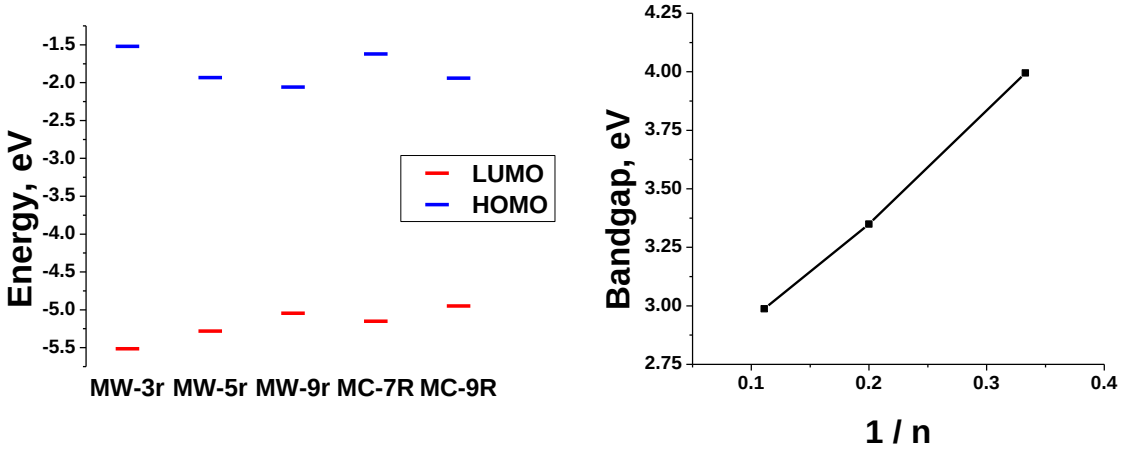

Figure 3-6. Energy levels and inverse correlation of bandgap of molecular wires with length

3.2.3 Optoelectronic properties

We then studied the properties of deprotected ladder molecule MC-9R. Its UV-visible spectrum doesn't depend on concentration meaning there is no strong aggregation or π-π stacking that can quench fluorescence. Fluorescence spectrum displays 2 peaks at 478 and 512 nm. Excitation spectrum matches closely with absorption spectrum meaning that small peaks in UV-vis are vibronic progression of energy levels. Large Stokes shift between maximum of fluorescence and maximum of absorption means that excited state undergoes significant geometry reorganization before emission. We measured quantum yield of fluorescence to be QY=5.2% with 9,10-diphenylanthracene serving as a standard.

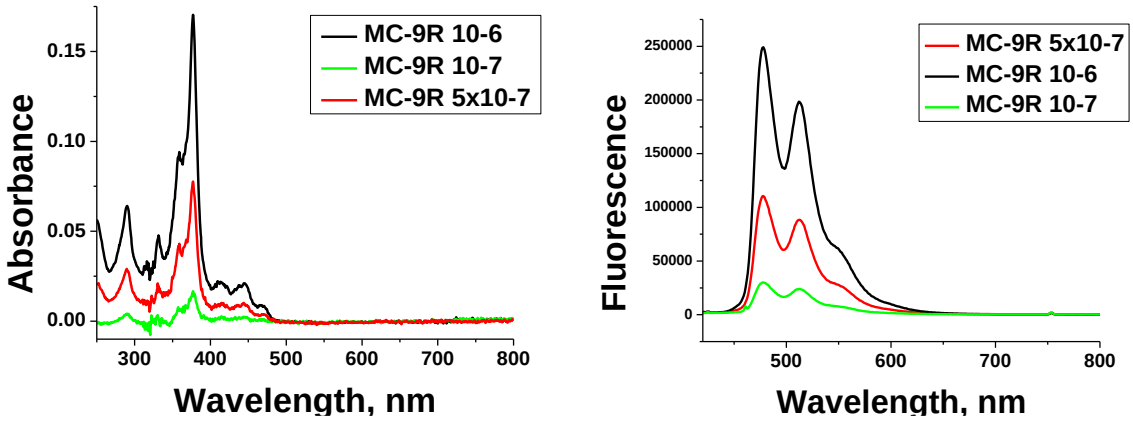

Figure 3-7. UV-vis and fluorescence spectra of MC-9R.

Time-dependent DFT calculations predict UV-visible spectrum to have 4 main transitions. The most intense of them promotes electron between HOMO-LUMO+1 and HOMO-2-LUMO. DFT predicted HOMO-LUMO gap 468nm matches very well to observed onset at 482nm.

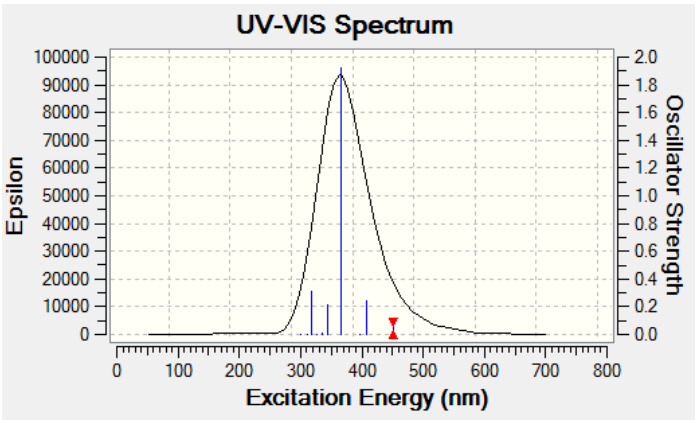

Figure 3-8. TDDFT predicted UV-vis spectrum of MC-9R

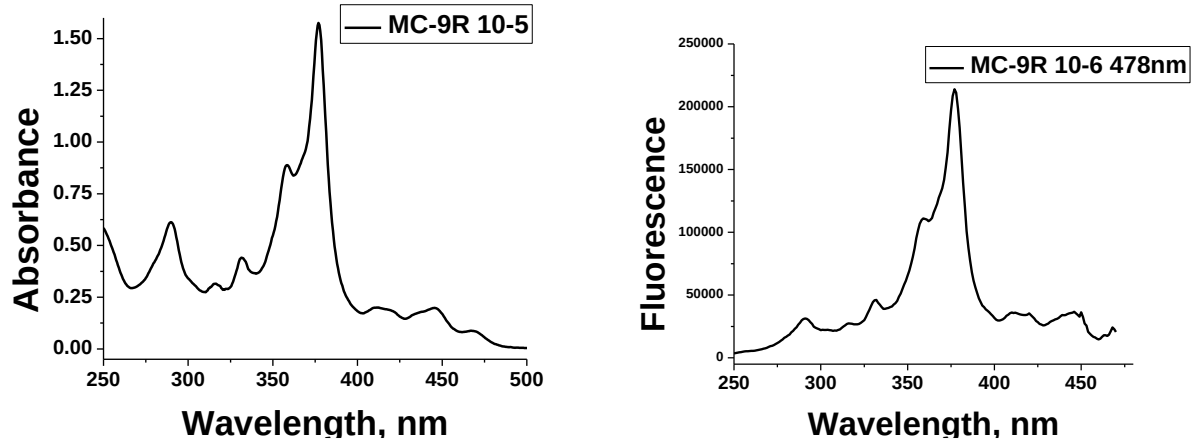

Figure 3-9. UV-vis absorption and excitation spectra of MC-9R.

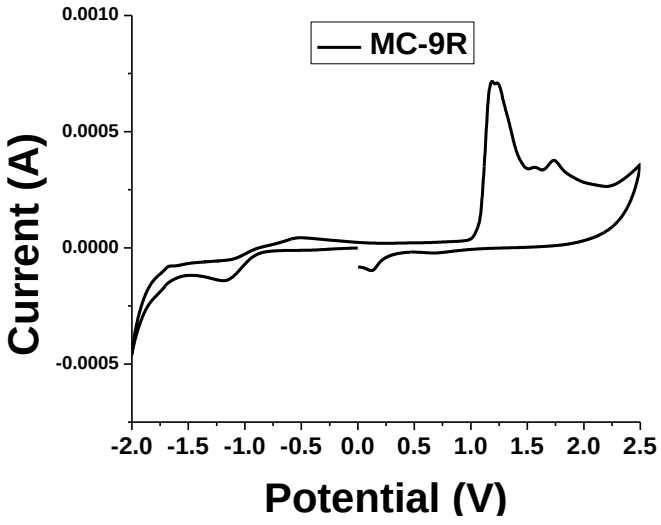

Figure 3-10. CV of MC-9R.

From CV HOMO energy is -5.43eV, and LUMO energy is -3.50eV. Cyclic voltammetry shows irreversible oxidation. CV was performed in films on the Pt electrode, and we observed degradation of the film. This could be expected from free 2-positions of thiophenes in compounds structure, which might allow reactivity with solvent or electropolymerization during the experiment. Since this issue might obscure properties of the π-system itself we decided to study electrochemistry of the parent TIPS-protected compound 6. This is valid because UV-vis and fluorescence spectra of TIPS protected and deprotected molecules match perfectly. For TIPS compound QY is 5.3% which again shows that TIPS group does not perturb the π-system.

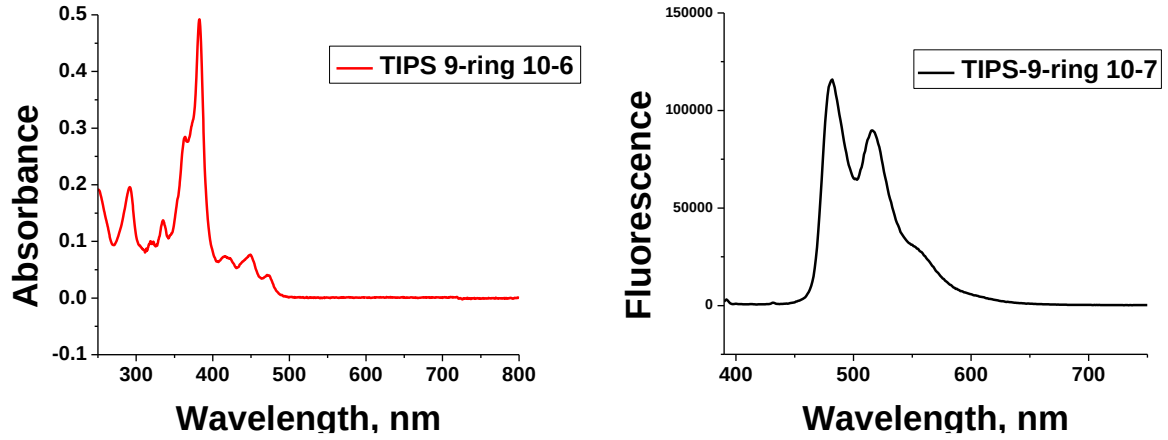

Figure 3-11. UV-vis and fluorescence spectra of TIPS protected 9-ring compound 6.

However, we discovered that TIPS groups do not add stability to the molecule during CV. Oxidation is still irreversible and occurs almost at the same potential as for MC-9R, giving HOMO -5.53eV, this implies that oxidation involves π-electrons rather than chemical reactivity at 2-position of terminal thiophenes.

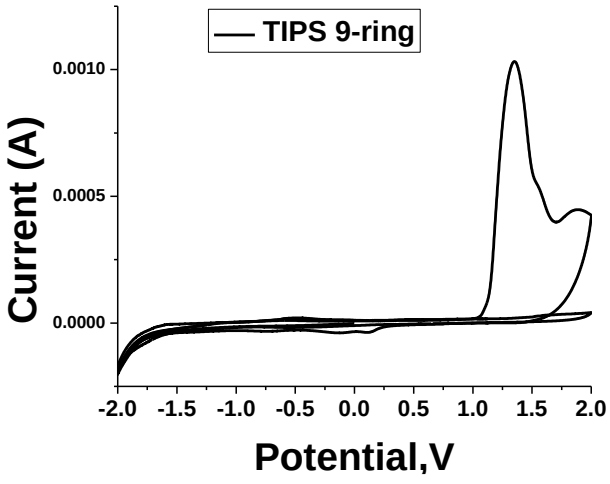

Figure 3-12. CV of TIPS protected 9-ring compound 6.

Comparison of IR spectra of the samples before (left) and after CV (right) shows appearance of a new peak at 1655 cm^{-1}. Literature values for the absorption of the carbonyl of benzodithiophene quinone is 1640 cm^{-1}. Therefore CV experiments likely lead to the oxidation of BDT units with elimination of ethyl-hexyl chains.

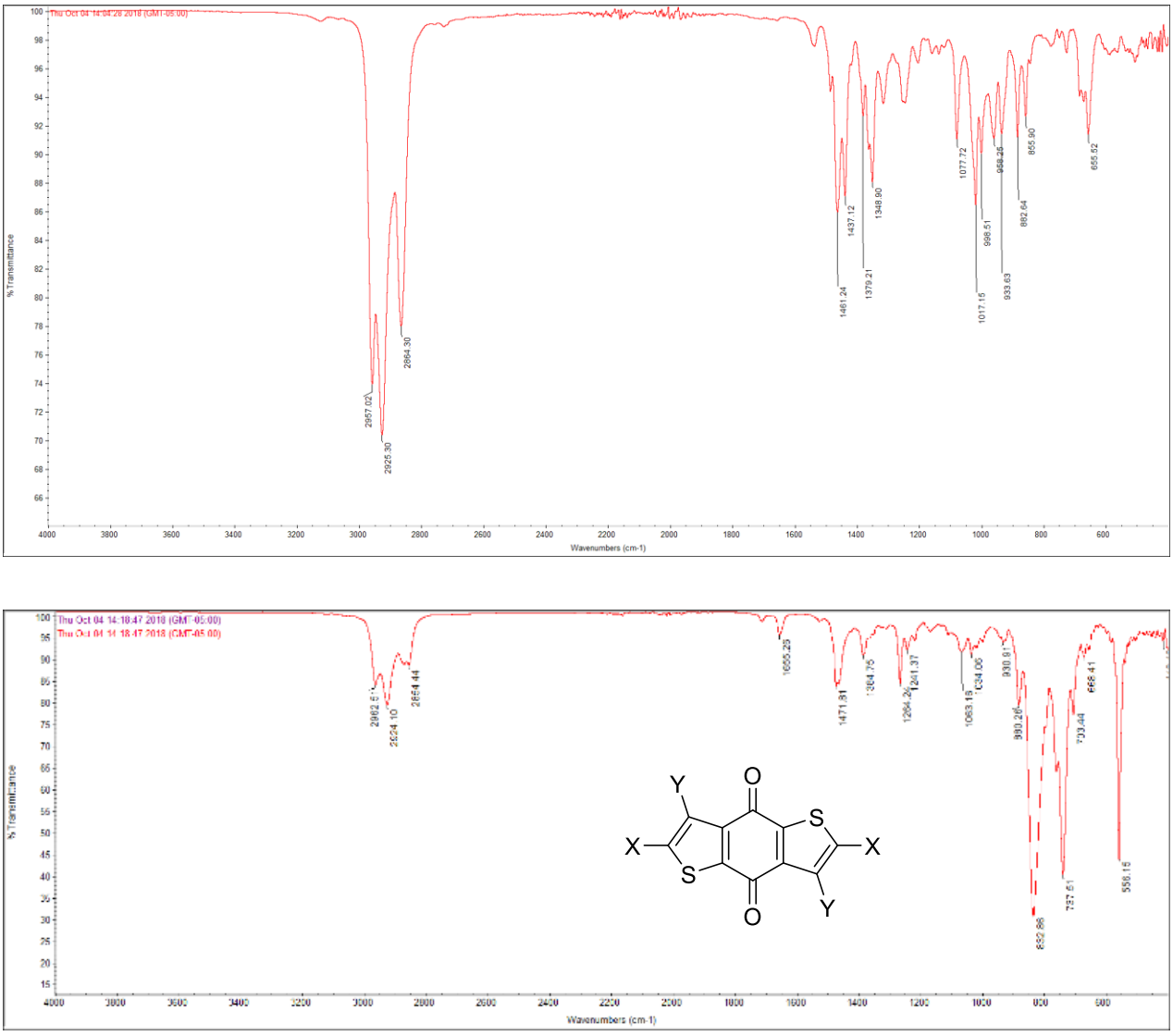

Figure 3-13. IR spectra of compound 6 before and after oxidation

We studied concentration dependence of UV-vis spectrum of MC-7R and concluded that it isn't prone to aggregation since there is no shifts in peak positions with dilution. There is a clearly

visible vibronic progression with peaks at 414, 391, 369, 342, 325, 290nm. Fluorescence spectrum shows 2 peaks at 421nm, 446nm. QY is 3.5%.

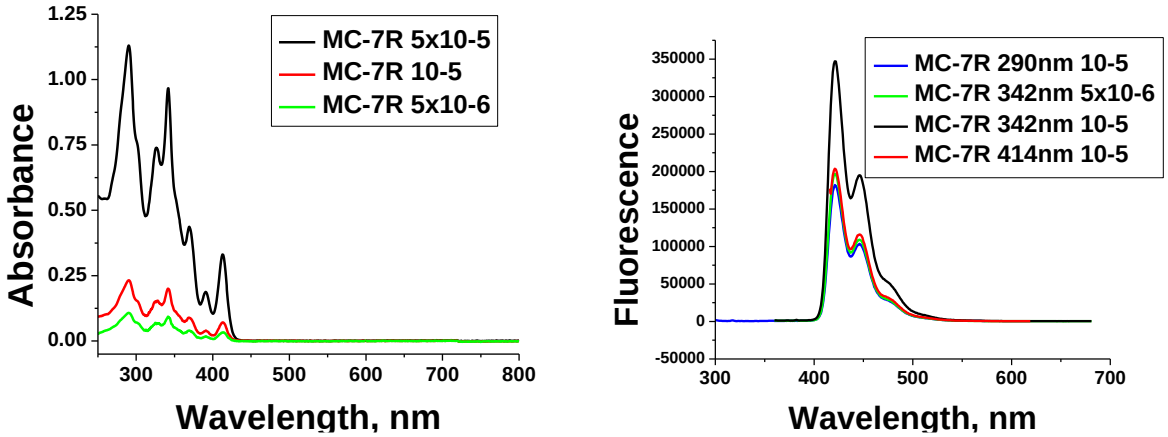

Figure 3-14. UV-vis and fluorescence spectra of MC-7R.

Excitation spectrum matches absorption spectrum very closely, meaning that small satellite peaks are indeed from vibrational levels and not some impurities.

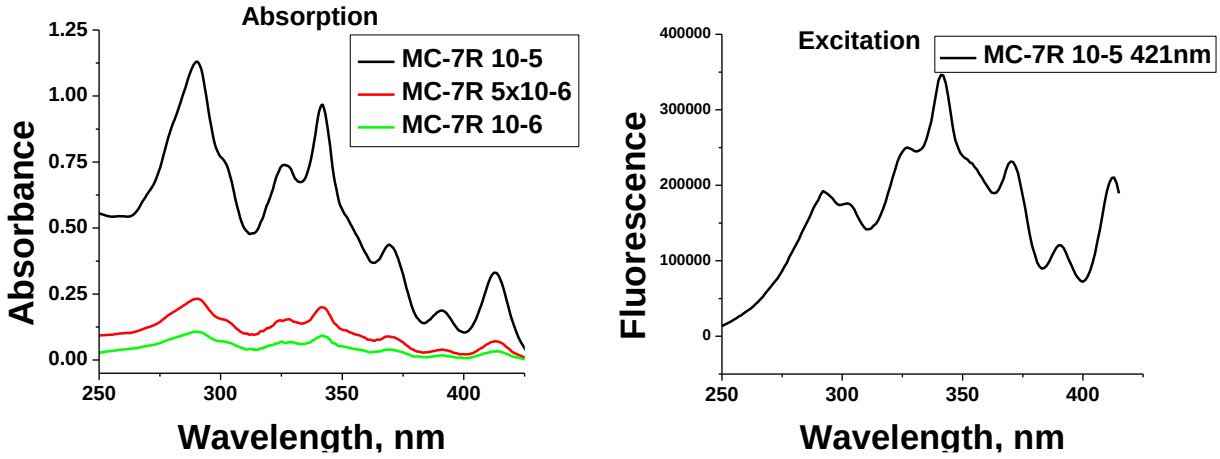

Figure 3-15. UV-vis (zoomed in) and excitation spectra of MC-7R.

Predicted UV-visible spectrum shows 3 major transitions: HOMO-LUMO, HOMO-1-LUMO, HOMO-LUMO+2, just like in the experimental UV-vis.

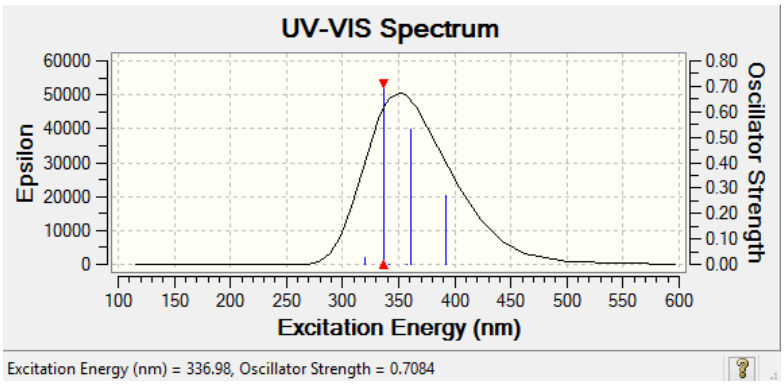

Figure 3-16. TDDFT predicted UV-vis spectrum of MC-7R.

CV oxidation is irreversible just like for MC-9R, which makes sense considering electron-rich nature of this molecule. From CV we can obtain HOMO energy -5.62eV and LUMO -3.51eV. Reduction onset near -1V is barely visible if plotted on the scale with oxidation.

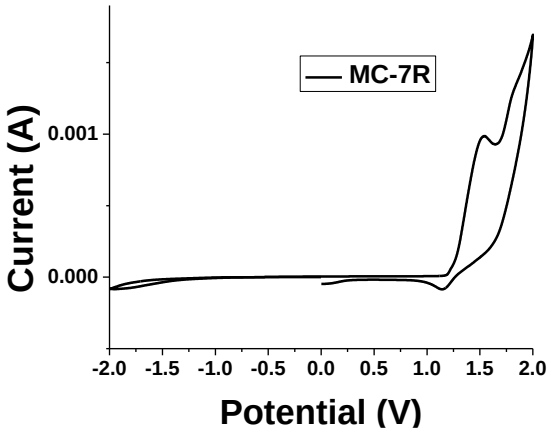

Figure 3-17. CV of MC-7R.

Comparison of 3, 7, 9 ring ladder molecules spectra shows that longer conjugation leads to red-shifted absorption and emission. Longer ladder structures show greater vibronic progression of energy levels as seen by red-shifted low intensity peaks in UV-vis. Extra peak and shoulder in fluorescence spectra in case of 9-ring compound must come from LUMO+1-HOMO and LUMO-

HOMO-2 relaxations (opposite to excitation), and in case of 7-ring compound LUMO-HOMO and LUMO-HOMO-1 since corresponding excitations are the most red-shifted.

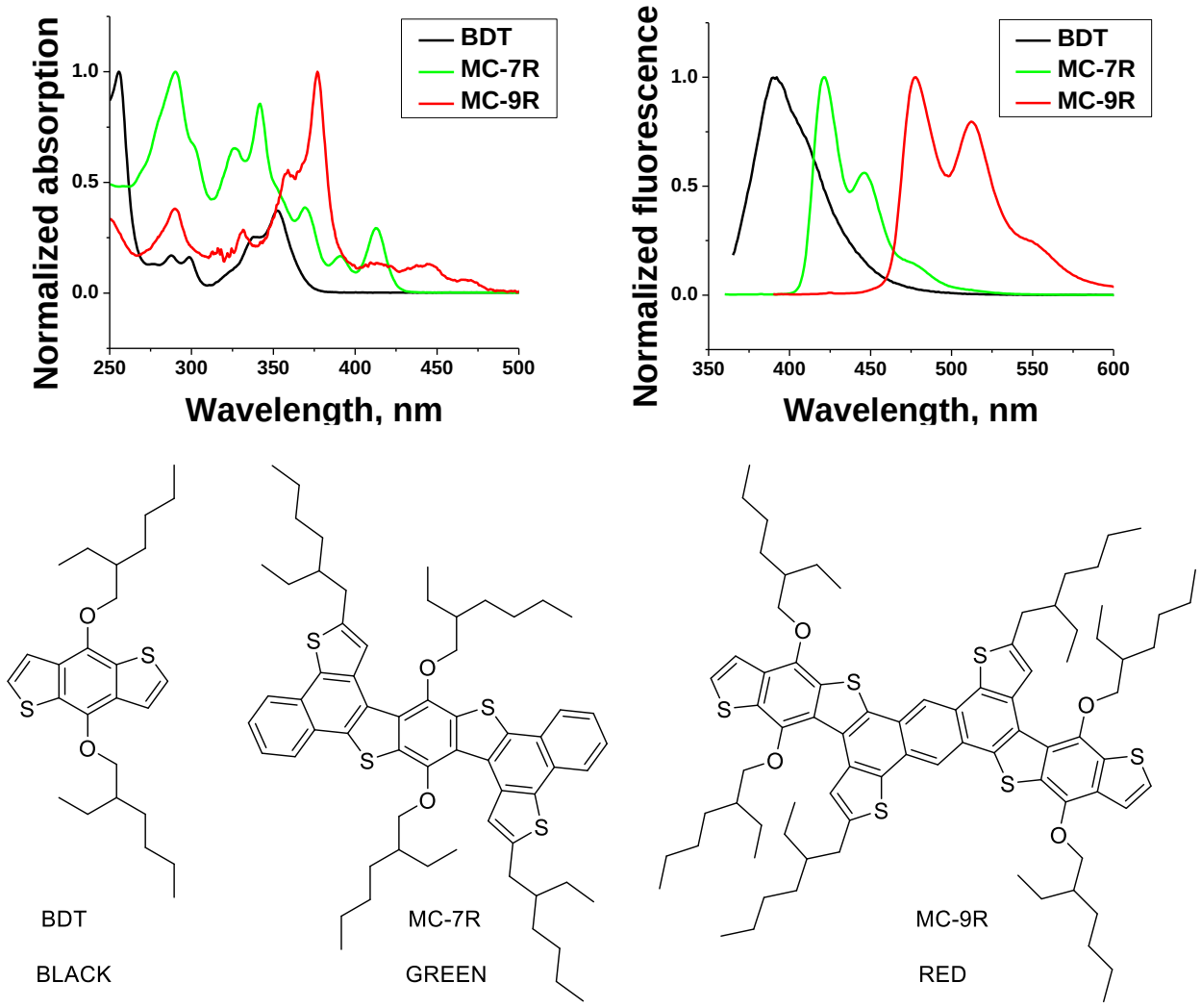

Figure 3-18. Comparison of UV-vis and fluorescence spectra of 3-ring, 7-ring and 9-ring ladder compounds.

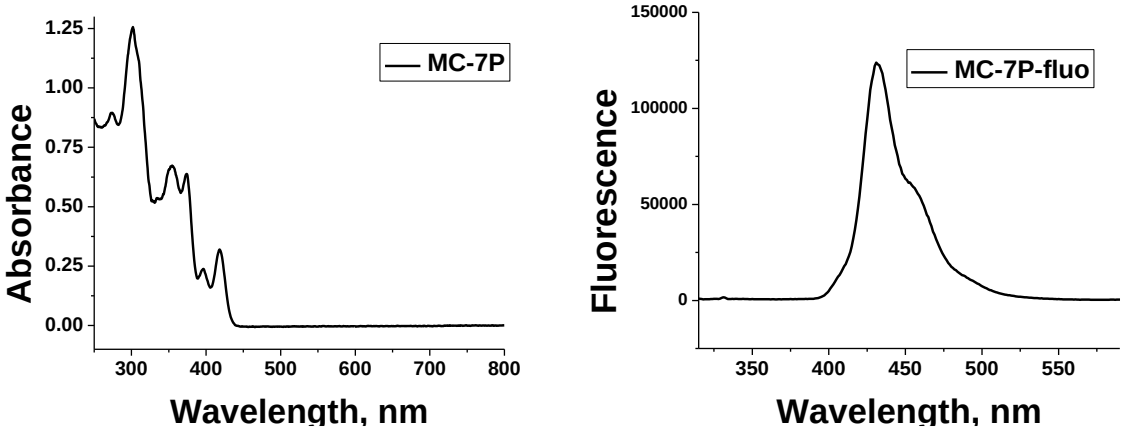

Figure 3-19. UV-vis and fluorescence spectra of MC-7P.

MC-7P just like other ladder molecules shows vibronic progression with peaks in UV-vis spectrum at 302nm, 355nm, 418nm. Its UV-vis is very similar to that without phenyl rings in MC-7R. Maximum fluorescence is at 430nm corresponding to the first peak in MC-7R spectrum, however second peak from MC-7R spectrum becomes a shoulder in MC-7P. This effect likely originates from phenyl rings presenting steric hindrance to hydrogens in 3-position of thiophene. This leads to twist in structure and blue-shift in fluorescence peak. CV shows HOMO -5.6eV; LUMO -3.3eV, similar to MC-7R.

MC-7P also exhibits rather low QY of 2.5% despite phenyl rings blocking solvent molecules from strongly interacting with the π-system. This means that it isn't thermal relaxation that hinders fluorescence. Another possibility is intersystem crossing to non-fluorescent triplet state that is facilitated by sulfur atoms with their greater spin-orbital coupling. In accordance with this idea future direction is synthesis of more nitrogen-rich ladder small molecules and polymers.

3.2.4 STM Break Junction experiments

To further investigate electronic properties of ladder molecules with fused aromatic rings we utilized 3, 5 and 9-ring molecular wires in scanning tunneling microscopy breakjunction (STM-BJ) experiments. In this setup, a compound is first deposited onto the gold surface. Thiol groups have great affinity for gold, therefore, MW-3r was deprotected in THF solution of ammonia, while MW-5r and MW-9r were deprotected in THF solution of TBAF to remove silyl protecting group. Then atomically sharp golden STM tip is lowered to the surface and gradually pulled away while measuring passing current. After this is done for thousands of times current-displacement curves with plateaus signifying that the molecular breakjunction was formed are selected for data processing. Conductance measurements were performed under 10mV bias yielding selection rates of 10-20%. All selected curves data is combined to create histograms presented in Fig. 3-21 – 3-23 on the right. Gaussian fitting of counts versus conductance values gives values in Table 3-2 for each molecular wire.

Table 3-2. Conductance values of synthesized molecular wires.

Compound	MW-3r	MW-5r	MW-9r
Conductance value $\log(\frac{G}{G_0})$	-2.21±0.24	-2.33±0.06	-1.98±0.23

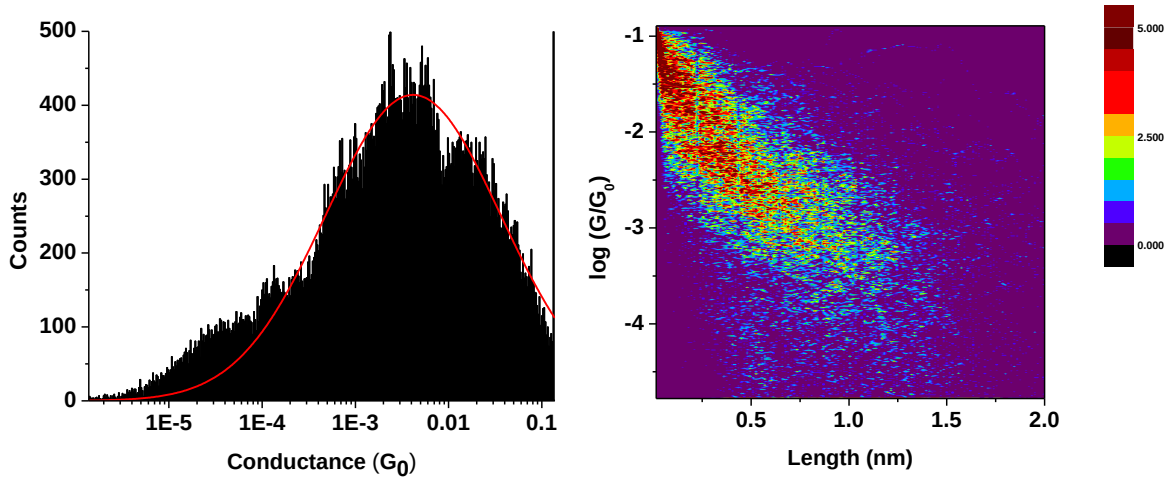

Figure 3-20. Conductance histogram for MW-3r

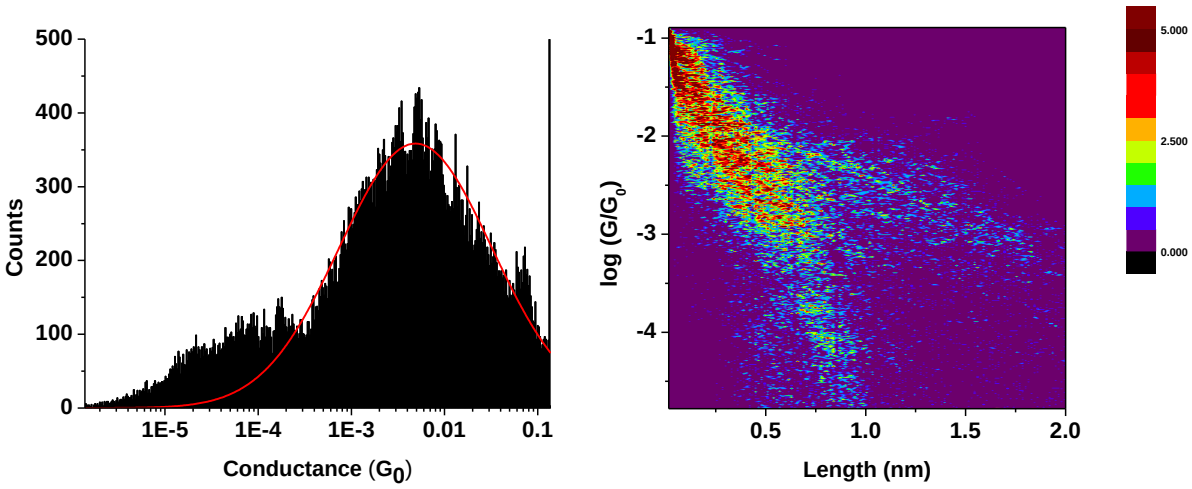

Figure 3-21. Conductance histogram for MW-5r

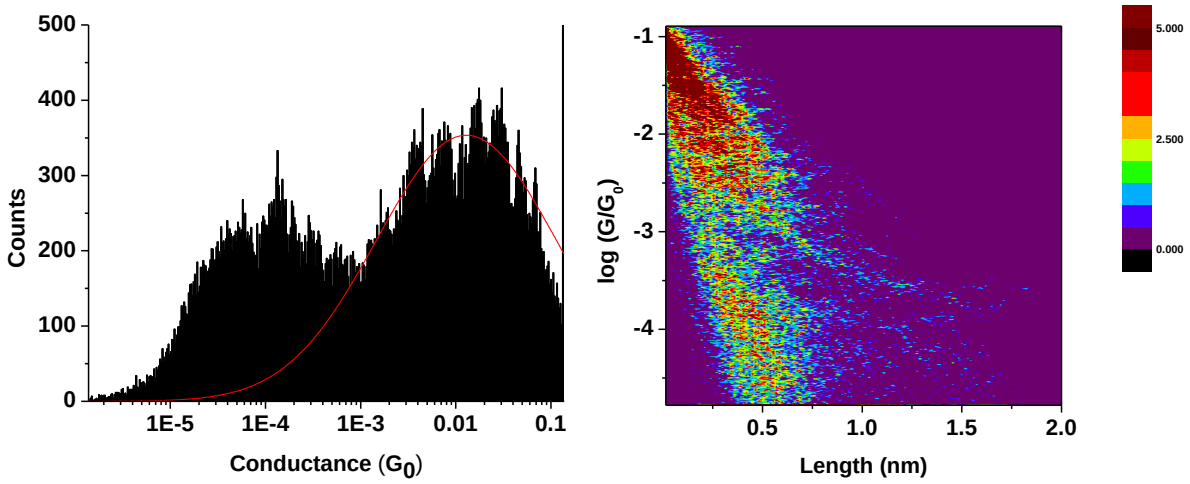

Figure 3-22. Conductance histogram for MW-9r.

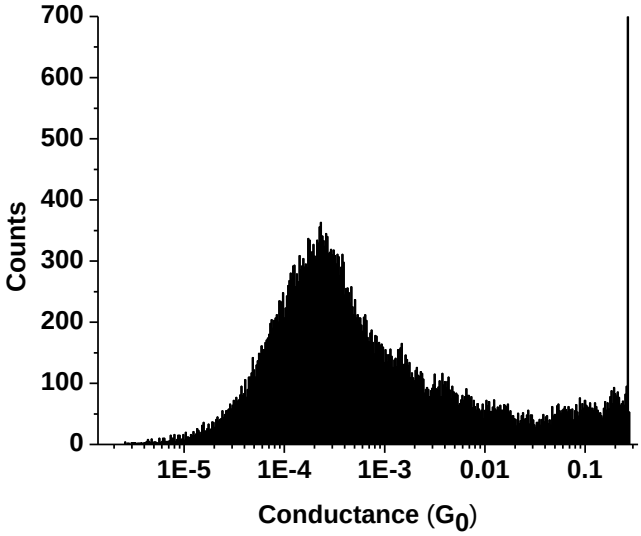

Figure 3-23. Conductance histogram for control experiment: MW-9r dissolved in mesitylene without any treatment with deprotecting agents

Second peak in conductance histogram of MW-9r can be reproduced exclusively in control experiment where deprotection step is skipped. Considering that it also corresponds to a very short distance, this lower conductance likely is due to the weaker binding of thiol groups to gold surface than that of R-S^{-}.

Conductance values of synthesized molecular wires drop going from 3-rings molecular wire to 5-ring, and then increase from MW-5r to MW-9r. This exceptional observation is in stark contrast with trends in the literature, as conductance through molecular wires sharply decreases over distance.[4] Histograms of conductance over length data, composed of individual conductance decay curves offer an insight into actual breakjunctions forming and theoretically should correspond with length of the conducting fragment. Most often the strongest interactions between gold atoms and anchoring groups lead to the break-junctions forming through the whole length of the molecule with rare exceptions. However if other heteroatoms are present in the structure they can bind to golden STM tip as well and form alternative current pathways (Fig. 3-25).[3] To distinguish these effects a closer examination of dependence of conduction over distance is required. In conductance histogram for MW-5r we already see a bimodal distribution, where histogram density splits into 2 arms for shorter and longer distances. The anomalously high conductance for MW-9r comes from the overwhelming proportion of short-distance breakjunctions in the histogram. From DFT calculations we expect breakjunctions to correspond to 1.06nm, 1.41nm and 2.33nm. These distances agree well with observed STM results for MW-3r and longer distance arm of MW-5r histogram. However shorter distance conduction for MW-9r is a strong evidence that breakjunction does not form over the whole molecule and instead gold tip forms a conduction path through "side" sulfurs (Fig. 3-25). This result is reminiscent of what was observed in a similar system where gold tip formed a bond with selenium atom from the side of the molecule effectively decreasing the conduction distance in half (Fig. 3-26).

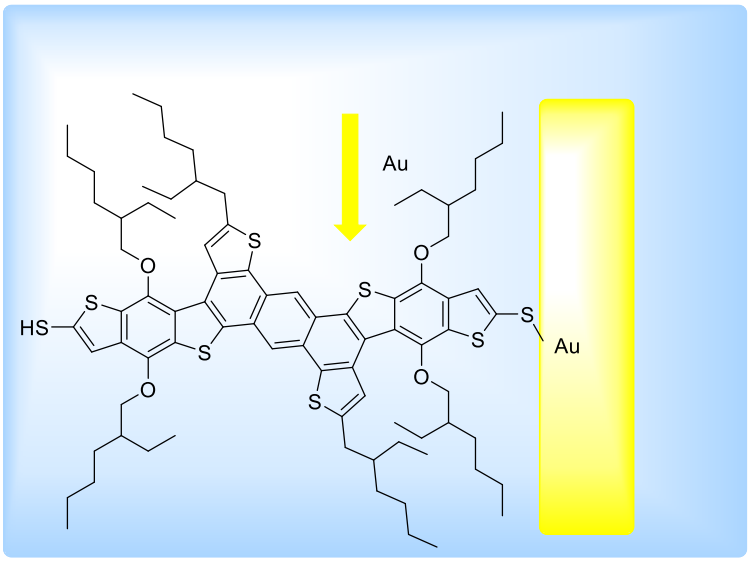

Figure 3-24. Schematic illustration of STM gold tip anchoring to the side sulfur atoms.

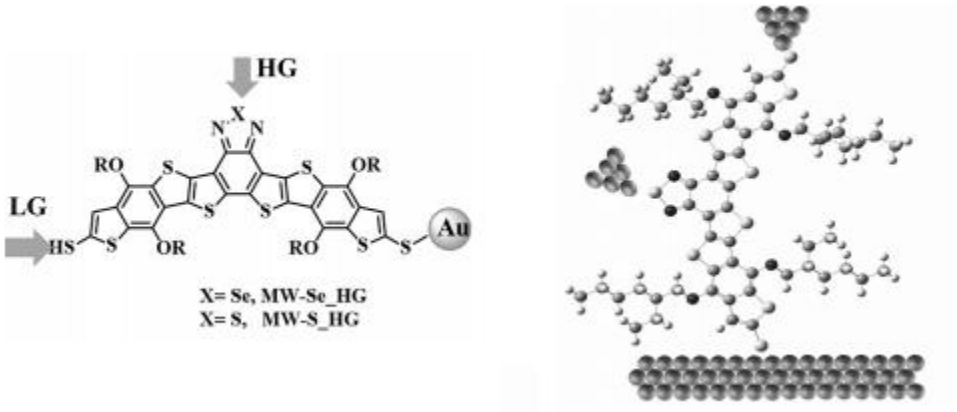

Figure 3-25. Schematic illustration of conductive pathways through molecular wires with heteroatoms in the middle of the molecule. [3]

3.3 Conclusions

We have synthesized a series of model compounds for completely fused ladder polymers, studied the conditions for their oxidation and also their optical and electronic properties. Our results show that longer conjugation leads to red-shifted absorption and emission. Longer ladder structures

show greater vibronic progression of energy levels as seen by red-shifted low intensity peaks in UV-vis, which can be used as evidence for ring fusion in conjugated polymers in the next chapters. Additionally we discovered that vibronic progression leads to a new visible red-shifted shoulder in fluorescence, unlike non-cyclized materials with only one peak. Low quantum yields of fluorescence are due to non-vibrational relaxation of ladder structures, facilitated by a large number of sulfurs providing heavy-atom effect with spin-orbital coupling as opposed to rotational and vibrational relaxation, since compound with orthogonal phenyl rings also has lower quantum yield of luminescence. Finally, we prepared a series of fused-ring ladder molecular wires, which by STM-breakjunction experiments show very little variation in conductance values.

3.4 Experimental section

Unless otherwise stated, all chemicals obtained from commercial suppliers were used without further purification. THF was distilled over sodium prior to use, toluene was passed through MBraun solvent purification system. Other solvents were purified by distillation prior to use. ^{1}H and ^{13}C NMR were recorded by using 400MHz Bruker DRX-400 or Bruker Avance II+ 500 MHz spectrometers. Mass spectra were obtained on Agilent 6224 Tof High Resolution Accurate Mass Spec (HRA-MS) system. Column chromatography was carried out on silica gel (silica 60M, 400-230 mesh). Optical properties were measured by using a Shimadzu UV-2401PC UV-Vis spectrophotometer. Compounds 1[103], 2[104], 4[105] were synthesized according to previously reported procedures.

Dibromodiioobenzene 1[103]: 1H NMR (CDCl3, ppm): δ 8.05 (s, 2H).

Compound 2[104]: 1H NMR (CDCl3, ppm): δ 7.00 (d, 1H), 6.87 (d, 1H), 2.80 (d, 2H), 1.58 (m, 1H), 1.36-1.26 (m, 8H), 0.88 (m, 6H), 0.34 (s, 9H).

Compound 4[105]: 1H NMR (CDCl3, ppm): δ 7.62 (s, 1H), 7.50 (s, 1H), 4.20 (d, 4H), 1.8 (m, 2H), 1.74-1.36 (m, 16H), 1.17 (d, 18H), 1.02 (m, 6H), 0.93(t, 6H), 0.44 (s, 9H).

Compound 3: Dibromodiioobenzene 1 (12.5 g, 25.6 mmol, 1eq), EHThSnMe$_3$ (18.39g, 51.2 mmol, 2 eq), $Pd(Ph_3)_2Cl_2$ (702mg, 1.0 mmol, 4% eq) were combined in a dry round bottom flask. After 3 nitrogen-vacuum cycles, anhydrous DMF (90ml) was added and solution was purged with nitrogen for 30 min. Solution was stirred at 80°C for 30h. Reaction mixture was cooled to rt and filtered through celite. DMF was evaporated under vacuum, residue was purified by gravity column chromatography using hexanes as eluent. Product isolated as a clear oil (8.5g, 53%). 1H NMR (CDCl3, ppm): δ 7.76 (s, 2H), 7.19 (d, 2H), 6.76 (d, 2H), 2.78 (d, 4H), 1.62 (m, 2H), 1.42-1.26 (m, 16H), 0.95-0.85 (m, 12H). ^{13}C NMR (CDCl3, ppm): δ 146.4, 137.2, 135.7, 135.5, 128.0, 125.3, 120.8, 41.4, 34.2, 32.5, 28.9, 25.6, 23.1, 14.2, 10.9. HRAMS m/z: $C_{30}H_{40}Br_2S_2$, Calcd, 622.0938. Found, (M^+), 622.0974.

Compound 5: Compounds 3 (0.5g, 0.8 mmol, 1eq) and 4 (3.06g, 4mmol, 2.5eq), $Pd(Ph_3)_2Cl_2$ (28.1mg, 0.04 mmol, 5% eq) were combined in a dry round bottom flask. After 3 nitrogen-vacuum cycles, anhydrous DMF (10ml) was added and solution was purged with nitrogen for 30 min. Reaction mixture was refluxed at 130 °C for 72h. DMF was evaporated in vacuo, the residue was purified by column chromatography on silica gel using hexanes-DCM gradient. Product is isolated as a viscous orange oil that solidifies over time (1.365g, quantitative). 1H NMR (CDCl3, ppm): δ 7.80 (s, 2H), 7.64 (s, 2H), 7.36 (s, 2H), 6.87 (d, 2H), 6.60 (d, 2H), 4.18 (d, 4H), 4.13 (d, 4H), 2.68 (d, 4H), 1.83-1.35 (m, 54H), 1.19 (d, 36H), 1.05-0.98 (m, 12H), 0.97-0.91 (m, 12H), 0.85-0.79 (m, 12H). ^{13}C NMR (CDCl3, ppm): δ 145.9, 144.4, 143.8, 141.7, 139.0, 136.8, 131.9, 130.2, 128.8, 127.3, 125.4, 120.9, 76.0, 75.7, 41.3, 40.8, 40.8, 34.1, 32.4, 30.8, 30.6, 29.5, 29.5, 29.0, 25.6, 24.1,

24.0, 23.3, 23.3, 23.1, 18.8, 14.3, 14.3, 14.2, 12.0, 11.5, 11.5, 10.9. HRAMS m/z: $C_{100}H_{154}O_4S_6Si_2$, Calcd, 1666.971. Found, (M^+), 1666.9649.

Compound 6: To a solution of compound 5 (400mg, 0.24 mmol, 1eq) in anhydrous DCM (40ml) was added dropwise at rt a solution of $FeCl_3$ (236mg, 1.44 mmol, 6eq) in 4 ml of nitromethane. Reaction mixture immediately turned dark-blue and was allowed to stir for 45min, then it was quenched by filtering through celite. Celite was washed with DCM, combined filtrates were washed with water and brine, concentrated in vacuo, and the residue was purified by column chromatography with hexanes-DCM gradient yielding product as a pale-yellow solid (99 mg, 25%). 1H NMR (CDCl3, ppm): δ 8.99 (s, 2H, br), 8.64 (s, 2H), 7.75 (s, 2H, br), 4.35 (br, 4H), 3.92 (br, 4H), 3.05 (br, 4H), 2.08 (m, 2H), 1.85 (m, 2H), 1.75-1.25 (m, 48H), 1.22 (d, 36H), 1.13 (t, 6H), 1.07 (t, 6H), 0.99 (t, 6H), 0.96-0.84 (m, 18H). ^{13}C NMR (CDCl3, ppm): δ 145.5, 144.2, 144.1, 138.6, 137.5, 136.1, 135.4, 133.8, 133.7, 130.1, 128.5, 128.0, 127.9, 127.1, 126.5, 125.9, 119.6, 78.9, 76.5, 42.0, 41.0, 40.2, 35.6, 32.8, 30.8, 30.4, 29.9, 29.5, 29.2, 29.1, 25.9, 24.2, 23.6, 23.5, 23.3, 23.2, 18.8, 14.5, 14.4, 14.3, 12.0, 11.6. HRAMS m/z: $C_{100}H_{150}O_4S_6$**Si**$_2$, Calcd, 1662.9397. Found, (M^+), 1662.9345.

Compound 8: 58%. ^{1}H NMR (500 MHz, $CDCl_3$) δ 7.66 (dd, *J* = 8.1, 1.3 Hz, 1H), 7.49 (dd, *J* = 7.7, 1.7 Hz, 1H), 7.31 (td, *J* = 7.6, 1.3 Hz, 1H), 7.17 – 7.12 (m, 2H), 6.76 (dd, *J* = 3.5, 1.0 Hz, 1H), 2.79 (d, *J* = 6.9 Hz, 2H), 1.63 (t, *J* = 6.1 Hz, 1H), 1.46 – 1.28 (m, 8H), 0.92 (td, *J* = 7.4, 5.4 Hz, 6H). ^{13}C NMR (126 MHz, $CDCl_3$) δ 145.67, 139.28, 135.75, 133.82, 131.85, 128.66, 127.51, 127.46, 125.18, 122.67, 41.51, 34.22, 32.53, 29.02, 25.71, 23.15, 14.29, 10.99. HRAMS m/z: $C_{18}H_{23}BrS$, Calcd, 350.0704. Found, (M^+), 350.0751.

Compound 9: 64%. ^{1}H NMR (500 MHz, $CDCl_3$) δ 7.63 (ddd, *J* = 7.4, 1.5, 0.7 Hz, 1H), 7.49 – 7.35 (m, 4H), 7.29 (td, *J* = 7.3, 1.4 Hz, 1H), 6.90 (d, *J* = 3.4 Hz, 1H), 6.69 (d, *J* = 3.4 Hz, 1H), 2.77 (d,

J = 3.4 Hz, 2H), 1.66 – 1.56 (m, 1H), 1.45 – 1.31 (m, 8H), 1.29 (d, *J* = 1.2 Hz, 12H), 0.95 – 0.87 (m, 6H). ^{13}C NMR (126 MHz, $CDCl_3$) δ 144.70, 142.70, 139.87, 134.35, 130.08, 129.37, 126.65, 125.81, 125.31, 83.94, 41.57, 34.26, 32.47, 28.99, 25.55, 24.82, 24.80, 23.18, 14.32, 10.96. HRAMS m/z: $C_{24}H_{35}BO_2S$, Calcd, 397.2487. Found, (M^+), 397.2499.

MC-7R: uncyclized precursor 47%: ^{1}H NMR (500 MHz, $CDCl_3$) δ 7.64 (d, *J* = 7.7 Hz, 2H), 7.53 – 7.44 (m, 4H), 7.40 (d, *J* = 7.2 Hz, 2H), 6.72 (d, *J* = 3.5 Hz, 2H), 6.50 (d, *J* = 3.6 Hz, 2H), 4.01 (d, *J* = 5.0 Hz, 4H), 2.63 (d, *J* = 5.5 Hz, 4H), 1.94 (p, *J* = 6.3 Hz, 2H), 1.60 (m, 2H), 1.53 – 1.15 (m, 32H), 1.02 – 0.74 (m, 24H). ^{13}C NMR (126 MHz, $CDCl_3$) δ 145.47, 144.52, 139.95, 139.35, 135.78, 132.26, 132.12, 131.19, 129.90, 129.70, 128.64, 127.01, 126.32, 125.49, 104.00, 79.09, 41.27, 40.41, 33.92, 32.39, 30.21, 29.19, 28.93, 25.50, 23.66, 23.25, 23.07, 14.29, 11.28, 10.90. HRAMS m/z: $C_{62}H_{80}Br_2O_2S_4$, Calcd, 1142.3408. Found, (M^+), 1142.3408. MC-7R 75% (poor solubility): ^{1}H NMR (500 MHz, $CDCl_3$) δ 8.60 (s, 2H), 8.30 (d, *J* = 7.1 Hz, 2H), 8.23 (d, *J* = 8.4 Hz, 2H), 7.64 (dd, *J* = 28.7, 21.5 Hz, 4H), 3.97 – 3.91 (m, 4H), 3.06 (d, *J* = 7.9 Hz, 4H), 1.69 (br s, 4H), 1.50 – 1.18 (m, 32H), 1.01 – 0.84 (m, 24H).

Compound 12[106]: 4.6% over 5 steps. ^{1}H NMR (400 MHz, $CDCl_3$) δ 7.64 (d, *J* = 7.4 Hz, 4H), 7.43 – 7.33 (m, 2H), 7.11 (d, *J* = 7.8 Hz, 4H), 3.97 (d, *J* = 5.7 Hz, 4H), 1.80 (p, *J* = 6.4 Hz, 2H), 1.66 – 1.23 (m, 16H), 0.96 (m, 12H), 0.36 (s, 18H).

MC-7P: 48%. ^{1}H NMR (400 MHz, $CDCl_3$) δ 8.21 – 8.17 (m, 2H), 8.15 – 8.11 (m, 2H), 7.67 (d, *J* = 8.8 Hz, 2H), 7.61 – 7.48 (m, 6H), 7.10 (d, *J* = 8.6 Hz, 4H), 6.09 (s, 2H), 4.07 – 3.90 (m, 4H), 2.56 (dd, *J* = 7.0, 2.6 Hz, 4H), 1.85 (p, *J* = 6.0 Hz, 2H), 1.72 – 1.37 (m, 18H), 1.29 (m, 16H), 1.09 – 0.84 (m, 24H). HRAMS m/z: $C_{74}H_{86}O_2S_4$, Calcd, 1134.5511. Found, (M^+), 1134.5382.

MC-9R: compound 6 (87mg, 0.053 mmol, 1eq) was dissolved in THF (20ml). TBAF solution (1M in THF, 0.25 ml, 0.25 mmol, 5eq) was added dropwise, color changes from orange to green, and reaction mixture was stirred overnight. Solution was concentrated and residue was purified by column chromatography using DCM-hexanes 1:9 as eluent. Compound 6 isolated as a yellow solid (61 mg, 90%). 1H NMR (CDCl3, ppm): δ 8.92 (s, 2H, br), 8.60 (s, 2H), 7.56 (d, 2H), 7.51 (d, 2H), 4.32 (d, 4H, br), 3.90 (d, 4H, br), 3.08 (d, 4H, br), 2.12 (m, 2H), 1.98 (m, 2H), 1.91 (m, 2H), 1.84 (m, 4H), 1.76-1.26 (m, 48H), 1.15 (t, 6H), 1.10 (t, 6H), 1.02 (t, 6H), 0.99-0.89 (m, 18H). ^{13}C NMR (CDCl3, ppm): δ 145.9, 144.8, 144.1, 136.0, 135.4, 133.8, 133.6, 132.0, 130.3, 128.0, 127.7, 127.4, 127.0, 126.4, 125.8, 120.4, 119.5, 79.2, 76.6, 42.0, 41.0, 40.1, 35.6, 32.8, 30.7, 30.3, 29.9, 29.4, 29.2, 29.1, 25.9, 24.1, 23.7, 23.5, 23.3, 23.3, 14.5, 14.4, 14.3, 11.6, 11.1, 11.0. HRAMS m/z: $C_{82}H_{110}O_4S_6$, Calcd, 1350.6728. Found, (M^+), 1350.6653.

Compound 15: MC-9R (340 mg, 0.25 mmol, 1 eq) was placed into a dry flask under nitrogen, 5 ml of THF was added. The solution was cooled to -78°C, n-BuLi (2.5 M in hexanes, 0.44 mL, 1.25 mmol, 5 eq) was added dropwise via a syringe, and the reaction was allowed to stir at -78 °C for 30 min, at rt for 30 min, and then cooled to -78°C again. Tetrabromomethane (414.5 mg, 1.25 mmol, 5eq) dissolved in 1ml of THF was added dropwise, and the reaction mixture was stirred and allowed to warm to rt overnight. Reaction was quenched with water and product was extracted with DCM, 3x5ml. Combined organic layers were dried over Na_2SO_4, filtered, and concentrated to provide yellow solid, which was further purified by filtering thru a short plug of silica, yielding 167 mg of hetaryl dibromide 15 (44%). 1H NMR (CDCl3, ppm): δ 8.93 (s, 2H), 8.53 (s, 2H), 7.52 (s, 2H), 4.27 (d, 4H, br), 3.84 (d, 4H, br), 3.05 (d, 4H, br), 2.06 (m, 2H), 1.96 (m, 2H), 1.87 (m, 2H), 1.80 (m, 4H), 1.72-1.22 (m, 48H), 1.12 (t, 6H), 1.07 (t, 6H), 0.99 (t, 6H), 0.96-0.86 (m, 18H). HRAMS m/z: $C_{82}H_{108}Br_2O_4S_6$, Calcd, 1506.4939. Found, (M^+), 1506.4789.

MW-9r: compound 15 (110 mg, 0.073 mmol, 1 eq), DIPEA (24 mg, 0.182 mmol, 2.5 eq), 2-(trimethylsilyl)ethanethiol (24.4 mg, 0.182 mmol, 2.5 eq) were combined in a round-bottom flask and degassed 3 times, vacuum-nitrogen. Toluene (0.5 ml) was added and solution was purged for 30s. $Pd_2(dba)_3$ (1.3 mg, 2% eq) and dppf (1.6 mg, 4% eq) were added and solution was purged another 30s. The solution was stirred under reflux for 12 h and cooled to r.t. The reaction mixture was filtered through celite, celite was washed with DCM. The filtrate was concentrated in vacuo and the residue was purified by flash column chromatography on silica gel to afford product as pale yellow oil, which could be crystallized from isopropanol to yield yellow solid (51mg, 46%). ^{1}H NMR (CDCl3, ppm): δ 8.95 (s, 2H), 8.56 (s, 2H), 7.46 (s, 2H), 4.30 (d, 4H, br), 3.87 (d, 4H, br), 3.12-3.03 (m, 8H), 2.08 (m, 2H), 1.96 (m, 2H), 1.87 (m, 2H), 1.80 (m, 4H), 1.73-1.24 (m, 48H), 1.11 (t, 6H), 1.09-1.05 (m, 10H), 0.99 (t, 6H), 0.95-0.85 (m, 18H), 0.07 (s, 18H). ^{13}C NMR (CDCl3, ppm): δ 145.1, 144.1, 143.8, 139.0, 135.8, 135.4, 134.8, 133.6, 132.0, 130.5, 127.9, 127.8, 126.9, 126.4, 125.7, 123.1, 119.4, 79.2, 76.7, 42.0, 42.0, 41.0, 40.1, 35.7, 33.9, 32.8, 30.6, 30.3, 29.9, 29.4, 29.4, 29.2, 29.1, 29.1, 25.9, 25.8, 24.1, 23.7, 23.5, 23.3, 23.3, 17.9, 14.5, 14.4, 14.3, 11.6, 11.2, 11.1, 11.0, -1.6. HRAMS m/z: $C_{92}H_{134}O_4S_8Si_2$, Calcd, 1614.7586. Found, (M^+), 1614.7557.

MW-3r was synthesized according to the previously described procedure[4] (49%). 1H NMR (CDCl3, ppm): δ 7.54 (s, 2H), 4.16 (d, 4H), 2.48 (s, 6H), 1.78 (m, 2H), 1.65 (m, 2H), 1.60-1.32 (m, 16H), 0.99 (t, 6H), 0.93 (s, 6H).

Compound 13[104]: 1H NMR (CDCl3, ppm): δ 7.54 (s, 2H), 6.92 (d, 2H), 6.77 (d, 2H), 6.76 (d, 2H), 6.65 (d, 2H), 2.73 (d, 4H), 1.63 (m, 2H), 1.38-1.23 (m, 16H), 0.94-0.86 (m, 12H).

Compound 14: To a solution of compound 7 (200mg, 0.0.25 mmol, 1eq) in anhydrous DCM (80ml) was added dropwise at rt a solution of $FeCl_3$ (243mg, 1.44 mmol, 6eq) in 4.5 ml of

nitromethane. Reaction mixture immediately turned dark-blue and was allowed to stir for 45min, then it was quenched by filtering through celite. Celite was washed with DCM, combined filtrates were washed with water and brine, concentrated in vacuo, and the residue was purified recrystallizations from isopropanol and isopropanol-toluene yielding product as a pale-yellow solid (45 mg, 22%).1H NMR (CDCl3, ppm): δ 8.49 (s, 2H), 7.64 (s, 2H), 7.29 (s, 2H), 2.98 (d, 4H), 1.78 (m, 2H), 1.50-1.23 (m, 16H), 1.01-0.90 (m, 12H). Note: poor solubility in CDCl3, peaks broadened. Chemical shifts of aromatic hydrogens are different than in paper[104]: 8.58 (s, 2H), 8.15 (s, 2H), 7.00 (s, 2H), however almost the same as in butyl-octyl version synthesized by Feng He: 8.54 (s, 2H), 7.65 (s, 2H), 7.27 (s, 2H). HRAMS m/z: $C_{38}H_{40}Br_2S_4$, Calcd, 782.038. Found, (M^+), 782.0346.

MW-5r: Compound 8 (40 mg, 0.05 mmol, 1 eq), DIPEA (16.2 mg, 0.125 mmol, 2.5 eq), 2-(trimethylsilyl)ethanethiol (16.8 mg, 0.125 mmol, 2.5 eq) were combined in a round-bottom flask and degassed 3 times, vacuum-nitrogen. Toluene (0.5 ml) was added and solution was purged for 30s. $Pd_2(dba)_3$ (1.3 mg, 2% eq) and dppf (1.6 mg, 4% eq) were added and solution was purged another 30s. The solution was stirred under reflux for 12 h and cooled to r.t. The reaction mixture was filtered through celite, celite was washed with DCM. The filtrate was concentrated in vacuo and the residue was purified by flash column chromatography on silica gel and then recrystallized from isopropanol-chloroform to yield yellow solid (32mg, 80%). ^{1}H NMR (CDCl3, ppm): δ 8.64 (s, 2H), 7.66 (s, 2H), 7.34 (s, 2H), 3.08-3.04 (m, 4H), 2.98 (d, 4H), 1.79 (m, 2H), 1.48-1.33 (m, 16H), 1.06-1.02 (m, 4H), 0.97 (t, 6H), 0.93 (t, 6H), 0.05 (s, 18H). ^{13}C NMR (CDCl3, ppm): δ 145.9, 137.3, 136.7, 133.9, 133.5, 133.1, 128.6, 125.5, 125.1, 121.3, 118.6, 41.8, 35.2, 35.1, 32.7, 29.1, 25.7, 23.2, 17.8, 14.3, 11.0, -1.6. HRAMS m/z: $C_{48}H_{66}S_6Si_2$, Calcd, 890.3027. Found, (M^+), 890.3031.

3.5 References

(79) Zheng, T.; Cai, Z.; Ho-Wu, R.; Yau, S. H.; Shaparov, V.; Goodson, T.; Yu, L. *J. Am. Chem. Soc.* **2016**, *138* (3), 868–875.

(80) Ma, J.; Feng, G.; Liu, F.; Yang, F.; Guo, Y.; Wu, Y.; Li, W. *Dye. Pigment.* **2019**, *165* (December 2018), 335–340.

(81) Hoang, M. H.; Park, G. E.; Phan, D. L.; Ngo, T. T.; Nguyen, T. Van; Park, C. G.; Cho, M. J.; Choi, D. H. *Macromol. Res.* **2018**, *26* (9), 844–850.

(82) Kan, B.; Feng, H.; Wan, X.; Liu, F.; Ke, X.; Wang, Y.; Wang, Y.; Zhang, H.; Li, C.; Hou, J.; Chen, Y. *J. Am. Chem. Soc.* **2017**, *139* (13), 4929–4934.

(83) Jacob, J.; Sax, S.; Piok, T.; List, E. J. W.; Grimsdale, A. C.; Müllen, K. *J. Am. Chem. Soc.* **2004**, *126* (22), 6987–6995.

(84) Bunz, U. H. F. *Acc. Chem. Res.* **2015**, *48* (6), 1676–1686.

(85) Bronstein, H.; Nielsen, C. B.; Schroeder, B. C.; McCulloch, I. *Nat. Rev. Chem.* **2020**, *4* (2), 66–77.

(86) Lee, J.; Kalin, A. J.; Yuan, T.; Al-Hashimi, M.; Fang, L. *Chem. Sci.* **2017**, *8* (4), 2503–2521.

(87) Rieger, R.; Müllen, K. *J. Phys. Org. Chem.* **2010**, No. 23, 315–325.

(88) Ito, H.; Segawa, Y.; Murakami, K.; Itami, K. *J. Am. Chem. Soc.* **2019**, *141* (1), 3–10.

CHAPTER 4

RING FUSION STRATEGY FOR LUMINESCENT LADDER POLYMERS

4.1 Introduction

Modern consumer and industrial devices requires highly efficient and stable light-emitting materials. Field of organic electronics especially needs new developments with blue light emitting materials with higher stability and efficiency, as blue light emitting elements are one of the basic components of modern displays. Although a great deal of progress has been made in the field of organic light emitting diodes (OLED), new approaches to device architecture require further innovation.

As manufacturing accounts for one of the large costs of consumer electronics, there is a greater interest in materials and devices that can combine several functions simultaneously. One of such developments is organic light emitting transistor (OLET) technology that combine light emission and transistor control in one device. [48]

However this combined device architecture places more stringent requirements on used materials. They must exhibit highly efficient luminescence, high ambipolar mobility and excellent processibility. There is an unavoidable challenge in that mobility and luminescence properties are at odds with each other. Intermolecular interactions like π-π stacking benefit charge transport, but simultaneously provide pathways for the excited states to undergo nonradiative relaxation.

Conjugated polymer materials allow many opportunities to tune both of these properties. Structure-property relationships across dimensions of monomer structures, alkyl chains length, molecular weight and distribution provide ample space for material optimization. We found that polymers with semi-ladder structures are promising to find compromise between counteracting luminescence and mobility properties.

There is a number of approaches in the literature to access ladder and semiladder structure. They can be divided into synthesis of conventional conjugated polymers with subsequent cyclization or incorporation of fused rings monomers into Stille or Suzuki polycondensation. Examples include oxidation of electron rich polymer[107], photochemical cyclization[89–91], or polycondensation of semiladder monomers[108]. Our approach involves synthesis of semiladder precursor polymers and then their oxidative cyclization to explore properties of ring fused conjugated ladder polymers.

4.2 Results and discussion

We designed 3 precursor polymers with twisted repeating units: TPB, TPF and PPF. The design idea is that these polymers exhibit severe steric hindrance in their side chains, which will have increased fluorescence because of "locked" molecular structures in solid states. Twisted repeating unit not only allows for blue light emission but also protects excited state from quenching and non-radiative decay.

Furthermore, these polymers have aromatic rings positioned for oxidative cyclization to generate "ladder" type fused rings. Ladder structure minimizes vibrational relaxation, increasing QY of fluorescence. Planar structure enhances mobility due to more efficient π-π stacking which allows charges, holes and electrons, to hop from one molecule to the next. However, a completely planar ladder structure will eliminate torsional barrier, which forces all p-orbitals on carbon atoms parallel and favors for interchain overlap. The excited state in a strongly overlapped film will be reduced due to excimer formation. Since fully twisted structure will not have satisfactory mobility for device, and fully ladder structure will have decreased fluorescence, it is necessary to continuously change the balance between luminescence and mobility and take the best of both worlds by varying the percent of "ladderized" units.

Scheme 4-1. Structures of synthesized materials.

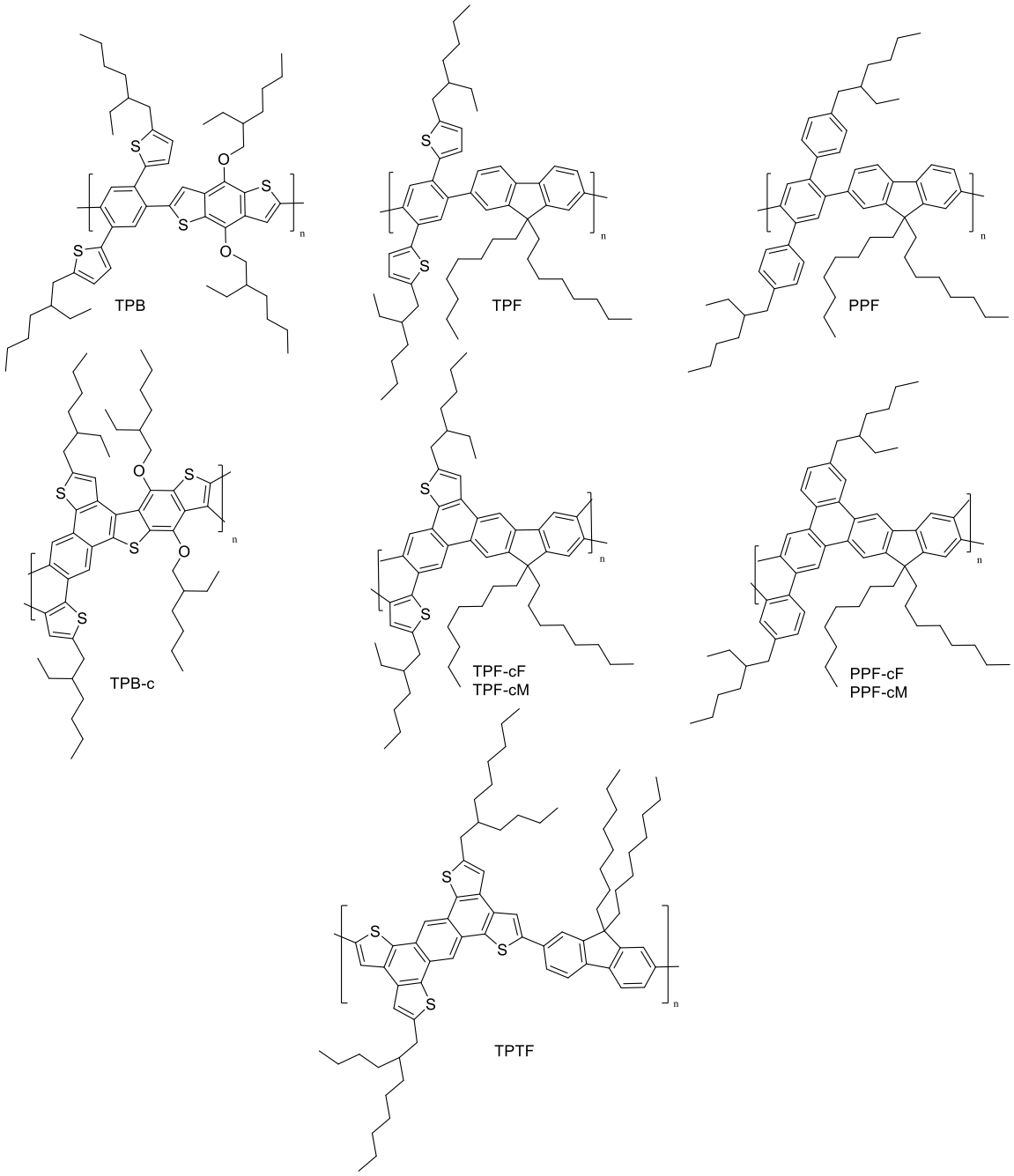

4.2.1 Synthesis

The polymer TPB consists of BDT-PhTh type of repeating unit because thiophene rings are more electron rich and thus more prone to oxidative cyclization. The TPF contains dialkylfluorene

in the place of the benzodithiophene, and PPF contains no thienyl moiety. These polymers are less electron-rich, but offer higher quantum yields, because of lack of sulfur atom that can diminish luminescence due to heavy-atom effect.

The TPB was synthesized according to scheme 4-2. The Stille cross-coupling of (2-ethylhexylthienyl)trimethyltin with dibromodiiodobenzene yields compound 3. Subsequent polymerization of compound 3 with ditin benzodithiophene gives non-cyclized polymer TPB. The TPB was oxidized by using several methods.

Scheme 4-2. Synthesis of TPB

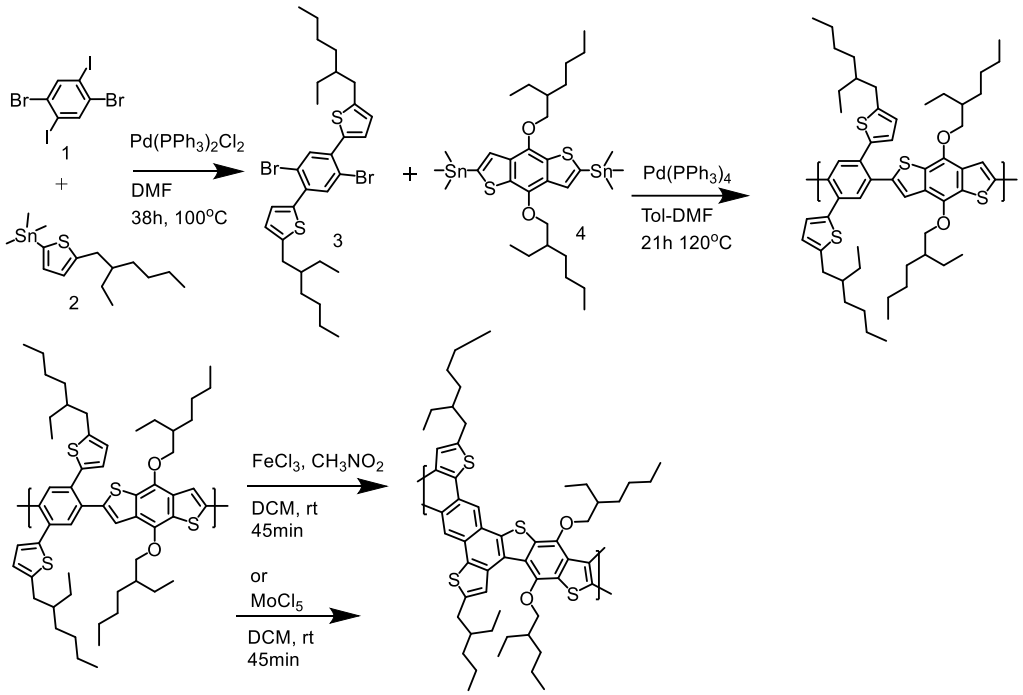

We have studied conditions for this reaction with model small molecule. Among various oxidants, $MoCl_5$ and $FeCl_3$ were found to be the best for the cyclization of model compound (Chapter 3).

For the synthesis of TPF we used dibromodioctylfluorene to react with BuLi at -78°C. After quenching with boronic ester we obtained diBpin monomer which was polymerized in Suzuki reaction to yield TPF. Next oxidation gives ladder polymers.

Scheme 4-3. Synthesis of TPF

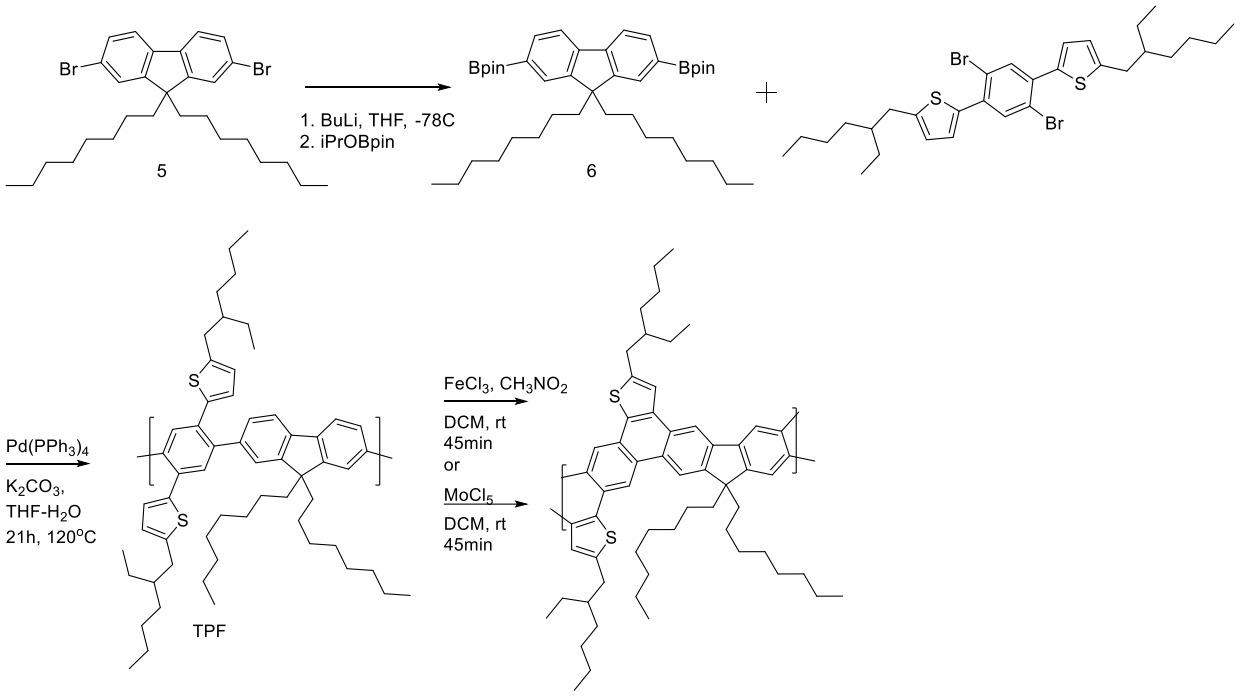

Synthesis of PPF begins with 4-iodobromobenzene which we coupled with ethylhexyl magnesium bromide and then exchanged bromine for Bpin with butyl lithium and isopropoxy pinacol ester of boronic acid. Cross-coupling with dibromodiiodobenzene gives dibromomonomer. For polymerization we used the same conditions as with TPF, however reaction had to be run longer to achieve similar molecular weight, because of greater steric hindrance of benzene rings compared to thiophenes.

Scheme 4-4. Synthesis of PPF

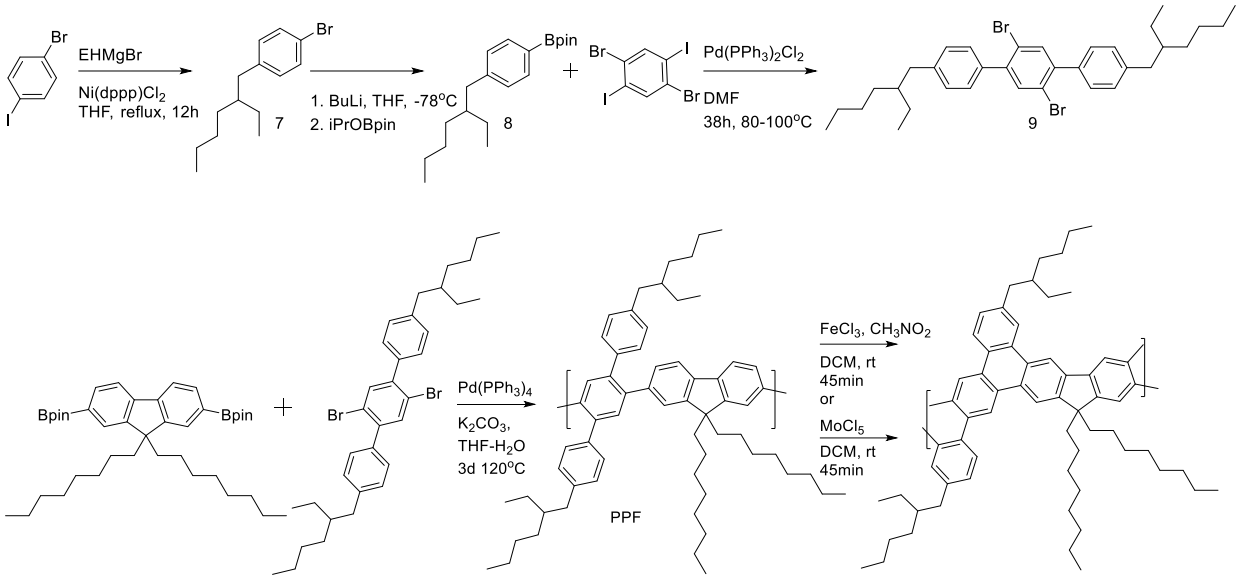

It is important to note that oxidation reactions have to be done under great dilution conditions with polymer concentration less than 0.1 g/L. Otherwise cross-linking of polymer chains occurs and the resulting materials are insoluble in organic solvents, like DCM, chloroform, toluene, chlorobenzene, nitrobenzene, DMF, trichloroethylene, THF, hexanes, methanol.

TPTF was synthesized by Stille polycondensation of previously described monomers with $Pd(PPh_3)_4$ catalyst in toluene-DMF mixed solvent.

Scheme 4-5. Synthesis of TPTF

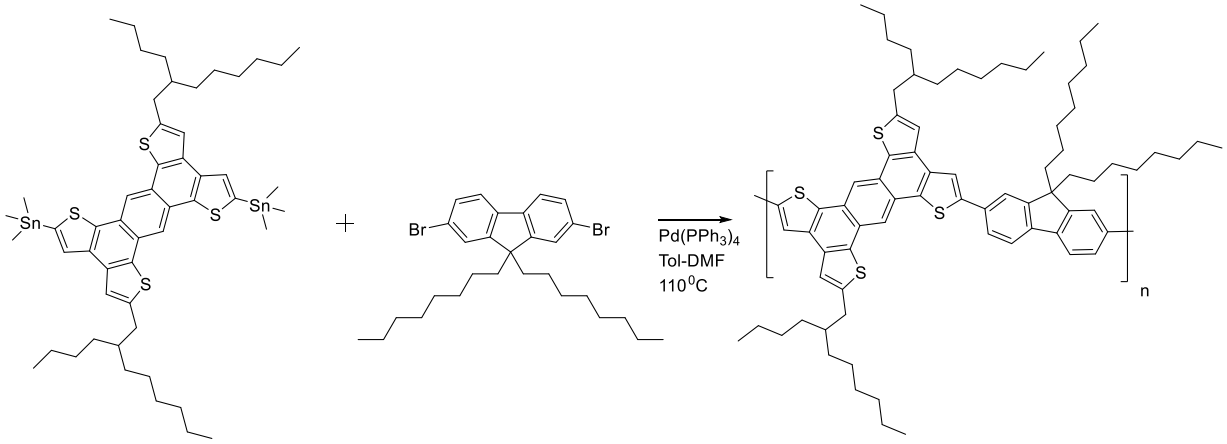

Due to solubility issues of completely cyclized ladder polymers it is impossible to prove the degree of cyclization with conventional methods, for example NMR. Due to this we compared IR spectra of these materials before and after chemical cyclization. For 3 studied systems C-H (aromatic) peaks in 3050-3000 cm^{-1} region underwent dramatic shift and reduction in intensity up to disappearing into the baseline after oxidation.

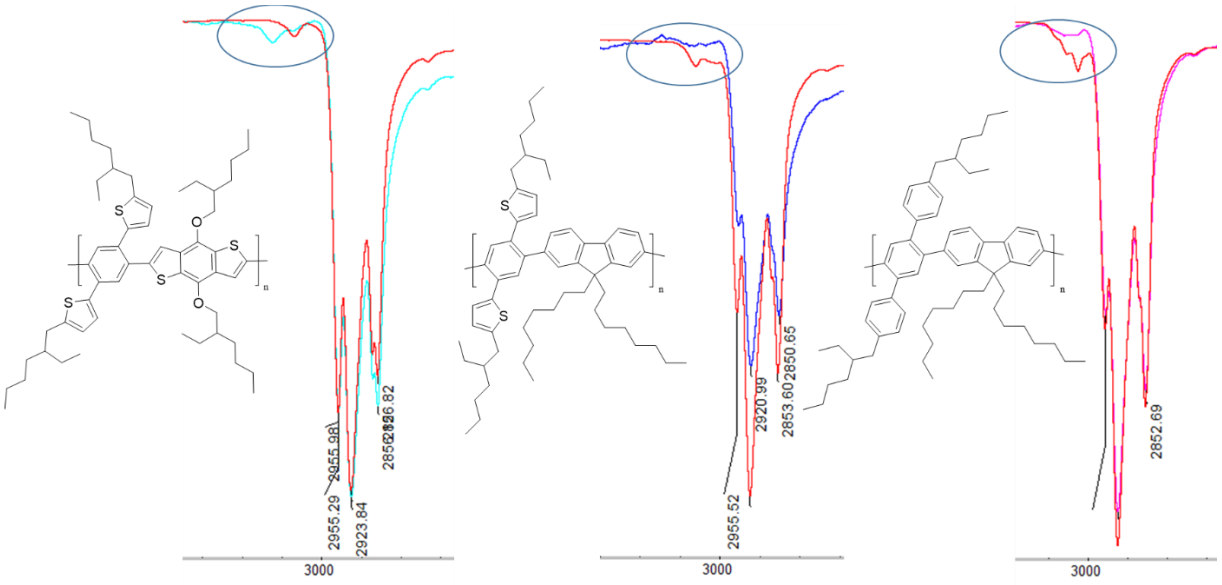

Figure 4-1. IR spectra before (red) and after (colored) cyclization of TPB, TPF and PPF

Table 4-1. Summary of properties of precursor polymers

Twisted	HOMO	LUMO	Eg,opt	Eg, el	QY	Mw	Mn	PDI
TPB	-5.46eV	-3.43eV	2.62eV	2.03eV	10.8%	63.9kDa	27.8kDa	2.3
TPF	-5.86eV	*	3.2eV	*	19.5%	99.7kDa	40.8kDa	2.44
PPF	-5.94eV	*	3.2eV	*	80.5%	51.5kDa	17.8kDa	2.9

*no reduction peak in CV.

4.2.2 DFT results for ladder polymers

DFT calculations at B3LYP level of theory using 6-31G** basis set for TPB-C predict a 17° twist for a trimer from end to end, indicating an effective conjugation. HOMO orbital has a greater contribution from electron-rich sulfurs and also from side thiophenes, whereas LUMO is more localized on the central carbon backbone. Interestingly length of chromophore encompasses only about 2 repeating units without extending further which explains blue emission despite overall large conjugation system of ladder polymer. DFT calculation also predicted TPB-C with HOMO -4.93 eV, LUMO -2.13 eV and bandgap 2.80eV.

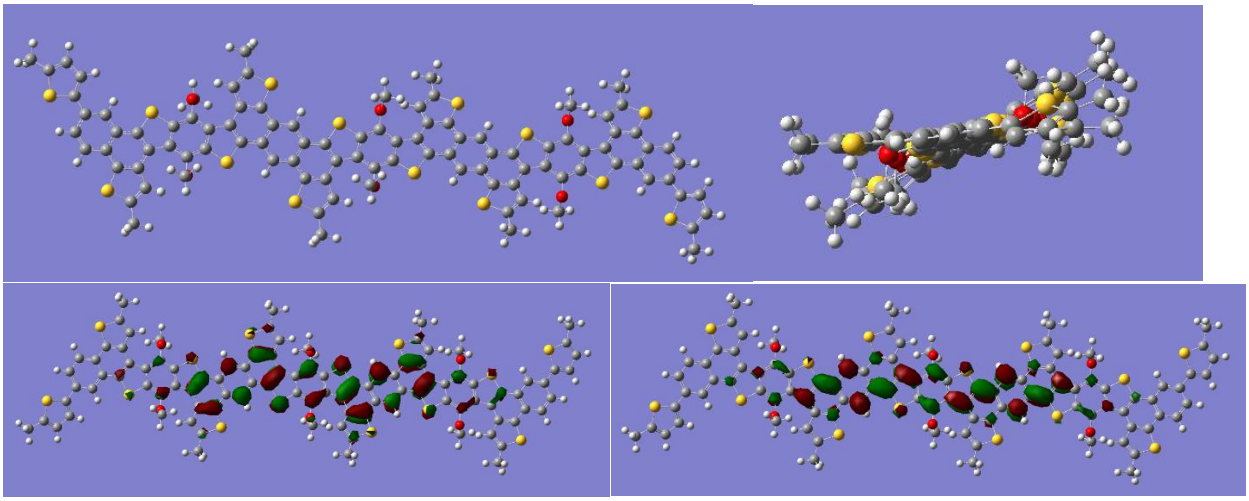

Figure 4-2. DFT results on conformation of trimer of TPB-c and HOMO/LUMO

DFT calculations on TPF-cF trimer predict a planar structure. Both HOMO and LUMO are localized to 2 repeating units. HOMO has contribution from side thiophenes, while LUMO is more extended along the polymer chain. Because frontier orbitals don't extend to the edges of calculated trimer we can expect short length of chromophore in ladder polymer as well, as manifested in blue absorption and emission. DFT results indicated a HOMO -5.09eV, LUMO -1.79eV and bandgap 3.30eV.

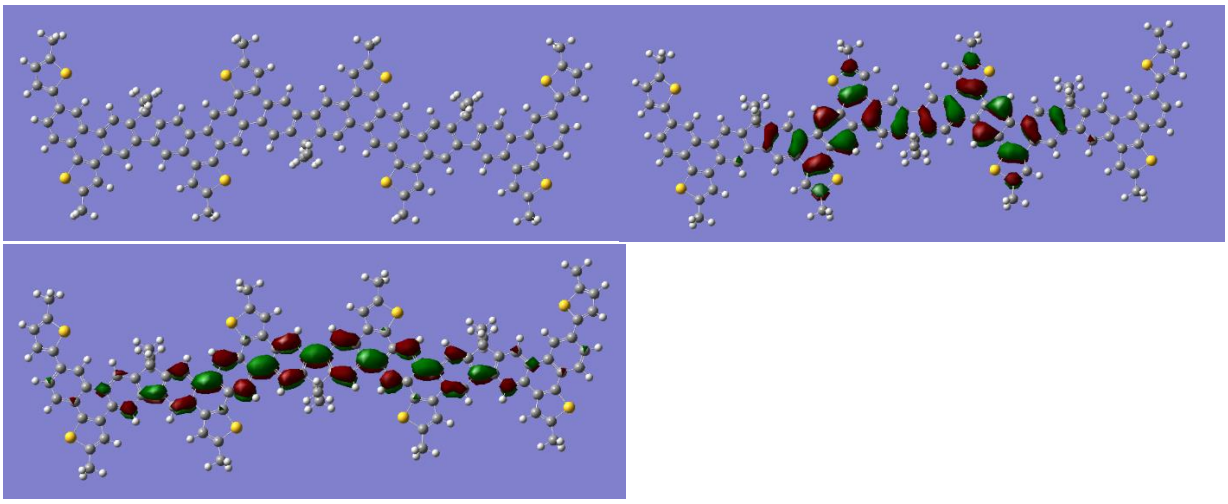

Figure 4-3. DFT results on conformation of trimer of TPF-cF and HOMO/LUMO

DFT calculations also predict PPF-CF a planar structure. Unlike thiophene containing trimers all-carbon oligomer has much more delocalized HOMO and has virtually no contribution from fused side rings. As a result HOMO and LUMO overlap to a great extent, which explains higher quantum yield of PPF-CF, since rate of relaxation of electron from LUMO to HOMO increases. DFT calculations predicted HOMO -5.08eV, LUMO -1.73eV, bandgap 3.35eV.

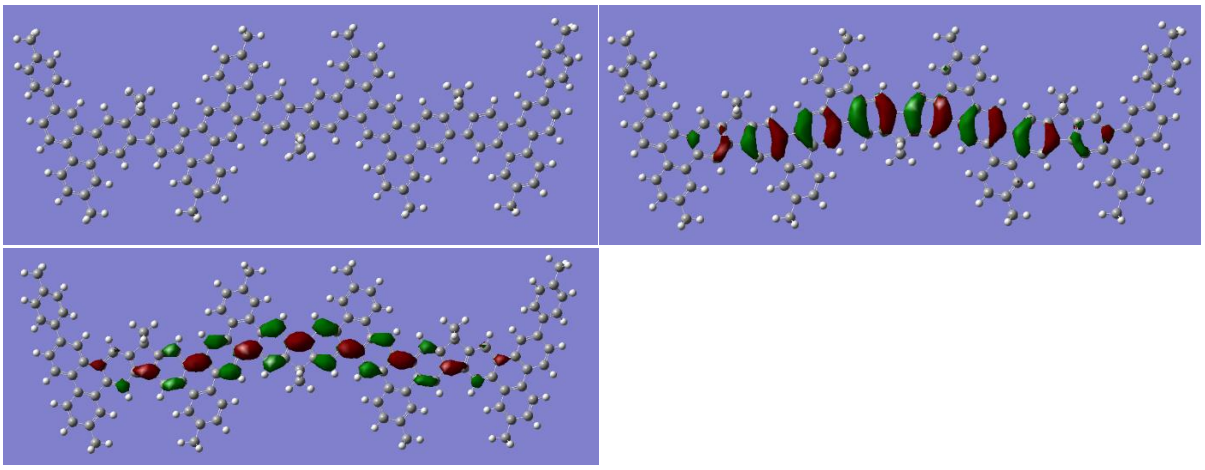

Figure 4-4. DFT results on conformation of trimer of PPF-cF and HOMO/LUMO

4.2.3 Optical properties

UV/vis absorption spectra indicate that non-cyclized polymer TPB exhibits 3 major peaks at 296, 319 and 407 nm, while cyclized polymer shows a peak at 299nm and 2 other peaks significantly red-shifted to 401nm and 506nm.

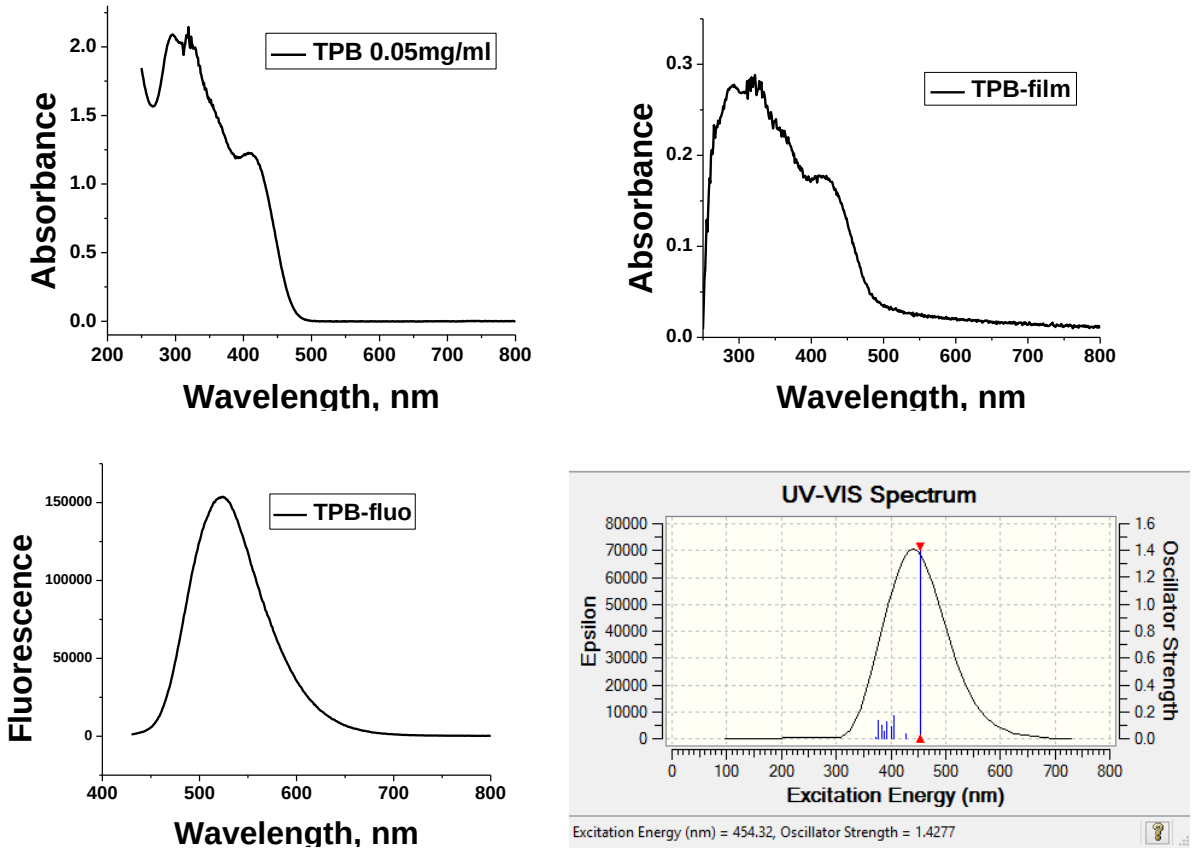

Figure 4-5. UV-vis spectra of TPB in solution and film. Fluorescence spectrum and TDDFT predicted UV-vis spectrum.

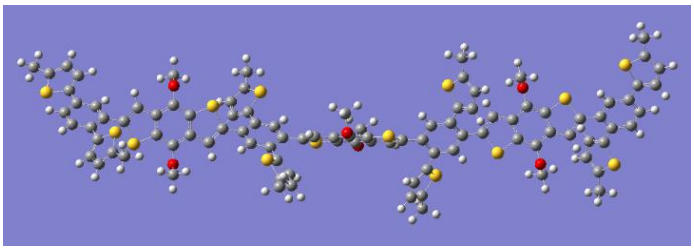

Figure 4-6. DFT predicted conformation of TPB

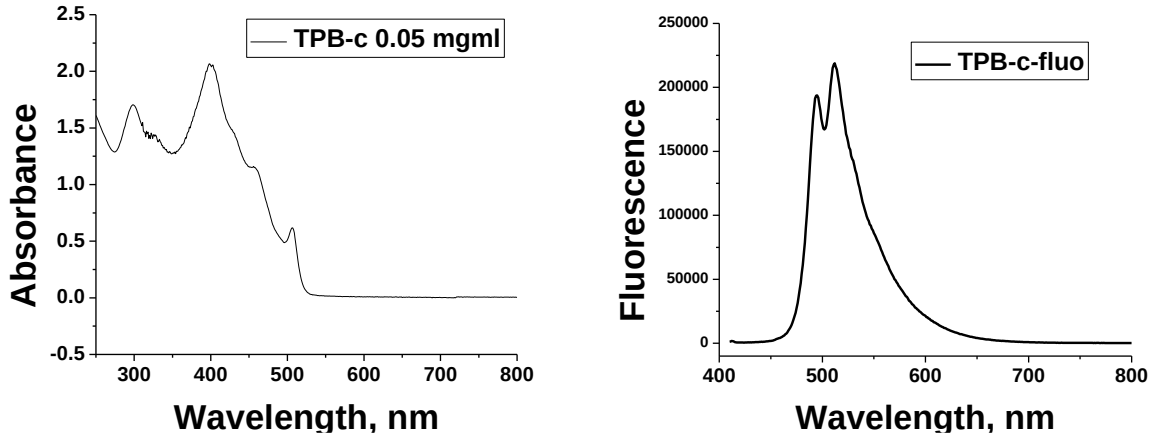

Figure 4-7. UV-vis and fluorescence spectra of TPB-c.

This shift is expected from planarization and greater conjugation. The changes in UV-vis and fluorescence spectra before and after oxidation indicate that ring fusion has occurred. Most red-shifted peak in TPB corresponds to HOMO-LUMO transition. DFT calculations indicate that the peak should be centered at 454nm which agrees reasonably well with peak at 407nm and onset at 470nm. Peaks deeper in the UV region originate from many transitions between, for example HOMO-2-LUMO and so on, and their combined oscillator strength exceeds the oscillator strength of a single HOMO-LUMO transition. That's why 296 and 319nm peaks are more intense than 407nm. DFT calculations for ladder polymer predict transitions at 505, 448 and 409 nm, very close to observed 507, 455 and 401nm. Interestingly theoretical predictions also work very well for relative intensity of the peaks with oscillator strength of transitions decreasing with increasing wavelength. Although calculations were done for 3 repeating units, this nearly exact match is an irrefutable evidence for complete cyclization. UV-vis spectra of both polymers do not show any shifts with concentration, however peaks in the spectrum of the film of TPB exhibit ca. 20 nm red shift presumably due to π-π stacking.

Another notable feature is that fluorescence spectrum of non-cyclized polymer displays a single peak at 522nm, whereas after cyclization there are 2 peaks at 495nm and 511nm similar to model ladder molecules synthesized and characterized by us before. It was found that cyclization doesn't lead to increased quantum yield of fluorescence. Polymer TPB exhibits QY 11%, and after ring fusion it is 8.3%. We think this is mainly due to sulfur atoms exhibiting heavy atom effect and greater interactions with solvent for the ladder structure, which allows for non-radiative relaxation.

In polymer TPF, the benzodithiophene is replaced with fluorine. The absorbtion spectrum of non-cyclized polymer blue-shifts and we have only one peak at 326 nm and an onset at 386 nm, which corresponds to optical bandgap of 3.2eV. Similar change occurs with fluorescence spectrum as well with fluorescence maximum blue-shifted to 434nm. DFT calculations predict a highly twisted structure for TPF, so that conjugation between monomer units must be very small. Wide peak at 326 nm with shoulders on both sides is comprised of many transitions from deeper occupied molecular orbitals to higher unoccupied molecular orbitals as predicted by TDDFT. Most red-shifted transition is predicted to be at 380 nm, which is very close to the observed onset and corresponds to HOMO-LUMO transition. Smaller number of sulfur atoms per repeating unit

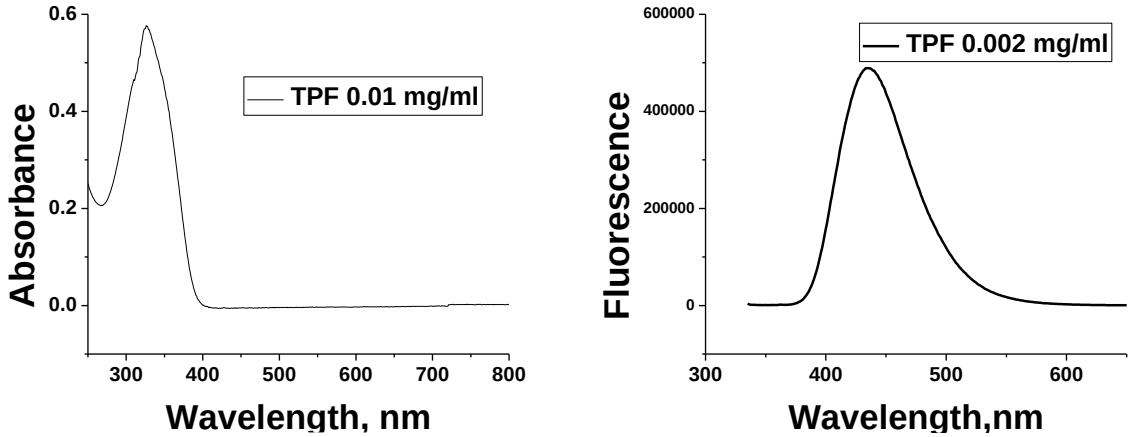

Figure 4-8. UV-vis and fluorescence spectra of TPF.

improves quantum yield of fluorescence to the value of 19.5% which is almost double that of TPB.

Cyclization of TPF predictably red-shifts absorption and fluorescence spectra, but also creates finer vibronic progression in absorption spectrum. TPF-CF has absorption peaks at 368nm, 390nm, 407nm, 435nm. These results match very well with time dependent DFT predictions of peaks at 422nm, which corresponds primarily to transition from HOMO-2 to LUMO, and 392nm, which corresponds to transition from HOMO to LUMO+2. Again the good match between predicted and observed wavelengths and also between relative peak intensity and oscillator strengths of transitions confirm that obtained material is indeed a ladder polymer. Fluorescence spectrum also has vibronic peaks with maxima at 438nm, 472nm and 482nm, which is significantly red-shifted from the precursor polymer TPF. After cyclization quantum yield of fluorescence significantly decreases to 7.4% if excited at 368nm, at 390nm excitation it is 8.5%, 8.6% at 407nm, and 8.5% at 435nm.

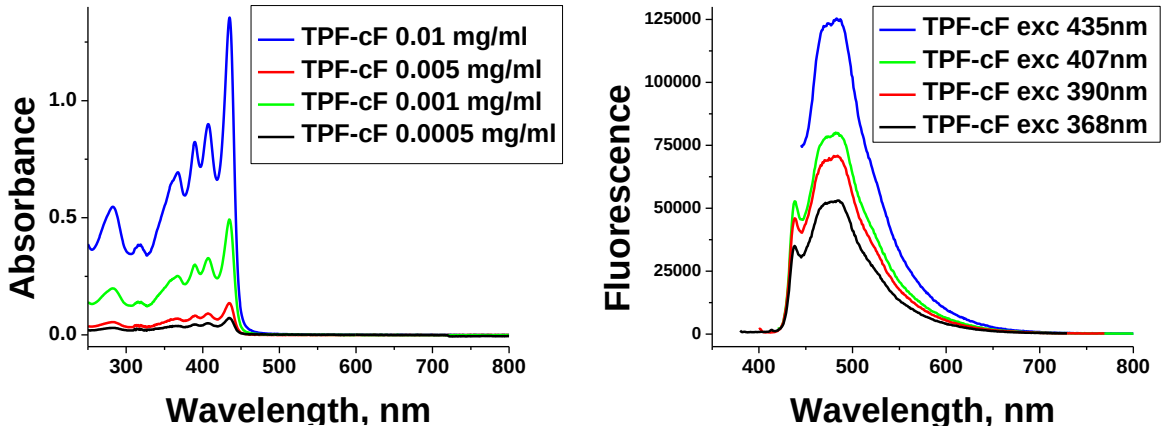

Figure 4-9. UV-vis and fluorescence spectra of TPF-cF.

Polymer TPF-CM was much less soluble in organic solvents and we had to take its spectrum in chlorobenzene instead of chloroform. Despite solvent change, absorption peaks exhibit very little shift from those of TPF-CF: peaks are at 360nm, 389nm, 408nm and 435nm.

Large peak at 286 nm probably corresponds to chlorobenzene interactions with polymer chain. Another evidence for strong solvation is that fluorescence of the polymer is completely quenched.

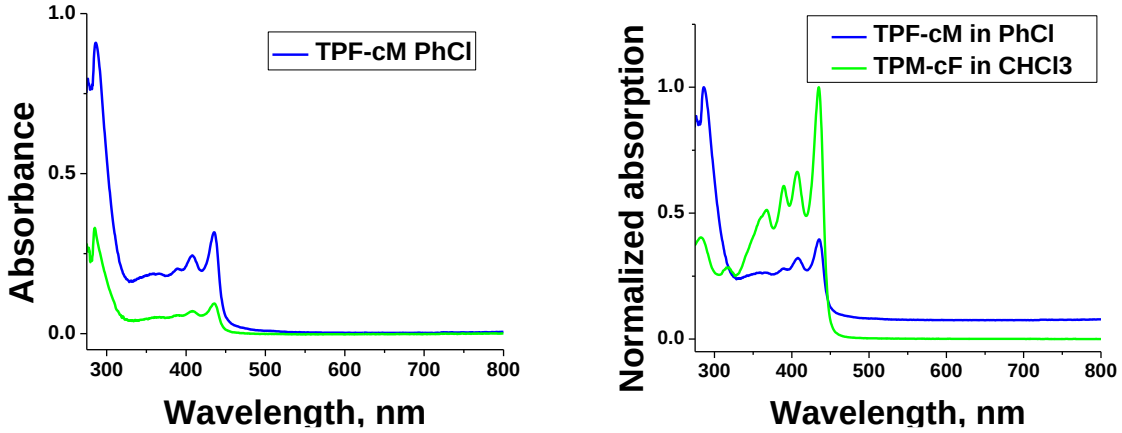

Figure 4-10. UV-vis and fluorescence spectra of TPF-cM.

Semiladder polymer TPTF has peaks at 337nm, 355nm, 399nm, 450nm, 481nm and onset at 505nm, which corresponds to optical bandgap of 2.46eV. This material like other ladder polymers also has 2 major peaks in fluorescence spectrum (480nm, 497nm). Its quantum yield of fluorescence is 42%. This semiladder polymer also has a well-defined vibronic progression in absorption and fluorescence spectra.

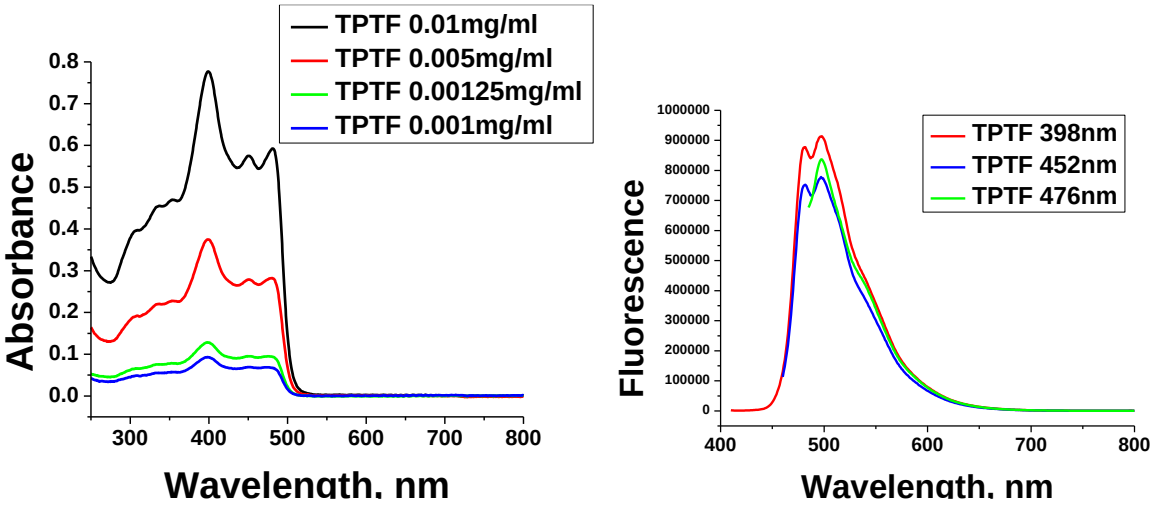

Figure 4-11. UV-vis and fluorescence spectra of TPTF.

PPF displays two major peaks in the absorption spectra at 283and 349nm with onset at 386 nm. This corresponds to optical bandgap of 3.2eV, the same as for TPF, which further corroborates individual fluorene as main chromophore.

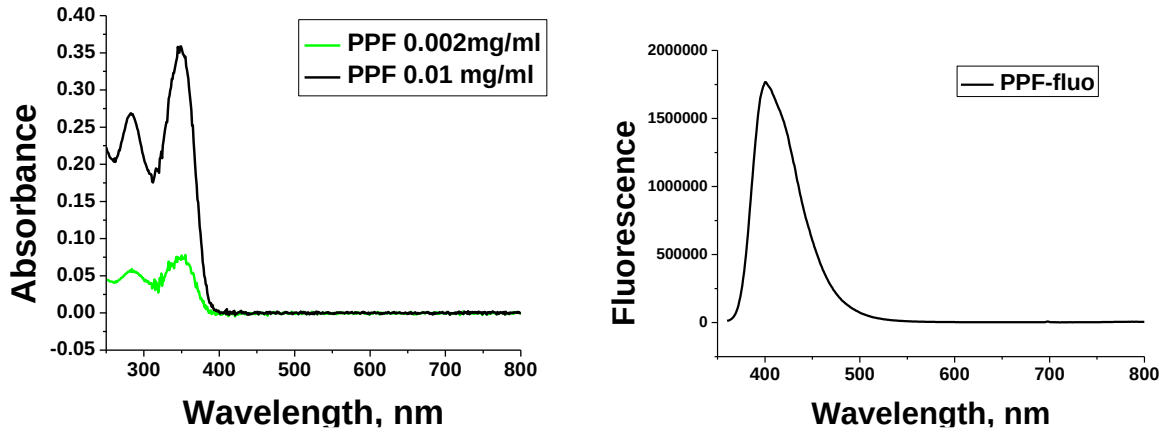

Figure 4-12. UV-vis and fluorescence spectra of PPF.

DFT results for PPF predict a highly twisted structure. TD DFT predicts a HOMO-LUMO transition at 367nm, which is right in between of observed largest peak at 349nm and onset at 386nm. Just like TPF fluorescence spectrum has only one peak at 401nm which further confirms fluorene as emitting unit. Quantum yield however is significantly increased to 80%. It is due to the absence of thiophenes in PPF structure.

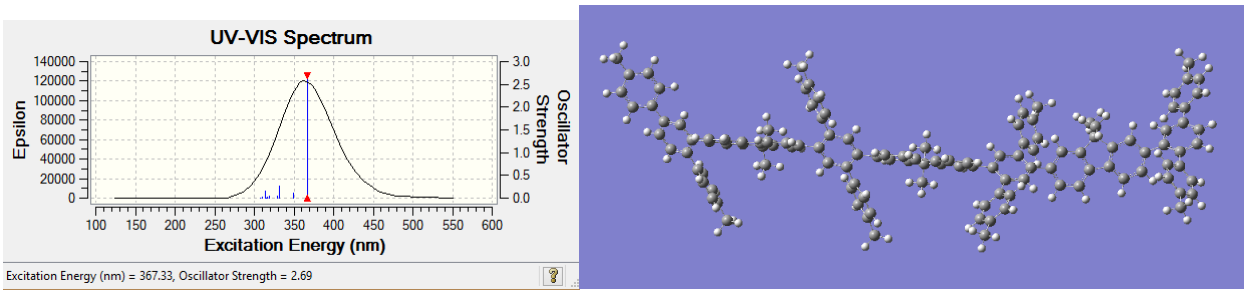

Figure 4-13. Predicted UV-vis spectrum and conformation of PPF.

Cyclized polymer PPF-CM exhibits major absorption peaks at 315nm, 345nm, 404nm and 431nm with clearly vibronic pattern similar to previous ladder polymers. TD DFT predicts

HOMO-LUMO transition at 425nm and transition at 355nm comprising of HOMO-LUMO+2 and HOMO-1-LUMO+1. Fluorescence spectrum also shows vibronic structure with main peaks at 434nm and 463 nm. Both absorption and fluorescence spectra are red-shifted compared with noncyclized PPF as expected due to planarization and greater conjugation. However, cyclization lead to polymers quantum yield of fluorescence decreases nearly twofold to 38.9% exciting at 404nm and 32.1% at 431nm.

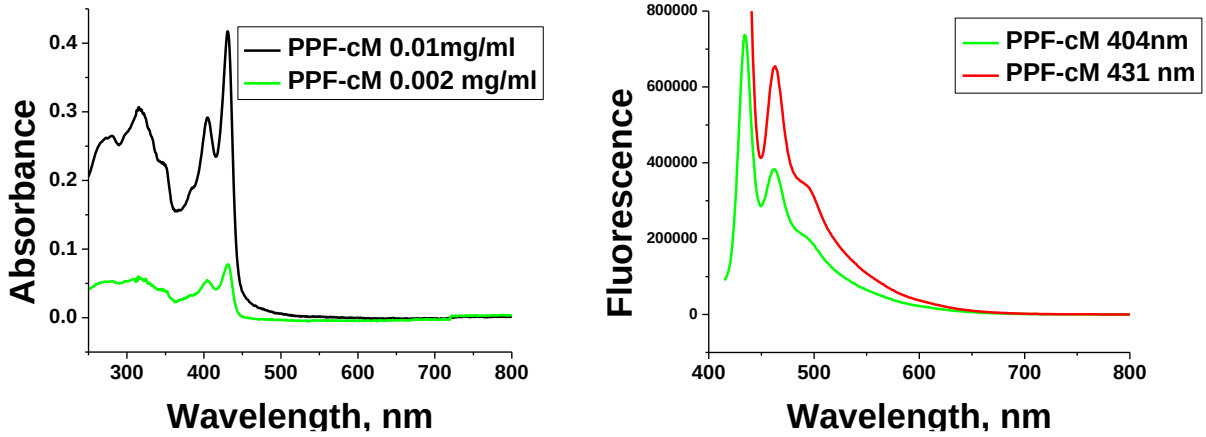

Figure 4-14. UV-vis and fluorescence spectra of PPF-cM.

It was observed that PPF can be electrochemically cyclized, leading to the same ladder polymer. The resulting materials exhibited identical absorption and fluorescence spectra with those obtained by chemical oxidation: CV obtained sample has absorption maxima at 403nm, 430nm and fluorescence peaks at 433nm, 460 nm. However the quantum yields of this cyclized polymers are higher: 55% (excited at 364nm), 72.1% (404nm) 54.9% (431nm).

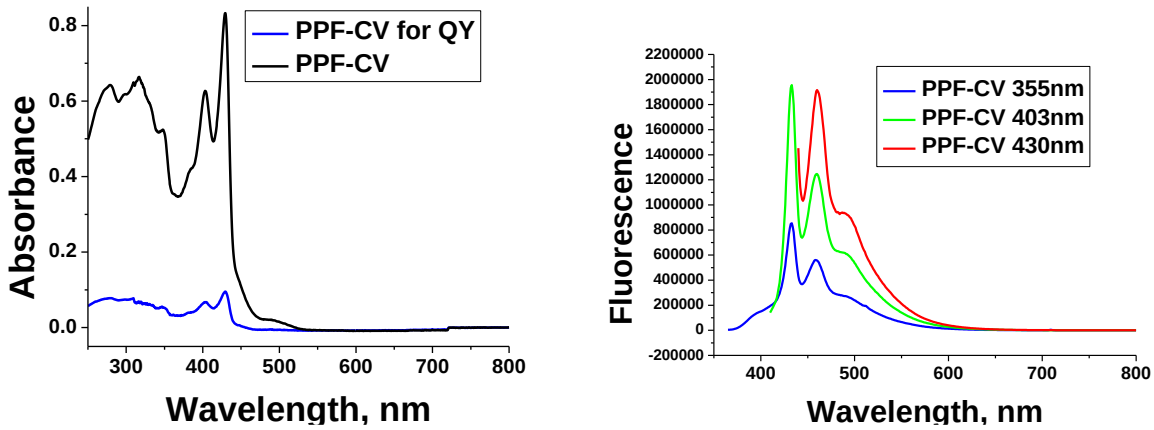

Figure 4-15. UV-vis and fluorescence spectra of electrochemically oxidized PPF.

Synthesized materials are not perfect ladder structures and must have non-cyclized defects. Comparing the spectra we can see that after-CV sample's spectrum is 1-2 nm blue shifted compared to PPF-cM. It must contain more of non-cyclized defects in its structure.

PPF-cF according to NMR estimate is cyclized to about 25%. Its absorption spectrum shows peaks at 350nm, 360nm, 375nm and fluorescence spectrum shows peaks at 411nm and 432nm. These values are between noncyclized and cyclized polymers, which is expected from partial cyclization. TDDFT calculations on trimers with different degrees of cyclization agree with these results.

This semi-ladder polymer has the highest quantum yield among synthesized materials: 350nm 82%, 355nm 91%, 360nm 91%, 375nm 75%.

Quantum yield of 91% is achieved due to planar fragments reducing vibrational modes of non-radiative decay of excited state, while twisted structures of non-cyclized units prevent quenching through interactions with other molecules and other polymer chains fragments.

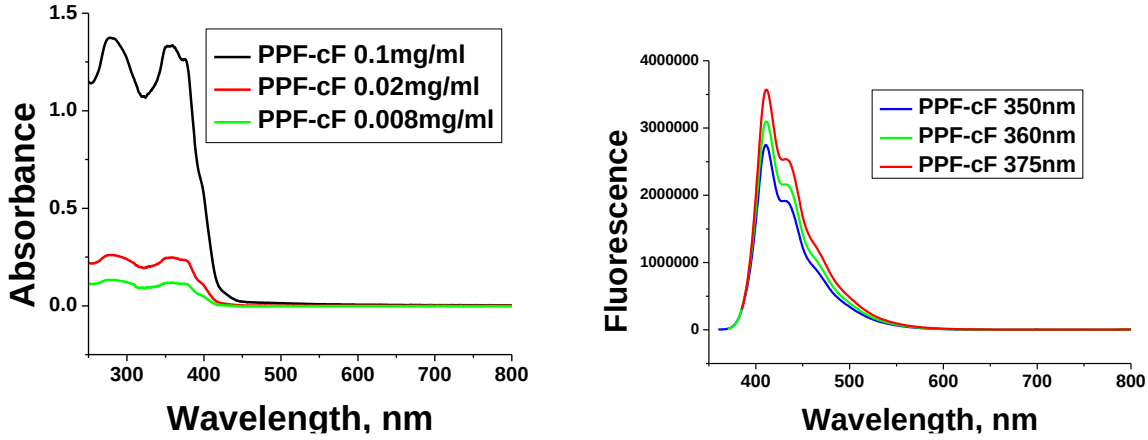

Figure 4-16. UV-vis and fluorescence spectra of PPF-cF.

Comparing experimental spectra of PPF cyclized by different methods reveals that $MoCl_5$ and electrochemical oxidation give polymer with nearly identical spectral properties. Their absorption spectra match very well with the spectrum predicted by TDDFT calculations for the completely planar ladder trimer: 2 major transitions with more intense red-shifted peak. Peaks do not match precisely, because trimer has shorter conjugation length than actual polymer and therefore must have blue shifted absorption and fluorescence maxima. Milder oxidation with $FeCl_3$

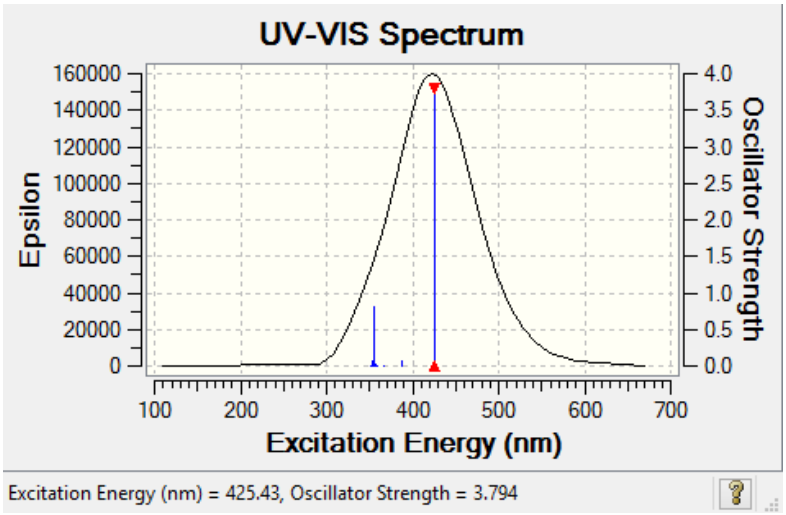

Figure 4-17. TDDFT predicted UV-vis spectrum of and fluorescence spectra of PPF-CM.

yields a material with peaks in between of non-cyclized and fully cyclized structures confirming semiladder character of this material.

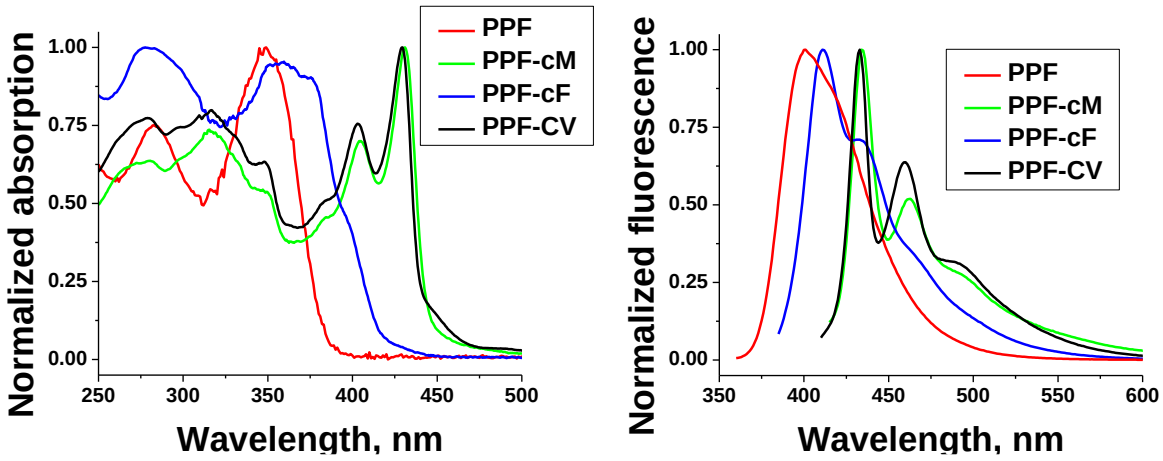

Figure 4-18. Comparison of different methods to cyclize PPF.

4.2.4 OLET properties

Synthesized materials were studied for OLET performance in trilayer architecture with PFN as electron-transporting layer and DPP-DTT as hole transporting layer. The B doped Si wafer was used as gate electrode, on which SiN_x layer modified with OTS acts as dielectric layer. The gold electrodes are used as drain and source.

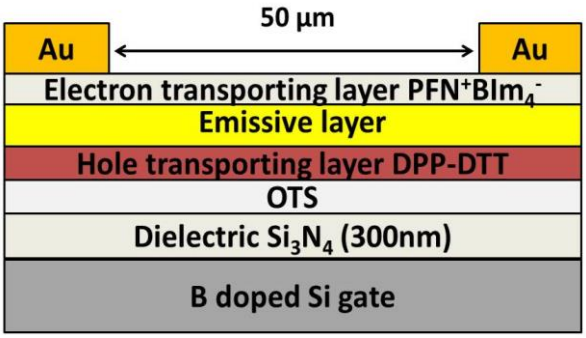

Figure 4-19. General device architecture.

Saturation in output curves at negative voltages shows FET behavior for TPB under hole transporting conditions, hole mobility is 0.0322 $cm^2\ V^{-1}\ s^{-1}$. Under positive voltages at low gate voltages current shows SCLC behavior without saturation meaning that current passes through the surface between electrodes. At 40V and higher gate voltage FET behavior is observed, however source-drain current is order of magnitude lower reflecting lower electron mobility of this material, 0.0166 $cm^2\ V^{-1}\ s^{-1}$. Green emission is consistent with fluorescence spectra.

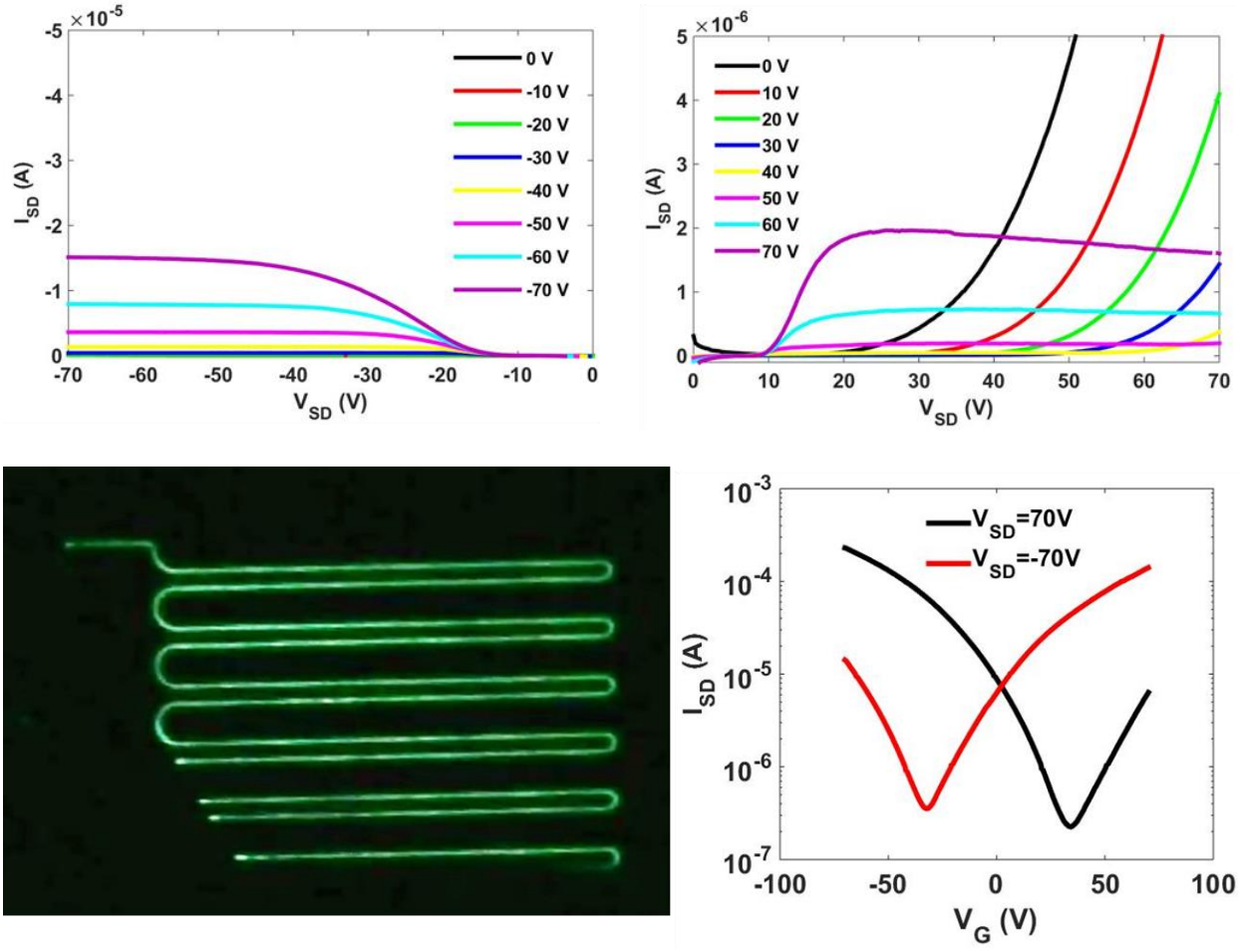

Figure 4-20. OLET device of TPB with $PFN^+BIm_4^-$.

TPF showed similar electronic properties with hole transport being a magnitude higher than electron transport, however there is no light emission in OLET device. This can be explained by

very high LUMO energy level, hole mobility is 0.0416 $cm^2\ V^{-1}\ s^{-1}$, electron mobility is 0.057 $cm^2\ V^{-1}\ s^{-1}$.

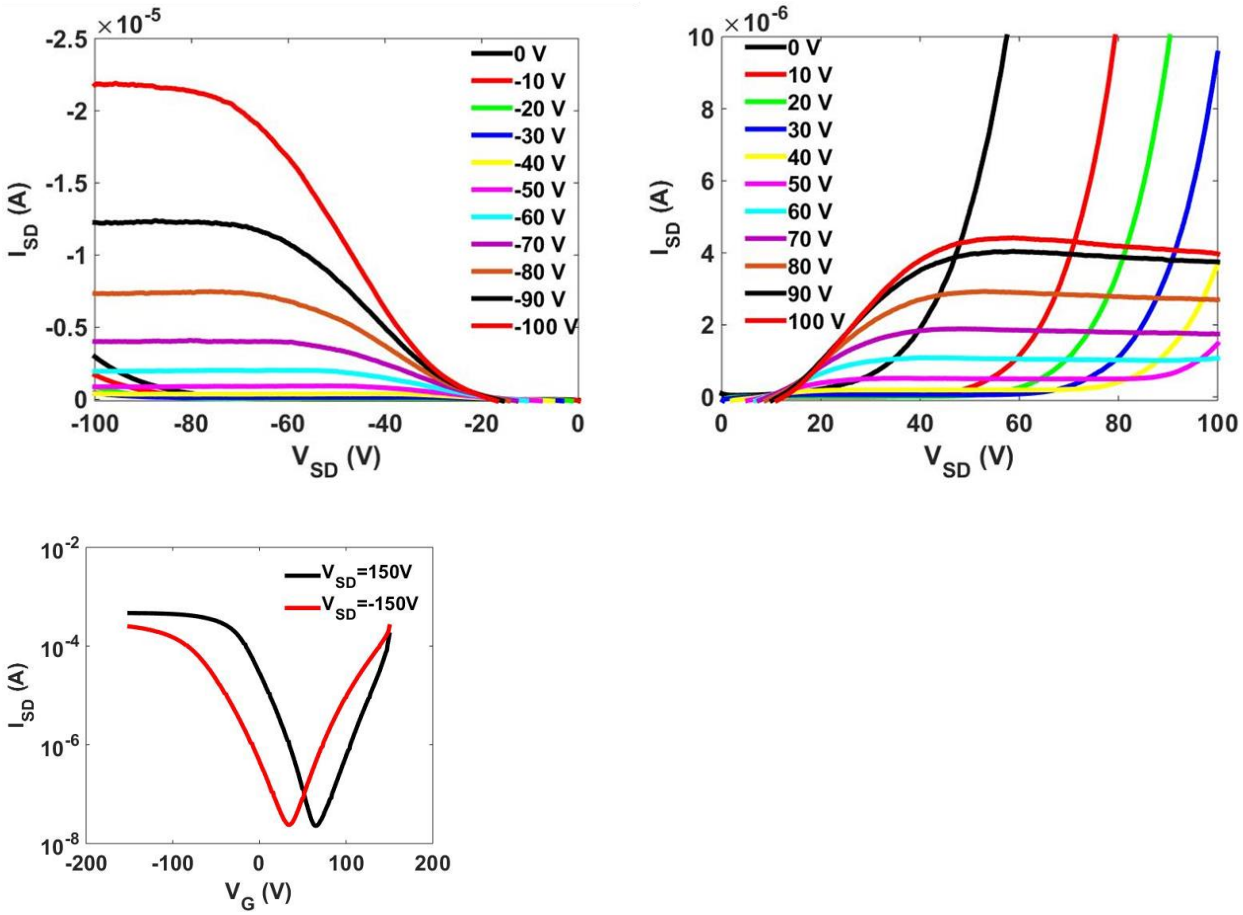

Figure 4-21. Transistor properties of TPF

PPF shows light emission due to more balanced hole and electron transport: hole mobility 0.052 $cm^2\ V^{-1}\ s^{-1}$, electron mobility 0.054 $cm^2\ V^{-1}\ s^{-1}$. Close values for different charge carrier mobilities help center the recombination zone to the middle of the channel and improve light emission compared to TPF. Current saturation for both holes and electrons is observed at -70V and 70V respectively.

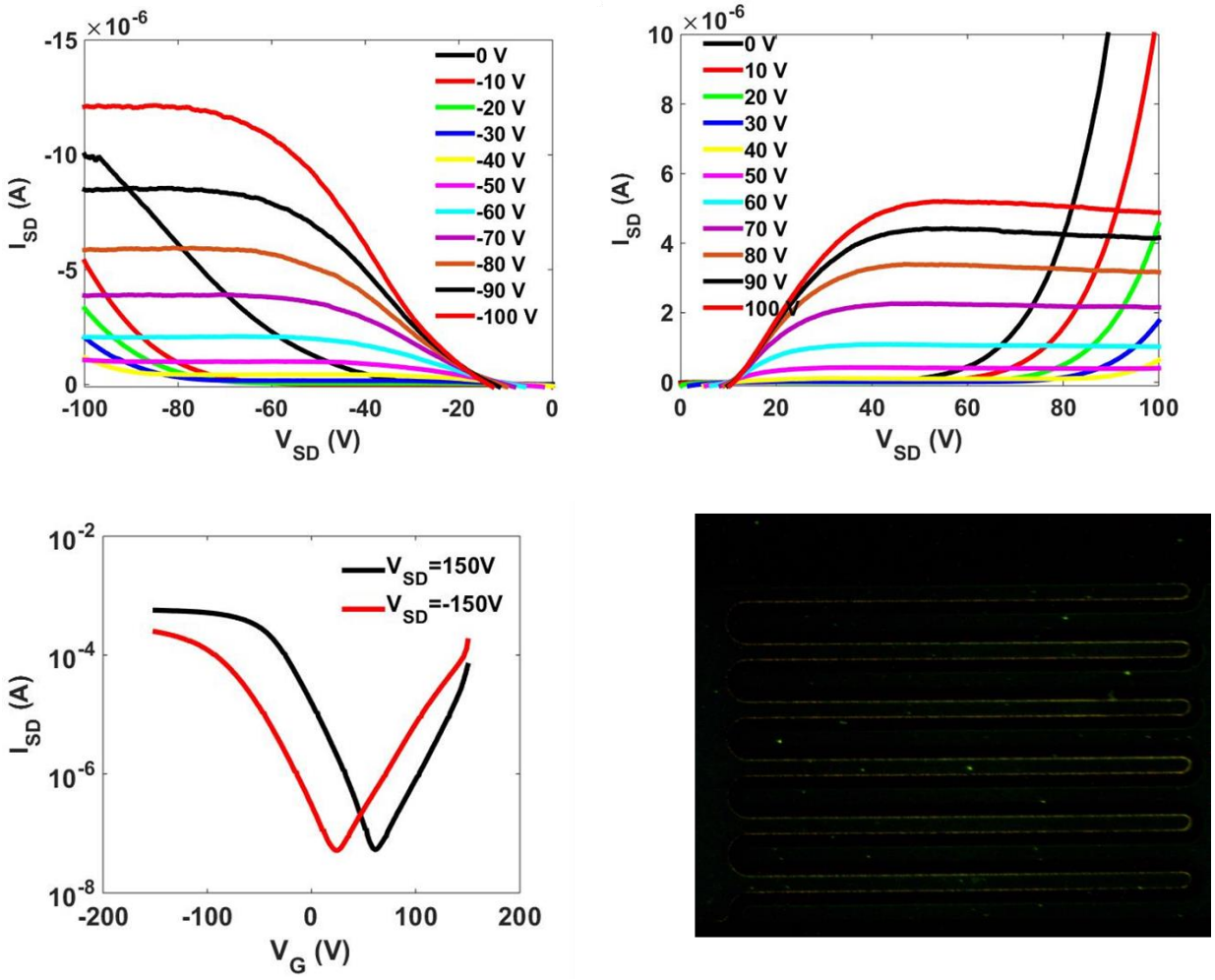

Figure 4-22. OLET performance of PPF

TPTF has hole mobility 0.0014 $cm^2\ V^{-1}\ s^{-1}$ and electron mobility 0.0095 $cm^2\ V^{-1}\ s^{-1}$. Despite these lower mobility values this material shows slightly better light emission due to larger chromophore fragment in the polymer structure.

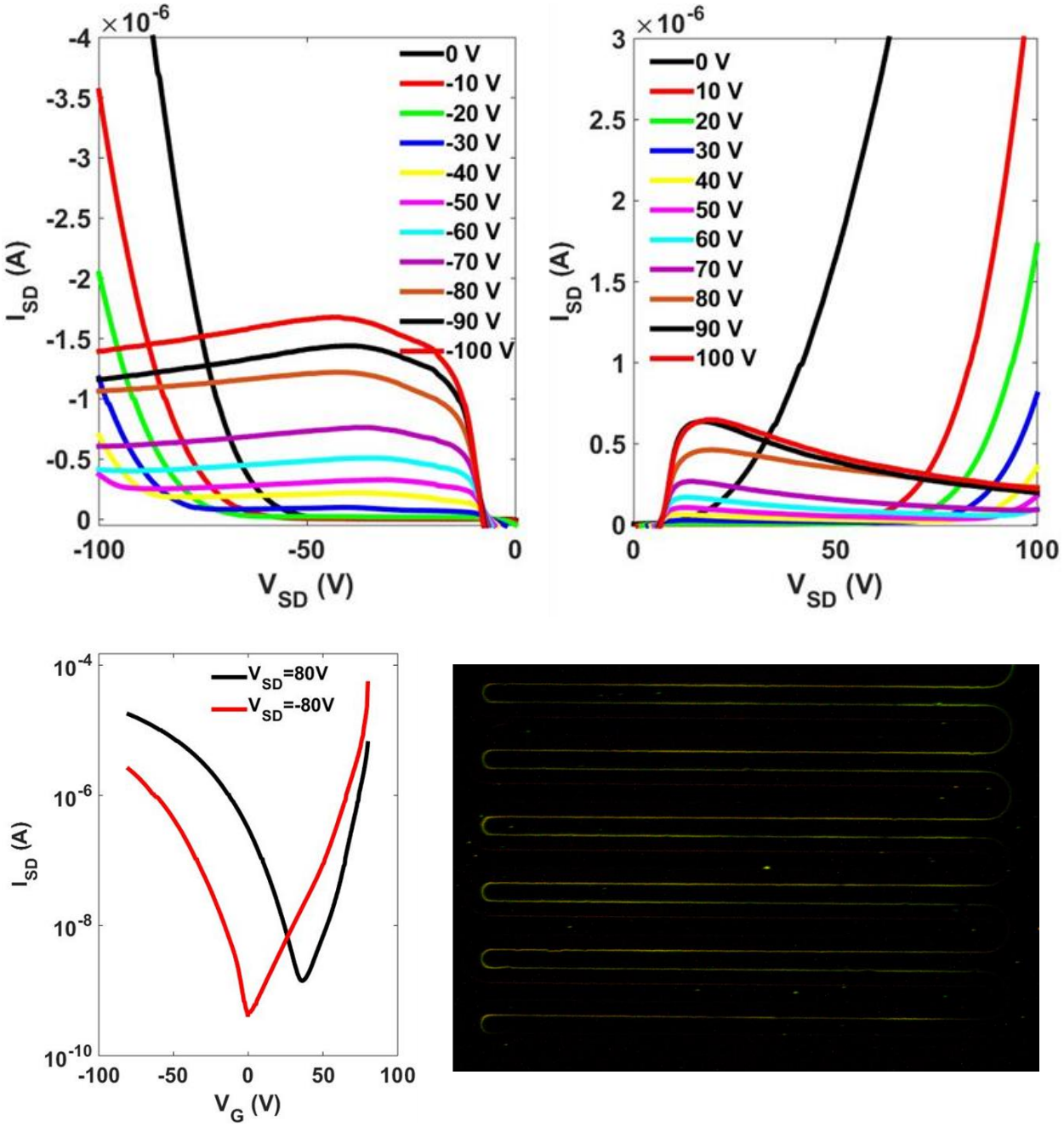

Figure 4-23. OLET properties of TPTF

PPF-CF is a predominantly a hole-transporting material: saturation behavior is observed from lowest gate voltage. For electron transport only at 100V gate voltage SCLC behavior switches to FET. Transfer graphs still show ambipolar V-shaped curves, consistent with hole mobility 0.0738 $cm^2 V^{-1} s^{-1}$ and electron mobility 0.0256 $cm^2 V^{-1} s^{-1}$. This high hole mobility, higher than

for other studied polymers, combined with largest quantum yield of fluorescence help explain why this material afforded brightest emission in OLET device. Blue emission is expected from fluorescence spectra and lack of donor-acceptor moieties in polymer structure.

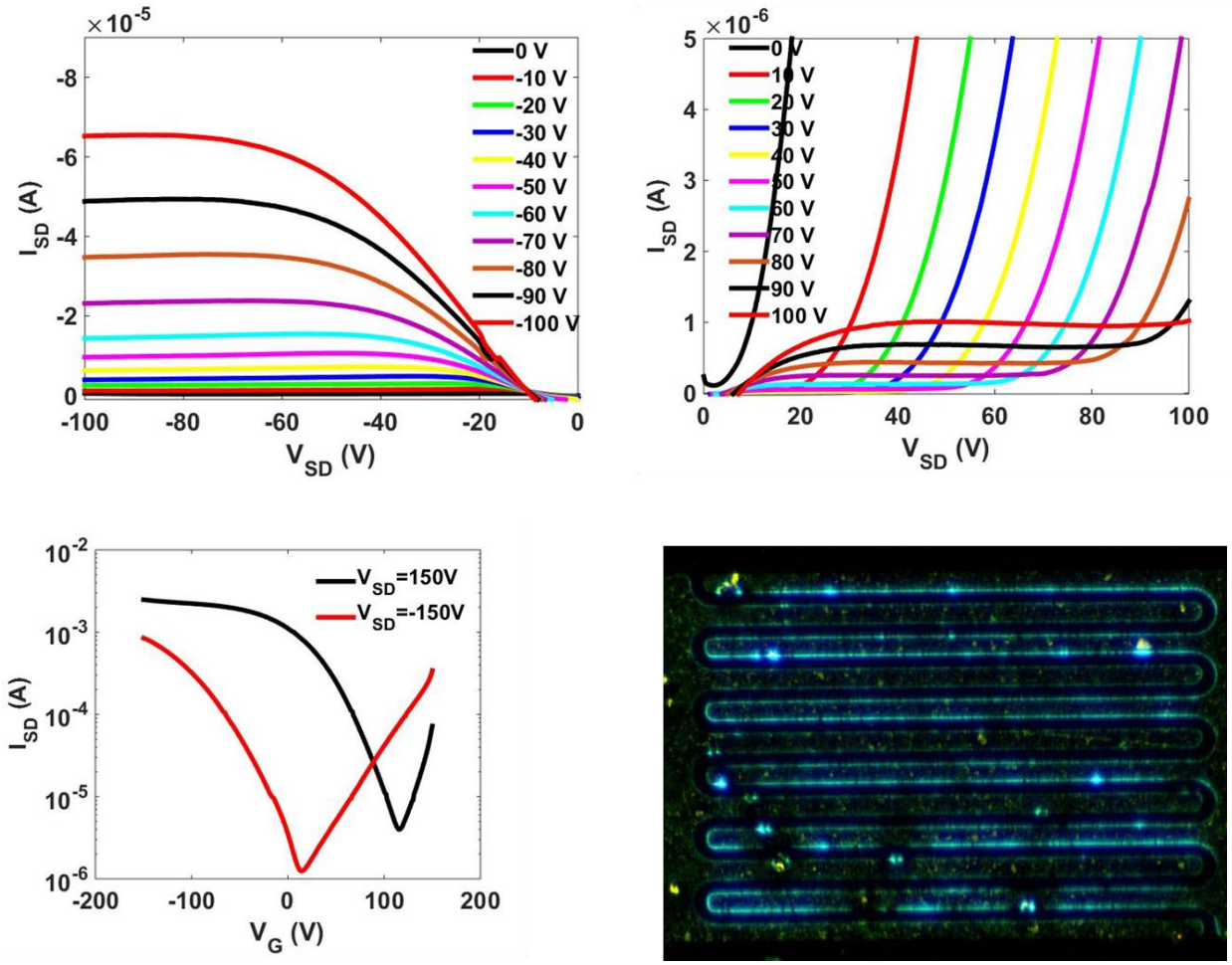

Figure 4-24. OLET performance of PPF-cF

4.3 Conclusions

We have synthesized a series of non-cyclized and cyclized ladder polymers. Electron-rich thiophene units provide easiest cyclization to get ladder structures, however provide lower quantum yields. Going from thiophene to all-carbon chromophores allows not only to increase

quantum yields of corresponding non-cyclized or ladder polymers but also to synthesize partially cyclized material. Resulting semiladder polymer has very high quantum yield of fluorescence and is a promising material for OLET application.

In non-cyclized polymers series TPF and PPF have the same optical bandgaps, however TPB has a smaller bandgap due to greater planarity and donor nature of BDT compared to fluorene. In fluorescence spectra red shift trend PPF-TPF-TPB clearly correlates with increasing the number of thiophene rings in the structure which reflects greater coplanarity and conjugation.

This trend repeats among fully cyclized polymers. For example, in a series PPF-cM-TPF-cM-TPB-c fluorescence peaks red shift 20-30nm.

As expected, cyclization red-shifts both absorption and fluorescence spectra for every polymer studied.

Electrochemical oxidation affords nearly the same materials as chemical oxidation by strong oxidant $MoCl_5$. This result is crucial because former proceeds in thin film, while the latter in solution. The match between optical properties of two materials means that degree of cyclization during solution oxidation is not limited by solubility of cyclized polymer.

Finally, we have found that semiladder structure is best in terms of light emission performance due to balance between charge transport and quenching of luminescence in solid state due to π-π interactions. Additionally, better solubility allows solution processing for these materials, while fully cyclized materials had insufficient solubility to afford good quality thin films. Semiladder polymer TPTF synthesized by polymerizing ladder-type monomer exhibited higher quantum yield of fluorescence (42%) than either of comparable materials with thiophene rings (8.3-19.5%). PPF-CF made by partial oxidative cyclization also exhibited higher quantum yield of fluorescence (91%), than either twisted or fully planar counterparts (32-80%).

4.4 Experimental section

Unless otherwise stated, all chemicals obtained from commercial suppliers were used without further purification. THF was distilled over sodium prior to use, toluene was passed through MBraun solvent purification system. Other solvents were purified by distillation prior to use. ^{1}H and ^{13}C NMR were recorded by using 400MHz Bruker DRX-400 or Bruker Avance II+ 500 MHz spectrometers. Mass spectra were obtained on Agilent 6224 Tof High Resolution Accurate Mass Spec (HRA-MS) system. Column chromatography was carried out on silica gel (silica 60M, 400-230 mesh). Optical properties were measured by using a Shimadzu UV-2401PC UV-Vis spectrophotometer. Molecular weights of polymers were determined by using GPC with a Waters Associates liquid chromatography equipped with a Waters 510 HPLC pump, a Waters 410 differential refractometer and a Waters 486 tunable UV-vis detector. Polystyrene standards were used for calibration and chloroform as eluent.

Compounds 1[103], 2[104], 4[109], 6[110], 7[111] were synthesized according to previously reported procedures.

Dibromodiioobenzene 1: 1H NMR (CDCl3, ppm): δ 8.05 (s, 2H).

Compound 2[104]: 1H NMR (CDCl3, ppm): δ 7.00 (d, 1H), 6.87 (d, 1H), 2.80 (d, 2H), 1.58 (m, 1H), 1.36-1.26 (m, 8H), 0.88 (m, 6H), 0.34 (s, 9H).

Compound 3: Dibromodiioobenzene 1 (12.5 g, 25.6 mmol, 1eq), EHThSnMe_3 (18.39g, 51.2 mmol, 2 eq), Pd(Ph_3)$_2$$Cl_2$ (702mg, 1.0 mmol, 4% eq) were combined in a dry round bottom flask. After 3 nitrogen-vacuum cycles, anhydrous DMF (90ml) was added and solution was purged with nitrogen for 30 min. Solution was stirred at 80°C for 30h. Reaction mixture was cooled to rt and filtered through celite. DMF was evaporated under vacuum, residue was purified by gravity column chromatography using hexanes as eluent. Product isolated as a clear oil (8.5g, 53%). 1H NMR (CDCl3, ppm): δ 7.76 (s, 2H), 7.19 (d, 2H), 6.76 (d, 2H), 2.78 (d, 4H), 1.62 (m, 2H), 1.42-1.26 (m,

16H), 0.95-0.85 (m, 12H). ^{13}C NMR (CDCl3, ppm): δ 146.4, 137.2, 135.7, 135.5, 128.0, 125.3, 120.8, 41.4, 34.2, 32.5, 28.9, 25.6, 23.1, 14.2, 10.9. HRAMS m/z: $C_{30}H_{40}Br_2S_2$, Calcd, 622.0938. Found, (M^+), 622.0974.

Compound 4[109]: ^{1}H NMR (500 MHz, $CDCl_3$) δ 7.51 (s, 2H), 4.18 (d, *J* = 5.4 Hz, 4H), 1.80 (h, *J* = 6.0 Hz, 2H), 1.76 – 1.46 (m, 8H), 1.46 – 1.34 (m, 8H), 1.02 (t, *J* = 7.4 Hz, 6H), 0.97 – 0.89 (t, *J* = 7.0 Hz, 6H), 0.44 (s, 18H).

Compound 7[111]: 47%. ^{1}H NMR (400 MHz, $CDCl_3$) δ 7.42 – 7.34 (m, 2H), 7.06 – 6.98 (m, 2H), 2.47 (d, *J* = 7.1, 2H), 1.57 – 1.46 (m, 1H), 1.36 – 1.21 (m, 8H), 0.92 – 0.81 (m, 6H). HRAMS m/z: $C_{14}H_{21}Br$, Calcd, 268.0827. Found, (M^+), 268.0826.

Compound 8: 43%. ^{1}H NMR (400 MHz, $CDCl_3$) δ 7.71 (d, *J* = 7.9 Hz, 2H), 7.16 (d, *J* = 8.0 Hz, 2H), 2.54 (d, *J* = 7.1 Hz, 2H), 1.64 – 1.53 (m, 1H), 1.45 – 1.31 (m, 16H), 1.31 – 1.21 (m, 4H), 0.93 – 0.83 (m, 6H). ^{13}C NMR (126 MHz, $CDCl_3$) δ 145.24, 134.69, 128.61, 83.45, 41.05, 40.36, 32.33, 28.84, 26.24, 25.40, 24.78, 23.03, 13.89, 10.75. HRAMS m/z: $C_{20}H_{33}BO_2$, Calcd, 315.261. Found, (M^+), 315.2566.

Compound 9: 30%. ^{1}H NMR (500 MHz, $CDCl_3$) δ 7.65 (s, 2H), 7.36 (d, *J* = 8.1 Hz, 4H), 7.24 (d, *J* = 8.2 Hz, 4H), 2.60 (d, *J* = 5.0 Hz, 4H), 1.67 – 1.59 (m, 2H), 1.37 – 1.25 (m, 16H), 0.94 – 0.87 (m, 12H). ^{13}C NMR (126 MHz, $CDCl_3$) δ 142.84, 142.02, 136.86, 135.38, 129.14, 129.05, 121.52, 121.51, 41.17, 40.08, 32.53, 29.02, 25.64, 23.19, 14.30, 10.96. HRAMS m/z: $C_{34}H_{44}Br_2$, Calcd, 610.181. Found, (M^+), 610.1798.

Compound 6[110]: 91%. ^{1}H NMR (400 MHz, $CDCl_3$) δ 7.80 (dd, *J* = 7.5, 1.0 Hz, 2H), 7.74 (br s, 2H), 7.71 (dd, *J* = 7.5, 0.8 Hz, 2H), 2.03 – 1.95 (m, 4H), 1.39 (s, 24H), 1.28 – 0.96 (m, 24H), 0.84 – 0.75 (t, *J* = 7.3, 6H).

Typical polymerization procedure, TPB: compound 3 (1.0066g, 1.61 mmol, 1 eq), compound 4 (1.2447g, 1.61 mmol, 1 eq), $Pd(PPh_3)_4$ (93 mg, 0.08 mmol, 5% eq), were combined in a dry round bottom flask. After 3 nitrogen-vacuum cycles toluene (26 ml) and DMF (6.5 ml) were added and the mixture was degassed by purging with nitrogen for 15 min. Reaction flask was submerged into preheated to 120°C oil bath and stirred at this temperature for 21h. Reaction mixture was cooled to room temperature and precipitated in methanol. Solid polymer was redissolved in chloroform and filtered through celite. Solution was concentrated and precipitated in methanol. Polymer was purified by Soxhlett extraction with methanol, acetone, hexanes and chloroform. Chloroform fraction was concentrated and precipitated in methanol, polymer was filtered and dried under vacuum for 24 hours (677mg, 46%). ^{1}H NMR (500 MHz, $CDCl_3$) δ 7.78 (s, 2H), 7.34 (s, 2H), 6.87 (d, *J* = 3.4 Hz, 2H), 6.61 (d, *J* = 3.7 Hz, 2H), 4.06 (br s, 4H), 2.74 – 2.62 (m, 4H), 1.75 – 1.69 (m, 2H), 1.64 – 1.46 (m, 10H), 1.47 – 1.31 (m, 8H), 1.31 – 1.17 (m, 16H), 0.97 (t, *J* = 7.4 Hz, 6H), 0.92 (t, *J* = 6.4 Hz, 6H), 0.82 (dt, *J* = 11.7, 7.0 Hz, 12H).

TPF:69%, chloroform fraction. ^{1}H NMR (500 MHz, $CDCl_2CDCl_2$, 373K) δ 7.72 (d, *J* = 8.1 Hz, 2H), 7.66 (s, 2H), 7.44 (s, 2H), 7.41 (d, *J* = 12.0 Hz, 2H), 6.67 (d, *J* = 3.4 Hz, 2H), 6.56 (br s, 2H), 2.73 (d, *J* = 6.7 Hz, 4H), 1.96 (br s, 4H), 1.60 (br s, 2H), 1.55 – 1.28 (m, 24H), 1.28 – 1.09 (m, 16H), 0.97 – 0.87 (m, 18H).

PPF: 78%, hexanes fraction. ^{1}H NMR (500 MHz, $CDCl_2CDCl_2$, 373K) δ 7.59 (s, 2H), 7.56 – 7.47 (m, 2H), 7.34 – 7.21 (m, 8H), 7.09 – 7.02 (m, 4H), 2.57 (d, *J* = 7.4 Hz, 4H), 1.82 (br s, 4H), 1.62 (s, 2H), 1.51 (br s, 4H), 1.42 – 1.26 (m, 20H), 1.27 – 1.02 (m, 16H), 0.96 – 0.82 (m, 18H).

TPTF: 61%. ^{1}H NMR (500 MHz, $CDCl_2CDCl_2$, 373K) δ 8.92 – 8.83 (br s, 2H), 8.03 – 7.71 (m, 8H), 7.56 (br s, 2H), 3.14 (br s, 4H), 2.29 (br s, 4H), 2.01 (s, 2H), 1.74 – 1.39 (m, 32H), 1.39 – 1.18 (m, 24H), 1.16 – 0.83 (m, 18H).

4.5 References

(90) Li, G.; Yoon, K.-Y.; Zhong, X.; Wang, J.; Zhang, R.; Guest, J. R.; Wen, J.; Zhu, X.-Y.; Dong, G. *Nat. Commun.* **2018**, *9* (1), 1687.

(91) Yoon, K.-Y.; Dong, G. *Mater. Chem. Front.* **2020**, *4* (1), 29–45.

(92) Zhang, N.; Lo, W. Y.; Jose, A.; Cai, Z.; Li, L.; Yu, L. *Adv. Mater.* **2017**, *29* (28), 1–5.

(93) Li, L.; Lo, W. Y.; Cai, Z.; Zhang, N.; Yu, L. *Chem. Sci.* **2016**, *7* (5), 3137–3141.

(94) Lo, W. Y.; Bi, W.; Li, L.; Jung, I. H.; Yu, L. *Nano Lett.* **2015**, *15* (2), 958–962.

(95) Ramachandran, R.; Li, H. B.; Lo, W.-Y.; Neshchadin, A.; Yu, L.; Hihath, J. *Nano Lett.* **2018**, *18* (10), 6638–6644.

(96) Fu, L.; Li, S.; Cai, Z.; Ding, Y.; Guo, X.-Q.; Zhou, L.-P.; Yuan, D.; Sun, Q.-F.; Li, G. *Nat. Catal.* **2018**, *1* (6), 469–478.

(97) Kong, W.; Finger, L. H.; Oliveira, J. C. A.; Ackermann, L. *Angew. Chemie* **2019**, *131* (19), 6408–6412.

(98) Huang, Y.; Wu, D.; Huang, J.; Guo, Q.; Li, J.; You, J. *Angew. Chemie Int. Ed.* **2014**, *53* (45), 12158–12162.

(99) Campeau, L.-C.; Thansandote, P.; Fagnou, K. *Org. Lett.* **2005**, *7* (9), 1857–1860.

(100) Gorsline, B. J.; Wang, L.; Ren, P.; Carrow, B. P. *J. Am. Chem. Soc.* **2017**, *139* (28), 9605–9614.

(101) Hull, K. L.; Lanni, E. L.; Sanford, M. S. *J. Am. Chem. Soc.* **2006**, *128* (43), 14047–14049.

(102) Takahashi, M.; Masui, K.; Sekiguchi, H.; Kobayashi, N.; Mori, A.; Funahashi, M.;

Tamaoki, N. *J. Am. Chem. Soc.* **2006**, *128* (33), 10930–10933.

(103) He, F.; Wang, W.; Chen, W.; Xu, T.; Darling, S. B.; Strzalka, J.; Liu, Y.; Yu, L. *J. Am. Chem. Soc.* **2011**, *133* (10), 3284–3287.

(104) Komiyama, H.; Adachi, C.; Yasuda, T. *Beilstein J. Org. Chem.* **2016**, *12*, 1459–1466.

(105) Zheng, T.; Lu, L.; Jackson, N. E.; Lou, S. J.; Chen, L. X.; Yu, L. *Macromolecules* **2014**, *47* (18), 6252–6259.

(106) Yuan, J.; Xiao, L.; Liu, B.; Li, Y.; He, Y.; Pan, C.; Zou, Y. *J. Mater. Chem. A* **2013**, *1* (36), 10639.

(107) Hirano, T.; Hanamura, H.; Inoue, M.; Ueda, S.; Watanabe, M.; Tanabiki, M.; Mikami, K. *Polymer (Guildf).* **2019**, *177* (May), 282–289.

(108) Yuan, D.; Awais, M. A.; Sharapov, V.; Liu, X.; Neshchadin, A.; Chen, W.; Yu, L. *Chem. Mater.* **2020**, *32* (11), 4672–4680.

(109) Liang, Y.; Feng, D.; Wu, Y.; Tsai, S. T.; Li, G.; Ray, C.; Yu, L. *J. Am. Chem. Soc.* **2009**, *131* (22), 7792–7799.

(110) Pasini, M.; Destri, S.; Porzio, W.; Botta, C.; Giovanella, U. *J. Mater. Chem.* **2003**, *13* (4), 807–813.

(111) Schulz, G. L.; Mastalerz, M.; Ma, C.-Q.; Wienk, M.; Janssen, R.; Bäuerle, P. *Macromolecules* **2013**, *46* (6), 2141–2151.

CHAPTER 5

LADDER CONJUGATED POLYMERS WITH NARROW BAND GAPS

5.1 Introduction

Nitrogen rich polyacenes are an interesting subclass of ladder polymers. Substituting carbon atoms for nitrogen not only provides a way to modulate and tune bandgap by increasing electron withdrawing ability of the corresponding moiety but also allows for reversible redox processes, which has found its applications in electrochromic materials.[112,113] This class of compounds can find applications as sensors[114], light emitters in OLED[115], phototransistors[116] and OFET materials.[117] These materials can be synthesized through condensation of diamines with carbonyl compounds.[118,119]

Electron-accepting nature of azaacenes and their extensive conjugation allow them to stabilize not only negative charges but radicals as well. Usually these species are quite unstable, however recently Wang et al. have for the first time isolated diradical dianions in pyrene-fused azaacenes.[120] These dianions are open-shell singlets, however the energy difference between singlet and triplet states is very small and thermally accessible, which opens possibility of use of such molecules in thermally activated delayed fluorescence (TADF) materials.

Imidazole fused azaacenes have been found to possess interesting properties for resistive memory devices.[121] Nonvolatile resistive memory technology is important for data storage , however these devices usually require high switching voltages. Donor-acceptor nature of azaacenes allowed to tune material energy levels and achieve < 2 V switching voltage. Additionally, azaacene structure offers a convenient condensation based synthetic approach.

Campbell et al. used CH – N substitution in [6]-helicene to create a chiral organic semiconductor detector for circularly polarized light.[122] Helicenes are known ortho-fused polyacenes which cannot be planar due to steric hindrance. Substituting one of the carbons for nitrogen allowed to provide not only intrinsic "handedness" of helicenes but also additional directionality for packing of these molecules in supramolecular columns leading to the improved photoresponse.

Seki et al. have created a hash mark # shaped molecule out 4 azapentacenes connected to each other.[123] This optically active molecule exhibits impressive circularly polarized luminescence with a quantum yield of fluorescence of 47 % and a dissymmetry factor of $2.5x10^{-3}$. These fluorescence properties highlight that ladder type planarization and carefully chosen steric environment around the chromophore are crucial in material design.

In this chapter, we synthesized ladder type of monomers and polymers, exhibiting narrow band gaps for further exploration as electric and optical materials. Basic synthesis and characterization were pursued.

5.2 Results and discussion

In order to leverage the beneficial properties of nitrogen rich polyacenes, we decided to introduce an azaacene unit into conjugated polymer backbone. We decided to focus our efforts on the compound 5r shown in Scheme 5-1 for several reasons. First, side chain connection through benzene rings allows to explore luminescent properties of these materials by preventing aggregation and quenching of fluorescence. One of the challenges in the field of organic electronics lies in the control of materials morphology. The way molecules or chains of a polymer are oriented relative to each other in the solid state has profound effect on materials electronic and

optical properties. Second, ester groups on central ring allow us an option to later planarize the repeating units in the polymer films by thermal cyclization, which would increase π-π stacking and improve mobility of these materials. Lastly, this monomer can be polymerized with different cross-coupling partners to modulate energy levels and vary other properties.

Conjugated polymers with strong π-π stacking have a fundamental problem of solubility. Strong interchain and intrachain interactions bestow good charge transport properties, however at the same time make the material harder to process. Our approach to this issue lies in creating functional materials that can undergo chemical changes in situ to create a larger π-system and improve charge transport of already cast films.

5.2.1 Synthesis

Our synthetic strategy is shown in scheme 5-1. First, 4-bromophenol was alkylated with 2-ethylhexylbromide. Next, Grignard reagent formation and addition to the aminobenzonitrile creates adjacent amino and ketone functionality that can participate in the condensation reaction with dimetyl cyclohexanedionedicarboxylate. Final oxidation with chloranil affords dibromomonomer 5r.

This dibromomonomer 5r can be used with either ditin or diboron functionalities in Stille and Suzuki polymerization. Due to phenyl rings being out of plane of the 5 fused rings π-system, there is no solubility issues, which typically limit the molecular weights of polymers. We carried out Suzuki cross-coupling polymerization of this monomer with 2,1,3-benzothiadiazole (BTD), dioctylfluorene (F) and 2-ethylhexylcarbazole (CBZ) pinacol boronic esters. Reactions proceeded in high yields in THF-H_2O mixed solvents with $Pd(PPh_3)_4$ catalyst but required extended reaction

times of 3-5 days to achieve reasonable molecular weights of polymers, which is typical for similar systems.

Scheme 5-1. Synthesis of key monomer 5r.

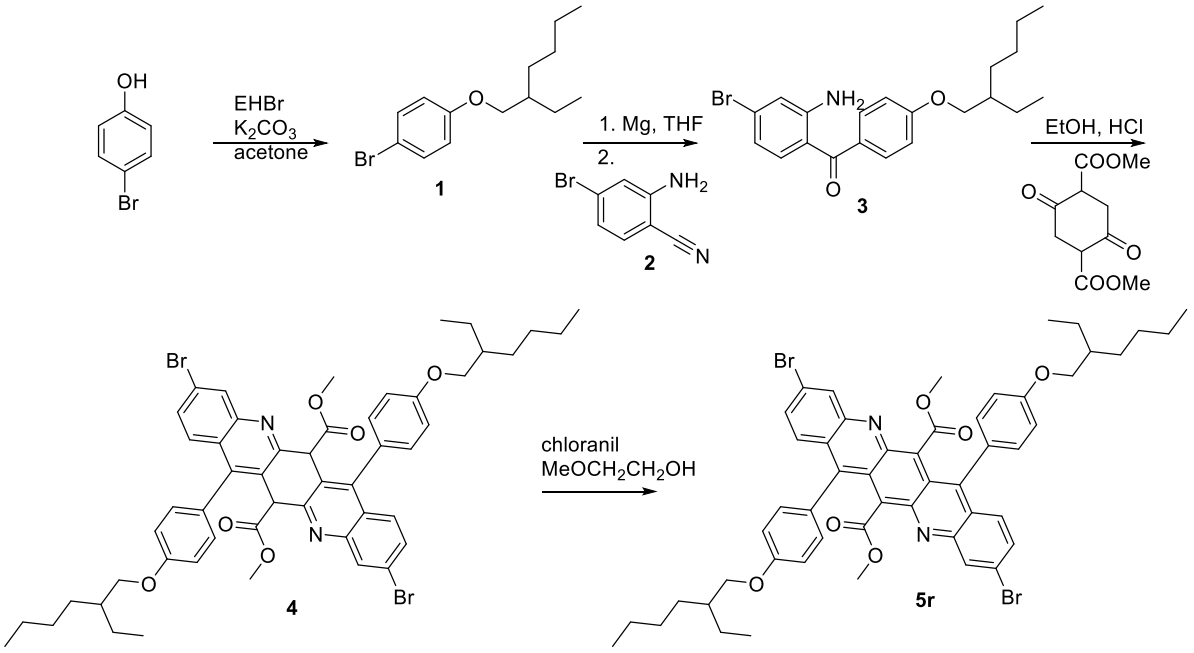

We also used Stille polycondensation for cross-coupling with thiophene-ended monomers. Stille reaction is much faster than Suzuki and usually reaction times of 24-36h are enough in toluene-DMF mixed solvent under $Pd(PPh_3)_4$ catalysis. Use of 4:1 mixture of toluene to DMF stabilizes polar intermediates in the catalytic cycle while still keeping the growing polymer chain in solution. Polymers 5r-BDT and 5r-TPTQ were obtained from monomer 5r coupled with ditrimethylstannyl bis-((5-(2-ethylhexyl)thienyl)-benzodithiophene (BDT) and thieno[2',3':4,5]pyrido[2,3-g]thieno[3,2-c]quinolone-4,10-dione (TPTQ). Significant molecular weights were reached for all polymerizations (Table 5-1).

Scheme 5-2. Suzuki polymerization leading to polymers 5r-F, 5r-BTD and 5r-CBZ

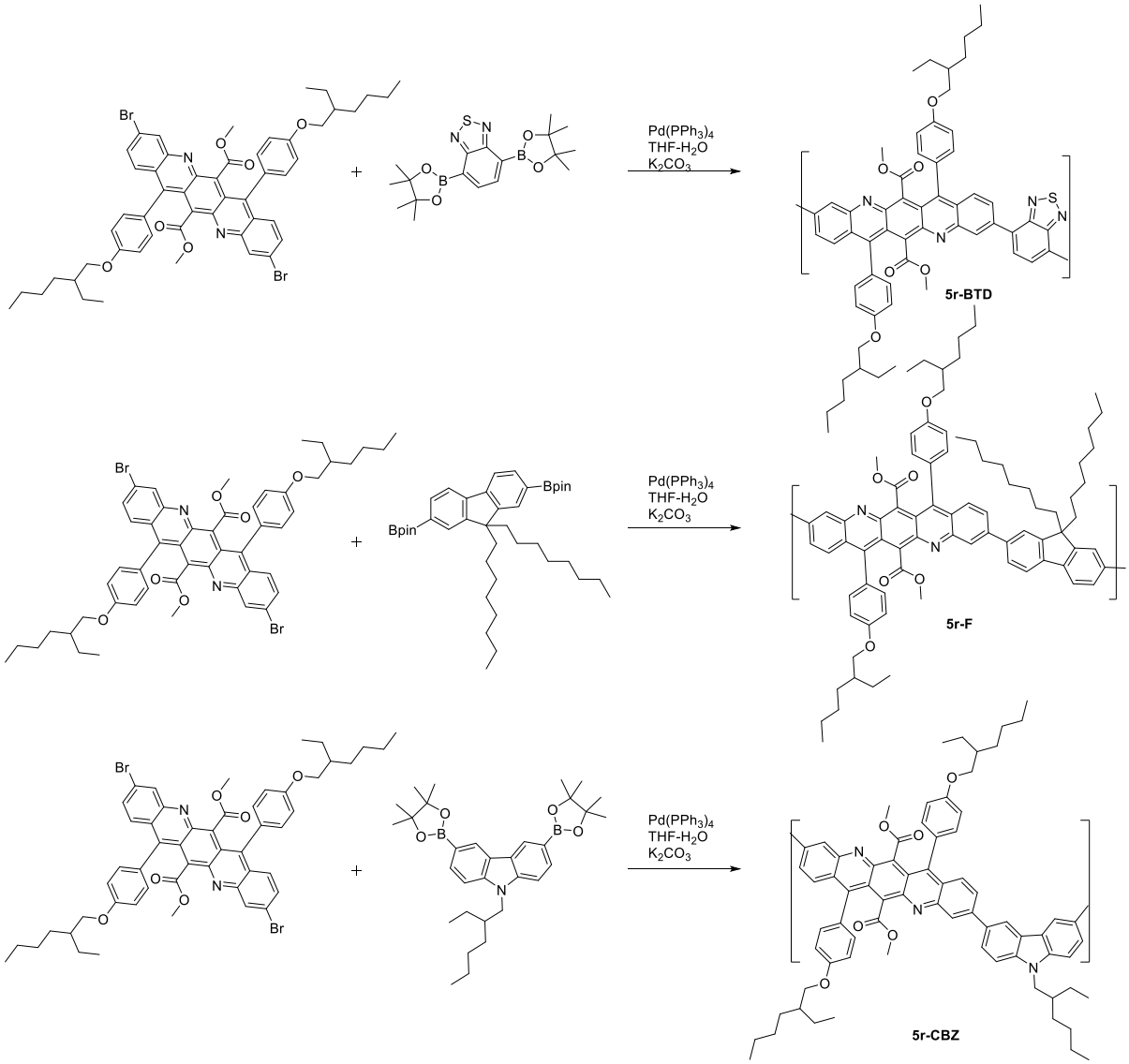

Phenyl moiety in side chains of 5r is necessary during synthesis to separate CH_2 group from activating carbonyl. When 2-ethylhexyl ketone was used instead of compound 3 desired condensation was accompanied by side reactions, leading to hard-to-separate impurities.

Scheme 5-3. Stille polymerization leading to polymers 5r-BDT and 5r-TPTQ

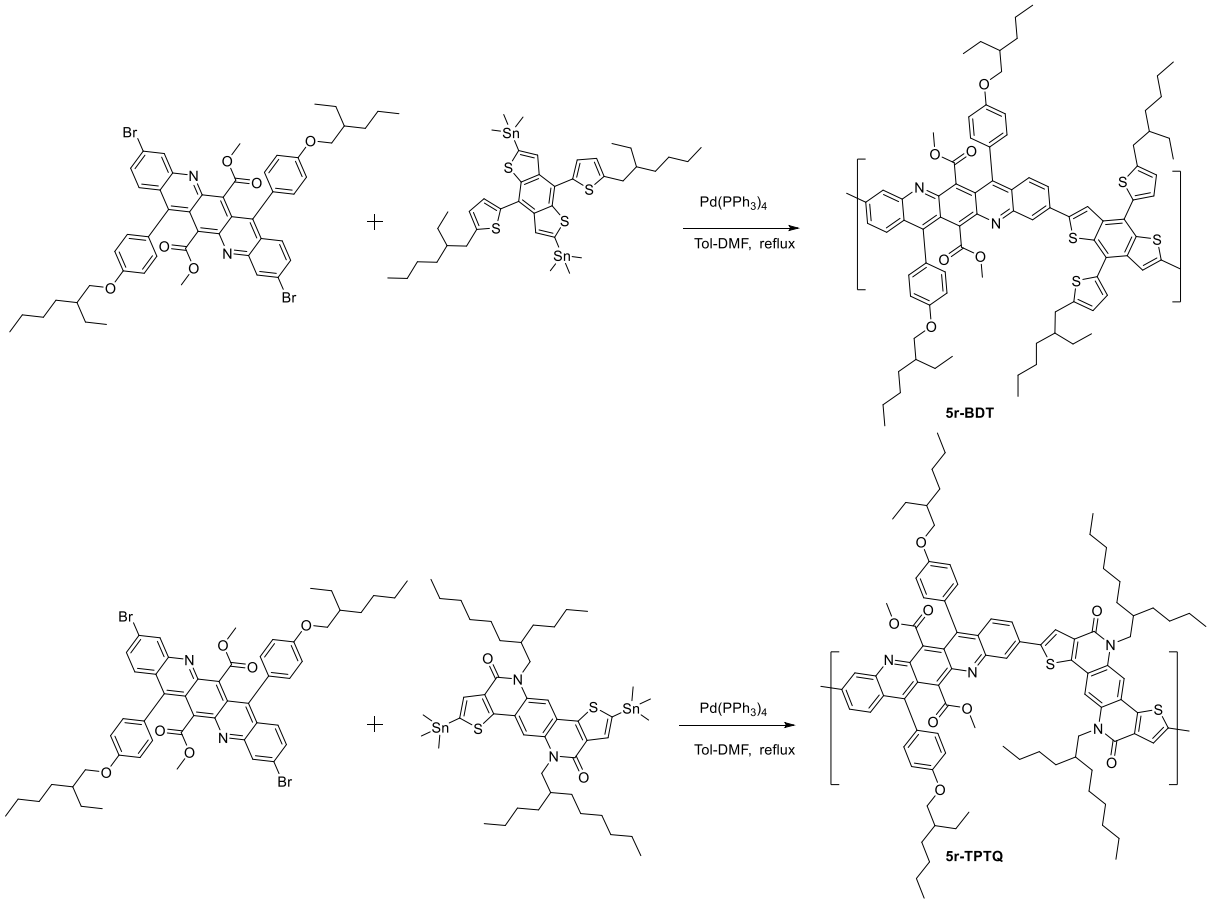

Additionally, we explored the synthesis of longer 9-ring monomer based on carbazole scaffold. First, dibromocarbazole 6 was nitrated. Electron-withdrawing nitrogroup activates bromine in ortho position for palladium catalyzed cyanation. Next, tin (II) dichloride reduces nitro group to amino group. Reaction with excess of Grignard reagent affords ketoamine 9, which can be used in condensation with dimetyl cyclohexanedionedicarboxylate. After oxidation with chloranil, unfortunately, the formed 9-ring compound azaacene is too sensitive to oxygen and light for purification due to its electron-rich nature.

Scheme 5-4. Synthetic route towards 9-ring ladder monomer.

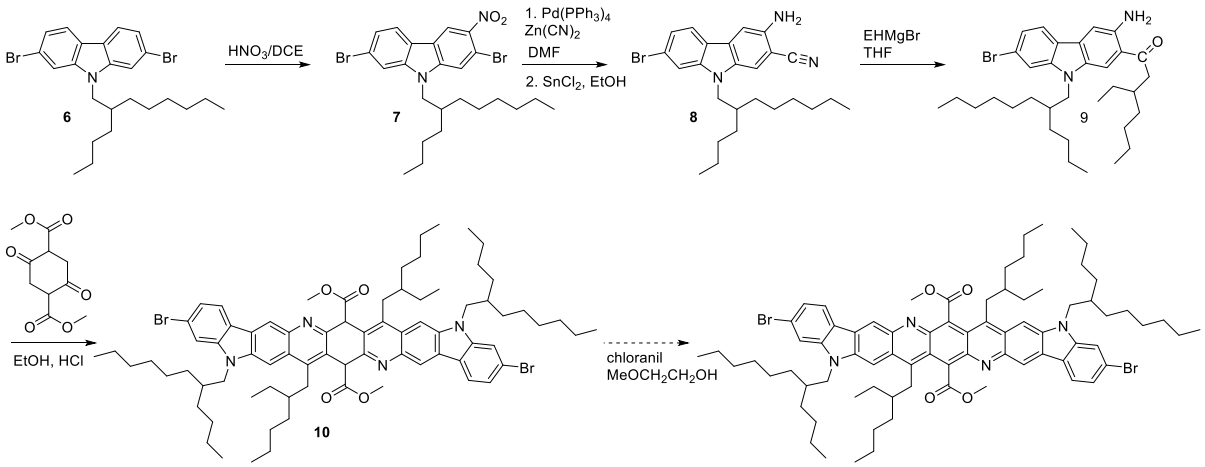

Table 5-1. Summary of materials properties.

Polymer	HOMO, eV	LUMO, eV	Eg,opt, eV	Eg, el, eV	QY	Mw, kDa	Mn, kDa	PDI
5r-F	-5.65	-3.76	1.88	1.90	3.4%	62.1	35.3	1.76
5r-BTD	-5.57	-3.82	1.86	1.76	0.3%	18.6	9.1	2.05
5r-BDT	-5.39	-3.62	1.71	1.77	0.3%	14.4	9.2	1.56
5r-CBZ	-5.40	-3.71	1.79	1.70	1.1%	38.2	22.1	1.73
5r-TPTQ	-5.60	-3.66	1.55	1.94	3.5%	23.8	12.3	1.94

5.2.2 DFT calculations

To better understand synthesized materials we performed ground state DFT calculations at B3LYP level of theory using 6-31G** basis set on symmetrical oligomers comprised of 3.5 repeating units. We found that for 5r-F HOMO energy level is predicted at -4.93eV, LUMO at -

2.88eV. While the structure is planar for the 5 fused rings moiety, dihedral angle between monomer fragments is estimated at 35.1°.

For 5r-BTD oligomer HOMO is estimated at -5.02eV, while LUMO at -3.07eV and dihedral angle is 36.5°. These energy levels reflect strong electron-withdrawing ability of benzothiadiazole as compared to fluorene.

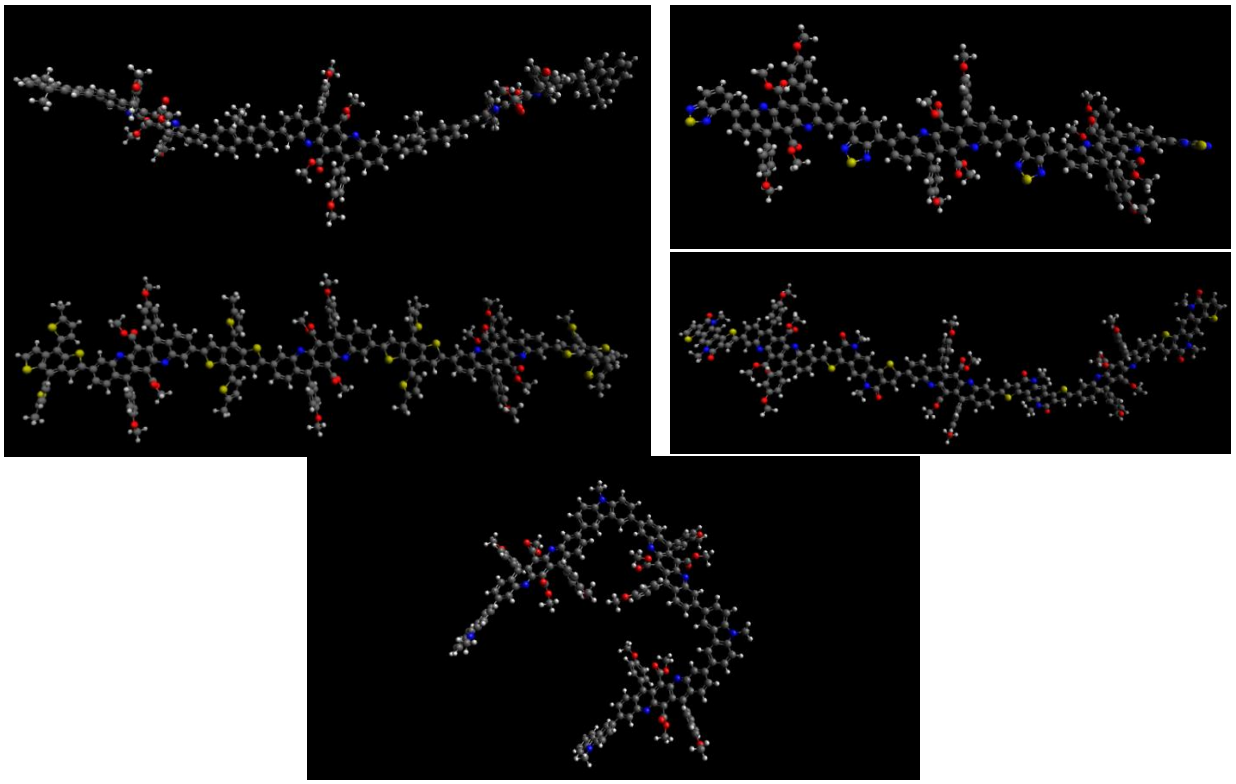

Figure 5-1. DFT optimized conformations of 5r-F, 5r-BTD, 5r-BDT, 5r-TPTQ and 5r-CBZ

As benzodithiophene unit is a strong donor 5r-BDT has HOMO energy -4.90eV and LUMO energy -2.96eV. Unlike previous cases dihedral 16.1° is much smaller due to less steric hindrance from thiophene compared to benzene. 5r-CBZ has HOMO energy level at -4.79eV and LUMO at -2.71eV highlighting electron donating contribution of carbazole to the frontier orbitals, dihedral angle is 35.9°. Due to carbazole geometry the angle between adjacent 5r monomers is 92.6°, which allows interesting folding possibilities for the polymer chain.

Most interestingly the ladder-ladder type 5r-TPTQ has HOMO energy of -5.10eV and LUMO at -3.14eV, quite close to the 5r-BTD. Like with 5r-BDT dihedral angle of 23° is smaller due to thiophene as a connection point.

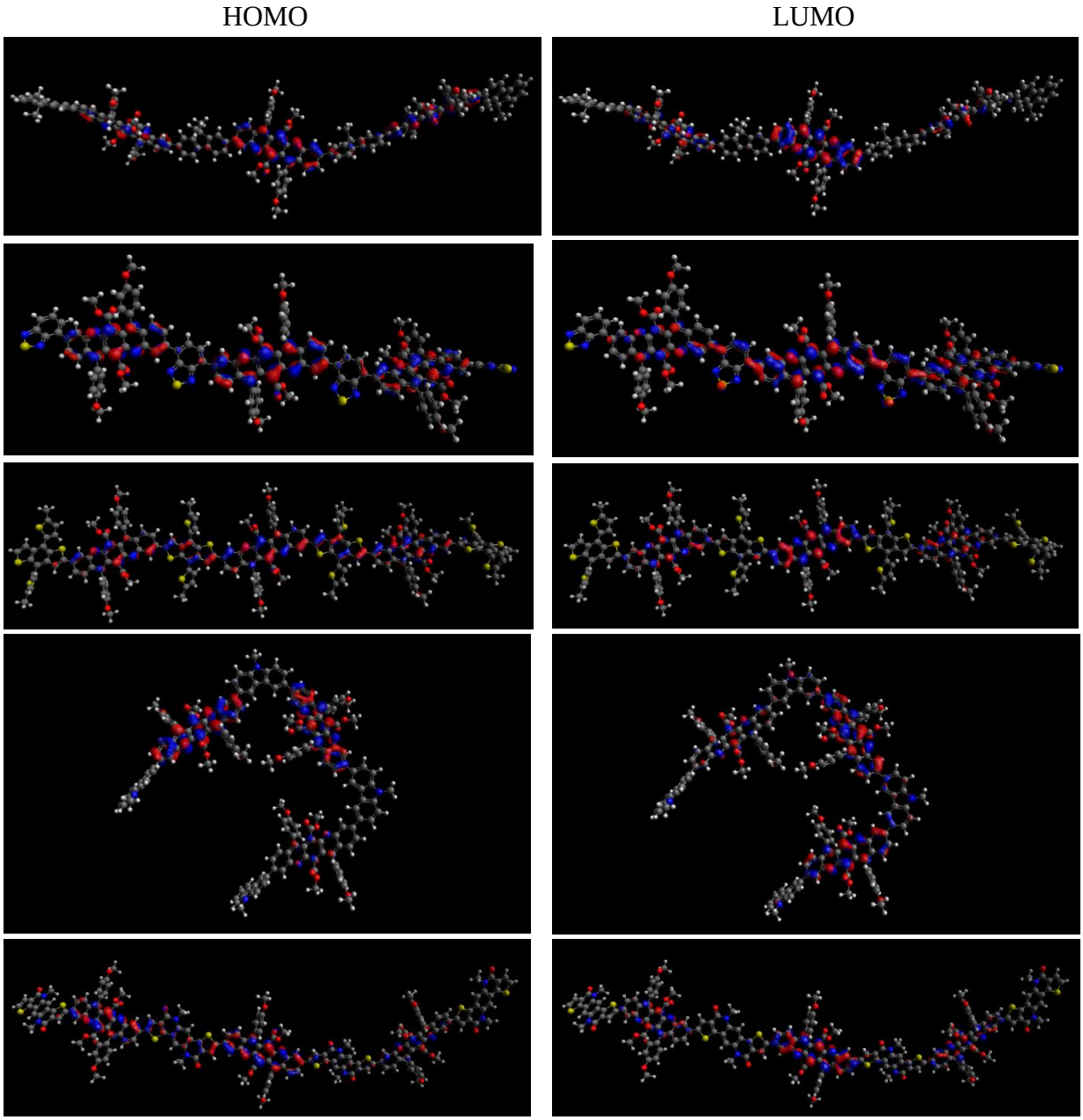

Figure 5-2. HOMO/LUMO orbitals of 5r-F, 5r-BTD, 5r-BDT, 5r-CBZ and 5r-TPTQ

It can be seen that frontier orbitals are generally localized on a planar 5 ring fragment, while donors have contributions only to HOMO, and acceptors only to LUMO.

We also performed time dependent DFT calculations at CAM-B3LYP level of theory using 6-31+G basis set for the first 10 transitions between ground and excited states for 5r-F, 5r-CBZ and 5r-TPTQ. A range-separated hybrid functional and basis set with diffuse orbitals are necessary to account for charge-transfer character of excited state in donor-acceptor systems.[124] Calculation results predict 2 bands of transitions in UV-visible absorption spectra with blue-shifted peaks having larger oscillator strengths and red-shifted peaks lower, which translates into lower intensity of absorption for red-shifted peaks. It can be concluded that most red-shifted peaks are comprised of many transitions with HOMO-LUMO dominating among others.

5.2.3 Optoelectronic properties

To understand electronic and energy level characteristics of the synthesized materials, we studied their UV-visible absorption and fluorescence spectra. Figure 5-3 shows UV-vis spectra of 5r-F, normalized by peaks at 336nm. It is clear that absorption spectra have a noticeable dependence on concentration. With increasing concentration, maximum at 373nm loses in intensity, while peaks at 488nm, 581nm and 630nm grow. This is evidence of weak aggregation of polymer chains in solution. Comparison with the spectrum of the polymer film before annealing shows that in solid state polymer chains are packed loosely and without strong interchain interactions, as the only difference from spectra in dilute solutions is broadening in UV region that can be attributed to different orientations of chromophores to each other. Excitation spectrum with monitoring emission at 650nm reproduces absorption spectrum closely, meaning, first, that there is only one absorbing and emitting chromophore, second, that all higher excited states relax to S_0, which fluoresces according to Kasha's rule, and third, that a peak at 488nm is actually comprised of at least 7 different transitions with similar energies.

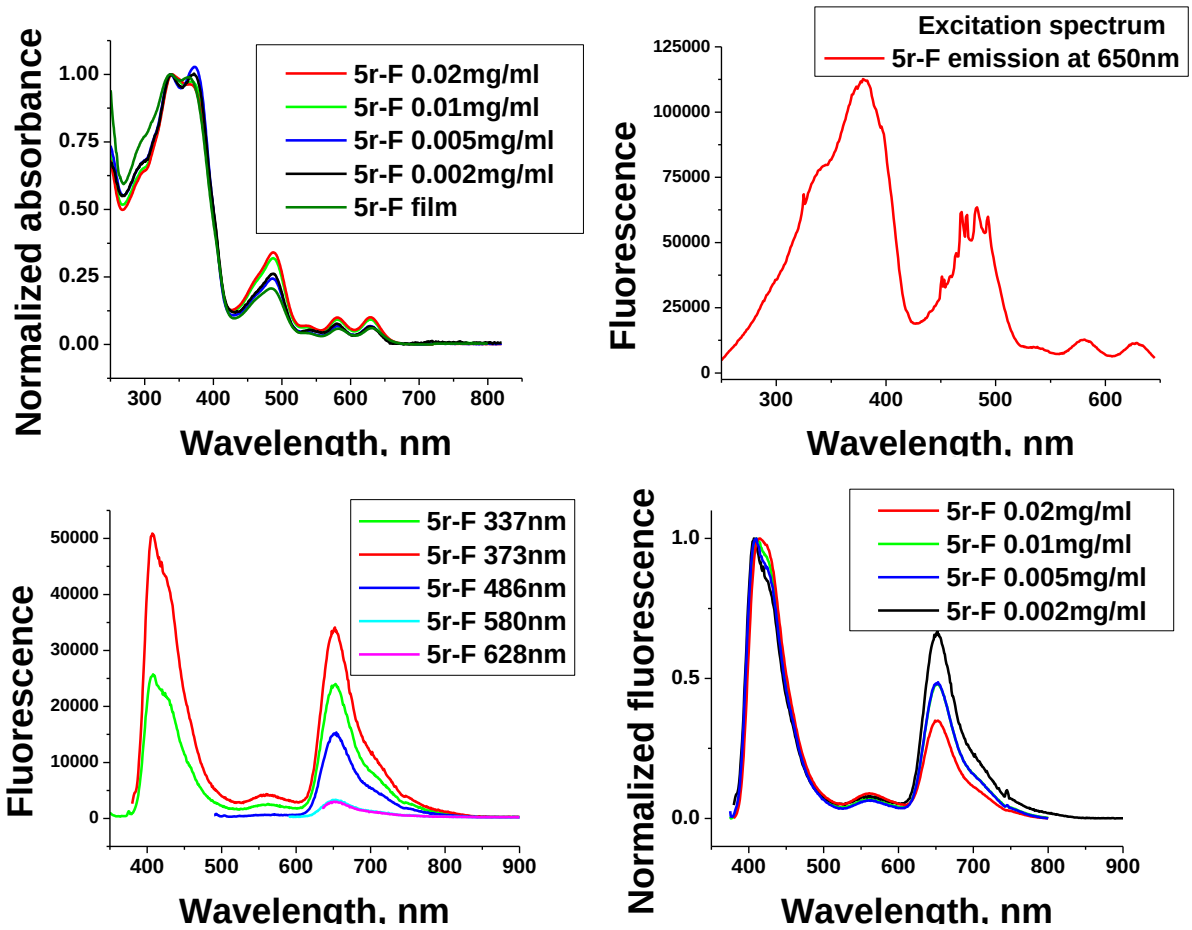

Figure 5-3. Normalized UV-vis, excitation and fluorescence spectra of 5r-F

Consistent with these conclusions, fluorescence spectra obtained with excitation at different wavelengths show no new peaks appearing. Fluorescence spectra of polymer solutions with different concentrations show that aggregation disproportionately reduces the intensity of emission at 651nm, while peaks at 409nm red-shift and become broader.

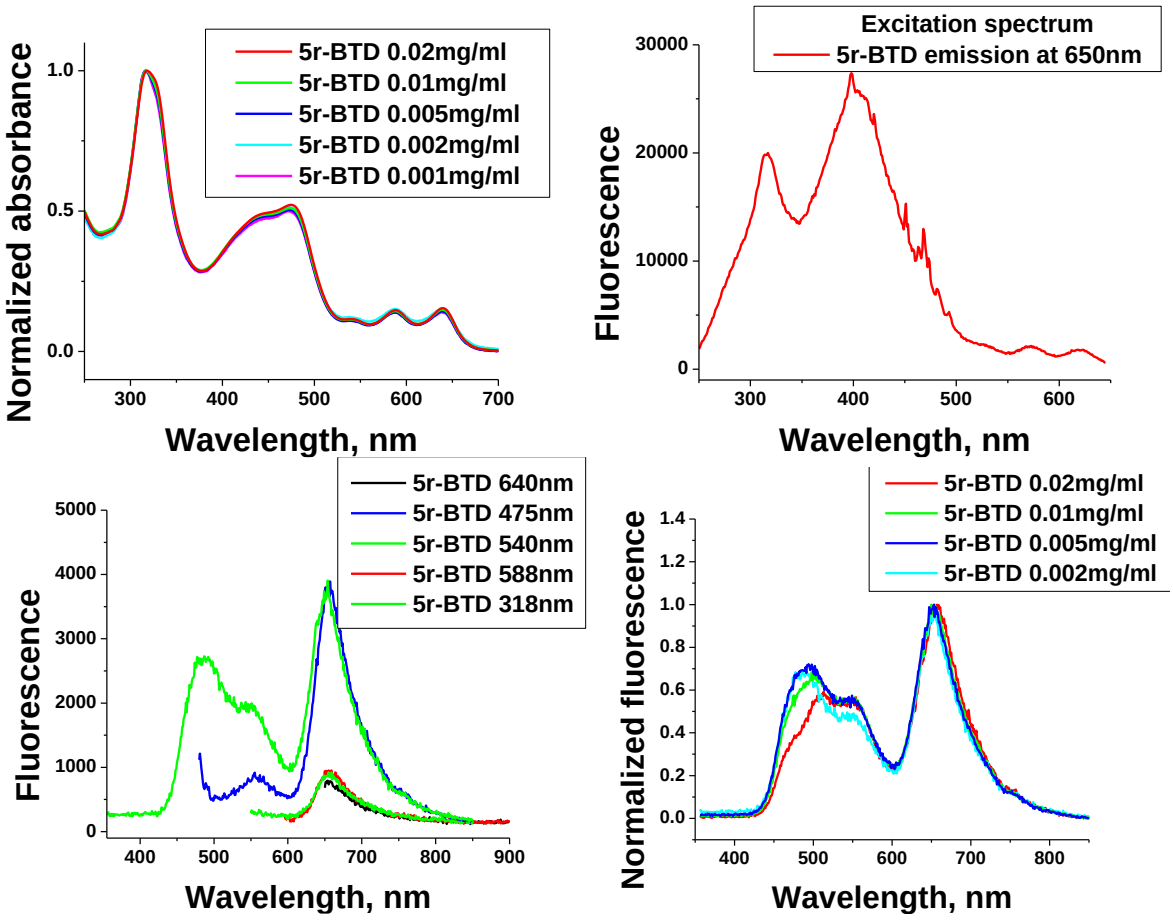

Figure 5-4. Normalized UV-vis, excitation and fluorescence spectra of 5r-BTD

UV-visible absorption spectra of 5r-BTD do not change with concentration, however in fluorescence spectra as concentration becomes larger peak at 487nm gradually redshifts to 513m, and loses intensity, signifying weak J-aggregation. Stronger aggregation is in line with 5r-BTD having less alkyl chain per repeating unit than 5r-F. Peaks in excitation spectrum match absorption spectra closely, meaning that emission occurs from the same relaxed excited state, and fluorescence spectra don't depend on excitation wavelength, allowing us to conclude that there is only one emissive chromophore.

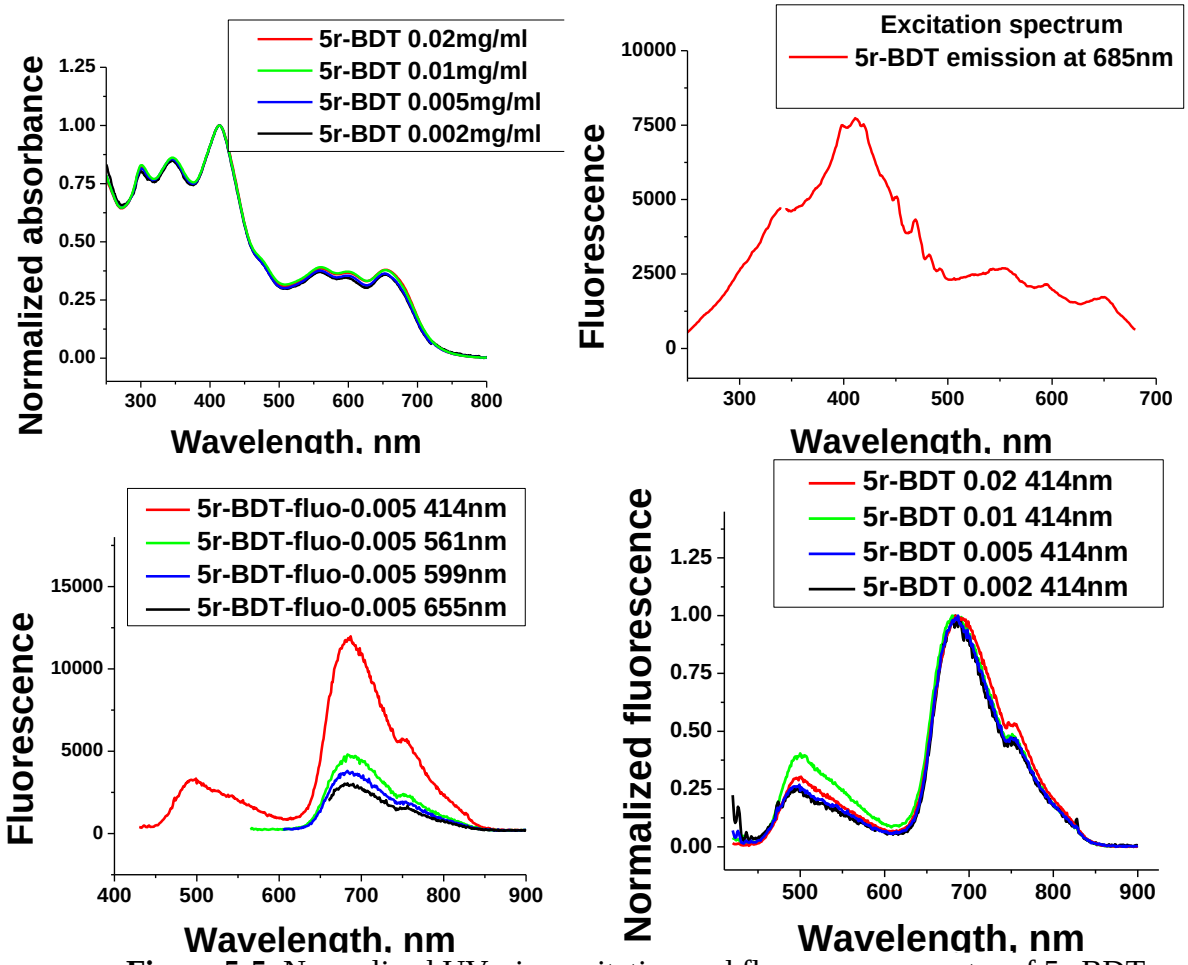

Figure 5-5. Normalized UV-vis, excitation and fluorescence spectra of 5r-BDT

UV-visible spectra of 5r-BDT is independent of concentration, while fluorescence spectra show small changes in relative peak intensity but not shape of the spectra or position of the peaks. Excitation spectrum matches absorption with 2 bands of peaks: 3 peaks of lower intensity in 550-650nm region and higher intensity band at 400nm and shorter wavelengths. Fluorescence spectra retain their shape irrespective of excitation wavelength. Similar observations hold for 5r-CBZ. For both polymers excitation spectra show that absorption peaks in 400-500nm region are comprised of a series of individual transitions.

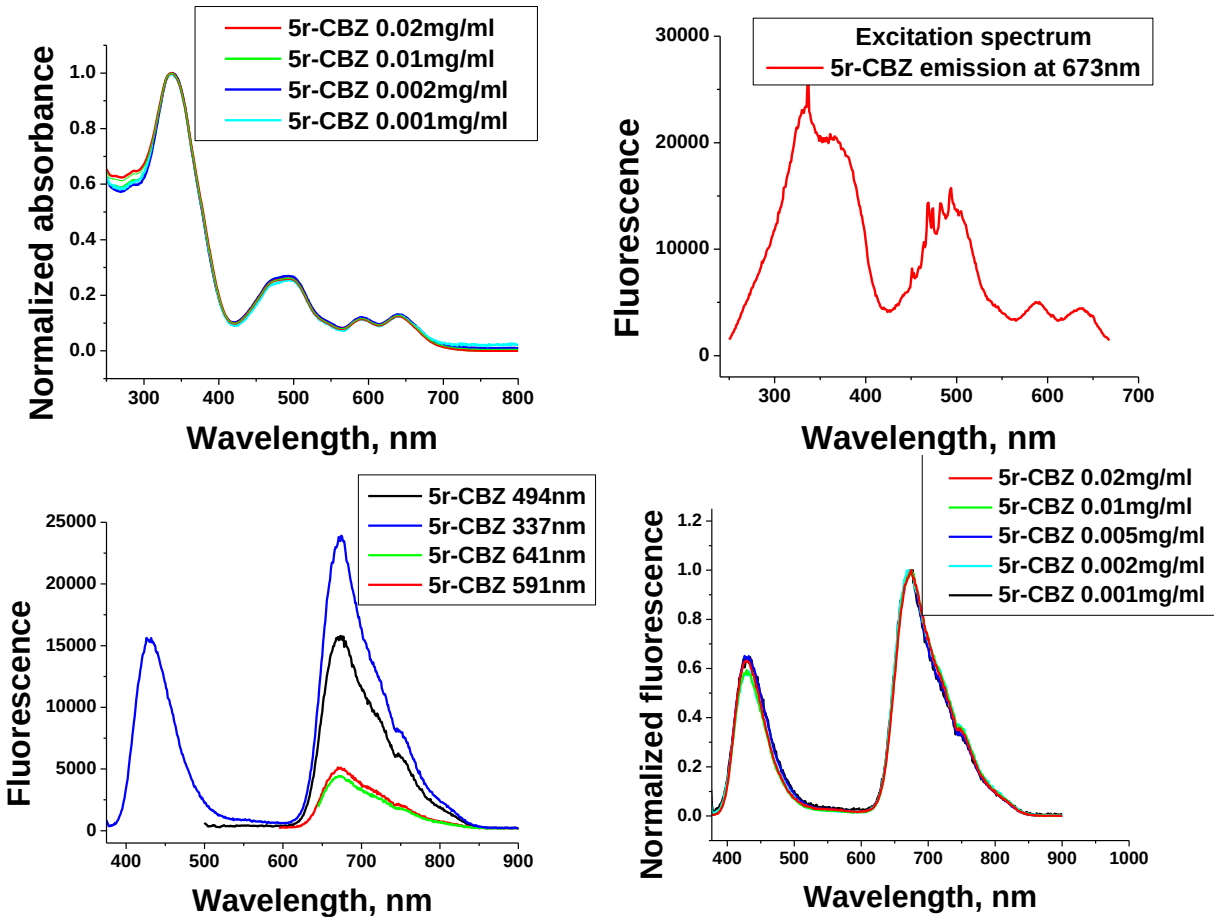

Figure 5-6. Normalized UV-vis, excitation and fluorescence spectra of 5r-CBZ

Polymer 5r-TPTQ is comprised of 2 semiladder monomers and as a consequence exhibits a more complicated UV-visible absorption spectrum. Fluorescence spectra are more complex as well: previous polymers exhibited 2 weak bands of fluorescence, whereas 5r-TPTQ has strong-luminescent peaks if excited at 433nm due to emission from TPTQ unit. Excitation spectra with provide additional support for this distinction. Excitation spectra monitoring emission at 469 and 540nm wavelengths match each other in shape, whereas excitation spectrum for 660nm fluorescence has different peaks at 330 and 400nm as well as near 500nm. This means that with excitation wavelength it is possible to switch emission either from 5r or TPTQ moiety.

Fluorescence as well as absorption spectra don't change on concentration indicating that these changes from previous polymers are not due aggregation.

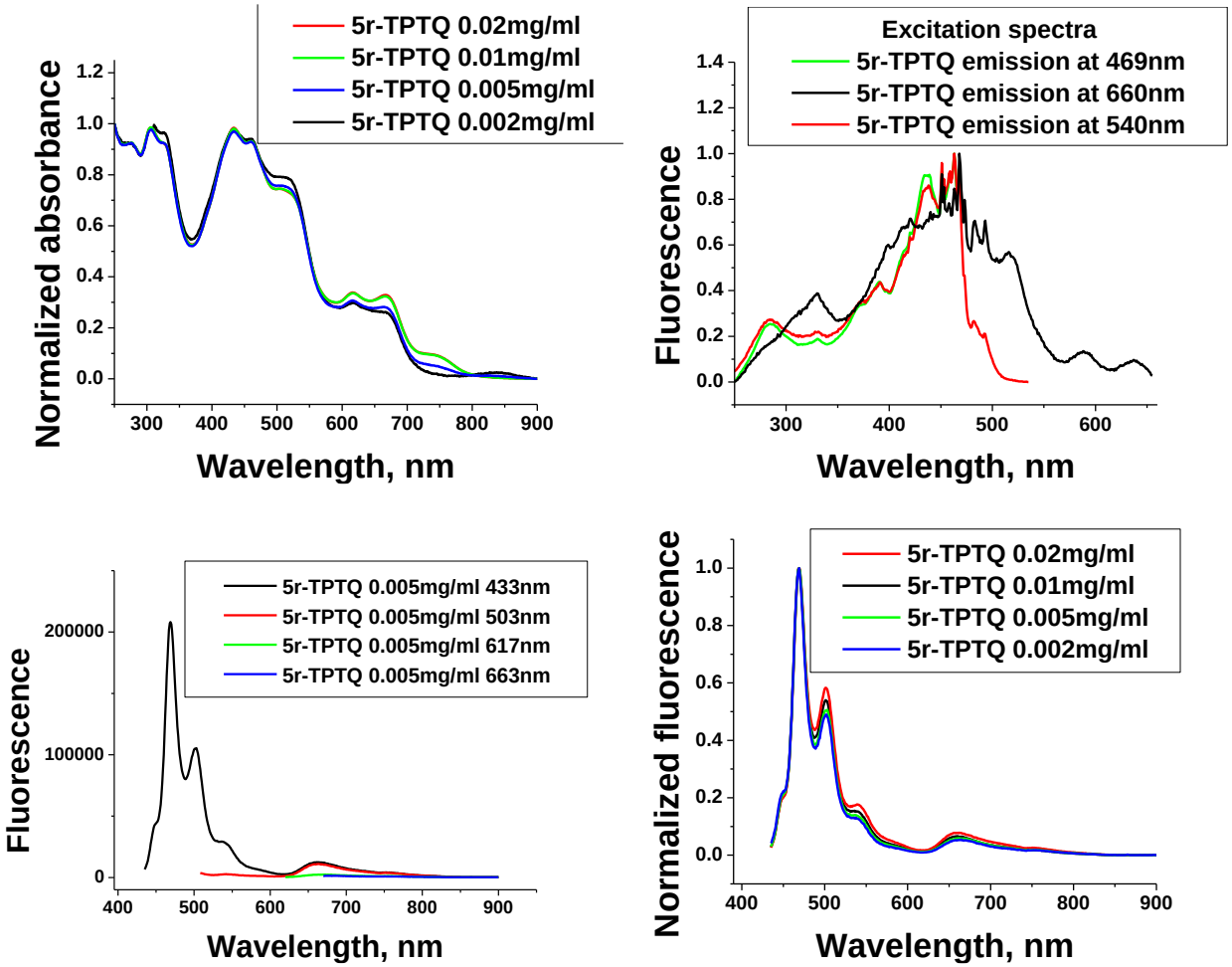

Figure 5-7. Normalized UV-vis, excitation and fluorescence spectra of 5r-TPTQ

5r-F has absorption onset at 660nm, 5r-BTD at 666nm, 5r-BDT at 725nm. 5r-CBZ 693nm and 5r-TPTQ at 801nm. This shows that among synthesized materials conjugation in the polymer chains is mainly determined by whether connection is through a 5-membered thiophene or 6-membered benzene ring.

5r monomer has 3 absorption bands with clear vibronic progression: the most intense at 300nm, 400-450nm and 500-650nm. Its fluorescence spectrum on the other hand has only 1 band

at 628nm irrespective of excitation wavelength, indicating that lowest energy emission from synthesized polymers originates from individual azaacene moieties.

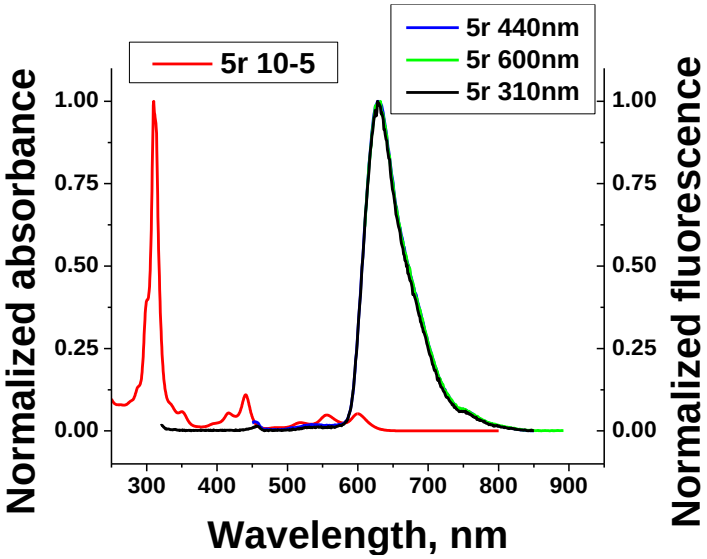

Figure 5-8. Normalized absorption and fluorescence spectra of 5r

Quantum yields of luminescence vary from 0.3 to 3.5% (Table 5-1). Polymers with sulfur atoms in the repeating unit 5r-BTD and 5r-BDT are less fluorescent because of heavy atom effect, while for 5r-CBZ almost perpendicular connection between monomers allows self-folding of individual polymer chains even in dilute solution and corresponding quenching.

Cyclic voltammetry experiments were performed to study electrochemical properties of synthesized polymers. Ferrocene standard was used as an energy level reference (-4.80eV). Cyclic voltammetry experiments for films of synthesized polymers showed in all cases reversible reduction and irreversible oxidation. Full-scan peaks for reduction and oxidation are independent of each other and reproduce separately in corresponding half-scans. Electrochemical reduction involves 2 electrons being donated sequentially to every azaacene moiety, as they can be stabilized on each repeating unit by 2 nitrogen atoms and 2 electron-withdrawing carboxylate groups as well as extensive conjugation. In all cases back-peaks are clearly visible on the cyclic voltammogram

and cathodic and anodic currents have similar magnitude. Electrochemical stability under these conditions was further proved by cycling experiments.

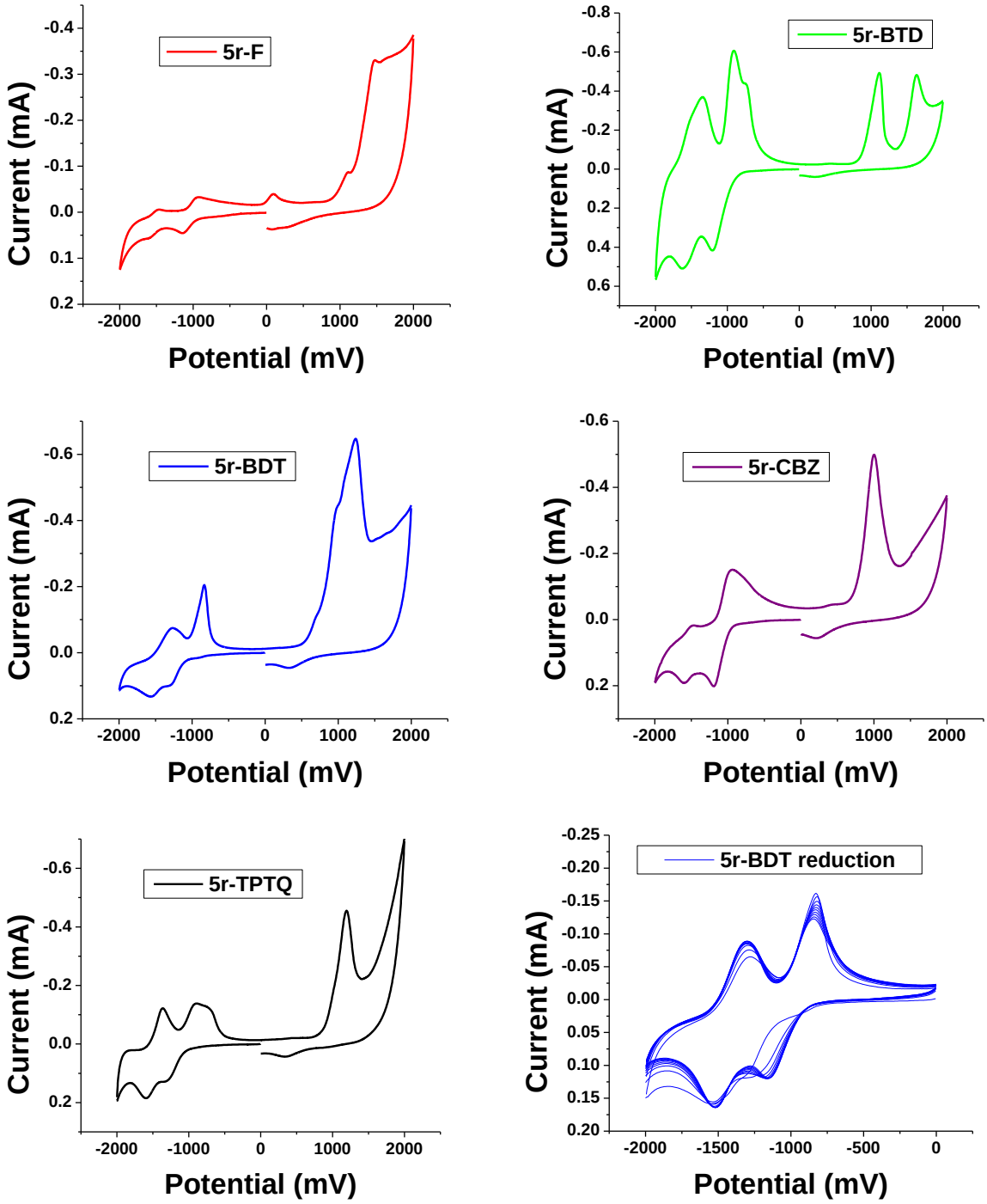

Figure 5-9. Cyclic voltammograms of synthesized materials

As an illustrative example, 10 cycles of reduction half-scans for 5r-BDT are shown in Figure 5-9. It can be noted that peaks of cathodic and anodic currents change very little in magnitude with cycling. On the other hand oxidation of the synthesized polymers is clearly irreversible with no observed back-peaks, and oxidation peak quickly disappears with cycling. 5r-BTD stands out among other materials because of its 2 well-separated oxidation peaks. Likely this is due to the least amount of side chains in this polymer, allowing greater conjugation and charge stabilization in the polymer backbone in the solid state.

Electrochemical and optical bandgaps of the polymers (Table 5-1) are within 0.1eV of each other for 5r-F, 5r-BTD, 5r-BDT and 5r-CBZ, however for 5r-TPTQ the difference is ca. 0.4eV. Optical bandgap is commonly smaller than electrochemical one due to hole-electron Coulomb stabilization in the exciton. This indicates that 5r-TPTQ excited state has greater charge transfer character than for other materials.

5.2.4 Thermal planarization of polymer repeating units

Thermogravimetric analysis showed that synthesized polymers have a wide range of decomposition onsets. Main source of decomposition of such molecules is electrophilic attack of methyl ester groups onto the nearby phenyl rings.[125]

Scheme 5-5. Thermal cyclization of 5r moieties.

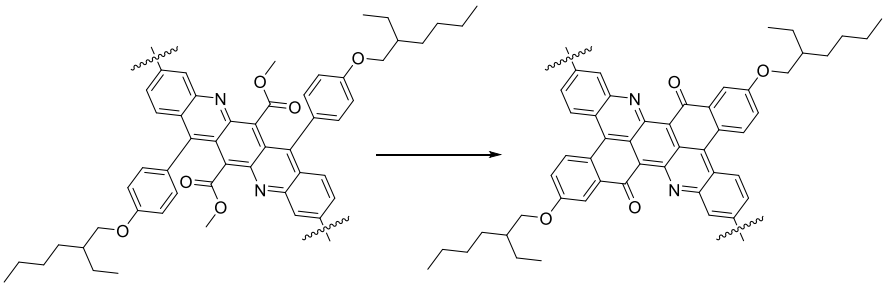

In the acceptor moiety, phenyl ring is expected to have smaller dihedral angle with main π-system than carboxylate due to more extensive conjugation. Therefore, electron donating groups on the fused 5-ring fragment facilitate electrophilic substitution by making the phenyl ring more electron rich and nucleophilic. Among comonomers benzodithiophene is most electron donating, then carbazole, then TPTQ. In TPTQ carbonyl group is cross-conjugated to the 2-position of thiophene, while electron-rich nitrogen atoms of the amide groups can still donate electrons. Connections through 5-membered thiophene rings allow better conjugation than through 6-membered phenyl rings because of smaller steric hindrance of C-H bonds due to larger C-C-C angles. Finally we would expect fluorene to be the weakest donor and benzothiadiazole to be an acceptor. Thermal stability of synthesized polymers increases in the series 5r-BDT < 5r-CBZ < 5r-TPTQ < 5r-BTD~5r-F, which is congruent with previous rationale.

Table 5-2. TGA properties of synthesized materials.

Polymer	5r-F	5r-BTD	5r-BDT	5r-CBZ	5r-TPTQ
Temperature of 5% loss, °C	321.4	319.5	176.5	238.6	294.3
2MeOH/$M_{w\ r.u.}$, %	5.4	6.8	4.6	5.9	4.4
T_g, °C	140.5	136.2	136.6	138.7	137.6, 175.3

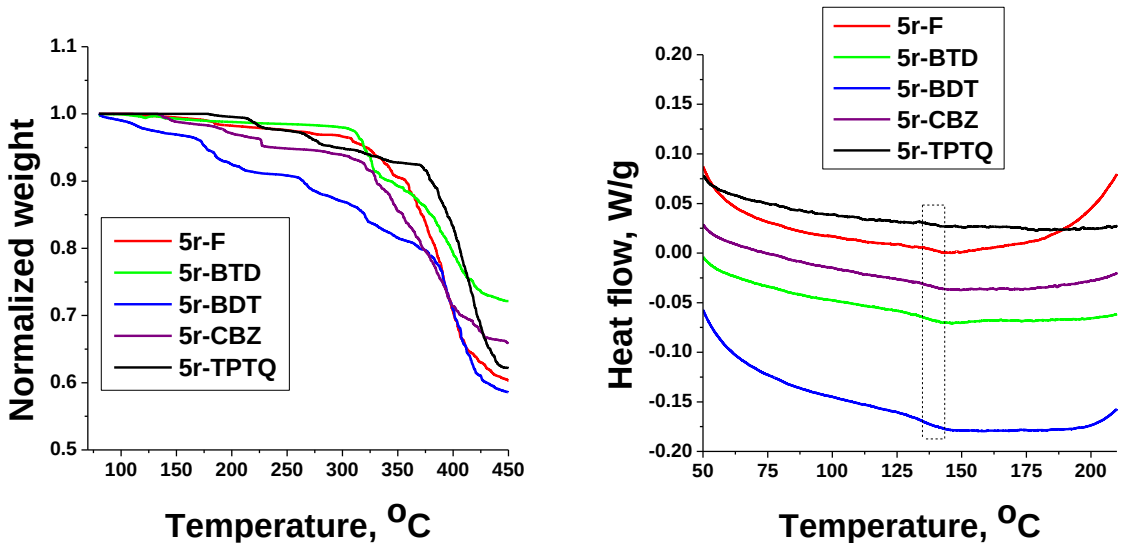

Figure 5-10. TGA and DSC (second heating) traces of synthesized polymers

During heating each repeating unit loses 2 equivalents of methanol, allowing us to compare theoretical loss of mass to the observed one for each material. According to TGA data 5r-F loses 5.4% from 308 to 346°C, ending in a plateau. 5r-BTD loses 6.6% of weight in a stepwise fashion upon heating from 300 to 329°C. 5r-BDT loses 4.9% from 270 to 323°C. 5r-CBZ loses 5.5% from 228 to 331°C. 5r-TPTQ loses 4.4% from 261 to 343°C in 2 steps. These changes are very close to those calculated theoretically in Table 5-2, occur in a similar range, considering the difference in chemical structure of polymers, and happen in a stepwise fashion as expected from a distinct chemical transformation. Therefore we attribute these processes to thermal cyclization.

Differential scanning calorimetry (DSC) results for second heating showed that all synthesized polymers are semicrystalline. DSC traces show glass transitions and no observed melting. Observed glass transition temperatures are in close range 136-141°C, with exception of 5r-TPTQ, which has a second glass transition at 175.3°C. Together with small change of heat capacity during glass transition this means that synthesized polymers have rigid backbones, and glass transition mainly involves untanglement of alkyl side chains.[126,127] Second glass transition of 5r-TPTQ is due to TPTQ being a larger comonomer than others and allowing more conformational flexibility for side chains.

Additionally, we studied the change in UV-vis absorption spectra of films of synthesized materials after annealing for 2h at different temperatures. Figure 5-11 shows absorption spectra of different polymers films before heating (top left) and spectra of films of each polymer normalized by maxima in 300-350nm region.

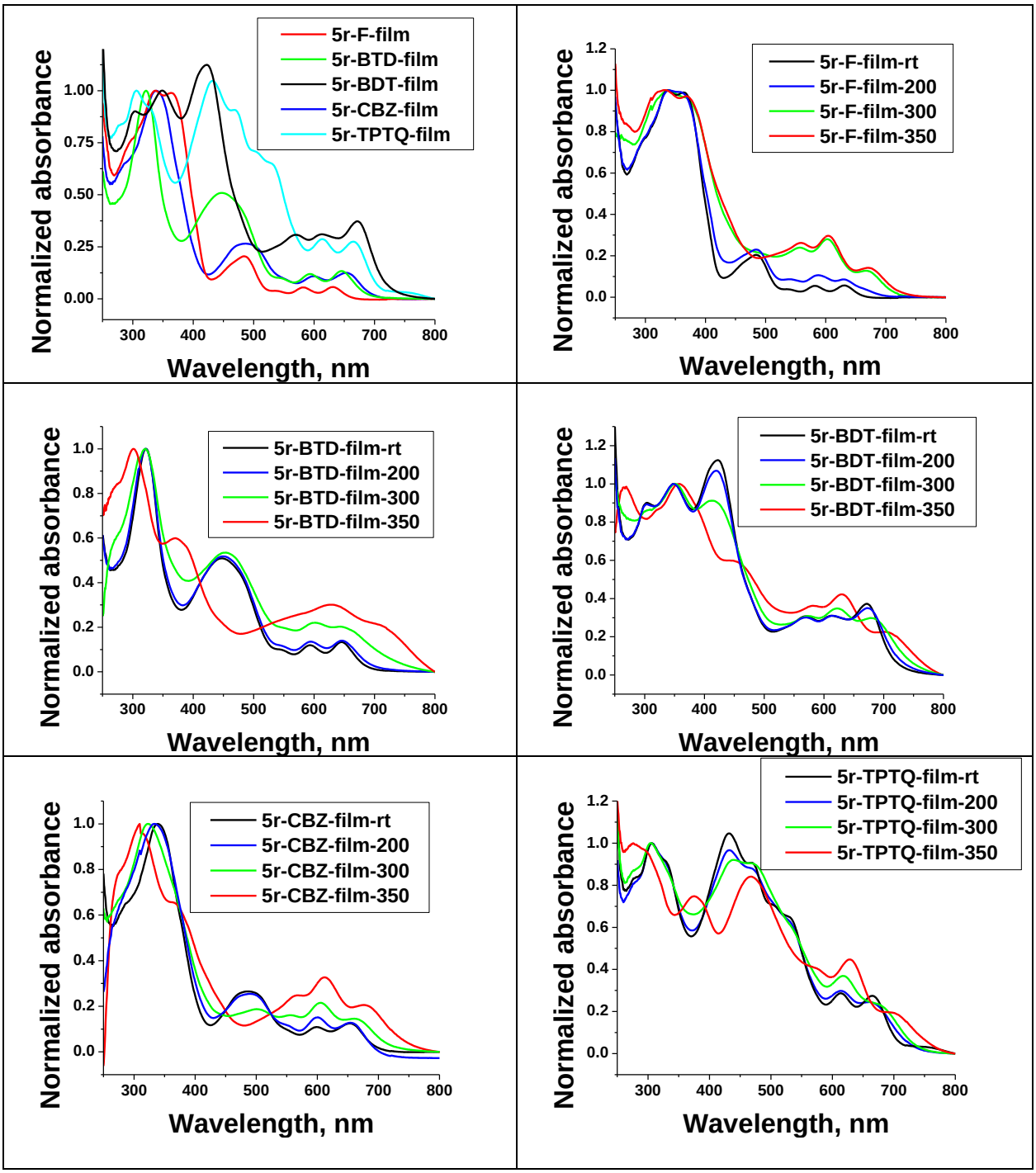

Figure 5-11. Absorption spectra of polymers films before and after heating

Comparison of spectra of all films at room temperature and 200°C shows only minor adjustments to peaks intensities. This lack of change clearly shows that at this temperature only annealing of films happens: polymer chains adopt preferable conformations and stack a little better

with each other leading to small differences in inter-chromophore interactions, tiny difference in transition dipole moments interactions leads to small differences of extinction coefficient for different transitions. However heating at higher temperatures at 300°C and 350°C is distinctly different. In all cases heating resulted in the increased absorption and bathochromic shift of peaks in 600-800nm region. Simultaneously, absorption in 400-500nm region decreases. For 5r-F 335nm and 360nm peaks become much broader, maximum at 485 nm disappears altogether. Conversely, peaks at 540nm, 580nm and 630nm increase in intensity and red-shift 20-40nm. 5r-BTD has a clear hypsochromic shift for a peak at 322nm going to 300nm, and this change happens only for the highest temperature. Peak at 445nm stays the same until 350°C, at which point it disappears and a new peak emerges at 371nm. Peaks at 600 and 650nm red-shift by 30-50nm, increase in intensity and become broader. 5r-BDT similarly has a peak at 422nm decreasing and peaks at 569nm, 615nm and 672nm red-shifting to 579nm, 630n and 706nm. 5r-CBZ spectra undergo same changes as 5r-BTD: peaks in UV region blue-shift, maximum at 486nm gradually disappears, while transitions at 551nm, 598nm and 654nm red-shift and increase in intensity. Spectra of 5r-TPTQ are undergoing the same progression, however there is an extra transition originating from TPTQ chromophore.

Thermal cyclization can also be confirmed by IR of samples before and after thermal treatment. For polymer 5r-BTD carbonyl peak broadens, reduces in intensity and shifts from 1732.6 cm^{-1} to 1727.51 cm^{-1}.

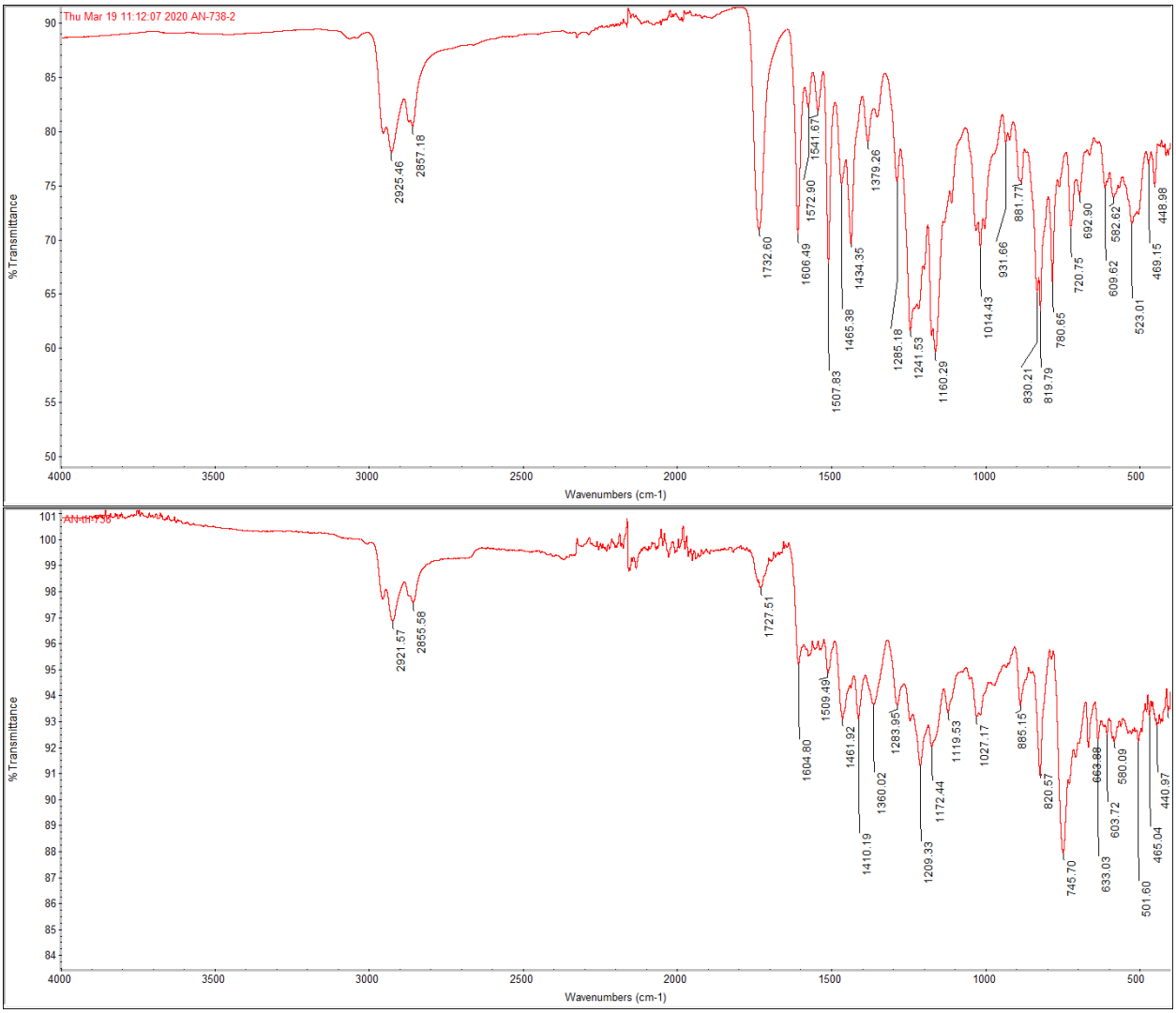

Figure 5-12. IR spectra of polymer 5r-BTD before and after thermal treatment

Similar changes occur for other polymer samples as well as monomer 5r. Greater conjugation usually reduces IR peak wavenumbers by reducing the effective bond order of a C=O group, however precise magnitude of this effect acutely depends on molecular structure. Small difference between non-cyclized and cyclized samples is due to cyclized carbonyl group participating relatively little with main polymer chain conjugation, because of positioning of electron withdrawing nitrogens. From the literature cross-conjugated compound A has IR peaks at 1740 (C=O) and 1610 (C=C) cm^{-1}, close to what is observed for our materials.[128] However, for

compound B where conjugation spans through the whole molecule corresponding peaks are at 1620 (C=O) and 1575 (C=C) cm^{-1}.[129] Therefore, we can conclude that IR evidence also supports successful cyclization.

Table 5-3. IR shifts for carbonyl peaks before and after thermal cyclization, cm^{-1}.

	5r	5r-F	5r-BTD	5r-BDT	5r-CBZ	5r-TPTQ
Before	1727.5	1738.41	1732.6	1734.79	1735.94	1736.34
after	1739.73	1737.58	1727.51	1736.31	1737.28	1737.58

Scheme 5-6. Compounds to illustrate dependence of carbonyl group IR frequency on conjugation.

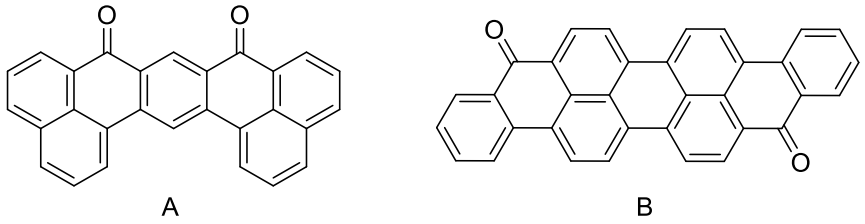

A B

5.2.5 FET properties

After performing studies on thermal cyclization we identified 350°C as an annealing temperature to completely drive chemical transformation in film. We decided to test how planarization of molecular structure would influence materials electrical conductivity. Charge carrier mobility in polymers inherently depends on interchain π-π stacking. For most materials intrachain charge transport is fast, and charge hopping between different polymer chains is the rate limiting step to charge transport. Synthesized pristine polymers have out of plane benzene rings and ester groups that should prevent any close contact at 5r monomer fragments. After chemical planarization this effect is removed and every repeating unit gains a large flat area that can form strong interchain contacts. More contacts and π-π interactions should allow charge carriers to hop from one chain to

the next easier. To this effect we studied FET performance of all synthesized polymers annealed at 100°C, when no chemical transformation takes place, and after thermal treatment at 350°C, when ester group attacks benzene rings and leads to ring fusion. The B doped Si wafer was used as gate electrode, on which SiO_2 layer modified with OTS acts as dielectric layer. The gold electrodes are used as drain and source. Before high temperature treatment none of the polymers showed any FET property. To our delight, after annealing at 350°C for 1h however all of the materials showed typical transfer and output curve profiles.

Table 5-4. FET data for annealed materials.

Material	5r-F	5r-BTD	5r-BDT	5r-CBZ	5r-TPTQ
$I_{on/off}$	10^2	10^1	10^2	10^1	10^1
V_{th}	43 V	80 V	23 V	39 V	80 V
μ_{h1}, 10^{-5} cm^2 V^{-1} s^{-1}	2.6	0.21	6.5	1.5	0.28

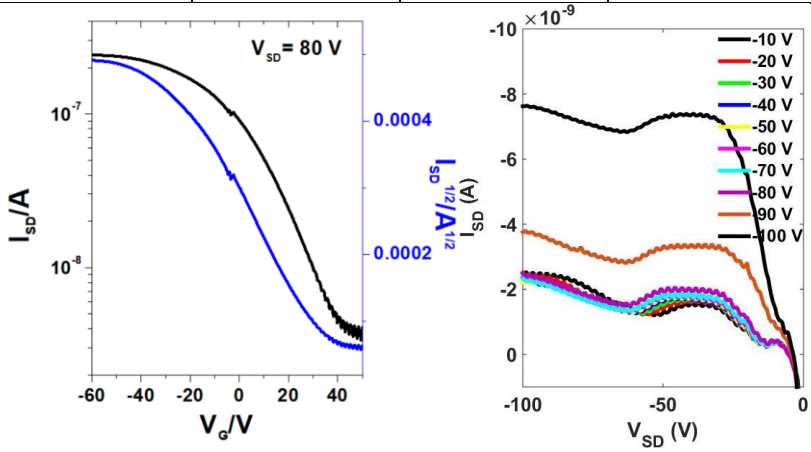

Figure 5-13. Transfer (left) and output (right) curves of 5r-F, 5r-BTD, 5r-BDT, 5r-CBZ, 5r-TPTQ after thermal treatment

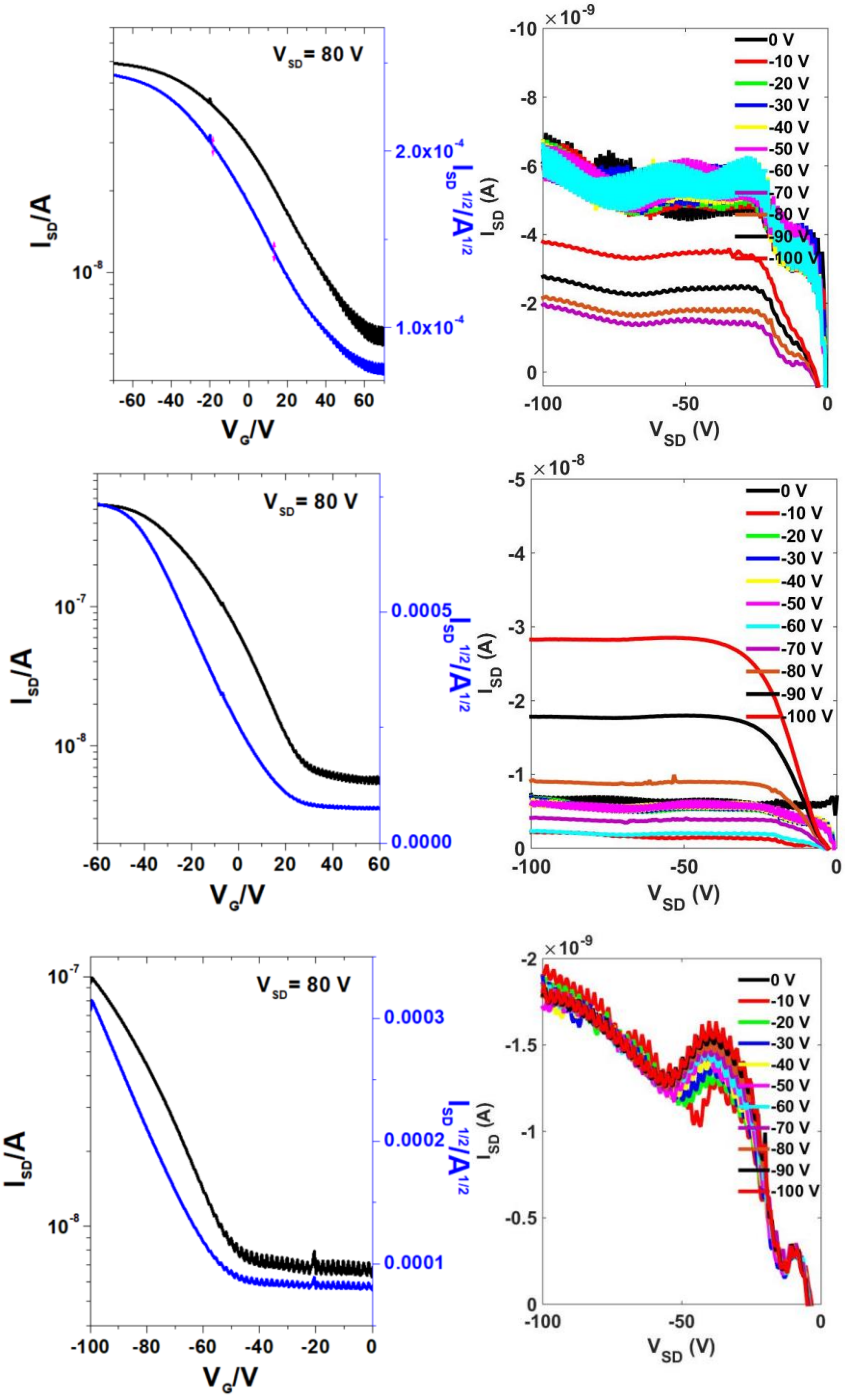

Figure 5-13. Transfer (left) and output (right) curves of 5r-F, 5r-BTD, 5r-BDT, 5r-CBZ, 5r-TPTQ after thermal treatment (continuation)

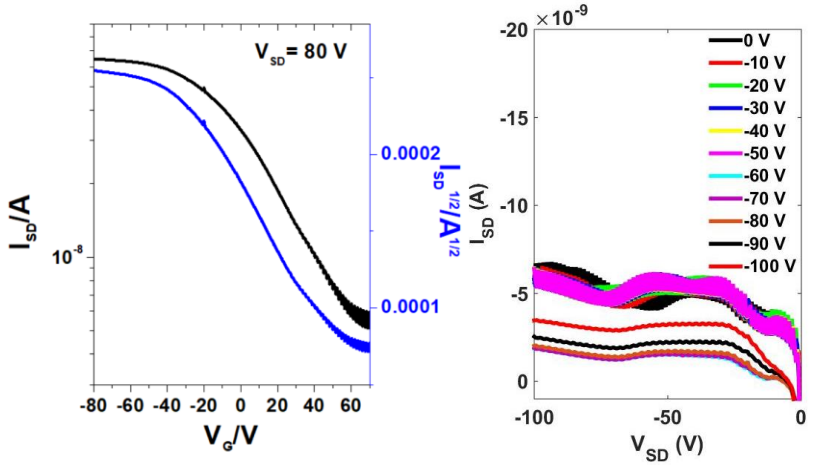

Figure 5-13. Transfer (left) and output (right) curves of 5r-F, 5r-BTD, 5r-BDT, 5r-CBZ, 5r-TPTQ after thermal treatment (continuation)

Although mobilities are not very high, it should be noted that it can be hard for polymer chains to rearrange themselves in the most efficient manner inside a film. All of these materials are p-type semiconductors with mobility decreasing in the order 5r-BDT > 5r-F > 5r-CBZ > 5r-TPTQ > 5r-BTD. HOMO energy level alignment with gold (-5.0 eV) plays an important role for injection of positively charged holes into the polymer, the closer HOMO of the polymer to the Fermi energy level of gold the easier the injection. Observed trend follows HOMO energy levels with exception of 5r-F, its higher mobility can be explained by highest molecular weight among the synthesized polymers allowing for more interchain contacts. We can conclude that in situ chemical planarization is a valid strategy to improve mobility properties of the materials.

5.3 Conclusions

We have synthesized a series of organic conjugated polymers based on azaacene moiety. A built-in functionality allows to thermally cyclize the repeating unit in the polymer chain in solid state. This methodology allows to extend π-conjugation perpendicularly to the direction of the main chain. After thermal cyclization, polymers become p-type of semiconductors. The

cyclization-planarization of repeating units is supported by the evidences in the changes of UV/vis absorption spectra, IR spectra and TGA results. This work shows that azaacene ladder molecules is an interesting electro-active motif with potentials for further exploration.

5.4 Experimental section

Unless otherwise stated, all chemicals obtained from commercial suppliers were used without further purification. THF was distilled over sodium prior to use, toluene was passed through MBraun solvent purification system. Other solvents were purified by distillation prior to use. ^{1}H and ^{13}C NMR were recorded by using 400MHz Bruker DRX-400 or Bruker Avance II+ 500 MHz spectrometers. Mass spectra were obtained on Agilent 6224 Tof High Resolution Accurate Mass Spec (HRA-MS) system. Column chromatography was carried out on silica gel (silica 60M, 400-230 mesh). Optical properties were measured by using a Shimadzu UV-2401PC UV-Vis spectrophotometer. Molecular weights of polymers were determined by using GPC with a Waters Associates liquid chromatography equipped with a Waters 510 HPLC pump, a Waters 410 differential refractometer and a Waters 486 tunable UV-vis detector. Polystyrene standards were used for calibration and chloroform as eluent.

Compound 1[106]: 4-bromophenol (5.19g, 30 mmol, 1 eq) was mixed with potassium carbonate (8.28g, 60 mmol, 2 eq), 2-ethylhexyl bromide (16 ml, 90 mmol, 3 eq) and 30 ml of acetone. Mixture was refluxed overnight. After cooling off the reaction mixture was filtered through celite, washed with acetone, concentrated in vacuo. Impurities were distilled off, residue dissolved in hexanes, filtered through celite and concentrated affording 5.69g of compound 1 (67%). ^{1}H NMR (400 MHz, $CDCl_3$) δ 7.35 (d, J = 8.8 Hz, 2H), 6.78 (d, J = 9.3 Hz, 2H), 3.78 (d, J = 5.7 Hz, 2H), 1.71 (p, J = 6.1 Hz, 1H), 1.57 – 1.36 (m, 8H), 1.36 – 1.24 (m, 8H), 1.00 – 0.83 (m, 6H).

Compound 3: Compound 1 (5.69 g, 20.0 mmol) in 10ml of anhydrous THF, was added dropwise to mixture of 0.73g of freshly crushed magnesium activated with 0.1 ml of 1M DIBAL-H and 5 ml of THF. Mixture was stirred at reflux for 2 hours and added to solution of compound 2 (1 g, 5 mmol) in 10 ml of anhydrous THF. Reaction mixture was stirred overnight. After quenching with methanol and filtration through celite, solution was concentrated in vacuo and residue purified by column chromatography with hexanes – DCM gradient to afford compound 3 (1.689g, 84%). ^{1}H NMR (400 MHz, $CDCl_3$) δ 7.64 (d, *J* = 8.5 Hz, 2H), 7.31 (d, *J* = 8.5 Hz, 1H), 6.94 (d, *J* = 8.5 Hz, 2H), 6.86 (d, *J* = 1.9 Hz, 1H), 6.70 (dd, *J* = 8.5, 1.9 Hz, 1H), 6.09 (br s, 2H), 3.90 (d, *J* = 5.4 Hz, 2H), 1.76 (m, *J* = 6.0 Hz, 1H), 1.60 – 1.40 (m, 4H), 1.34 (dq, *J* = 7.2, 4.6, 3.6 Hz, 4H), 1.02 – 0.86 (m, 6H). ^{13}C NMR (126 MHz, $CDCl_3$) δ 196.86, 162.23, 151.32, 135.10, 131.58, 131.51, 128.20, 119.20, 118.38, 117.39, 113.86, 70.52, 39.17, 30.38, 28.97, 23.74, 22.97, 14.06, 11.05.

Compound 4: Compound 3 (1.689 g, 4.2 mmol, 2.5 eq), dimethyl 2,5-dioxo-1,4-cyclohexanedicarboxylate (0.381g, 1.7 mmol, 1 eq) were mixed with 13 ml of ethanol and mixture was purged with nitrogen for 10 min. 6 M Hydrochloric acid (0.14ml) was added and the mixture was refluxed for 24 hours. After cooling the solid was filtered off and recrystallized from ethanol (1.418 g, 86%). ^{1}H NMR (500 MHz, $CDCl_3$) δ 8.36 – 8.32 (m, 2H), 7.50 (dd, *J* = 9.0, 2.0 Hz, 2H), 7.39 (dd, *J* = 8.9, 0.5 Hz, 2H), 7.32 (dt, *J* = 7.3, 1.9 Hz, 2H), 7.10 – 7.02 (m, 6H), 5.39 (s, 2H), 3.96 (dt, *J* = 5.7, 1.9 Hz, 4H), 3.62 (s, 6H), 1.82 (p, *J* = 6.0 Hz, 2H), 1.64 – 1.46 (m, 8H), 1.39 (d, *J* = 6.6 Hz, 8H), 1.04 – 0.93 (m, 12H). ^{13}C NMR (126 MHz, $CDCl_3$) δ 169.97, 160.01, 155.43, 148.99, 148.05, 131.52, 130.72, 130.28, 128.38, 126.55, 126.51, 125.55, 124.11, 115.06, 115.03, 115.00, 70.64, 54.14, 53.26, 39.56, 30.72, 29.26, 24.08, 23.26, 14.31, 11.33. HRAMS m/z: $C_{52}H_{56}Br_2N_2O_6$, Calcd, 962.2505. Found, (M^+), 962.2507.

Monomer 5r: compound 4 (1.418g, 1.47 mmol, 1eq), chloranil (0.5g, 2 mmol, 1.3 eq) and methyl cellosolve (6ml) were refluxed overnight. Mixture was cooled to room temperature. After addition of water, product was extracted with DCM 3 times. Organic layers were combined, dried with sodium sulfate and concentrated. Column chromatography with hexanes - DCM gradient afforded monomer 5r (1.29g, 91%), purple flakes. ^{1}H NMR (500 MHz, $CDCl_3$) δ 8.25 (d, *J* = 1.7 Hz, 2H), 7.50-7.41 (m, 2H), 7.33 – 7.27 (m, 4H), 7.15 – 7.03 (m, 4H), 4.05 – 3.94 (br, 4H), 3.60 (s, 6H), 1.84 (m, *J* = 6.1 Hz, 2H), 1.64 – 1.44 (m, 8H), 1.42-1.35 (dq, *J* = 7.1, 3.4 Hz, 8H), 1.04 – 0.93 (m, 12H). ^{13}C NMR (101 MHz, $CDCl_3$) δ 160.12, 150.22, 147.31, 142.50, 133.88, 133.62, 132.55, 132.16, 130.55, 128.50, 126.67, 126.43, 125.79, 122.66, 113.95, 70.89, 52.40, 39.56, 30.72, 29.29, 24.07, 23.24, 14.29, 11.31; HRAMS m/z: $C_{52}H_{54}Br_2N_2O_6$, Calcd, 960.2349. Found, (M^+), 960.2345.

Typical polymerization procedure, 5r-F: 5r (250.00mg, 0.2596 mmol, 1 eq), F-$Bpin_2$ (166.85 mg, 0.2596 mmol, 1 eq), $Pd(PPh_3)_4$ (15 mg, 0.013 mmol, 5% eq), were combined in a dry round bottom flask. After 3 nitrogen-vacuum cycles THF (5 ml) and aqueous potassium carbonate (2M, 0.6ml, 1.2 mmol, 4 eq) were added and solution was degassed by purging with nitrogen for 15 min. Reaction flask was submerged into preheated to 100°C oil bath and stirred at this temperature for 5 days. Reaction mixture was cooled to room temperature and precipitated in methanol. Solid polymer was redissolved in chloroform and filtered through celite. Solution was concentrated and precipitated in methanol. Polymer was purified by Soxhlett extraction with methanol, acetone, hexanes and chloroform. Chloroform fraction was concentrated and precipitated in methanol, polymer was filtered and dried under vacuum for 24 hours (228mg, 74%). ^{1}H NMR (500 MHz, $CDCl_2CDCl_2$, 373K) δ 8.60 (br s, 2H), 8.36 (br s, 2H), 7.88 (br s, 4H), 7.83 (br s, 2H), 7.65 (d, *J* = 16.9 Hz, 2H), 7.53 (d, *J* = 8.7 Hz, 2H), 7.26 – 7.20 (m, 6H), 4.15 (d, *J* = 21.9 Hz, 4H), 3.72 (s,

6H), 2.19 (br, 2H), 1.97 (br, 4H), 1.76 – 1.46 (br m, 12H), 1.29 – 1.03 (br m, 28H), 1.00 – 0.81 (m, 18H); IR (ATR): ν/cm^{-1} 2925.64, 2855.33, 1738.41, 1608.26, 1513.03, 1466.04, 1433.56, 1398.42, 1285.10, 1244.98, 1175.39, 1013.75, 817.77; GPC: Mn=35.3 kDa, Mw=62.1, PDI=1.76.

5r-BTD: 125mg, 51%, chloroform fraction. IR (ATR): ν/cm^{-1} 2925.46, 2857.18, 1732.60, 1606.49, 1572.90, 1541.67, 1507.83, 1465.38, 1434.35, 1379.26, 1285.18, 1241.53, 1160.29, 1014.43, 931.66, 881.77, 830.21, 819.79, 780.65, 720.75, 692.90, 609.62, 582.62, 523.01, 469.15, 448.98; GPC: Mw=18.6 kDa, Mn= 9.1 kDa, PDI=2.05.

5r-BDT: 105.4mg, 33%, chloroform fraction. IR (ATR): ν/cm^{-1} 2954.19, 2922.96, 2855.97, 1734.79, 1607.75, 1508.65, 1435.68, 1377.68, 1353.27, 1241.35, 1211.68, 1172.73, 1160.26, 1029.57, 1014.38, 818.70, 779.54, 718.62, 665.19, 612.37, 572.27, 509.36, 449.13; GPC: Mw=14.4 kDa, Mn= 9.2 kDa, PDI=1.56.

5r-CBZ: 167mg, 77%, chloroform fraction. IR (ATR): ν/cm^{-1} 2953.86, 2926.15, 2857.81, 1735.94, 1607.06, 1543.51, 1508.52, 1463.33, 1432.93, 1380.41, 1350.06, 1284.25, 1242.78, 1208.18, 1173.16, 1160.79, 1028.92, 923.34, 878.89, 830.29, 803.73, 781.47, 714.83, 657.74, 567.07, 524.43, 451.87; GPC: Mw=38.2 kDa, Mn= 22.1 kDa, PDI=1.73.

5r-TPTQ: 289mg, 91%, chloroform fraction. IR (ATR): ν/cm^{-1} 2952.93, 2923.62, 2854.96, 1736.34, 1648.63, 1607.39, 1508.74, 1463.81, 1435.25, 1379.10, 1354.86, 1286.47, 1242.95, 1212.82, 1173.54, 1161.26, 122.77, 1030.27, 1014.85, 877.57, 851.46, 832.17, 819.50, 779.80, 764.40, 720.66, 611.31, 574.63, 520.33, 44.80; GPC: Mw=23.8 kDa, Mn= 12.3 kDa, PDI=1.94.

5.5 References

(113) Rajca, A.; Boratyński, P. J.; Olankitwanit, A.; Shiraishi, K.; Pink, M.; Rajca, S. *J. Org. Chem.* **2012**, *77* (5), 2107–2120.

(114) Bryant, J. J.; Zhang, Y.; Lindner, B. D.; Davey, E. A.; Appleton, A. L.; Qian, X.; Bunz, U. H. F. *J. Org. Chem.* **2012**, *77* (17), 7479–7486.

(115) Biegger, P.; Stolz, S.; Intorp, S. N.; Zhang, Y.; Engelhart, J. U.; Rominger, F.; Hardcastle, K. I.; Lemmer, U.; Qian, X.; Hamburger, M.; Bunz, U. H. F. *J. Org. Chem.* **2015**, *80* (1), 582–589.

(116) Wu, Y.; Yin, Z.; Xiao, J.; Liu, Y.; Wei, F.; Tan, K. J.; Kloc, C.; Huang, L.; Yan, Q.; Hu, F.; Zhang, H.; Zhang, Q. *ACS Appl. Mater. Interfaces* **2012**, *4* (4), 1883–1886.

(117) Li, J.; Zhang, Q. *ACS Appl. Mater. Interfaces* **2015**, *7* (51), 28049–28062.

(118) Müller, M.; Koser, S.; Tverskoy, O.; Rominger, F.; Freudenberg, J.; Bunz, U. H. F. *Chem. – A Eur. J.* **2019**, *25* (24), 6082–6086.

(119) Xie, Y.; Fujimoto, T.; Dalgleish, S.; Shuku, Y.; Matsushita, M. M.; Awaga, K. *J. Mater. Chem. C* **2013**, *1* (21), 3467.

(120) Chen, C.; Ruan, H.; Feng, Z.; Fang, Y.; Tang, S.; Zhao, Y.; Tan, G.; Su, Y.; Wang, X. *Angew. Chemie* **2020**, *59*, 1–7.

(121) Zhao, K.; Yu, F.; Liu, W.; Huang, Y.; Said, A. A.; Li, Y.; Zhang, Q. *J. Org. Chem.* **2020**, *85* (1), 101–107.

(122) Yang, Y.; da Costa, R. C.; Fuchter, M. J.; Campbell, A. J. *Nat. Photonics* **2013**, *7* (8), 634–638.

(123) Inoue, Y.; Sakamaki, D.; Tsutsui, Y.; Gon, M.; Chujo, Y.; Seki, S. *J. Am. Chem. Soc.* **2018**, *140* (23), 7152–7158.

(124) Adamo, C.; Jacquemin, D. *Chem. Soc. Rev.* **2013**, *42* (3), 845–856.

(125) Kitahara, K.; Nishi, H. *J. Heterocycl. Chem.* **1988**, *25* (4), 1063–1065.

(126) Qian, Z.; Galuska, L.; McNutt, W. W.; Ocheje, M. U.; He, Y.; Cao, Z.; Zhang, S.; Xu, J.; Hong, K.; Goodman, R. B.; Rondeau- Gagné, S.; Mei, J.; Gu, X. *J. Polym. Sci. Part B Polym. Phys.* **2019**, *57* (23), 1635–1644.

(127) Xie, R.; Weisen, A. R.; Lee, Y.; Aplan, M. A.; Fenton, A. M.; Masucci, A. E.; Kempe, F.; Sommer, M.; Pester, C. W.; Colby, R. H.; Gomez, E. D. *Nat. Commun.* **2020**, *11* (1), 893.

(128) Allinson, G.; Bushby, R. J.; Jesudason, M. V.; Paillaud, J.-L.; Taylor, N. *J. Chem. Soc. Perkin Trans. 2* **1997**, No. 2, 147–156.

(129) Sakamoto, T.; Pac, C. *J. Org. Chem.* **2001**, *66* (1), 94–98.

APPENDIX

^{1}H AND ^{13}C SPECTRA FOR NEW COMPOUNDS

Figure A-1. ^{1}H and ^{13}C spectra of compound 2-5

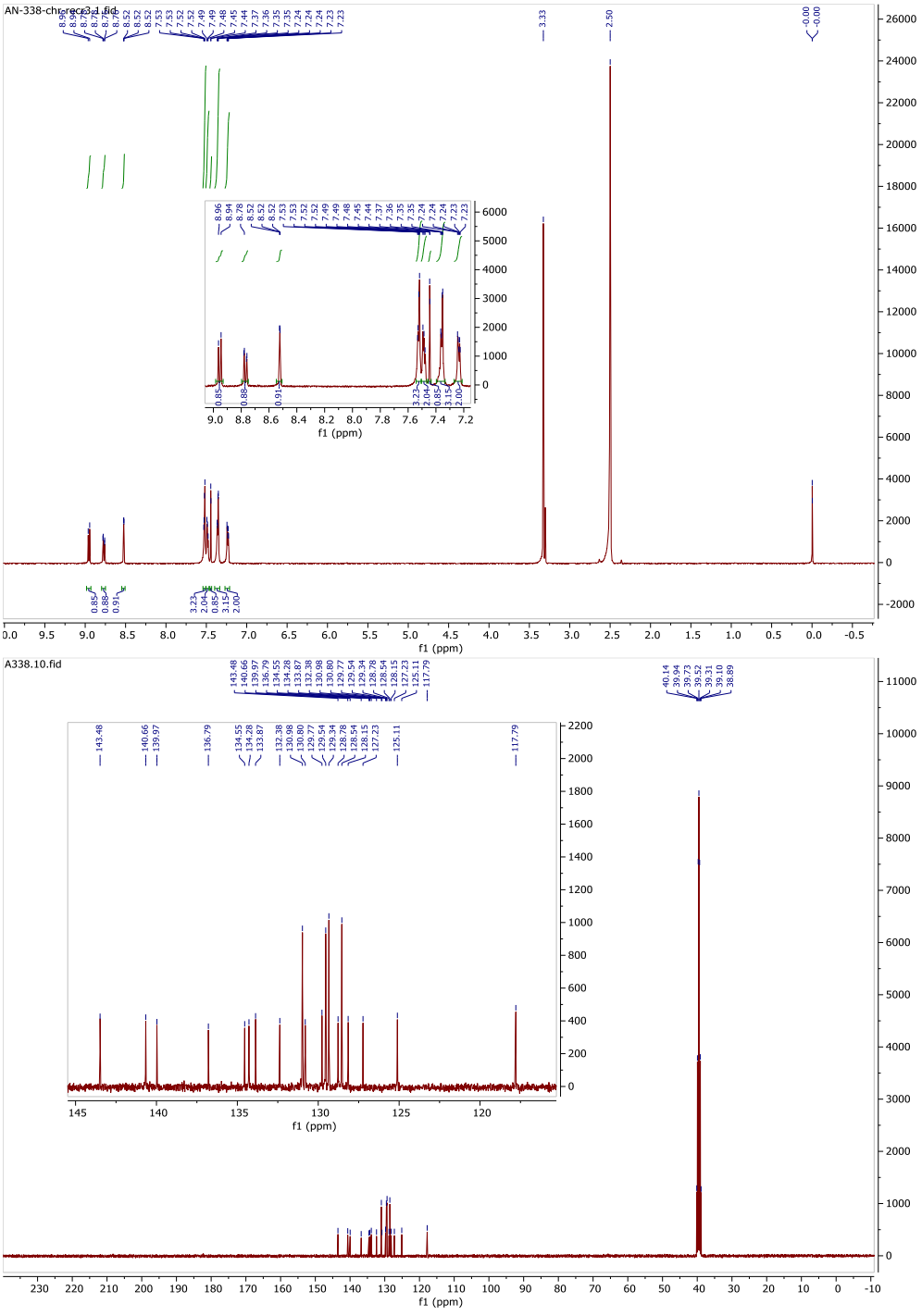

Figure A-2. ^{1}H and ^{13}C spectra of compound 2-12

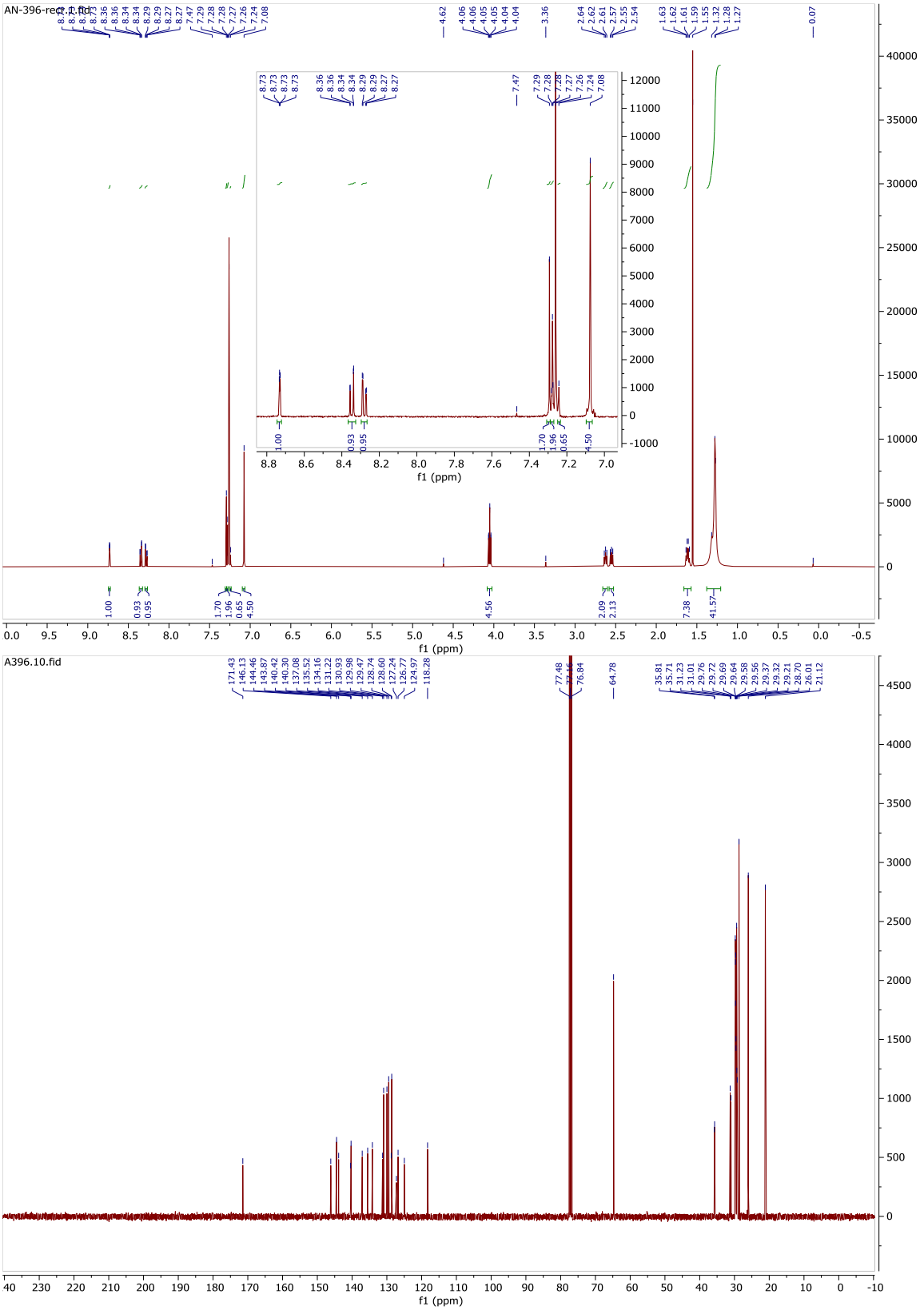

Figure A-3. ^{1}H spectra of polymers PTQ-A and PTQ-40

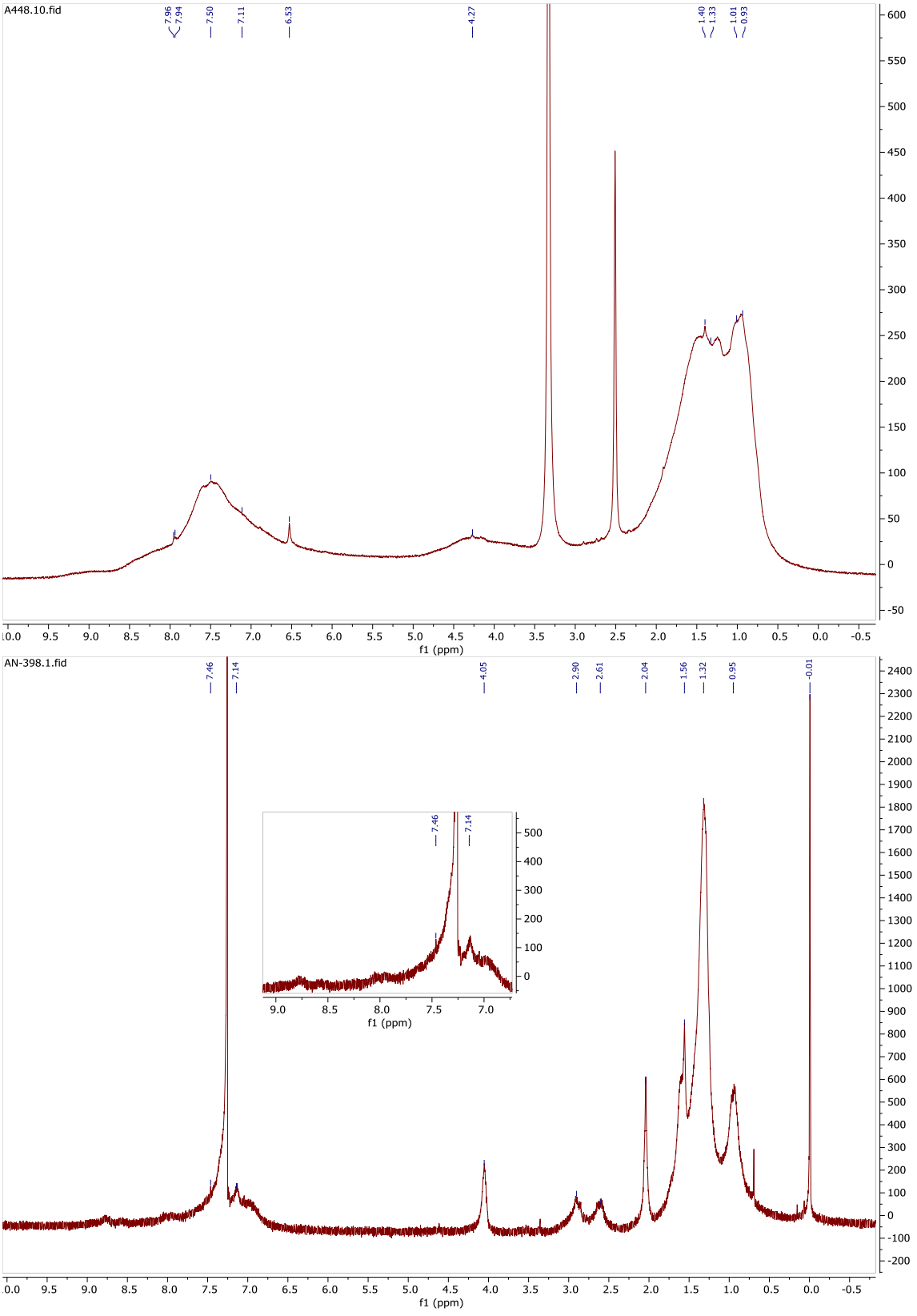

Figure A-4. ^{1}H spectra of polymers PTQ-16 and PTQ-B

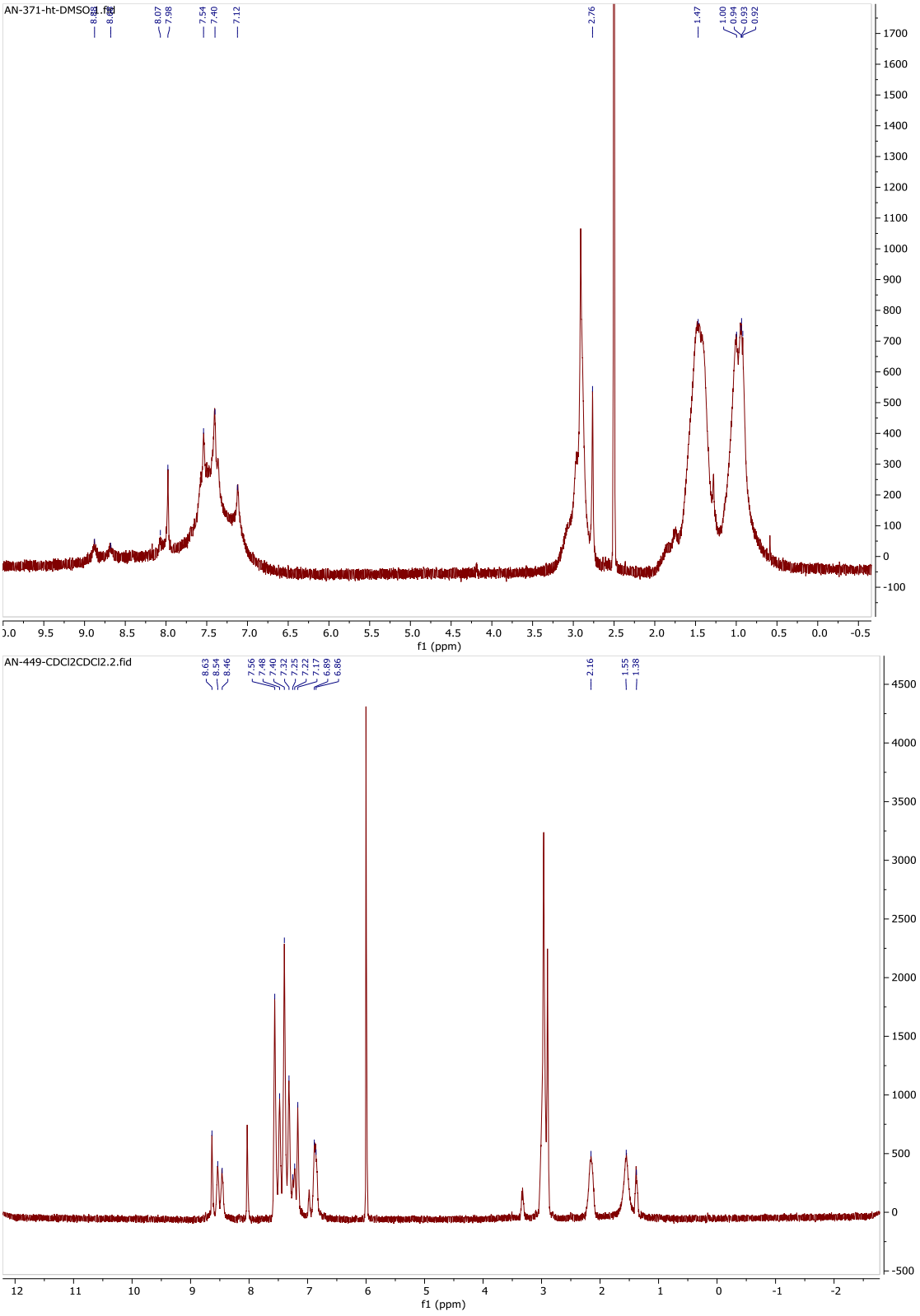

Figure A-5. ^{1}H and ^{13}C spectra of compound 3-3

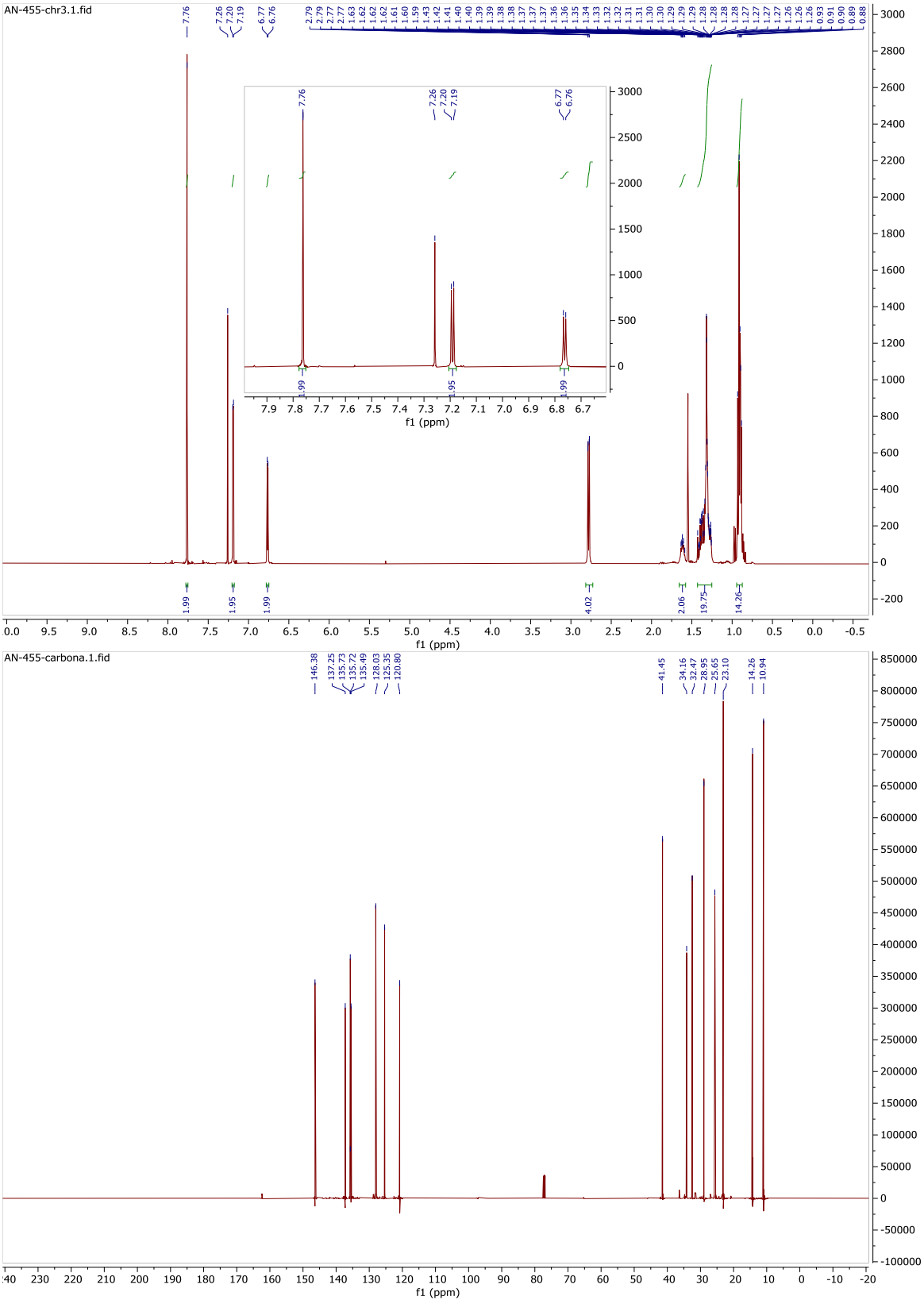

Figure A-6. ^{1}H and ^{13}C spectra of compound 3-5

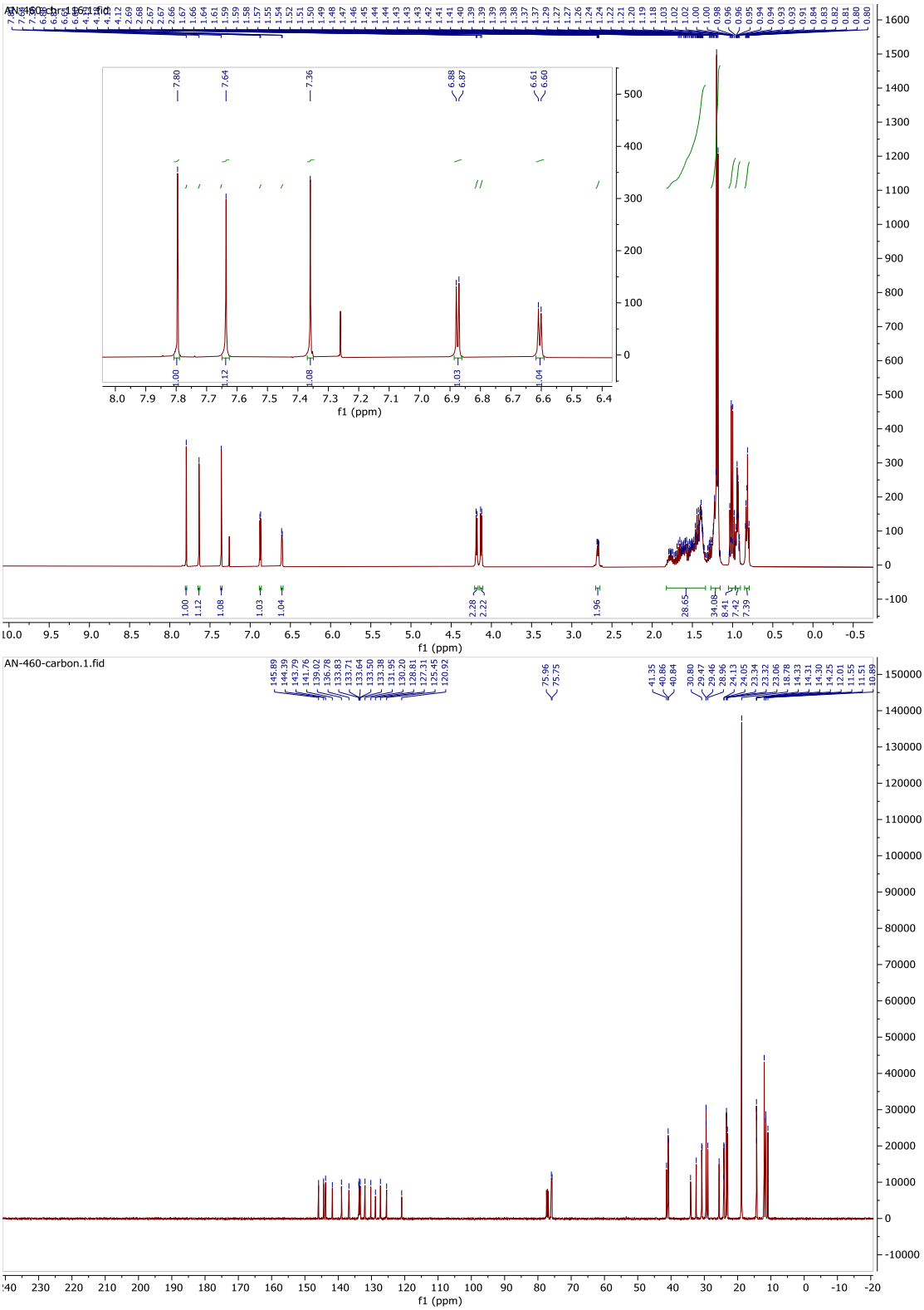

Figure A-7. ^{1}H and ^{13}C spectra of compound 3-6

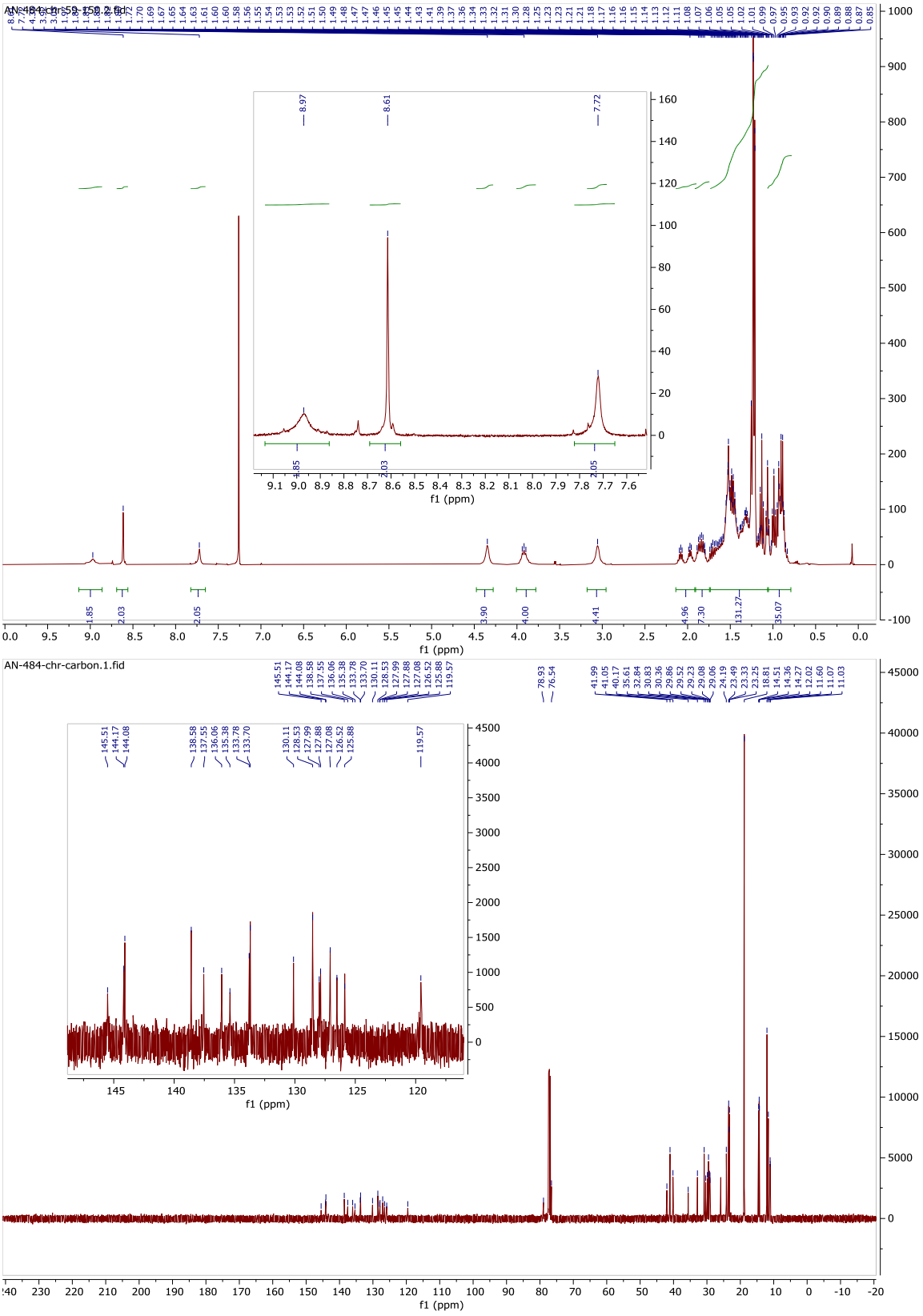

Figure A-8. ^{1}H and ^{13}C spectra of compound 3-8

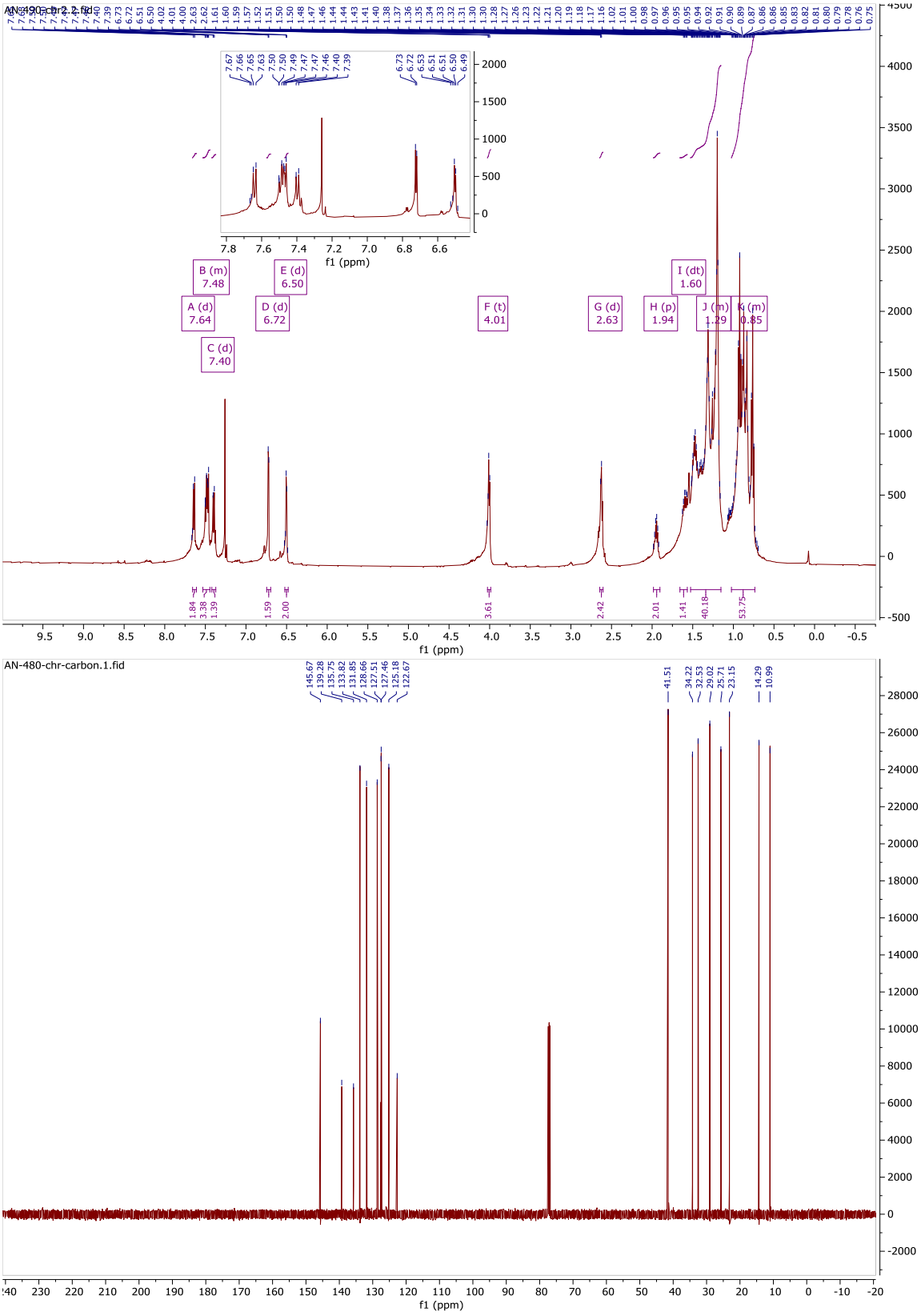

Figure A-9. ^{1}H and ^{13}C spectra of compound 3-9

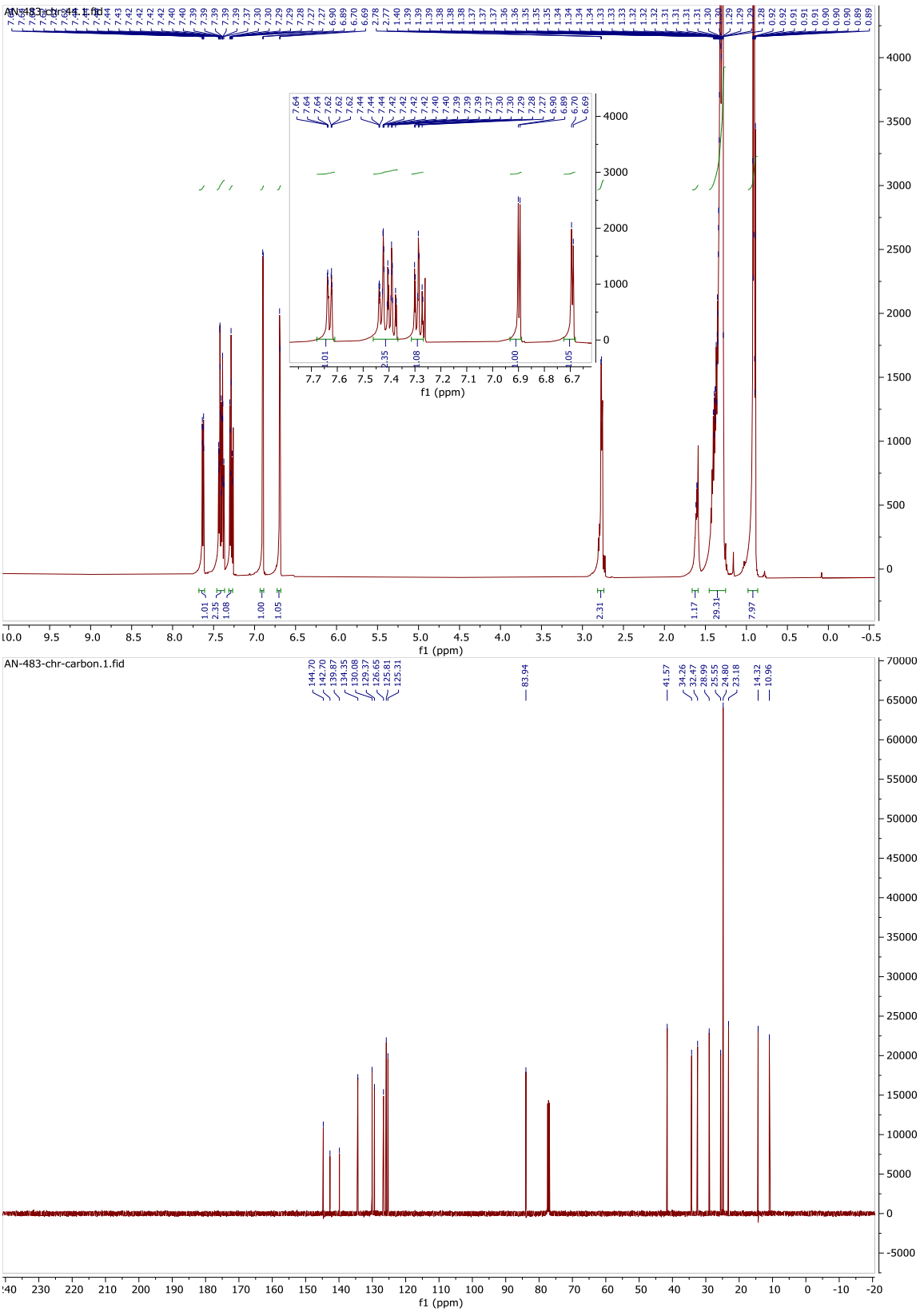

Figure A-10. ^{1}H and ^{13}C spectra of uncyclized precursor to MC-7R

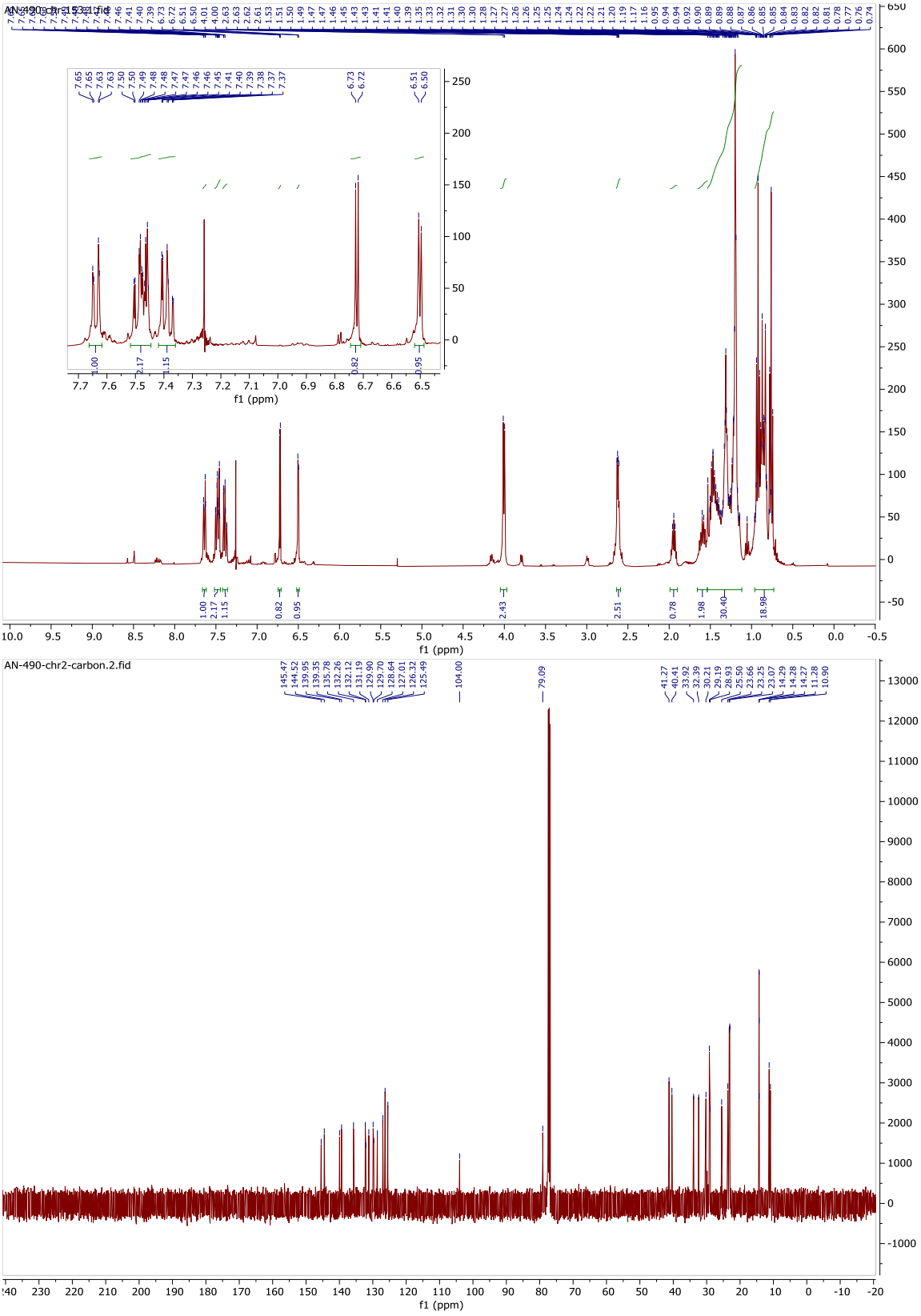

Figure A-11. ^{1}H spectrum of compound MC-7R (poor solubility)

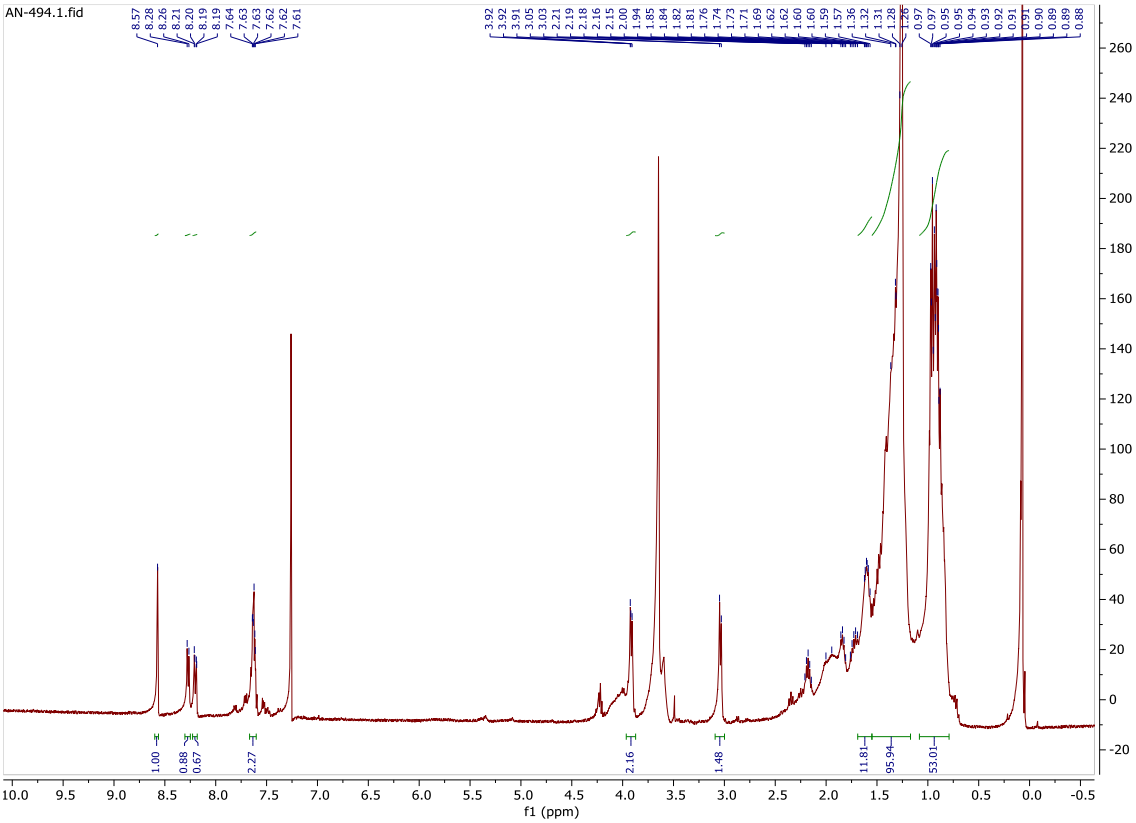

Figure A-12. ^{1}H and ^{13}C spectra of compound MC-7P

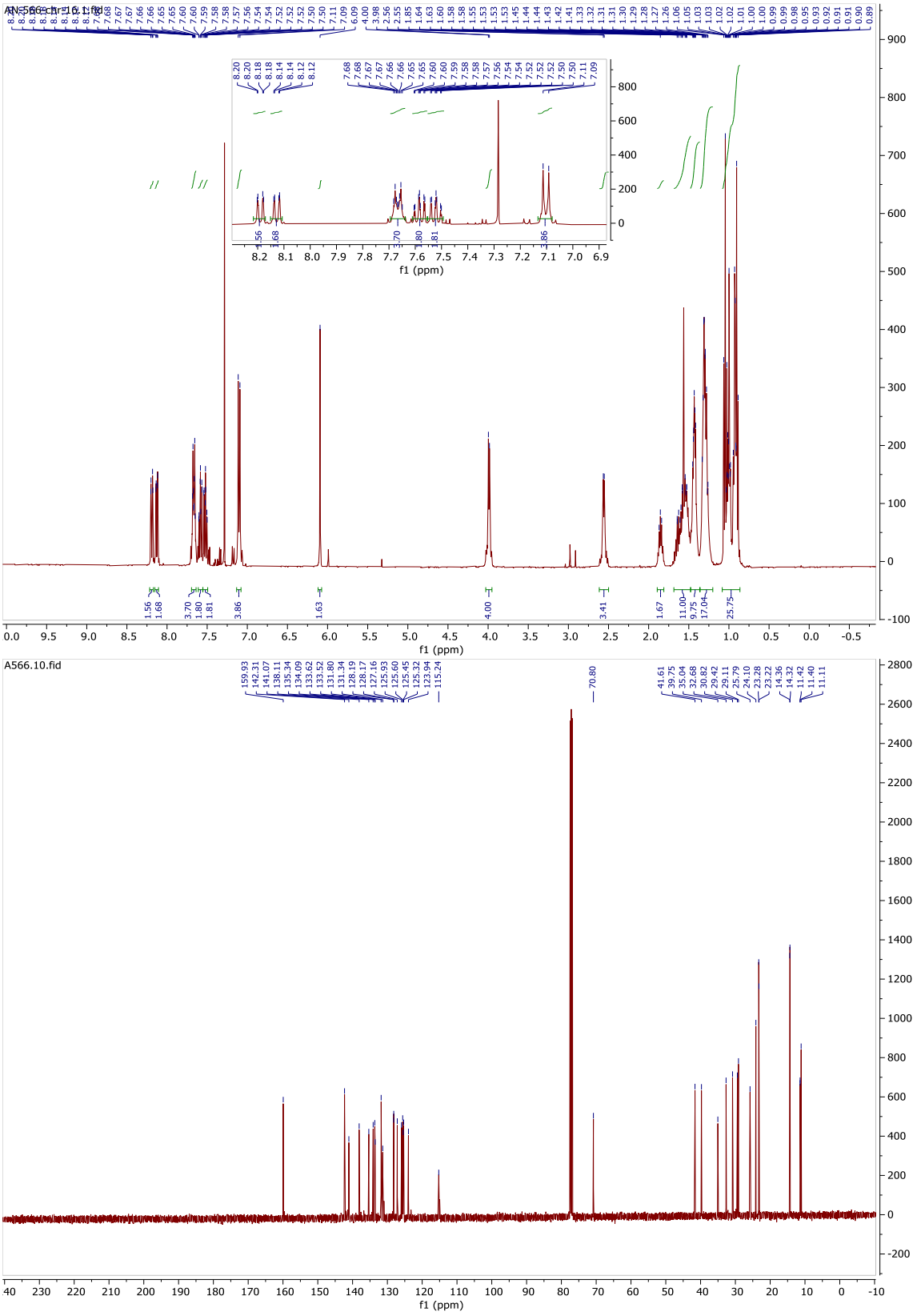

Figure A-13. ^{1}H and ^{13}C spectra of compound MC-9R

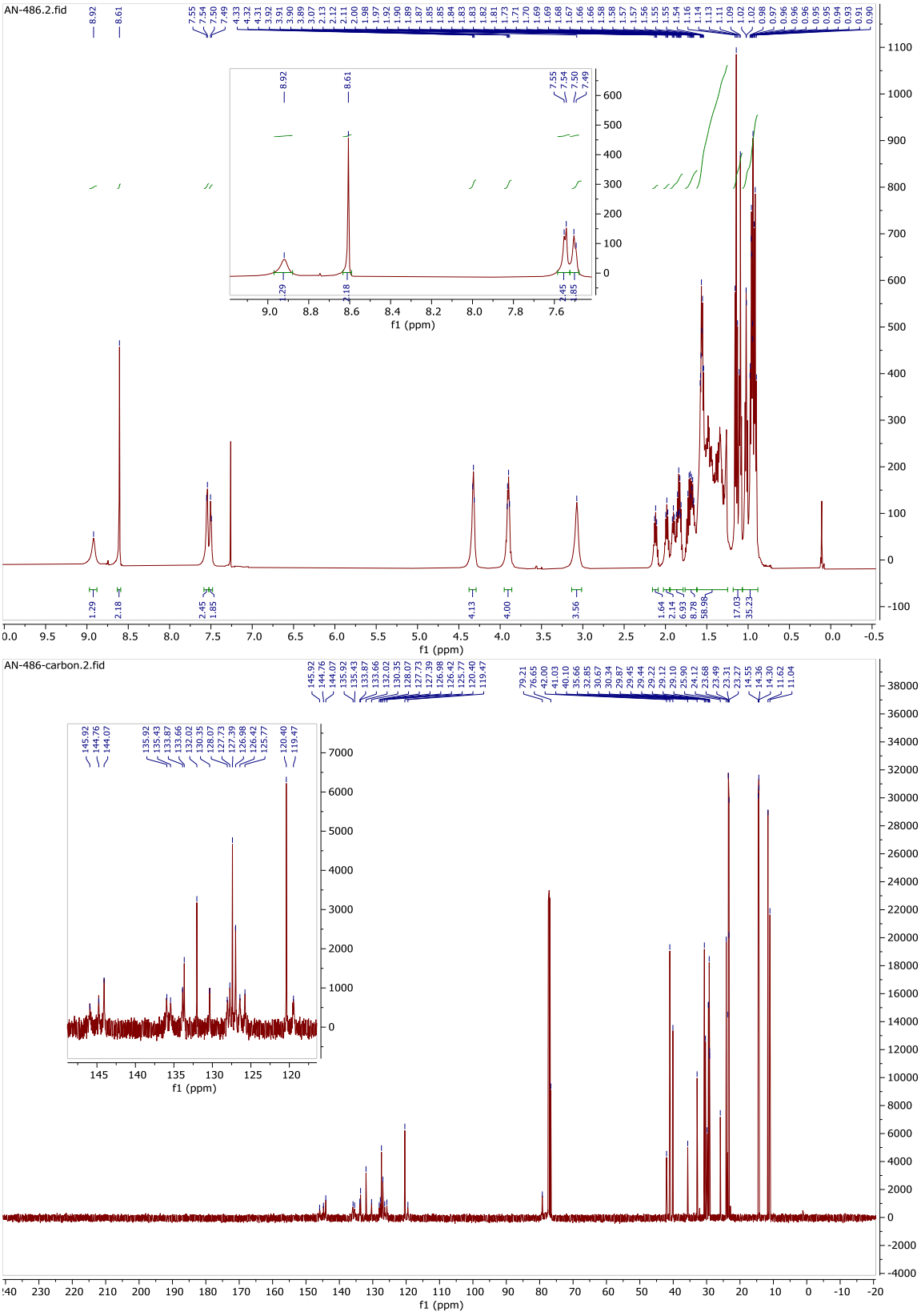

Figure A-14. ^{1}H and ^{13}C spectra of compound MW-9r

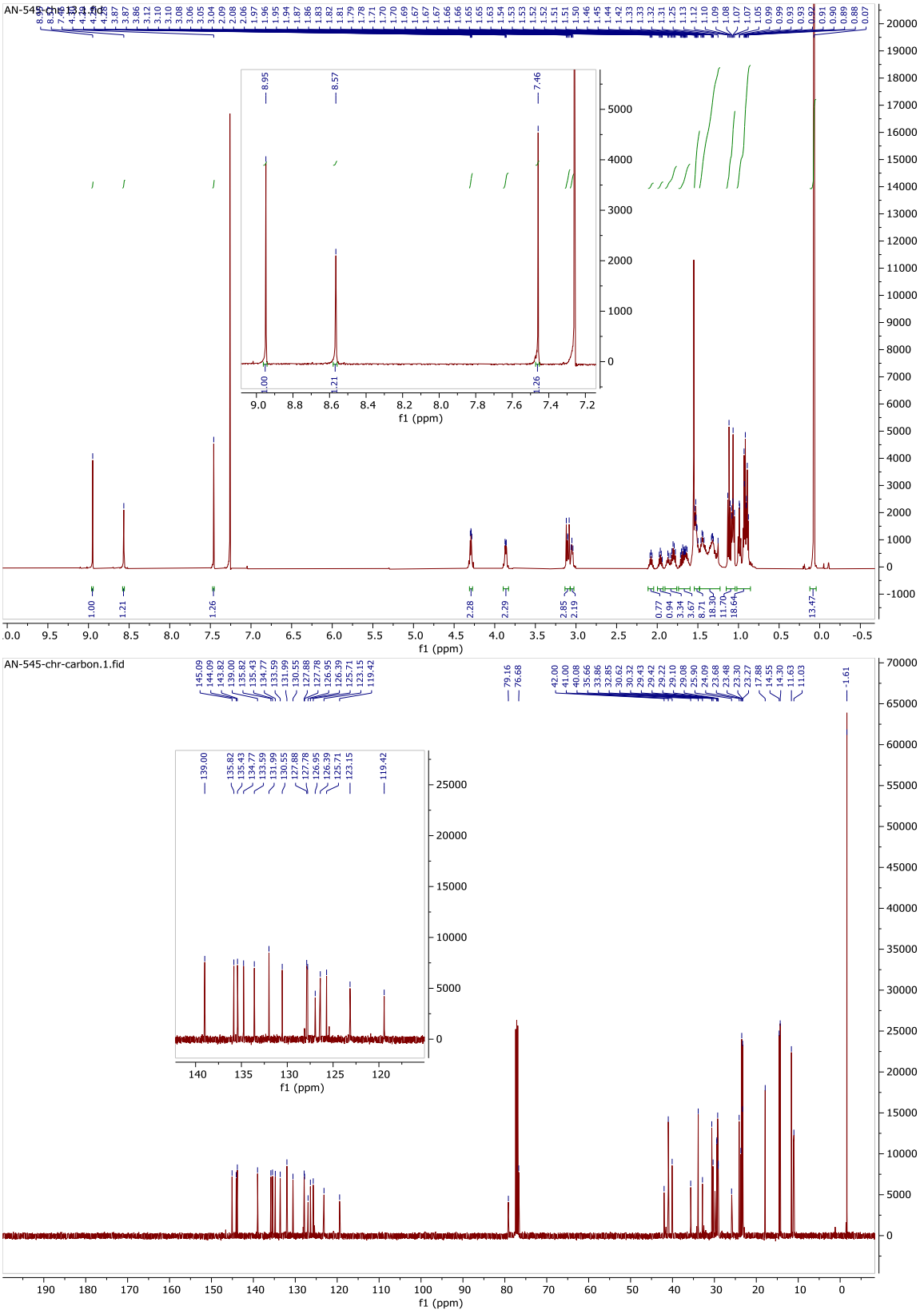

Figure A-15. ^{1}H and ^{13}C spectra of compound MW-5r

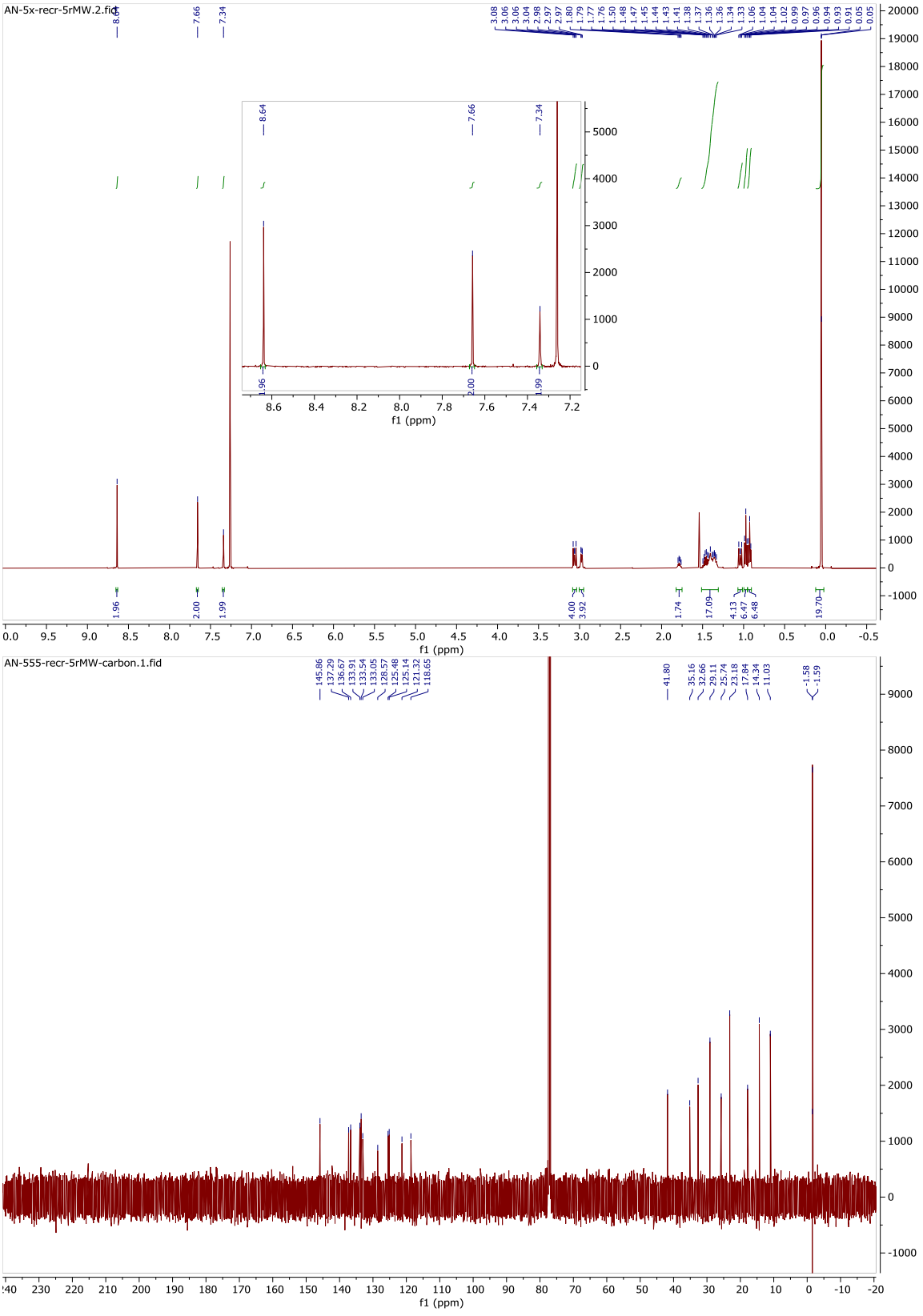

Figure A-16. ^{1}H and ^{13}C spectra of compound 4-8

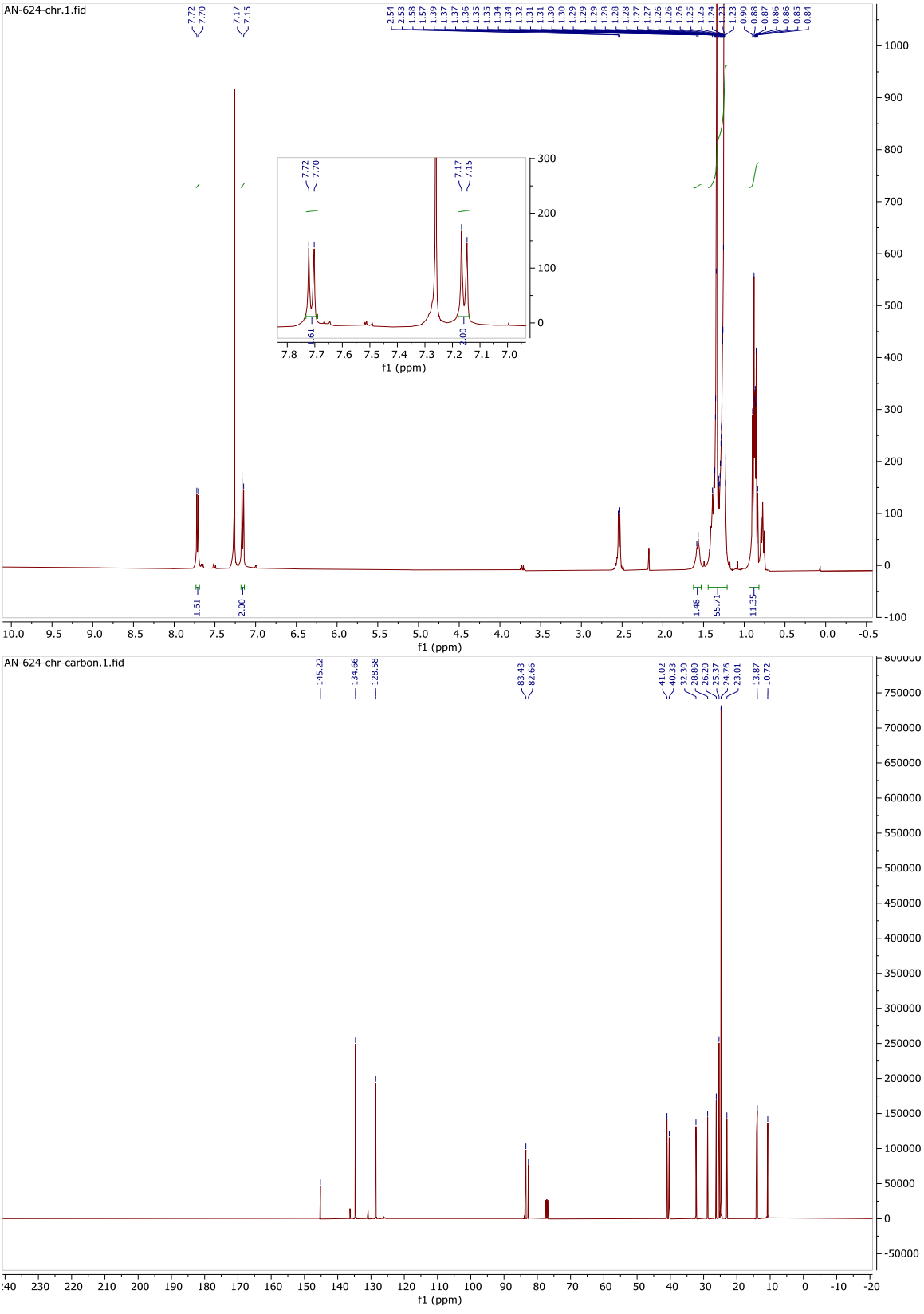

Figure A-17. ^{1}H and ^{13}C spectra of compound 4-9

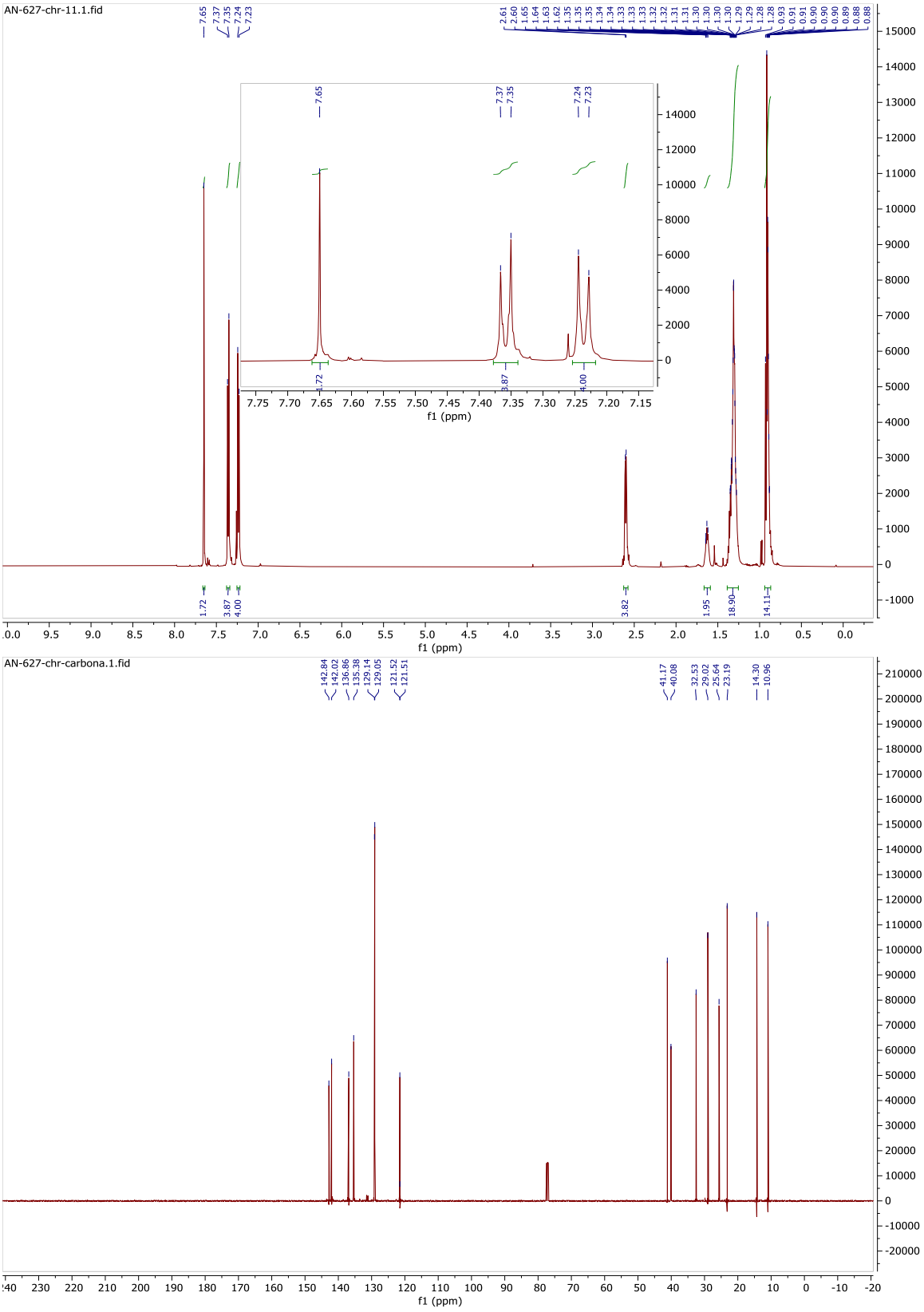

Figure A-18. ^{1}H spectra of polymers TPB (top) and TPF (bottom)

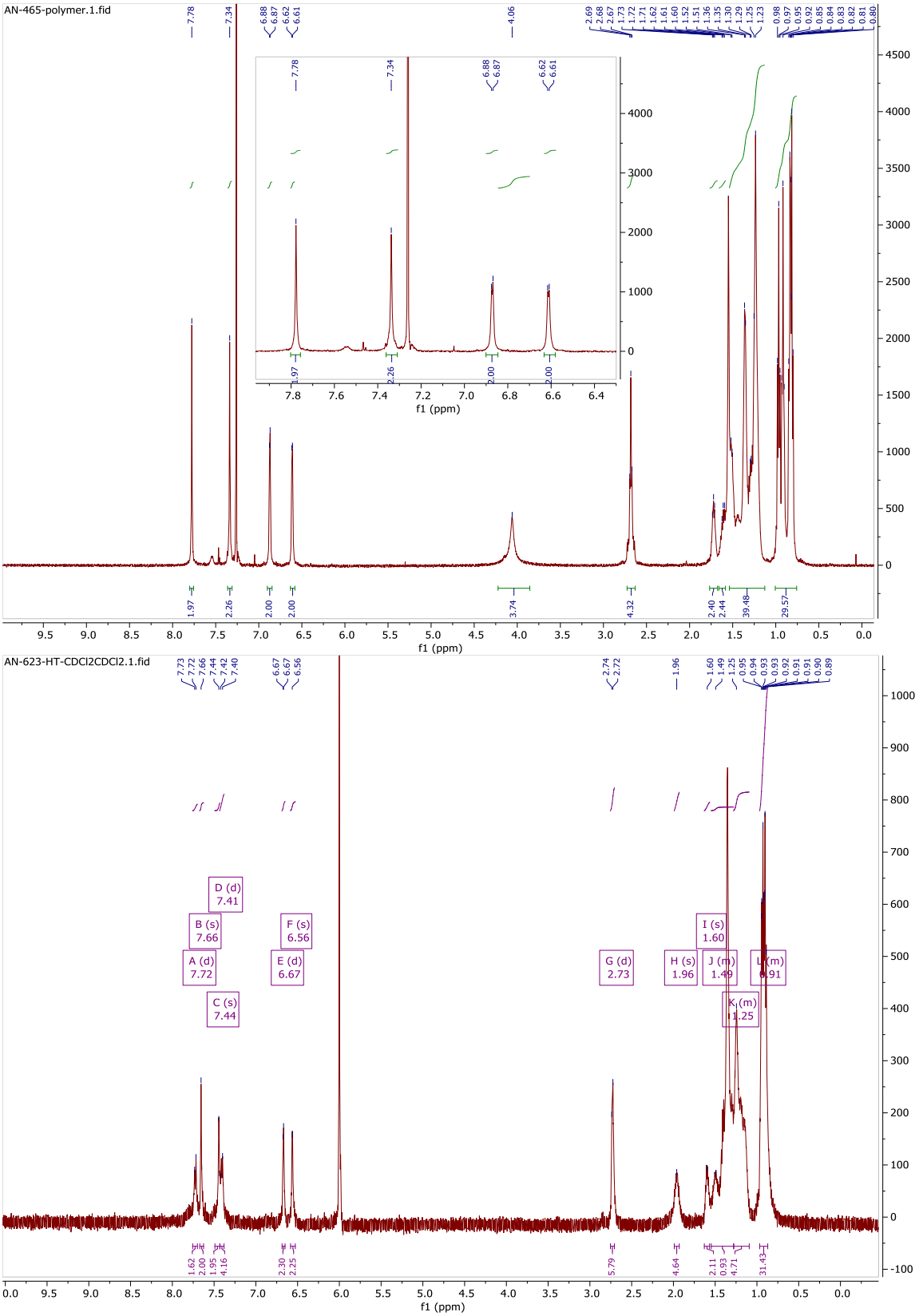

Figure A-19. ^{1}H spectra of polymers PPF (top) and TPTF (bottom)

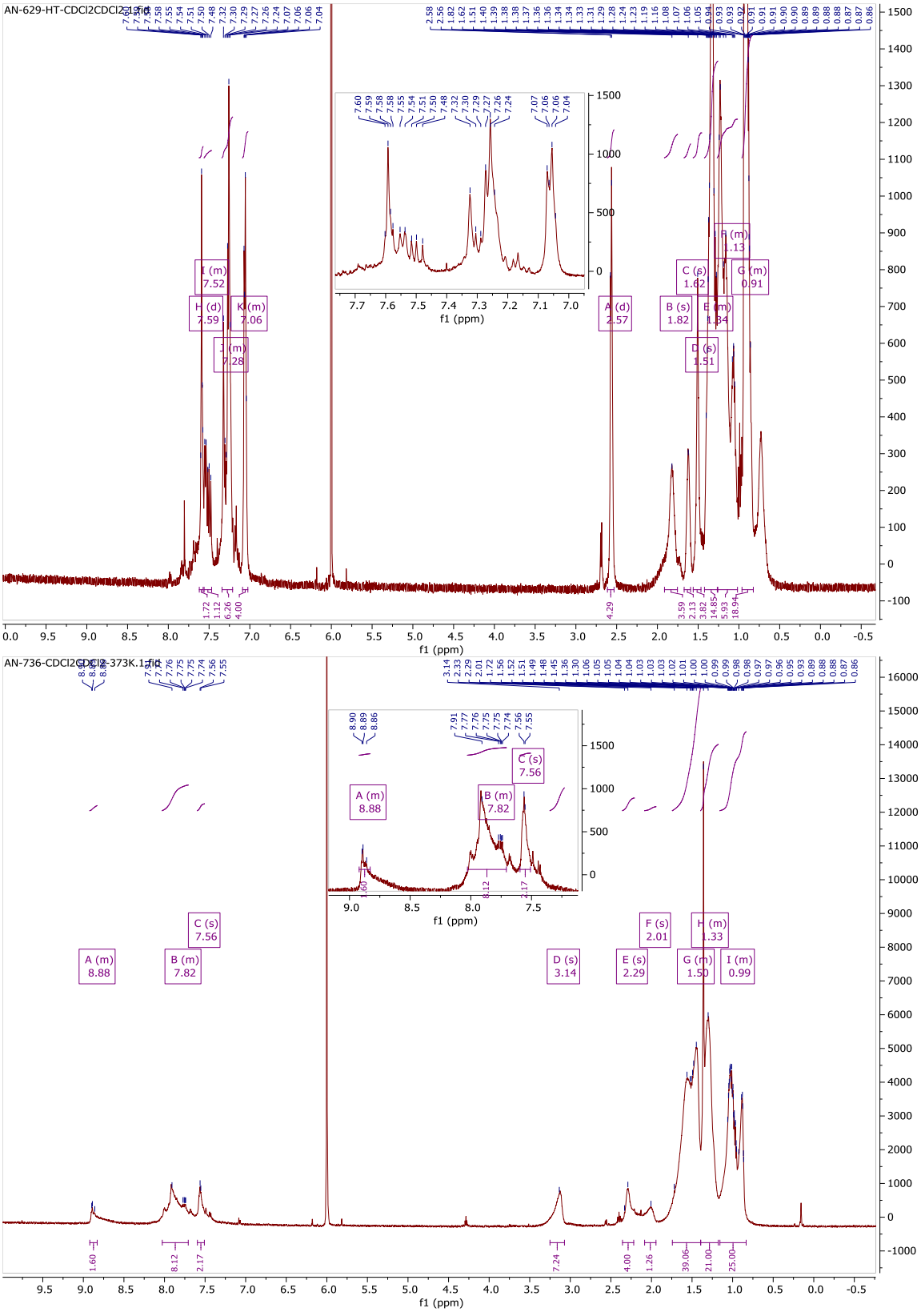

Figure A-20. ^{1}H and ^{13}C spectra of compound 5-3

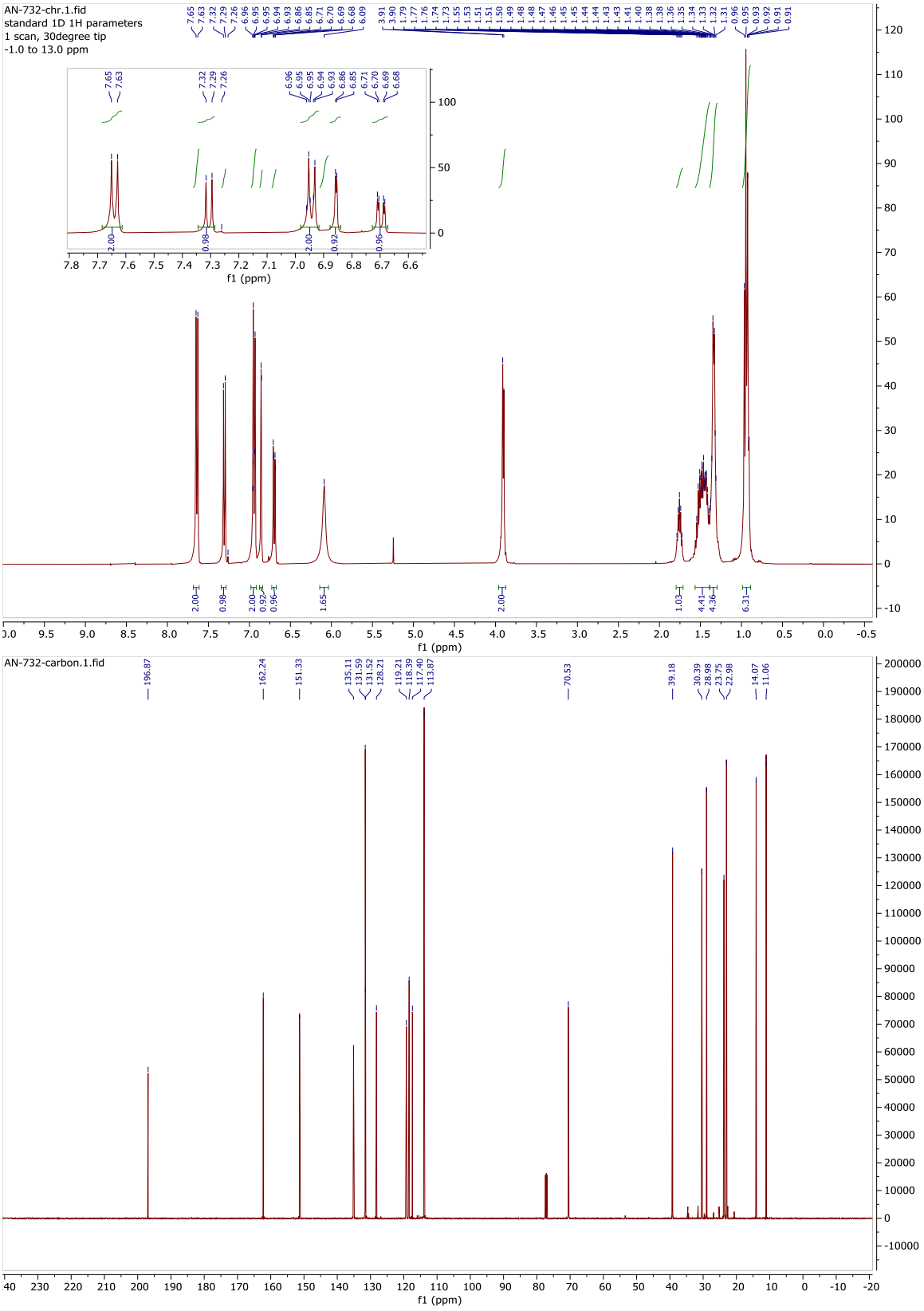

Figure A-21. ^{1}H and ^{13}C spectra of compound 5-4

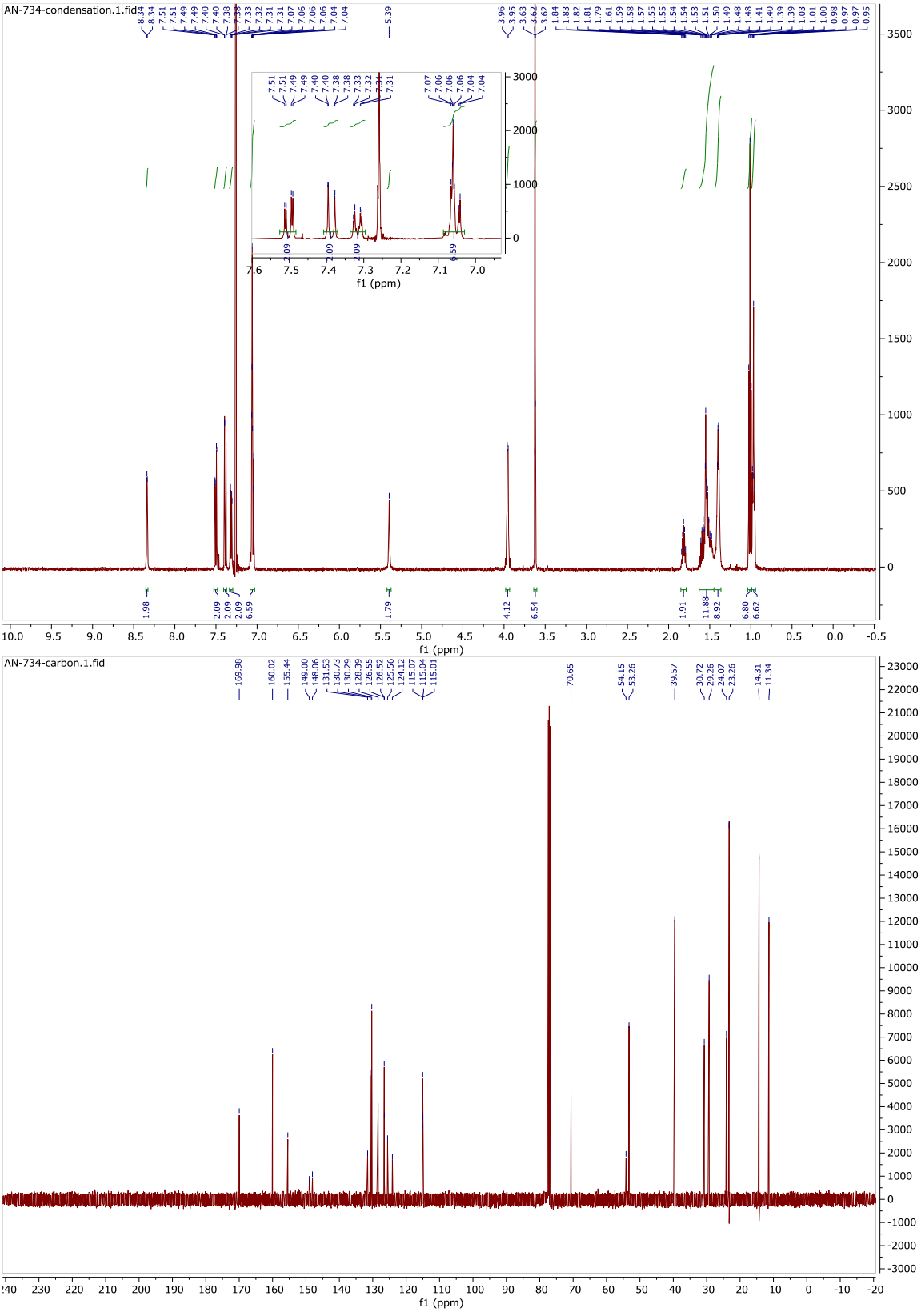

Figure A-22. ^{1}H and ^{13}C spectra of compound 5r

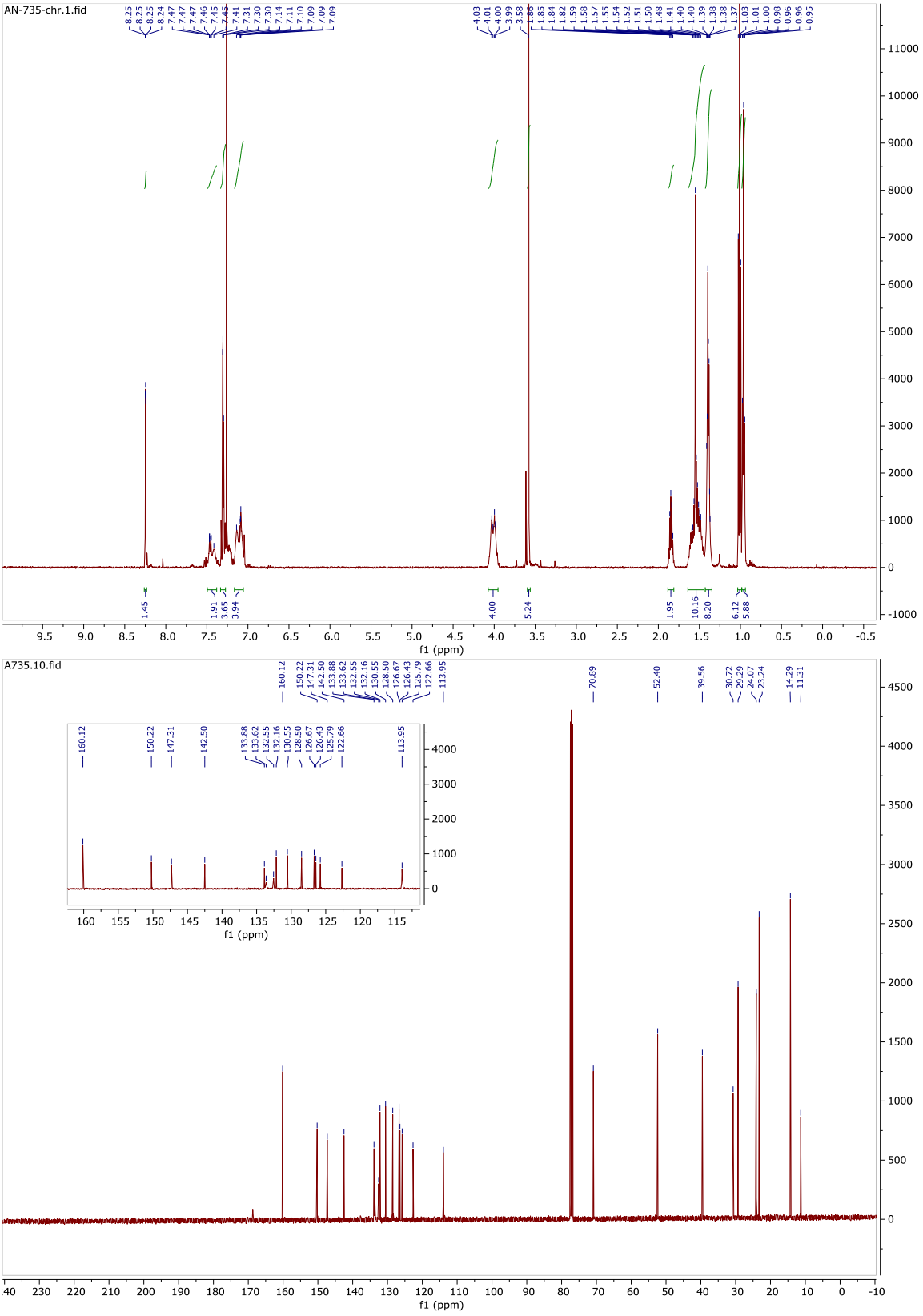

Figure A-23. ^{1}H spectra of polymers 5r-F (top) and 5r-BTD (bottom)

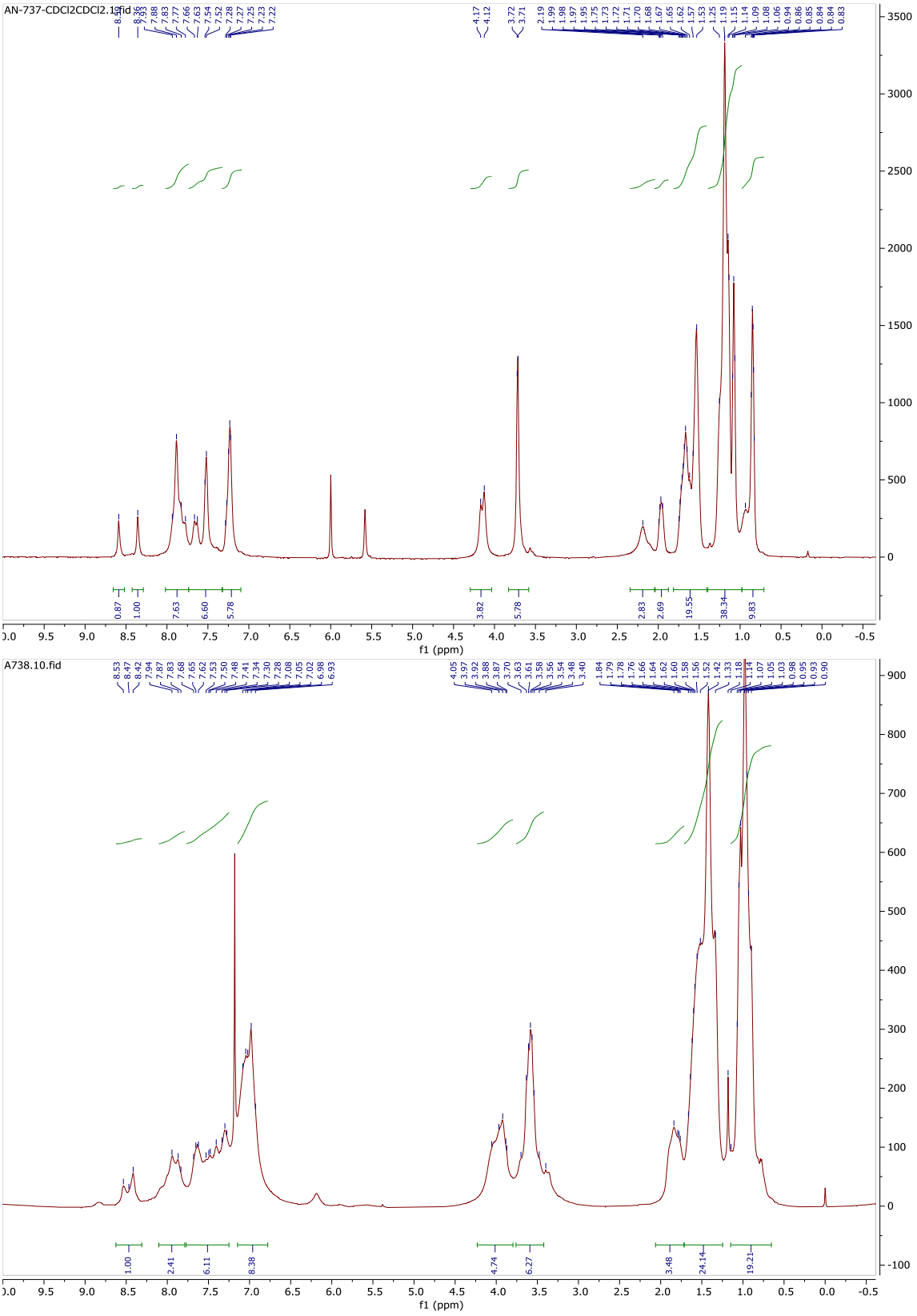

Figure A-24. ^{1}H spectra of polymers 5r-BDT (top) and 5r-CBZ (bottom)

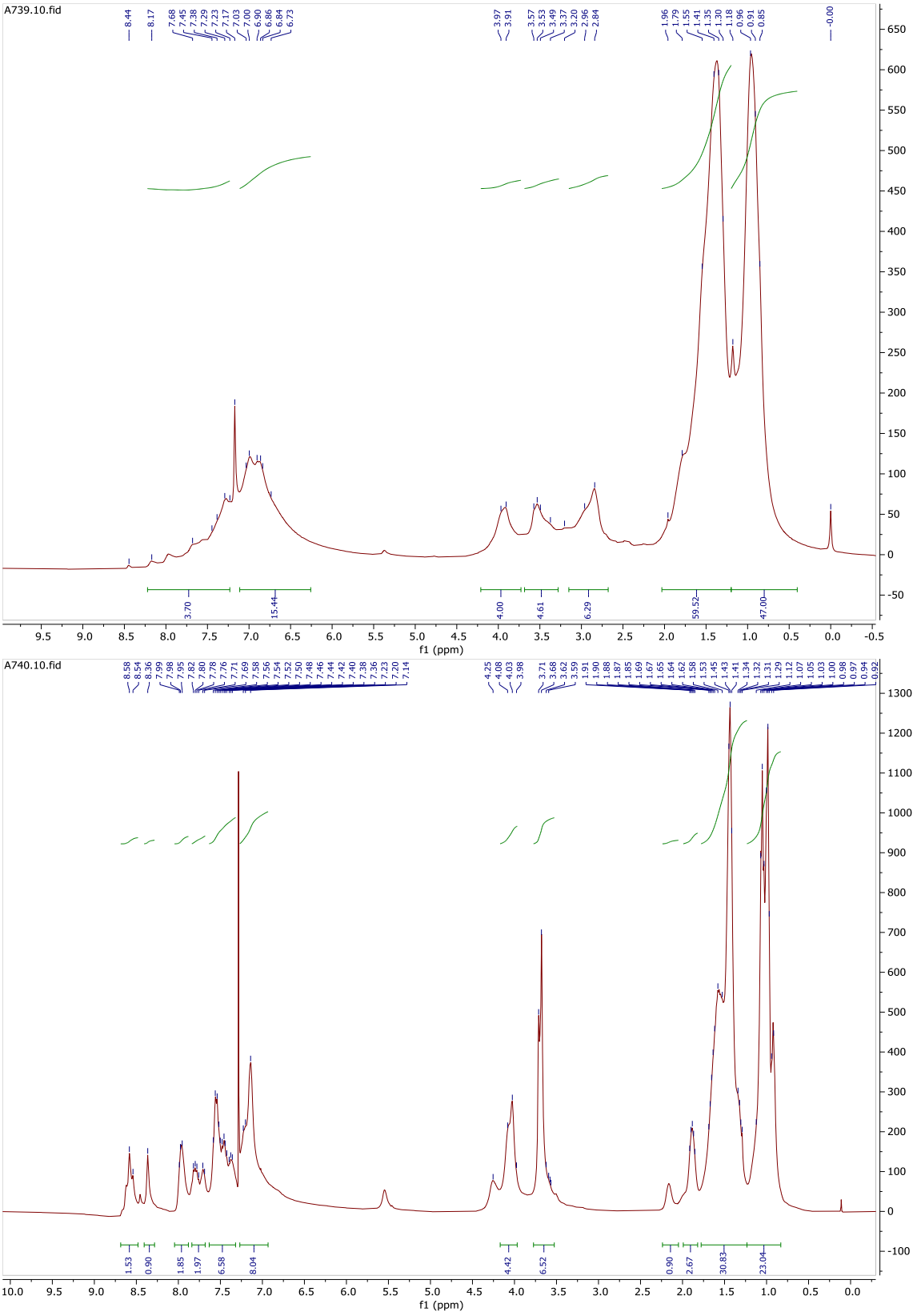

Figure A-25. ^{1}H spectrum of polymer 5r-TPTQ

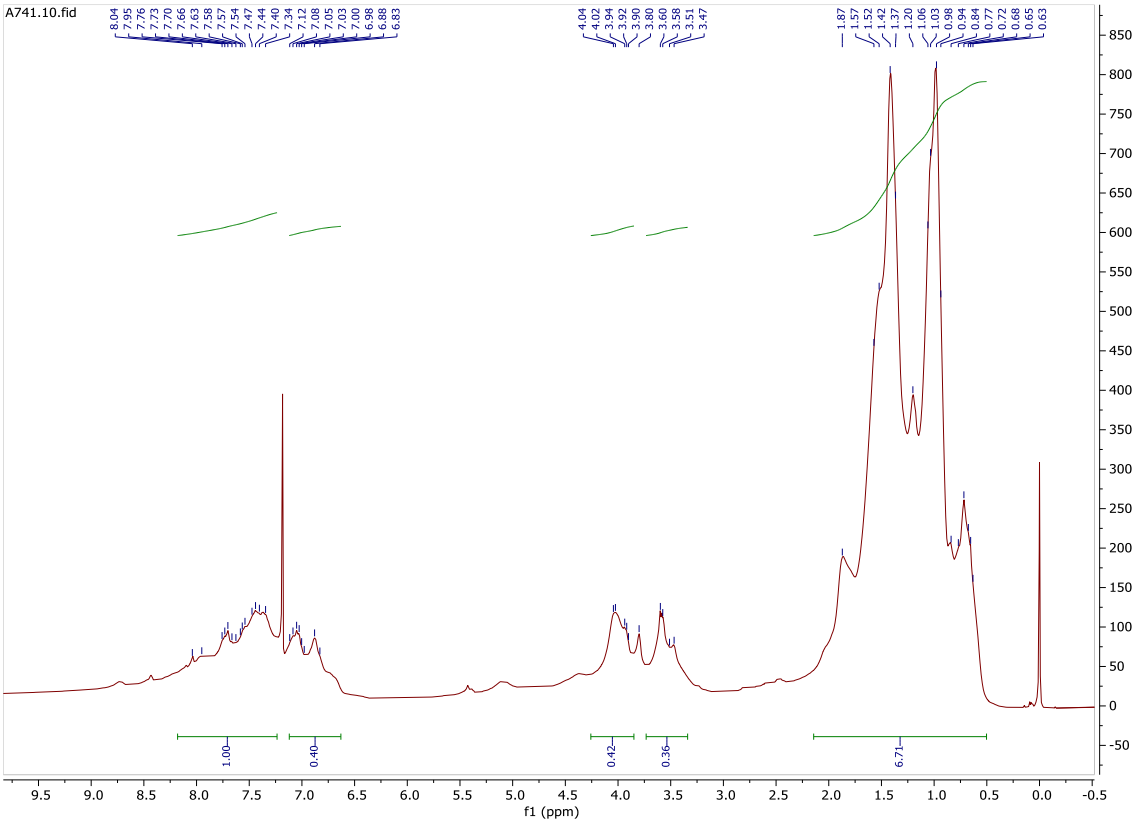

Figure A-26. ^{1}H and ^{13}C spectra of compound 5-7

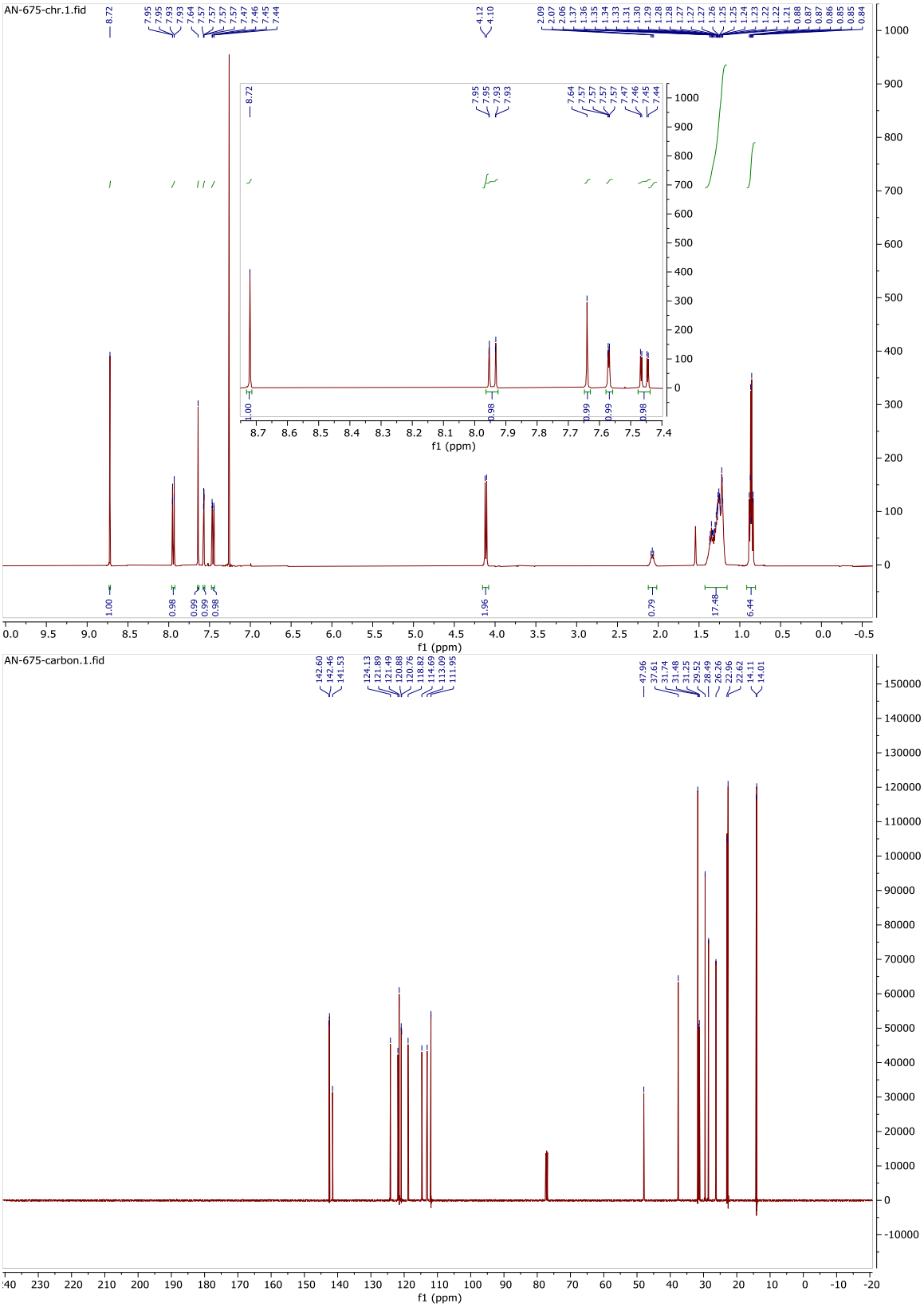

Figure A-27. ^{1}H and ^{13}C spectra of compound 5-8